# The astrophysics of energetic x-ray binaries

## Thesis

UNRESTRICTED

# The Astrophysics of Energetic X-ray Binaries

Richard Neil Ogley B.Sc. M.Sc.

A thesis submitted to the

Open University

for the degree of

Doctor of Philosophy

in the Faculty of Science

December 1998

Author number: M7205126
Date of submission: 15 December 1998
Date of award: 26 January 1999

# RESEARCH DEGREES CENTRE

# LIBRARY AUTHORISATION FORM

Please return this form to the The Research Degrees Centre with the two bound copies of your thesis to be deposited with the University Library.
All students should complete Part 1. Part 2 only applies to PhD students.

Student: RICHARD NEIL OGLEY PI: M7205126

Degree: PHD

Thesis title: THE ASTROPHYSICS OF EVECTIC X-RAY BINARIES

## Part 1 Open University Library Authorisation [to be completed by all students]

I confirm that I am willing for my thesis to be made available to readers by the Open University Library, and that it may be photocopied, subject to the discretion of the Librarian.

Signed: R.N Ogley Date: 30/1/99

## Part 2 British Library Authorisation [to be completed by PhD students only]

If you want a copy of your PhD thesis to be available on loan to the British Library Thesis Service as and when it is requested, you must sign a British Library Doctoral Thesis Agreement Form. Please return it to the Research Degrees Centre with this form. The British Library will publicise the details of your thesis and may request a copy on loan from the University Library. Information on the presentation of the thesis is given in the Agreement Form.

Please note the British Library have requested that theses should be printed on one side only to enable them to produce a clear microfilm. The Open University Library sends the fully bound copy of theses to the British Library.

The University has agreed that your participation in the British Library Thesis Service should be voluntary. Please tick either (a) or (b) to indicate your intentions.

[a] ☑ I am willing for the Open University to loan the British Library a copy of my thesis. A signed Agreement Form is attached.

[b] ☐ I do not wish the Open University to loan the British Library a copy of my thesis.

Signed: R.N Ogley Date: 30/1/99

# Abstract

This thesis is a study of the X-ray binary Cygnus X-3, and related objects, using primarily observations at radio, sub-mm and infrared wavelengths. I find the emission mechanism to be synchrotron in the radio and sub-mm, while the infrared emission is thermal from the hot wind. The upper limit to the synchrotron emission is interpreted as being due to spectral ageing and implies a magnetic field strength of 7 T at a distance of 700 $R_{\odot}$ from the centre of the system.

The nature of the companion star in Cyg X-3 was investigated by mid-infrared observations using the *ISO* satellite. I find that the spectrum shows a steady decrease and flattening at longer wavelengths which is consistant with a standard wind emission. Thus the complete quiescent spectrum from Cyg X-3 shows two different emission mechanisms and covers a full 5 decades of frequency.

High sensitivity and high time resolution radio photometry, taken during a minor flare period, reveal rapid (10 minute) increases and decreases in intensity which severely constrain the size of plasmons. Brightness temperatures of typically $10^{10}$ K are found.

I also consider models for the superluminal expansion and contraction of the Cyg X-3 source, observed on a milli-arcsecond scale by Newell et al. (1998). The elliptical shape and the superluminal contraction are particularly hard to explain. Models involving photon beams illuminating shells, or propagating

photon patterns are the most plausible.

A thorough survey for maser emission from these sources has produced strong upper limits and improved our understanding of the circumstellar environment of Cyg X-3.

This thesis has probed the radio-jet X-ray binaries, and made significant advances, opening up more questions about the nature of these sources and new areas of research.

# Frontispiece

"Lion wa tora no ana ni haitte usagi no ko o gaka kara tsukiotosu no ni mo zenryoku o tsuksu to iu"

"A lion will exert itself to the utmost, even when entering a tiger's den, to throw baby rabbits off the cliff"

– Ataru Moroboshi, *Urusei Yatsura Ep 17, Story 34*

# Acknowledgements

First and foremost I would like to thank my supervisor Jocelyn Bell Burnell for help over the course of my PhD. She has taught me many things including diplomacy, scientific skills, English, methods, when to keep my mouth shut, and why PPARC need a section on their grant forms for bribes. But above all she has been a great friend and really good to work for.

As it should be with PhD theses, there are more people to thank than space available. Half of those I owe gratitude to due to professionalism and help in work, and to the other half I owe thanks for the distractions from work. And even these classes overlap.

I wish to thank my collaborators over the years. Anita Richards, thanks for the spectral lines, the caffeine lines, the colourful lines, and the conversational lines. Much of this work has been done with her patient help explaining all kinds of bits and pieces. Also thanks for sending me to Aus for the third time. Rob Fender, thanks for the many comments on bits of work I sent you, and as one ex SJBB-er to another, if I follow in your footsteps, do I have to wear those jumpers? To the many people at Jodrell Bank who have listened to my questions, and told me the best way of doing things: Ralph (for the XRBs), Simon and Tom (for the Merlin), Peter T (for the arrangements), Peter W (for the focusing), Paddy (for the jets), and numerous other off-line/on-line people like Andy, Bev, Pat... To other collaborators I wish to thank Guy Pooley and Elizabeth Waltman for their undivided attention to monitoring these sources,

telling everyone what is going on, and patiently giving out data and telling us all what it means.

Of my friends, and this list is far too small, I would like to thank Tim Ash for taking me down the pub, and for entering into our many shouting matches in the office, let's hope some of the Compact Array photos never get out into the open, although I still think he rigged the World Cup sweepstake. Half of this PhD would not be on track without his help. Indra Bains, for confiding in me and knowing what's going on, again taking some of the credit for helping the PhD along. Michelle Felton, for being Eeny-Meeny :). Nick "contrafibulations" Tothill, for his handy way of being in London for the RAS meetings, together with Matt making many evenings in our fine capital ones to remember. Matt Kenworthy for, together with Nick, helping in London, and finally making it in time one disastrously funny night in Milton Keynes. Duncan Law-Green, for being an fellow otaku, and in one way or the other supplying half of the quotes in this thesis. Stewart Eyres, for a level-headed look at the world in the face of such Idiotically Stupid Observatories. Kaz Hall for taking over when light-weight-Tim couldn't. Stewart Newell, for getting out to become a spy while the going was good, and Busaba Hutawarakorn for letting me see Thailand, not getting me into trouble, and taking all my photos.

And finally, I wish to thank all those people in Milton Keynes who make a nasty place nice (and these are in no order whatsoever): Dips, Diana, Chris, Niall, Mond, Gill, Hannah, G.T., Bea, Cheryl, Julie, Pete's (the weird, the other,

the office, the cleaner), the people in the shops in Kents Hill and Oldbrook and the bloke who left his trousers and boots in the middle of the city centre.

> "A battered old television on which it was only possible to watch Open University Study Courses, because if it tried to show anything more exciting it would break down".
>
> – Douglas Adams, *So Long, and Thanks for all the Fish*

For my family

# Contents

# List of Figures

# List of Tables

# Chapter 1

# Introduction

"The huge yellow somethings went unnoticed at Goonhilly, they passed over Cape Canaveral without a blip, Woomera and Jodrell Bank looked straight through them – which was a pity because it was exactly the sort of thing they'd been looking for all these years.

"Miles above the surface of the planet the huge yellow somethings began to fan out. At Jodrell Bank, someone decided it was a time for a nice relaxing cup of tea".

– Douglas Adams, *The Hitch Hiker's Guide to the Galaxy*

## 1.1 Stellar evolution

There are many different types of stars, and the majority that we see are on the main sequence. The logical explanation for this is that stars start out as one type, spend most of their life on the main sequence, then end up as another type. Why stars alter their type and what happens when they become gravitationally bound into pairs is the topic of this section.

The core of a star is where the energy is generated and is the most important region of the star. Stellar cores exist in two main states: (a) a perfect gas where pressure, density and temperature are related by $P \propto \rho T$; and (b) a degenerate gas where the particles can either be non-relativistic with $P \propto \rho^{5/3}$, or relativistic so $P \propto \rho^{4/3}$. This difference between the pressure dependence of a perfect gas and a degenerate gas is fundamental to whether a star can cool down (in the case of white dwarfs and neutron stars) or has to evolve.

For the majority of a star's life on the main sequence and giant branches the core behaves as a perfect gas. The dependence on temperature together with the system being gravitationally bound gives the star a negative specific heat – any loss in energy causes the star to heat up. This is a consequence of the virial theorem which is formulated in the following way. The total energy of any star is the sum of the internal energy, $U$, and the gravitational energy, $\Omega$. For a bound gravitational system the gravitational energy is equal to $\Omega = -GM^2/R$, and if the star is in hydrodynamical equilibrium then the gravitational force on the outer layers is exactly balanced by the internal pressure in the star. The

total thermal energy, $U$, is equal to half of the gravitational energy so $2U = -\Omega$. To be in hydrostatic equilibrium the sum of these quantities must be zero hence $\Omega + 2U = 0$ and since the energy of the star is $E = \Omega + U$, the total energy of the star is negative.

The virial theorem has dramatic consequences for a star undergoing gravitational contraction which releases an amount of energy, $-\Delta\Omega$. The change in the thermal energy related by the virial theorem is equal to $\Delta U = -\frac{1}{2}\Delta\Omega$ which leaves an excess amount of energy $(-\frac{1}{2}\Delta\Omega)$. This excess energy is usually lost by radiation. So contraction lowers the total energy of the star, it becomes more tightly bound, some energy is radiated into space and the star gets hotter.

While the core remains a perfect gas the situation above continues until the star obtains a positive specific heat. The internal pressure is now independent of temperature so the core becomes degenerate. The star is now a white dwarf or a neutron star which can loose energy by lowering its temperature.

Without nuclear fuel stars contract on a Kelvin-Helmholtz time scale, $t_{\rm KH}$, where

$$t_{\rm KH} = \frac{-\Omega}{L} = \frac{GM^2}{RL} = 3 \times 10^7 \frac{\rm M_\odot^2}{\rm R_\odot L_\odot} \ \ {\rm yr}. \tag{1.1}$$

Stars will evolve on this time scale unless there is an additional source of energy, provided by nuclear burning. The time scale for nuclear burning, $t_{\rm nuc}$, is governed by the efficiency of H to He conversion, the initial mass of the star and

its luminosity. This can be expressed as

$$t_{\rm nuc} = \frac{\eta M c^2}{L} = 10^{10}\,\frac{\rm M_\odot}{\rm L_\odot}\ {\rm yr} \qquad (1.2)$$

where for the numerical evaluation an efficiency of $\eta = 0.007$ has been assumed.

The fate of a star depends on its structure, composition and mass. The evolution off the main sequence is complicated, and depends on all of the above variables. However some main points can be established.

- As nuclear burning of hydrogen into helium occurs in the core, the atomic weight increases. This lowers the pressure which allows the core to contract. As the star must still obey the virial theorem the temperature and pressure in the core now rise. As the supply of nuclear fuel in the core diminishes the core continues to contract.

- When the temperature rises both the energy generation in the core and the temperature gradient increase. The consequence of these factors are the luminosity and radius both increase.

- If the star is massive enough then the increased temperature in the core will initiate helium and higher-mass fuel burning.

This is the first stage of evolution past the main sequence stage. Subsequent evolution now depends on the core mass.

In very low mass stars ($M \lesssim 1\ {\rm M_\odot}$) core contraction occurs until the core

becomes electron degenerate. The temperature in the core is not high enough to ignite higher elements and the star becomes a white dwarf.

In higher mass stars ($1 \lesssim M \lesssim 3$ $M_\odot$), the core also becomes degenerate, but the non-degerate outer layers continue to contract onto the core. The increased temperature from the contraction of the outer layers is transported to the core and a helium flash occurs, when helium burning is initiated in one rapid event. The star is now burning helium in a way common to high-mass stars.

If the star is more massive than about 3 $M_\odot$ then the core does not become degenerate and isothermal. After core hydrogen is depleted, overall contraction causes shell hydrogen burning which will eventually run out and cause the core to contract further, forming a red giant. The temperature increase in the core contraction is sufficient to ignite helium without the helium flash stage. Core helium burning occurs over a timescale of $10^6$ yr (as opposed to seconds in a helium flash). The star is now in layers of hydrogen and helium. When the helium is depleted in the core then helium shell burning may start. Whether the star then goes through contraction and slow carbon burning, or whether a carbon flash occurs again depends on the mass of the star. This process of element ignition will occur until the core becomes degenerate and does not undergo an element flash. Intermediate mass stars may just form a degenerate core, but the more massive stars will evolve through a supernova into a neutron star or black hole.

As a star evolves, its temperature and the radiation it emits changes. The

sudden change of a high mass star from the main sequence to giant and sub-giant can create dramatic changes in the envelope of the star and this sudden change has an effect on the star's surroundings. When a high mass star reaches the supernova phase of its life, the resultant neutron star has an enormous gravitational potential so that the radiation it emits is highly affected. Both gravitational red shift (Taylor et al. 1979) and frame-dragging (Harding & Muslimov 1998) have been demonstrated by binary pulsars, and the interaction between the stellar environment and the radiation field cannot be ignored. The final state of any massive star is either an isolated neutron star or, barring Hawking radiation, is a black hole which is reached either by accretion collapse of a neutron star or by collapse of a super-massive star. The gravitational potential of a black hole is so large that it will have a dramatic consequence on its environment.

## 1.2 Binary stars

The majority of stars are binaries, but most binary stars have separations in which the interaction between the two stars is limited to gravitational attraction. There are no other second-order gravitational effects (which are important in close binary systems and are discussed in later sections), and radiation has little or no effect on the stars.

Kepler's third law is fundamental to the physics of binary stars, and for two

gravitational point masses, $M_a$ and $M_b$, the period, $P$, and separation, $a$, are related by

$$P^2 = \frac{4\pi^2 a^3}{G(M_a + M_b)}. \tag{1.3}$$

If the period is measured in years, separations measured in AU and masses measured in solar masses then the period and binary separation is

$$P_y = \frac{a_{AU}^{3/2}}{(M_a + M_b)^{1/2}}. \tag{1.4}$$

For an example, $\alpha$ Cen has a binary period of 79.92 years and the two stars have spectral types G2V and K1V which would give them a combined mass of around 1.8 solar masses. The mean separation of these stars is therefore 23 AU, which is far beyond the region in which any second-order gravitational effects take place.

Most binary stars are in detached orbits (like $\alpha$ Cen), and nothing surprising happens. As the stars evolve, they loose mass by means of He conversion from H, the mass being lost by energy transport; and the binary slowly separates. While slow for the case of $\alpha$ Cen, giants and supergiants have a higher mass loss rate due in part to their higher mass and therefore faster element conversion, but also due to stellar winds. In these systems, the binary separation can increase at a considerable rate. Typically, in the case of widely separated binaries, the binary system will slowly drift apart in time.

When one considers the close binary stars, with periods of days or shorter, interaction between the two stars occur. All interacting binary systems are evolved, and the main feature governing how the binary will behave is the mass ratio of the stars. Systems with a compact object have the most interaction between the two stars. This is because the compact star has a higher gravitational potential than a non-compact star. In this thesis we will name the compact object the primary, and denote its mass by $M_1$ measured in solar masses. The companion to the compact object we will name the secondary, and denote its mass by $M_2$. In evolved binaries the compact object is usually initially the more massive star, but if mass transfer occurs before the star becomes a compact object the secondary can gain mass and become the more massive star.

The gravitational potential of the system, $\Phi_R(r)$, can be written as

$$\Phi_R(r) = -\frac{GM_1 M_\odot}{|r - r_1|} - \frac{GM_2 M_\odot}{|r - r_2|} - \frac{1}{2}|\omega \wedge r|^2 \qquad (1.5)$$

where $r_1$ and $r_2$ are the position vectors for the centre of masses of the two stars, and $\omega$ is the rotational velocity of the binary (Frank et al. 1992). The potentials for a binary with primary mass $M_1 = 1.4$ (measured in solar masses), and secondary mass $M_2 = 0.35$ (a mass ratio, $q \equiv M_2/M_1$, of 0.25) is shown in figure 1.1. The system has three points of equal gravitational attraction, $L_1$, $L_2$ and $L_3$. The regions inside each star's potential joined at the $L_1$ point is called a Roche lobe. Different types of binary systems are classed by the degree

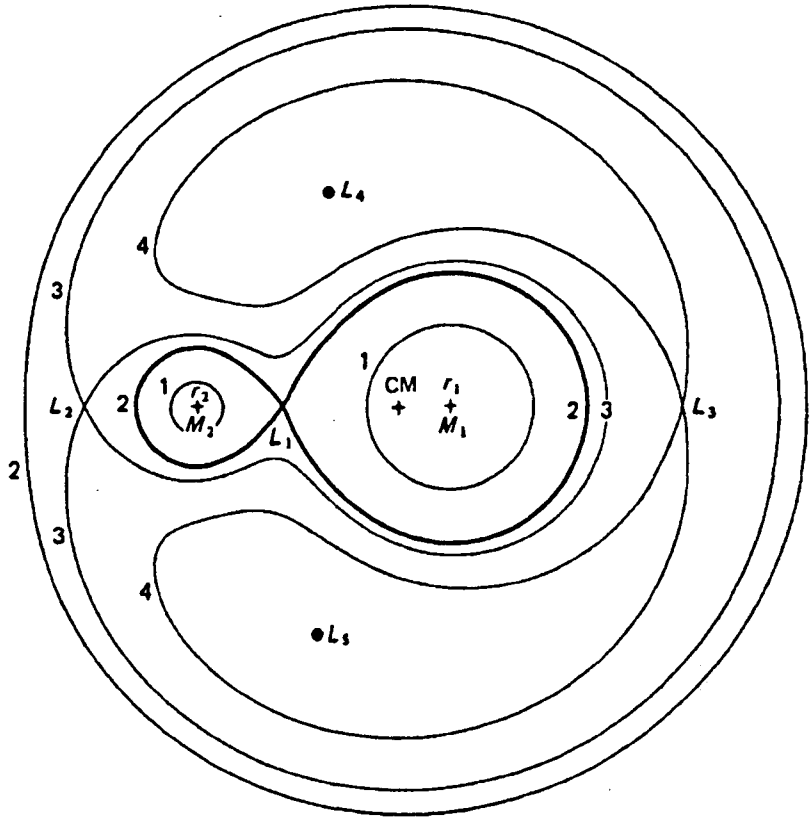


Figure 1.1: The gravitational potentials for a binary system. The primary star's mass is $M_1 = 1.4$ (measured in solar masses) and the secondary star's mass is $M_2 = 0.35$ (a mass ratio of 0.25). Contour lines show regions of gravitational potential between the two stars. $L_1, L_2$ and $L_3$ are the Lagrangian points – saddle points. $L_4$ and $L_5$ are the Trojan points – gravitational wells.

of filling of the Roche lobes.

### Separated binary

If the separation between the two stars in the binary is large the size of the Roche lobes for both stars is also large, and mass transfer by Roche lobe overflow does not occur. The two stars are separated which is the most common type of binary system.

### Common-envelope binary

If the binary separation is small, and both stars evolve so their envelopes fill the Roche lobes a common-envelope binary system can exist. The system is rotating, and an extreme case can occur when frictional forces between the primary and the envelope dissipate angular momentum; the primary then decreases its separation with the secondary until it settles into the core of the secondary producing in effect one star. If the system consists of a giant star and a neutron star it is called a Thorne–Żytkov object. These stars are rare however and it is believed there are less than 10 in the Galaxy, based on binary formation and merging rates (Ergma 1995).

### Contact binary

If the secondary star's envelope expands, which occurs between the main sequence and giant phases, then the envelope can extend past the $L_1$ point. At this stage, the secondary is too large for its orbit, and mass transfer between

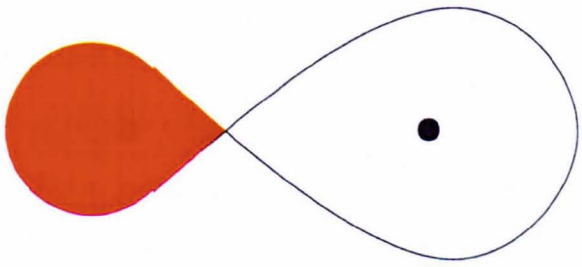

Figure 1.2: A binary with the secondary star in Roche lobe overflow. The star attempts to expand past its Roche lobe, but can only expand at the $L_1$ point where the gravitational potential is a common minimum between the two stars.

the two stars occurs. Mass is transfered through the $L_1$ point into the potential of the primary. At this stage in the binary, the secondary is said to be undergoing Roche lobe overflow, and the binary is now in a state of mass transfer. A diagram of this is shown in figure 1.2.

Because the system has angular momentum, the mass transfered from the secondary into the primary's potential cannot fall strait onto the compact object. The mass travelling in a stream assumes a Keplerian orbit with separation at the $L_1$ distance around the primary. The matter has a small inward velocity and therefore assumes an elliptical orbit around the primary. The orbit quickly circularises, and together with a torque due to viscous forces, the matter sets up an accretion disc around the compact object. This is shown in figure 1.3.

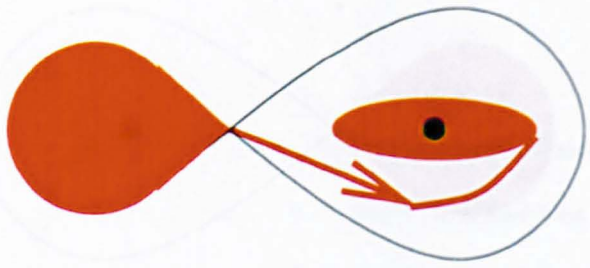

Figure 1.3: The formation of an accretion disc occurs as matter is flowing through the $L_1$ point with angular momentum thus forming a circular orbit. Viscous torques provide an angular momentum loss thus creating a disc around the primary.

### 1.2.1 Low-mass binaries

If the secondary star in an evolved binary is a low mass star ($M_2 \lesssim 3$) then the system is classified as a low-mass binary. The low-mass binaries (LMBs) have short periods and therefore small separations; consequently the size of the Roche lobes are small in these systems. If the secondary star evolves off the main sequence to a giant stage then its radius will increase. If the size of the secondary star becomes large enough that it fills its Roche lobe then the system will become a contact binary. Mass transfer will then occur between the two stars.

### 1.2.2 High-mass binaries

The alternative to a low-mass secondary is a high-mass secondary. The periods associated with these systems are longer than those for their low-mass counterparts, due to the larger separation between two higher mass objects. Roche

lobe overflow can still occur in high mass binaries despite the larger Roche lobe, because of the increased radius of the massive star when it goes through He, C and N shell burning. Binary systems with massive star components evolve in a complicated way. For an example, consider the case of a 20 $M_\odot$ primary and a 6 $M_\odot$ secondary. As the more massive star evolves it can transfer mass to its companion reversing the mass ratio, and then explode in a supernova. What was the 20 $M_\odot$ primary is now a 2 $M_\odot$ black hole, and the 6 $M_\odot$ secondary is now a 20.6 $M_\odot$ giant (Bowers & Deeming 1984). Now the secondary evolves at a faster rate due to its higher mass, expanding into a blue supergiant; mass is accreted onto the compact primary first by the strong wind, and then by Roche lobe overflow.

For a system with a large stellar wind and a compact primary in orbit around the secondary[1], a small percentage of the wind is gravitationally bound to the compact object, and a small accretion disc is set up around it. We now have Bondi–Hoyle accretion which is shown in figure 1.4. If the secondary star has a wind with a velocity $v_w$ which is blown onto the primary star as it orbits around the secondary, all material within a radius $r_{acc}$ will accrete onto the secondary. This radius is calculated by equating the potential energy of the primary with

[1] As the mass ratio for the two stars increases, the centre of mass can usually be taken as the centre of the secondary star – to a first approximation.

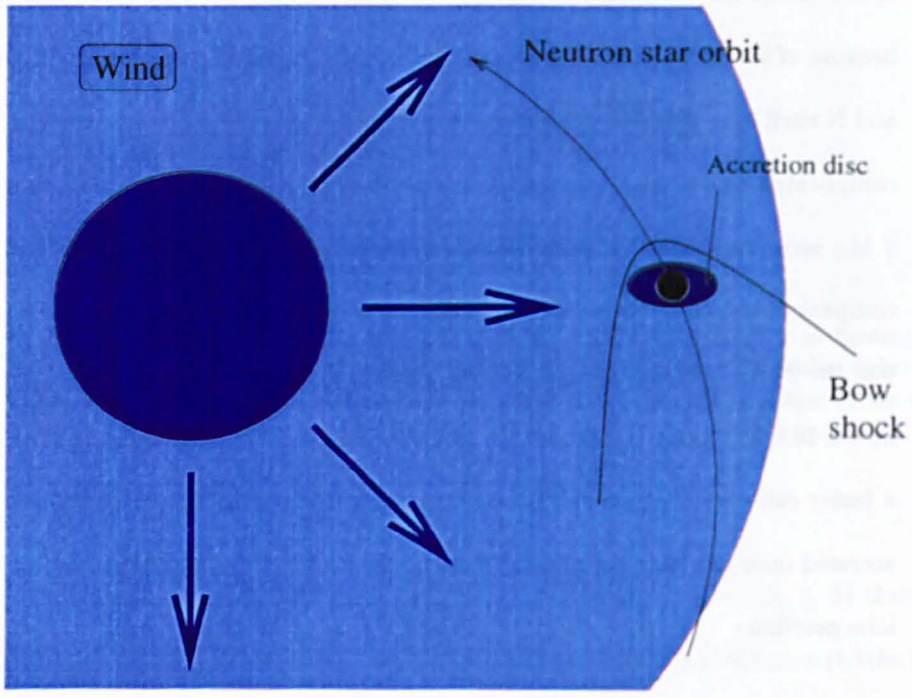


Figure 1.4: A diagram of Bondi–Hoyle or wind accretion. The wind of the secondary has a velocity which is comparable to the rotational speed of the primary around the centre of mass. A certain percentage of wind is captured by the gravitational field of the compact object and an accretion disc is set up around it.

the kinetic energy of the wind.

$$r_{\rm acc} = \frac{2GM_1{\rm M}_\odot}{v_{\rm rel}^2} \tag{1.6}$$

where $v_{\rm rel}$ is the relative velocity between the wind and primary's orbital velocity, $v_{\rm rel}^2 = v_{\rm orb}^2 + v_{\rm w}^2$, $v_{\rm orb}^2 = GM_2{\rm M}_\odot/a$, and $M_1$ is the mass of the compact object (accretor), $M_2$ is the mass of the companion star (the donor). The

amount of material accreted onto the secondary star is the amount of material within this radius,

$$\dot{M} = \pi r_{\rm acc}^2 v_{\rm rel} \rho, \tag{1.7}$$

and if the wind is uniform then the density can be written as

$$\rho = \frac{\dot{M}_{\rm w}}{4\pi a^2 v_{\rm w}}. \tag{1.8}$$

The fraction of the wind that is accreted can therefore be written as

$$\frac{\dot{M}}{\dot{M}_{\rm w}} = \left(\frac{M_1}{M_2}\right)^2 \frac{\left(v_{\rm orb}/v_{\rm w}\right)^4}{\left(1+\left(v_{\rm orb}/v_{\rm w}\right)^2\right)^{3/2}}. \tag{1.9}$$

For a primary of 1.06 $M_\odot$, a secondary of 16.8 $M_\odot$ and a period of 3.9 days (SMC X-1), $v_{\rm orb}$ = 190 km $s^{-1}$. If a wind mass loss rate of $\dot{M}_{\rm w} = 10^{-5}$ $M_\odot$ $yr^{-1}$ and a wind velocity of 2,000 km $s^{-1}$ is assumed then the mass accreted onto the primary is $3 \times 10^{-10}$ $M_\odot$ $yr^{-1}$, or 0.00003% of the mass in the wind.

Perhaps the most extreme case of this is of Be star X-ray binaries where initially the system is a detached binary with the compact object in a highly elliptical orbit around a Be star. As the compact object reaches periastron, wind accretion from the secondary causes the system to flare in the optical region giving it a long on-off cycle of emission.

### 1.2.3 Binary evolution

The consequence of Roche lobe overflow is that mass transfer between the two stars will occur. This will cause the binary to evolve in some way. Any mass transfer will change the mass ratio between the two stars, but it will also alter the period and binary separation due to the exchange of angular momentum.

To see how the Roche lobes evolve, a characteristic radius for the distance between the Roche lobe and the centre of mass for the star needs to be established. An approximate formula for the distance to the $L_1$ point for the secondary, $R_2$ is given by

$$\frac{R_2}{a} = \frac{0.49q^{2/3}}{0.6q^{2/3} + \ln(1 + q^{1/3})} \tag{1.10}$$

where $a$ is the binary separation, and $q$ is the ratio of the masses, $q = M_2/M_1$ (Eggleton 1983). For mass ratios in the range $0.1 \leqslant q \leqslant 0.8$, the approximate form

$$\frac{R_2}{a} = \frac{2}{3^{4/3}} \left( \frac{q}{1+q} \right)^{1/3} \tag{1.11}$$

can be used (Paczyński in Frank et al. 1992). Any evolution at this stage depends on the loss of angular momentum in the binary as material is transported from

the secondary to the primary. The angular momentum in the system is

$$J = M_1 M_2 \left( \frac{Ga}{M_1 + M_2} \right)^{1/2} \mathrm{M}_{\odot}^{3/2} \tag{1.12}$$

so logarithmically differentiating this equation with respect to time and rearranging the equation, the binary separation evolves as

$$\frac{\dot{a}}{a} = 2\frac{\dot{J}}{J} - 2\frac{\dot{M}_2}{M_2}(1 - q)\,. \tag{1.13}$$

To derive this equation, we assume that all the mass lost by the secondary is accreted onto the primary, so $\dot{M}_1 + \dot{M}_2 = 0$. If such conservative mass transfer occurs there is no net loss of angular momentum and hence $\dot{J} = 0$. The evolution of the binary separation depends on whether the mass loss is from the more or less massive star. If the transfer is from the more massive star then the separation increases, whereas if the transfer is from the less massive star the separation decreases.

The rate of mass transfer, and indeed whether mass transfer will occur at all depends on the size of the Roche lobe, which is characterised by equations 1.10 and 1.11. The differentiation of equation 1.11 gives

$$\frac{\dot{R}_2}{R_2} = \frac{\dot{a}}{a} + \tfrac{1}{3}\frac{\dot{M}_2}{M_2} \tag{1.14}$$

which substituting the equation for separation increase gives a Roche lobe dis-

tance increase for the secondary of

$$\frac{\dot{R}_2}{R_2} = 2\frac{\dot{J}}{J} - 2\frac{\dot{M}_2}{M_2}\left(\frac{5}{6} - \frac{M_2}{M_1}\right). \tag{1.15}$$

The type of evolution of the Roche lobe now depends on the mass ratio. If $M_2/M_1 > 5/6$ then mass transfer shrinks the Roche lobe and unless the secondary can shrink to accommodate this, mass overflows and is dumped out of the binary on a thermal (or dynamical) time scale. This form of evolution is unstable and rather short lived. If $M_2/M_1 < 5/6$ then the Roche lobe will expand and mass transfer will only occur if the star expands to fill its larger Roche lobe (as can occur as the star ascends the giant branch) or the binary loses angular momentum. It is the latter of these scenarios which is the more likely.

### 1.2.4 Disc formation...

#### ...by Roche lobe overflow

The transfer of material from the secondary to the primary occurs at the $L_1$ point in the system and because the binary is rotating, the matter has a high angular momentum. It cannot directly fall onto the surface of the primary star, but instead orbits in the binary plane at a Keplerian orbit, $R_{\rm circ}$. The orbital

speed of the material at the $L_1$ point is

$$v_{L_1} = \left( \frac{GM_1 M_\odot}{R_{\rm circ}} \right)^{1/2} \tag{1.16}$$

which can be re-written by substituting the orbital velocity and period to be

$$\frac{R_{\rm circ}}{a} = (1+q) \left( \frac{b_1}{a} \right)^4 \tag{1.17}$$

where $b_1$ is the distance of the $L_1$ point from the centre of mass. Plavec & Kratochvil (in Frank et al. 1992) approximated $b_1/a$ to be

$$\frac{b_1}{a} = 0.500 - 0.227 \log q \tag{1.18}$$

and using this approximation the circularisation radius becomes

$$\frac{R_{\rm circ}}{a} = (1+q) \left( 0.500 - 0.277 \log q \right)^4 . \tag{1.19}$$

A more convenient form can be used if the circularisation radius is written in terms of the orbital period rather than the binary separation. In this form equation 1.19 becomes

$$R_{\rm circ} \simeq 4 M_1^{1/3} (1+q)^{4/3} \left( 0.500 - 0.277 \log q \right)^4 P_{\rm day}^{2/3} \ {\rm R}_\odot . \tag{1.20}$$

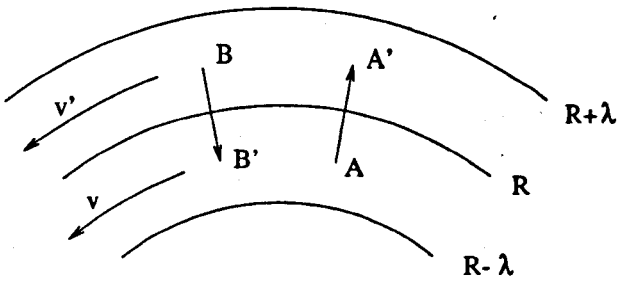


Figure 1.5: A cartoon of two annuli in differential rotation. Material is in chaotic motion and therefore mass is transported from $A$ to $A'$ and $B$ to $B'$ in equal amounts. Due to the disc having a different angular momentum at a radius $R+\lambda$ and $R-\lambda$, viscous torques are setup in the disc.

Of course there are problems for disc formation if the circularisation radius is less than the stellar radius (see section 1.3.2).

In normal systems the matter stream creates a ring of material at $R_{\rm circ}$ around the primary star. Because gas collisions, shocks etc. will dissipate energy, the matter stream loses energy and its radius around the primary shrinks. With continuous matter transfer and energy loss, the matter creates a disc around the primary. The material in the disc is in Keplerian rotation, and is therefore in differential rotation. If one considers two concentric annuli at a radii $R+\lambda$ and $R-\lambda$ as shown in figure 1.5 then random motions in the gas will transport material between the two annuli. If $\lambda$ is a length of order the mean free path length then an equal mass of material is transported between the surface between $A$, $A'$ and $B$, $B'$. Since the two annuli are at different radii and are in differential rotation, there is a difference in angular momentum between $R-\lambda$ and $R+\lambda$. The chaotic motion across the boundary will set up a viscous torque, $G(R)$, on

the disc due to the differential rotation with the form

$$G(R) = 2\pi R\tilde{v}\lambda\Sigma R^2\Omega' \tag{1.21}$$

where $\tilde{v}$ is the velocity of material across the boundary layer, $\lambda$ is the mean free path of the gas (so $\tilde{v}\lambda$ is the kinematic viscosity), $\Sigma$ is the surface density of the disc ($\Sigma = \int \rho \, dz$) and $\Omega'$ is the orbital velocity gradient across the disc ($d\Omega/dR$). Note that for a solid disc, $\Omega'$ is zero and there are no viscous torques.

### ...by Bondi–Hoyle accretion

If the secondary star is massive enough and the primary star is a compact object then because of the large mass ratio, it is unlikely that the Roche lobe of the secondary will be filled. Mass transfer can only occur if the secondary has a strong wind. As discussed in section 1.2.2, as the primary orbits around the secondary, if the kinetic energy of the wind is less than the gravitational energy of the primary then material will accrete onto the primary by Bondi–Hoyle accretion.

The geometry of Bondi–Hoyle accretion is shown in figure 1.6. The wind is supersonic with respect to the compact object and so as the primary ploughs into the wind, a bow shock around the star with an axis along the relative velocity of the wind and the star is formed. The relative velocity $v_{\rm rel}$, given by $v_{\rm rel}^2 = v_{\rm w}^2 + v_{\rm orb}^2$, is inclined at an angle $\beta$ to the wind velocity axis where

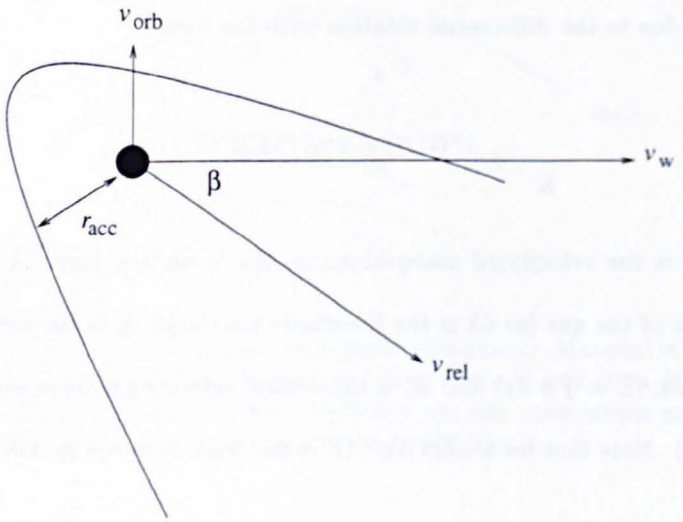


Figure 1.6: Bondi–Hoyle accretion geometry. The supersonic wind creates a bow shock around the neutron star aligned with the relative velocity axis, at an angle $\beta$ to the wind velocity.

$\tan\beta = v_{\rm orb}/v_{\rm w}$. The accretion radius is given by

$$r_{\rm acc} = \frac{G^3 M_1^3 {\rm M}_\odot^3 \omega^2}{v_{\rm rel}^8} \tag{1.22}$$

where $\omega$ is the orbital velocity of the compact object. This equation can be re-written by substituting Kepler's law as

$$r_{\rm acc} = \frac{4\pi^2 G^3 M_2^2 {\rm M}_\odot^2}{v_{\rm rel}^8 P^2}. \tag{1.23}$$

An investigation of the types of accretion for different types of X-ray binary, together with an introduction to individual sources is given below.

## 1.3 Radio-jet X-ray binaries

This thesis concentrates on work carried out on radio-jet X-ray binaries (RJXRBs). While the class of X-ray binaries is large, these objects are only a small subset of XRBs. While radio radiation is the least energetic of the electromagnetic spectrum, the radio emission from X-ray binaries comes from the most energetic process, synchrotron emission. The morphology of RJXRBs is similar to X-ray binaries in that a compact object is orbiting (or orbited by) a secondary star from which matter is being transfered. This matter is heated up to X-ray temperatures and X-rays will most likely come from an accretion disc or wind accretion cylinder very close to the compact object.

The emission of synchrotron radiation needs a large input of energy to accelerate the electrons to relativistic velocities and therefore the logical place for this to occur would be close to the compact object together with the X-ray gas. However, the density of electrons around that region would create an optically thick medium for the radio photons which would render them undetectable. One mechanism for acceleration of electrons and ejection of electrons from an optically thick medium are jets. The accretion mechanism both accelerates the electrons to create synchrotron radiation and also ejects the jets. However radio jets are rare; out of 200 known X-ray binaries only $\sim$ 25 have radio emission, and out of these only about a third have confirmed radio jets. For a review see Fender et al. (1997a). In order of jet discovery these are

**SS 433** This source was observed to have radio jets by Spencer (1979) and consists of a neutron star with an OB star companion. Hjellming & Johnston (1981) mapped the outflow with the VLA and confirmed the existence of 0.3 $c$ jets. This source is the most studied of all radio jet binaries and is in a minority for having an optical counterpart.

**Cygnus X-3** Despite the source having been discovered over 30 years ago (Giacconi et al. 1967) it is the most enigmatic of all RJXRBs. Frequent radio monitoring has discovered a number of emission states, but while jets have been reported, no two maps have shown the same ejecta moving (see chapter 4 in this thesis.)

**LSI+61° 303** This source periodically flares with a measured expansion following the outburst (Massi et al. 1993).

**Cir X-1** Radio jets from this source have been associated with flaring activity, similar to LSI+61° 303 (Stewart et al. 1993).

**GRS 1915+105** The first relativistic jet source in the Galaxy; it shows classical superluminal motion (Mirabel & Rodríguez 1994). Recent radio and X-ray monitoring have provided information on the structure of emission to rival Cyg X-3, and it is quickly becoming the most studied RJXRB.

**GRO J1655−40** Shortly after the discovery of the superluminal motion in GRS 1915+105, Tingay et al. (1995) discovered a similar phenomenon in GRO J1655−40. This source has a semi-eclipsing optical counterpart, and

a well-determined mass for the compact object (making it a black hole) has been determined.

This thesis is a detailed collection of work on two radio-jet X-ray binaries: Cygnus X-3 and GRS 1915+105. A complete observing programme was undertaken on other RJXRBs as well as the above two sources in a wide search for maser emission; however since that programme failed to detect maser emission from these sources they are not further discussed here.

### 1.3.1 GRS 1915+105

#### Radio emission

The radio emission from GRS 1915+105 follows no logical pattern and can exist in any of five states: (a) flaring, (b) quenching, (c) quasi-periodic oscillations, (d) periodic oscillations and (e) chaotic behaviour. An example of the radio flux at 2.25 GHz over a period of approximately one year is given in figure 1.7. Data are taken from the Green Bank Interferometer (GBI) and show both flaring and quenching behaviour. However during the quenched times (MJD 50760–50900), the flux is not constant, but highly variable on minute timescales.

Quasi-periodic oscillations of flares on 20–40 minute timescales have been observed from the source at 15 GHz with the Ryle telescope (Pooley & Fender 1997). On these timescales the source does not follow any logical pattern with many states observed. The period can be constant then suddenly change, there are times when small gaps occur with no flaring, and the source then restarts its

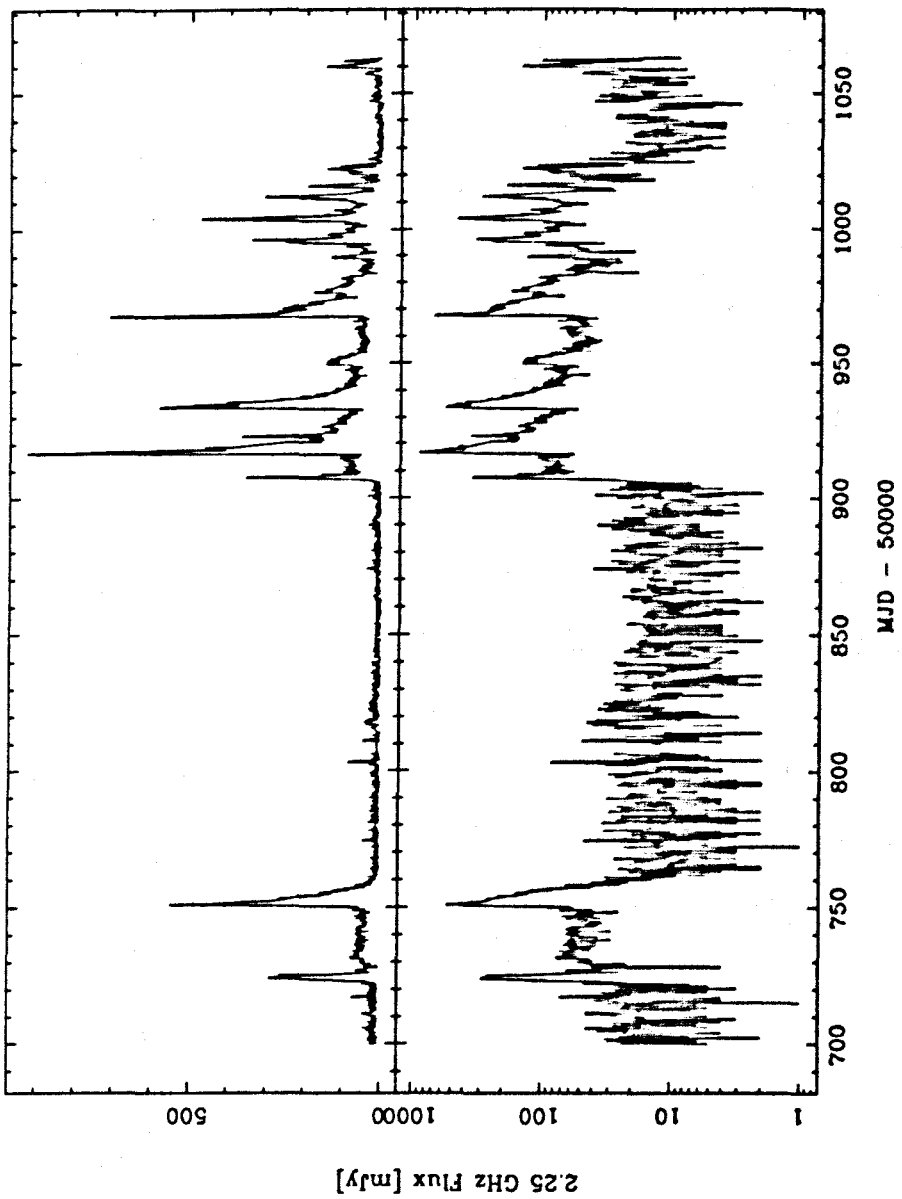


Figure 1.7: GRS 1915+105 photometry over a year at 2.25 GHz from the Green Bank Interferometer. Lower panel is a logarithmic flux scale and shows that what is apparently constant zero flux between MJD 50760 and 50900 is rapid small scale fluctuations. RMS error in the data is typically 4 mJy.

periodic oscillations, there are also times of constant non-variable flux. Pooley & Fender (1997) attempted to correlate the radio variability with *XTE* ASM X-ray data, however different states in the radio did not match any of the different states in the X-rays, apart from one phenomenon, X-ray dips (see below).

The one dramatic observation of this source at radio wavelengths was the discovery by Mirabel & Rodríguez (1994) that following a major flare, a bipolar jet was discovered with jet speeds at 1.25 and 0.65 $c$. This constituted the first discovery of a Galactic superluminal source; jets inclined at 70° to the line of sight with velocities of 0.92 $c$ fit the observed data. Recent radio mapping at a higher resolution with the MERLIN array (Fender et al. 1998a,b) showed a similar structure but with a slightly higher jet velocity and different orientation angle. This could indicate that a deceleration of the jets occurred between the MERLIN and VLA angular distances for the jet ($\sim$ 500 mas and 1250 mas respectively), or more probably that the ejection mechanism differed slightly between the two events. The MERLIN observations were the first to make poliarmetric measurements and show the jets to be progressively depolarising with time, consistent with adiabatic expansion and a decrease of the magnetic field. Figure 1.8 shows the MERLIN images for four epochs after the major flare at MJD 50751.

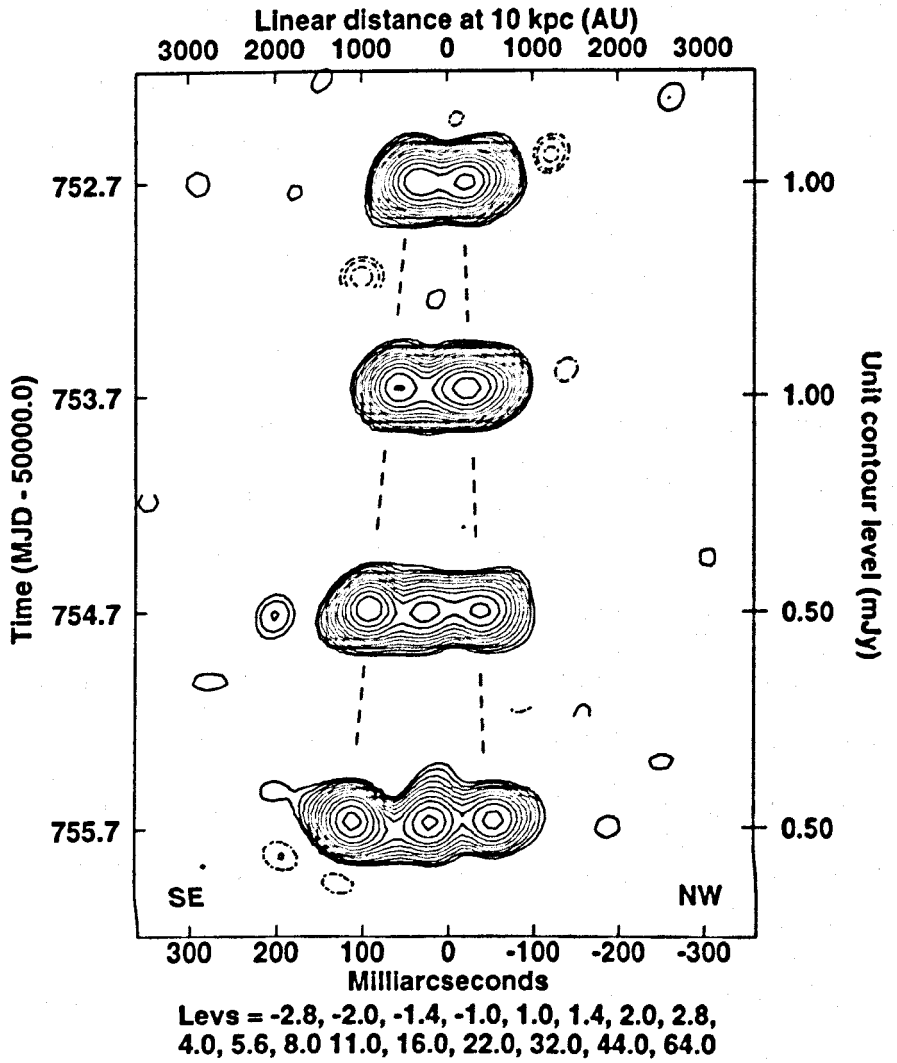


Figure 1.8: MERLIN images of the bipolar jet structure in GRS 1915+105 following a major flare. The superluminal effect is apparent in the increased velocities and intensities of the forward facing (SE) jet (Fender et al. 1998a).

### Infrared emission

GRS 1915+105 was first observed in the infrared by Chaty et al. (1996) who detected a variable component in the JHK band. They did not observe any orbital modulation, but high time resolution while the source was in a radio QPO state show infrared quasi-periodic oscillations (Fender et al. 1997b) indicating the infrared emission is linked to the radio. It has been postulated that this infrared emission is also synchrotron in origin. Spectroscopy (Castro-Tirado et al. 1996) shows the system to have H and He lines which increase in strength when it is in an active X-ray state. There has been a report of an infrared jet from the source (Sams et al. 1996) although detection of such a feature was never repeated and its existence is seriously in doubt.

More recently Mirabel et al. (1997) took multi-wavelength observations of the source at radio, infrared and X-ray wavelengths when the system was in a variable state. Shortly after an X-ray dip (see below), infrared and then radio emission peaked indicating the generation of a jet travelling through an progressively thinning medium. The correlation of radio and infrared flares with that particular emission mechanism in the X-rays strongly suggest the presence of infrared synchrotron emission. Figure 1.9 shows the multi-wavelength data for the source.

Recently (1998 07 31 for two nights) I was involved in high time-resolution sub-mm photometry using the SCUBA instrument on the JCMT. During an active radio period the sub-mm flux was also variable indicating a good link

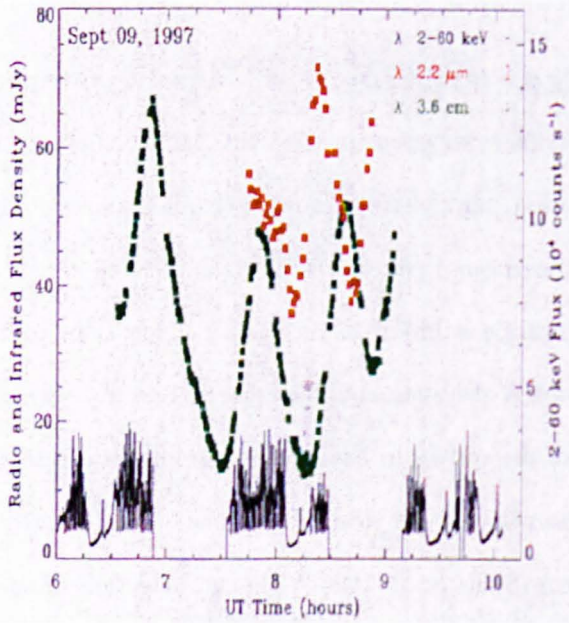


Figure 1.9: Observations of GRS 1915+105 at 3.6 cm (green), 2.2 μm (red) and 2–60 keV (black). Approximately 15 minutes after an X-ray dip at 0815 UT, first the infrared then the radio emission peaks. The X-ray dips are thought to occur at the creation time of radio jets, which we see when the ambient medium becomes progressively optically thin first at infrared wavelengths then at radio wavelengths (Mirabel et al. 1997).

between the radio and infrared synchrotron emission (analysis in progress).

### X-ray emission

The X-ray emission from these energetic X-ray binaries gives us information about the region close to the compact object. In the case of GRS 1915+105 it is generally assumed the compact object is a black hole. However (as is usually the case with these sources) no standard model for black hole accretion and

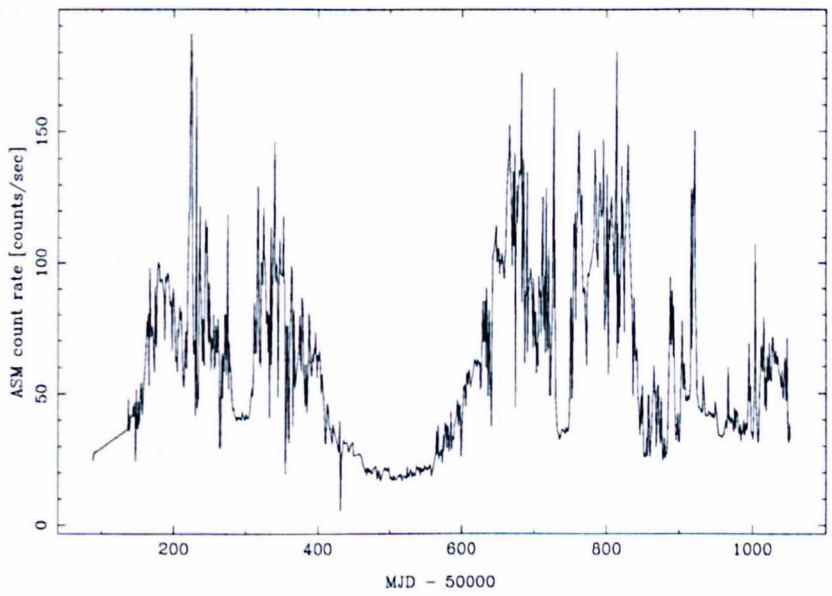


Figure 1.10: X-ray photometry of GRS 1915+105 by the *XTE* ASM instrument at 2–10 keV. Counts are absolute with the Crab at a level of 75 counts $s^{-1}$. Dips on this time scale (e.g. MJD 50300) are not the same as the X-ray dips in figure 1.11.

X-ray production fits the observed X-ray emission. To show typical variability in the source figure 1.10 shows 3 years of monitoring data – averaged over daily time bins. There exists a great wealth of structure. Although the X-ray dip shown at MJD 50300 looks similar to the dips shown in figure 1.9, they are on very different time scales and are probably unconnected.

Both GRS 1915+105 and GRO J1655−40 are black hole candidates. The canonical black hole candidate goes through four different states – a very-high

(VHS), high/soft (HS), intermediate (IS) and low/hard (LS) state – which depend on the accretion rate. The stable intervals in the X-ray light curves are consistent with this picture of a canonical black hole candidate. The emission arises from a disk at a black body temperature of 1–2 keV and an inner radius of a few dozen km (Belloni et al. 1997).

While a stable X-ray state is useful in predicting possible morphologies, the source does not behave in an agreeable way all the time. These occur during periods of rapid X-ray variability and show as 'square wave' dips in the light curve. Two examples of these are given in figures 1.11 and 1.12. A proposed model for the interpretation of the X-ray variability involves the appearance and disappearance of the inner region of the accretion disc (Belloni et al. 1997).

### 1.3.2 Cygnus X-3

#### Radio emission

As in GRS 1915+105, the radio emission from Cyg X-3 follows no obvious pattern. The standard states of emission are (a) a quiescent state with radio flux around 100 mJy at 2 GHz, (b) a minor flare episode when radio flux increases from quiescence up to 1 Jy and (c) a major flare episode when radio flux increases from quiescence to over 1 Jy. There also exists a quenched state which precedes a major flare; the quenched flux is around 10 mJy. The 1 Jy cutoff between the minor and major flare states is an arbitrary value; however there is evidence

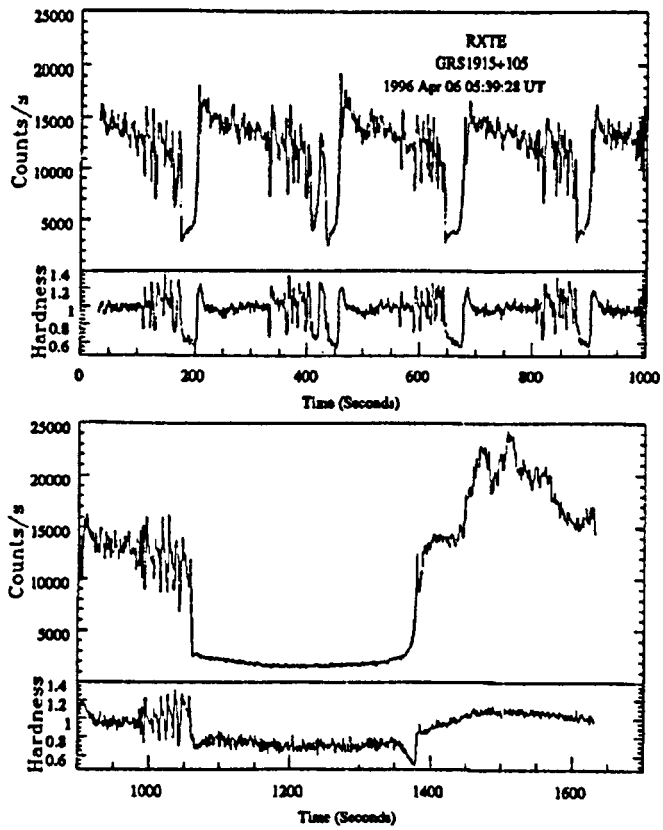


Figure 1.11: X-ray dips observed in GRS 1915+105. Small intermediate dips were observed which were terminated by a very long dip. The X-ray variability increases with time while the source is in the 'on' state (Greiner et al. 1996).

that minor and major flare episodes are intrinsically different in their creation mechanism (Newell 1996). An example of the three main states of radio emission is shown in figure 1.13. The time interval between different flare states is never constant.

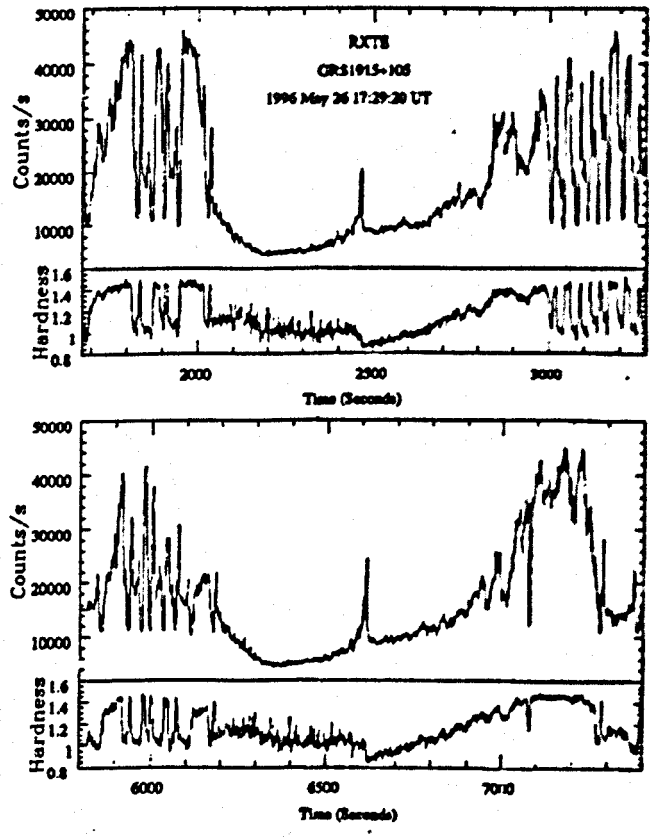


Figure 1.12: Another example of X-ray dips, but these show an intermediate dip spike (Greiner et al. 1996). The spectral change at the spike time indicates a structural change, possibly the onset of jet ejection.

*Major and minor flare events*

It appears that the interval between major flare periods in Cyg X-3 is 18 months. Figure 1.14 shows data at 2.25 GHz from MJD 50400 to 51070, for a period of around 22 months. Only data over 1 Jy has been selected. Between MJD 50460 to 50620 major flares occur, but there were no major flare episode

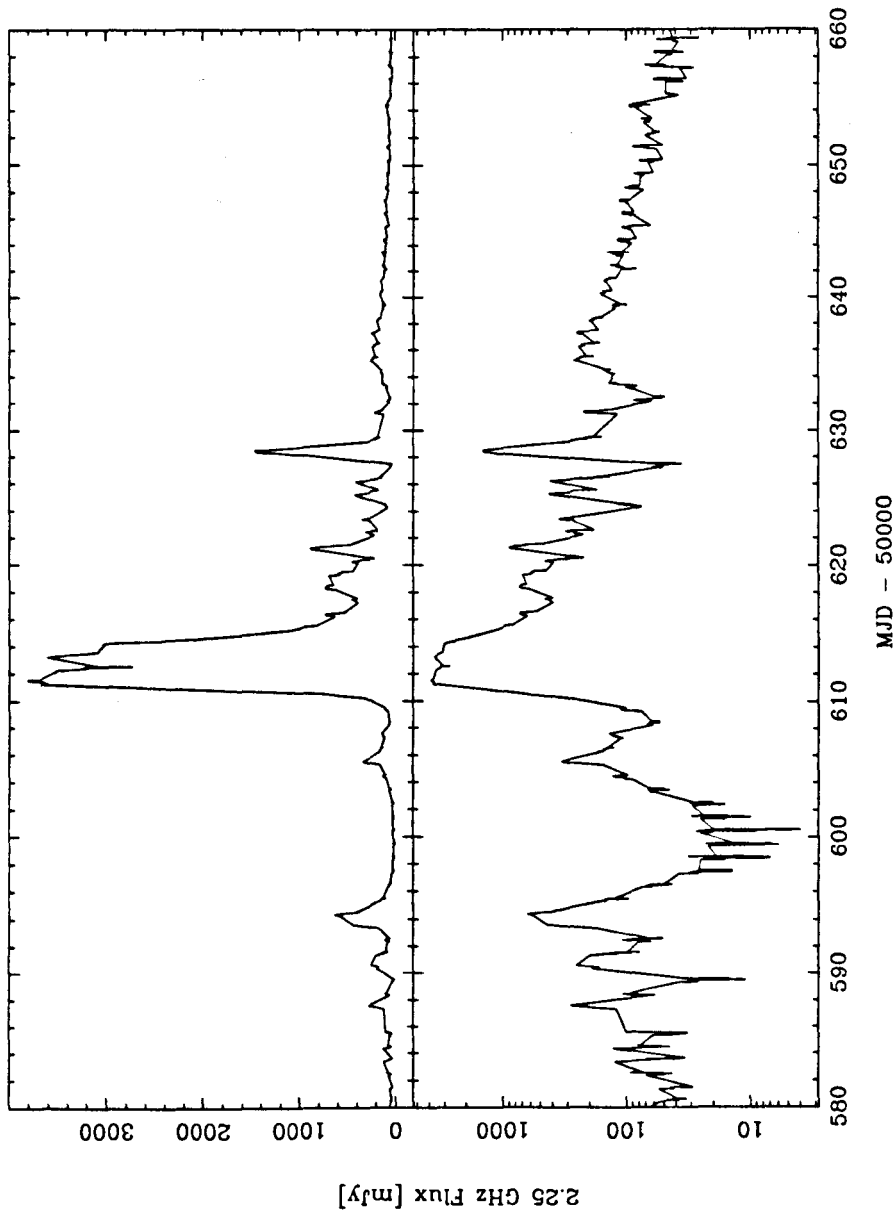


Figure 1.13: Radio photometry of Cyg X-3 at 2.25 GHz from the Green Bank Interferometer. Both panels show flux, the lower panel is a logarithmic flux scale. Data shows a number of states: major flares occurred at MJD 50610 and 50629, minor flares occurred between 50588 and 50596 (as an example) and a quenching period between 50596 and 50604 occurred before the flare activity. Data after MJD 50630 show some level of quiescence.

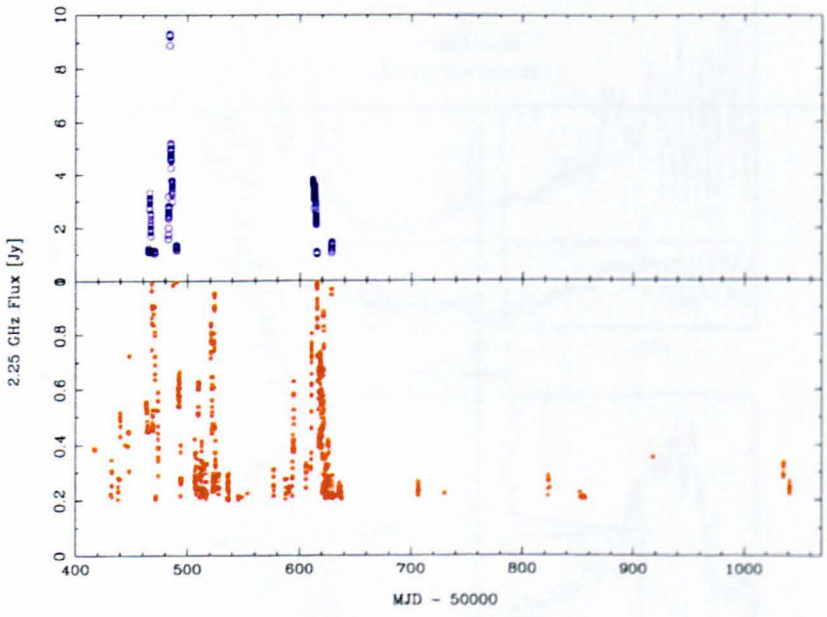


Figure 1.14: Cyg X-3 photometry at 2.25 GHz showing major flare events (blue) and minor flare events (red). Data covers a 22-month interval and a number of major flares occurred which does not support an 18-month major-flare period. A minor flare period generally existed with a major flare episode, a number of weeks before or after the major flare. A cutoff of 200 mJy was used for the minor flares so not to confuse the data with a quiescence level of 100 mJy.

in the previous 14 months which would support this 18 month hypothesis. However, the 18 month cycle is generally thought to only contain one major flare event, and this is not the case shown in this figure.

The minor flare state occurs when the flux at 2.25 GHz leaves the quiescent value of $\sim$ 100 mJy, and increases up to 1 Jy. Minor flares are shown in the lower panel of figure 1.14 and accompany the major flare episodes. While a level of minor flare activity can exist for a number of weeks before or after a major

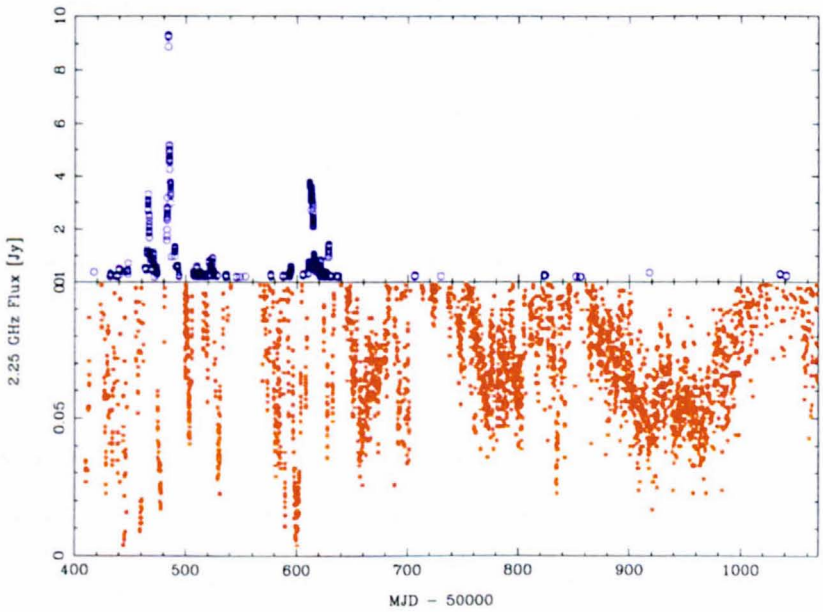


Figure 1.15: Cyg X-3 quenching events at 2.25 GHz (red) together with the flare (major and minor) events (blue). For the majority of the time between MJD 50400 and 51070 Cyg X-3 has a flux below 100 mJy. While most quenching events below 50 mJy resulted in a flare, the extended quenched period between MJD 50900 and 51000 did not result in the expected major flare.

flare, the existence of a minor flare does not necessarily accompany a major flare (for example MJD 50520, 50705, 50820...).

*Quenching*

Preceding a flare event there generally exists some form of quenching. This occurs as a significant reduction in the quiescent flux of 100 mJy, usually to around 10–50 mJy. The amount of quenching is significant and the correlation between flare and quenching is shown in figure 1.15. As one can see, there is significant deviation from any expected flare behaviour.

| Radio state | Flux at 8.3 GHz | Spectral index ($S \propto \nu^{\alpha}$) |
|---|---|---|
| Normal Quiescence | $\sim$ 100 mJy | $\alpha = +0.25$ |
| Quenching | $\lesssim$ 30 mJy | $\alpha = -0.50$ |
| Pre-flare quiescence | $\sim$ 100 mJy | $\alpha \sim +1.2$ |
| Flare and post flare | $>$ 1 Jy | $\alpha \rightarrow 0 \rightarrow -0.5 \rightarrow +0.25$ |

Table 1.1: The different spectral states for Cyg X-3 between data at 2.25 and 8.3 GHz from the GBI (Waltman et al. 1995). These states to the data are in time order and usually all occur with a major flare.

*Spectral behaviour*

With a chaotic flare behaviour one would expect a complicated evolution of spectral index. Much work was done by Waltman et al. (1995) on the evolution of the spectral index between 2.25 and 8.3 GHz GBI data. Analysing data in early 1994 they identify 4 different spectral states which are strongly linked to different flux states. The flux and spectral states are given in table 1.1.

A plot of the spectral index for data between MJD 50400 and 50650 (the two major flare events) together with the flaring events is shown in figure 1.16. There is some evidence of classical spectral behaviour as reported in table 1.1, but over the time range shown in figure 1.16 there is a large spread of spectral indices over all the flux states. If one averages the data over all the data range, the spectral index is $\alpha = 0.08 \pm 0.2$, or zero within errors

*Morphology*

While it would be useful to obtain a detailed image of Cyg X-3, in any of radio, infrared or X-ray bands, this has proved a difficult problem due to the variability of the source. For a detailed discussion and interpretation of radio

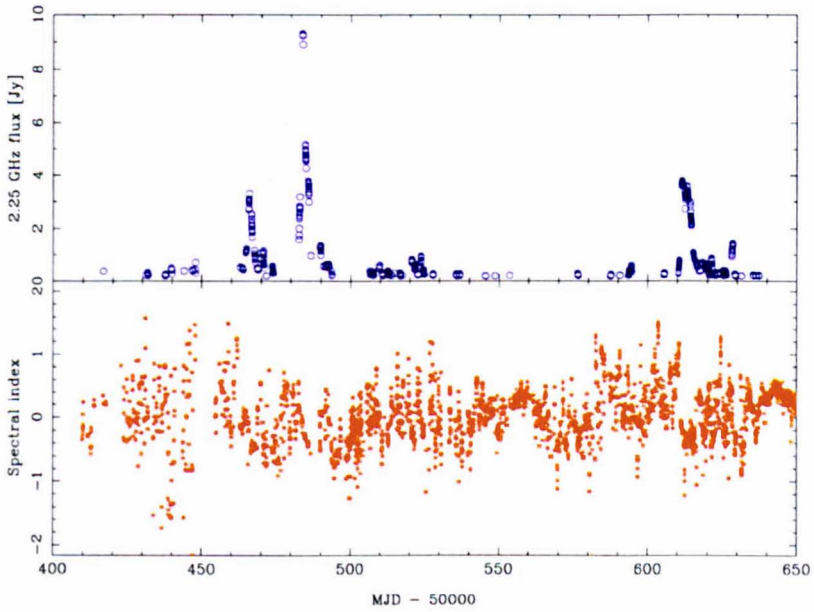


Figure 1.16: The spectral index for Cyg X-3 for data at 2.25 and 8.3 GHz from the GBI for a time covering the two major flares (MJD 50400 to 50650). While there exists some evidence of standard spectral behaviour (for example the flare at MJD 50615), the spectral index is variable; averaged over this whole data set and all flux states the spectral index is zero.

mapping of Cyg X-3 see Chapter 4 in this thesis.

From the X-ray observations Cyg X-3 must have a compact object as its primary. Whether this is a neutron star or a black hole is the subject of some debate; however an X-ray spectrum shows a signature common to accreting neutron stars and dissimilar from that of firm black hole candidates (Maisack et al. 1994). From this evidence I would favour a neutron star. From spectroscopic infrared observations of emission lines by van Kerkwijk et al. (1992), the secondary star in the system is thought to be like a Wolf–Rayet star of the

WN7 class[2]. The evidence suggests we have a very unusual binary system, a high mass binary with a very short 5 hour period.

Given the above information, some binary parameters can be estimated. The fixed variable in all analysis is the orbital period which is $P = 4.8$ hours. Also, since a variable mass for the compact object would cause many problems, it is usual to fix the mass to be the canonical neutron star mass of $M_1 = 1.44$. If the secondary star is a Wolf-Rayet then it will have a mass of around $10 \leqslant M_2 \leqslant 50$. With masses in this range, the binary separation can be calculated. From equation 1.3, the binary separation is $3.3 \leqslant a \leqslant 5.3\ R_\odot$. Not only is this very small for a binary, but the range is also very narrow: $a = 4.3 \pm 1.0\ R_\odot$.

The small binary separation for this system raises a large number of questions. Firstly, what is the size of the secondary? If it is a massive star then it will have to be larger than a solar radius and if so how close does the orbit of the neutron star come to the secondary. Even though the Wolf-Rayet star in Cyg X-3 may not be a typical WR, a WR photospheric radius can be calculated based on the star's mass. If one defines a photospheric edge at which the optical depth is unity then the radius at which this edge occurs can be written as

$$r_c = \frac{\alpha \sigma_T \dot{M}}{4\pi m_p v_\infty}, \tag{1.24}$$

[2]Recently Fender et al. (1999) have observed Cyg X-3 with a high resolution spectrometer on the Multiple Mirror Telescope (MMT). The quiescent spectrum shows He II and N V lines which match an early-type WN star. However, when the system is in outburst, strong twin-peaked He I lines appear. Furthermore, after an outburst strong He I absorption with a P Cygni profile was seen. They, (Fender et al. 1999), interpretate this as emission from a flattened disc after a period of increased wind density.

where $\alpha = 0.5$ if the wind is fully ionised He, $\sigma_T$ is the Thompson cross section, $\dot{M}$ is the mass lost in the wind, $m_p$ is the mass of the proton and $v_\infty$ is the velocity of the wind at infinity. If one writes the mass loss rate in the form $\dot{M} = 10^{-6}\ M_2\ \mathrm{M}_\odot\ \mathrm{yr}^{-1}$ (van Kerkwijk et al. 1996), and the wind velocity in km $\mathrm{s}^{-1}$ then $r_c$ can be written as

$$r_c = 290\ M_2 v_\infty^{-1}\ \mathrm{R}_\odot. \tag{1.25}$$

For the range of masses of the Wolf–Rayet stars, the optical photosphere has a radius in the range of $1.6 \leqslant r_c \leqslant 8.6\ \mathrm{R}_\odot$. This has the rather unfortunate consequence that for the larger masses the photospheric radius is larger than the binary separation, $0.48 \leqslant r_c/a \leqslant 1.6$. Thus the neutron star will be ploughing through a significantly dense region of the star. Also, given that the compact object will have been more massive than the secondary star in order that the primary will first undergo a supernova explosion and create the compact object before the secondary evolves into a compact object, I favour a lower mass of the Wolf–Rayet star in the 10–20 $\mathrm{M}_\odot$ range.

Following the above argument, we have a system with a 15 $\mathrm{M}_\odot$ primary which is losing mass in a wind at the rate of $\dot{M} \simeq 2 \times 10^{-5}\ \mathrm{M}_\odot\ \mathrm{yr}^{-1}$ and with a velocity of $v_\infty \simeq 1800$ km $\mathrm{s}^{-1}$. It is being orbited by a neutron star with a canonical mass of $M_1 = 1.44$ at a distance of 3.6 $\mathrm{R}_\odot$. The orbital velocity of the neutron star around its orbit is $v_{\mathrm{orb}} = 890$ km $\mathrm{s}^{-1}$ and so the neutron

star is travelling through the wind at a relative velocity of $v_{rel} = 2000$ km s$^{-1}$, summed in quadrature. Using equation 1.6, the accretion radius of material captured in a disc around the neutron star by Bondi-Hoyle accretion can be calculated. $r_{acc} = 0.14$ R$_\odot$ and while this is small, it is larger than the radius of a neutron star. So an accretion disc can be set up in the system. The density of material at the accretion radius of the neutron star can be calculated also, using equation 1.7. With $r_{acc}$, $v_{rel}$ and $\dot{M}$ given above, $\rho = 17$ kg m$^{-3}$.

### 1.3.3 What does Cyg X-3 look like?

As one can see in the previous section, Cyg X-3 is complicated. The system is active over many different spatial scales. An overall picture of the binary is therefore required for a complete description of the system. When a particular observation investigates the Wolf-Rayet wind, or the interaction of jets with their environment, these different observations take place at different distances and places in the system.

To help give a coherent picture, presented in this thesis, a cartoon of Cyg X-3 will accompany each different section of work highlighting where the emission comes from and where it is relavent. Figure 1.17 shows the significant morphology on the larger scales. This is useful in providing the framework for other sizes. An example of the application of this cartoon is shown in figure 1.18 where the photospheric radii at 2-15 GHz are shown (see section 5.2.2 for an application of this).

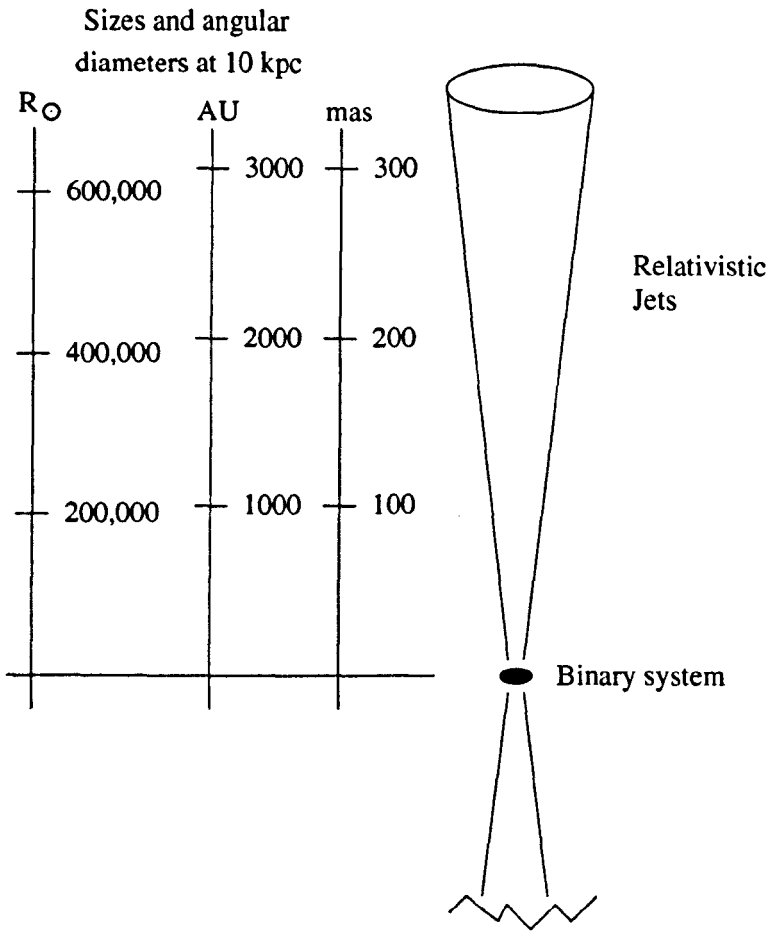


Figure 1.17: A cartoon showing Cyg X-3 on the largest scale.

## 1.4 Conclusions

The complexity and variety of binary star research is both rewarding and frustrating. The Radio Jet X-ray Binaries are the most energetic Galactic sources with close binary orbits and huge gravitational potentials which accelerate rel-

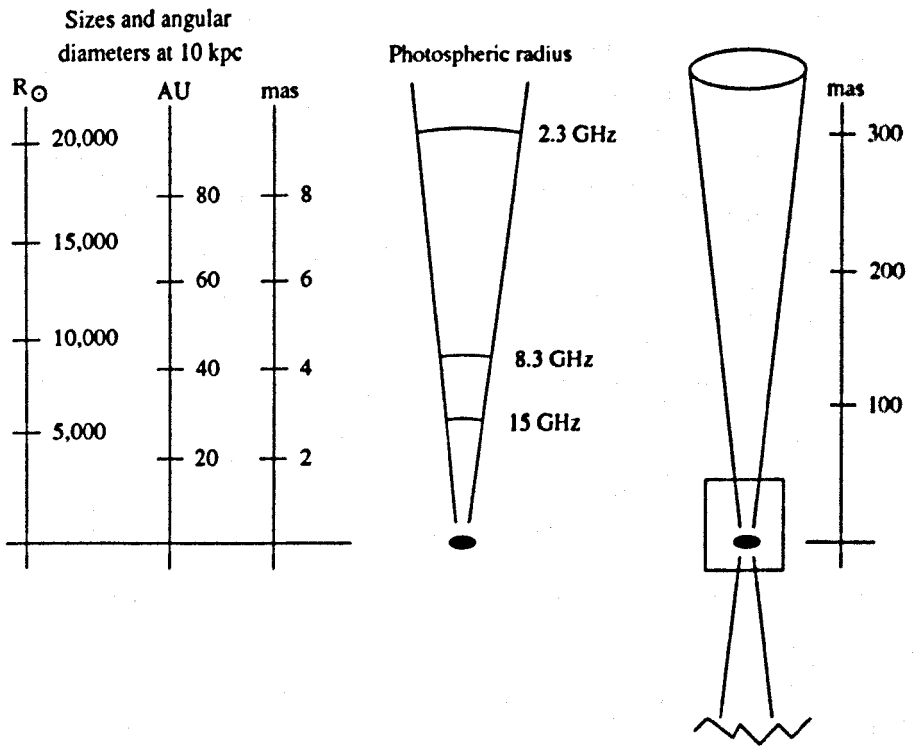


Figure 1.18: A cartoon showing Cyg X-3 on the scale of the photospheric radii given in section 5.2.2

ativistic jets from the systems. As one can see from the sections about GRS 1915+105 and Cygnus X-3, there is an enormous difference in the behaviour of these two sources, and it is a challenge to understand completely what is happening.

The remainder of this thesis tackles some of the important questions concerning both GRS 1915+105 and Cyg X-3, using a mixture of observational evidence and theoretical investigations. Chapters in this thesis include:

**Masers.** A maser search of all the main RJXRBs at both the water and hydroxyl maser frequencies. While no maser emission was found, the resulting upper limits to any emission allow physical parameters of the systems to be investigated.

**Superluminal motion.** Cyg X-3 was observed to show non-classical superluminal motion. This chapter investigates some theoretical models for the source to explain its rather baffling behaviour.

**Multi-epoch MERLIN photometry** An extensive search programme was initiated to map jets from Cyg X-3 on the MERLIN angular scale, following a minor flare. The flaring behaviour prevented mapping of the source, but photometric observations provided the finest time resolution of flares to date, and an investigation into the flare temperature.

**Sub-mm photometry.** The first multi-wavelength photometric observation of Cyg X-3 in a minor flare state which included sub-mm observations is presented in this chapter. The result – that synchrotron emission at 350 GHz is evident in the source – provides the first reliable upper limit to the magnetic field in the jets.

**Infrared photometry** The first infrared photometric observation of Cyg X-3 at 4–15 μm is presented in this chapter.

While a number of significant observations have been taken, this thesis is by no means complete in terms of our understanding of these enigmatic sources.

However, I doubt that an entire career studying microquasars could provide all the answers to these fascinating denizens of the Universe.

## Papers resulting in work presented in this thesis

The following papers which relate to work presented in this thesis have been published.

- Ogley R.N., Bell Burnell S.J., Newell S.J., 1997, MNRAS, 285, 187, "Comments on the superluminal motion in Cyg X-3".
- Ogley R.N., Bell Burnell S.J., Fender R.P., 1997, Vistas Astron., 41, 65, "Modelling of infrared emission from Cyg X-3 and the UKIRT IRCAM3 point spread function".
- Ogley R.N., Bell Burnell S.J., Fender R.P., 1998, Astrophysics and Space Science, 255, 205, "ISOCAM observations of Cyg X-3: Search for a hot stellar wind".
- Ogley R.N., Bell Burnell S.J., Fender R.P., Pooley G.G., Waltman E.B., van der Klis M., 1998, 2nd Workshop on Galactic sources with Relativistic Jets, Ogley R.N., Bell Burnell S.J., eds, New Astr. Rev., 42, 88, "Magnetic field estimation in Cyg X-3's jet".
- Ogley R.N., Bell Burnell S.J., Fender R.P., 1997, in Accretion phenomena and related outflows; IAU Col. 163, Wickramasinghe, D.T, Bicknell, V and Ferrario, L. eds, 121, 775, "Infrared emission around Cyg X-3".

# Chapter 2

# Maser emission from X-ray binaries?

**Lisa:** "...and I'm studying for the math fair.

If I win, I'll bring home a brand new protractor".

**Homer:** "Too bad we don't live on a farm".

– The Simpsons, *Dead Putting Society*

## 2.1 Introduction to masers

Maser emission occurs when the distribution of molecular energies between two levels is inverted with respect to the Boltzmann-distribution, and the molecules emit radiation by stimulated emission. Cosmic maser emission (Molecular /

Microwave Amplification by Stimulated Emission of Radiation) was first discovered by Weaver et al. (1965) at 1665 and 1667 MHz. Observations of W 3 and W 49 provided OH emission lines with unusual line-ratios. The theoretical line-ratios of OH in thermal equilibrium are 5:9 for the 1665:1667 lines in an optically thin gas. The line-ratios approach 1:1 as the optical depth approaches $\infty$; so observed line-ratios of 1655:1667 greater than 1 would be impossible if the molecular gas is in thermal equilibrium. Weaver's interpretation of this was that the OH-1655 line was blended with an emission line of *mysterium*, at approximately the same frequency. They did not observe *mysterium* in absorption!

More non-thermal line emission was discovered from $H_2O$ molecules (Cheung et al. (1969) and quickly followed by methanol ($CH_3OH$) and silicon monoxide (SiO) (Barrett et al. 1971; Snyder & Buhl 1975). There now exist both Galactic and extragalactic masers with many different lines. The majority of Galactic masers occur in two classes of sources: evolved variable stars and star forming regions. Extragalactic masers mainly occur in active galaxies.

### Circumstellar masers

This class of masers exists in environments around Mira, OH-IR and red supergiant stars. The maser emission comes from very thin shells, which expand and are expelled as the source pulsates. This class of objects is highly evolved, has high mass-loss rates of between $10^{-8}$ and $10^{-4}$ $M_\odot$ $yr^{-1}$ and has a high infrared emission component – due to their envelopes of dust.

The stellar wind from these stars is enriched in heavy elements transported from the interior of the star by convection. The wind condenses to form molecules at the stellar surface ($\geq 10^{11}$ m). At a few stellar radii dust also forms when the temperature drops to around 1,000 K. Radiation pressure then propels the material out to distances $> 10^{15}$ m, and different emission lines form at varying distances from the star.

At temperatures around 1,300 K close to the stellar surface, SiO masers are found. The molecule is rotationally and vibrationally excited to produce maser emission from 43 GHz upwards. SiO maser emission is not found beyond around 5 $R_\star$ where the SiO congeals with the dust and is transported out.

With a shell of dust being pushed out by radiation pressure, as one moves away from the central star the temperature decreases and the environment becomes favourable for the formation of $H_2O$ masers. At 22 GHz the maser emission is produced by collisional excitation of water. $H_2O$ is not a hardy molecule, but is prone to dissociation by UV. Dust is very important; it shields the molecule from UV radiation, both from the star, but also from the interstellar medium. The conditions at which this occurs are usually around 15 AU from the star, where densities are $\leqslant 5 \times 10^{15}$ m$^{-3}$, and temperatures are around 1,200–700 K.

In circumstellar envelopes the main source of OH is probably photodissociation of $H_2O$ . The most common masing lines at 1665/1667 and 1612 MHz are radiatively pumped and require temperatures of 100–400 K (1665/7 MHz) or

$\sim$ 50 K (1612 MHz). Recent *ISO* results (Sylvester et al. 1997) confirm that infrared lines from dust provide the pumping radiation. While the dust provides a convenient source of infrared radiation. Its density is sufficiently low that it does not shield the $H_2O$ from UV radiation and the $H_2O$ dissociates back into an OH radical. The OH zones are the farthest from the star at distances of up to $10^{16}$ cm, and hence have the lowest temperatures, around 100 K.

A schematic diagram of the position and conditions of the shells of maser emission is given in figure 2.1.

### Masers in star-forming regions

Observations of circumstellar masers have provided the astronomer with a large amount of information; the regions around star-forming regions are not as well explained as circumstellar masers. Star-forming regions are in giant molecular clouds, which extend over a large region of space, up to 30 pc in diameter, and have masses of around $3 \times 10^5$ $M_\odot$. From a giant cloud a hierarchy of smaller clumps can condense which will form into the stars. As these stars collapse they heat up their surroundings, and the more massive stars undergo dramatic mass-loss, not in shells as with supergiants or Miras, but in bipolar jets. Shocks are therefore created as the jets plough into the surrounding ISM.

Associated with massive star-forming regions are H II regions. As massive stars form, UV radiation creates bubbles of ionised hydrogen. At the boundaries of the bubbles with the interstellar medium there are ionisation fronts, and

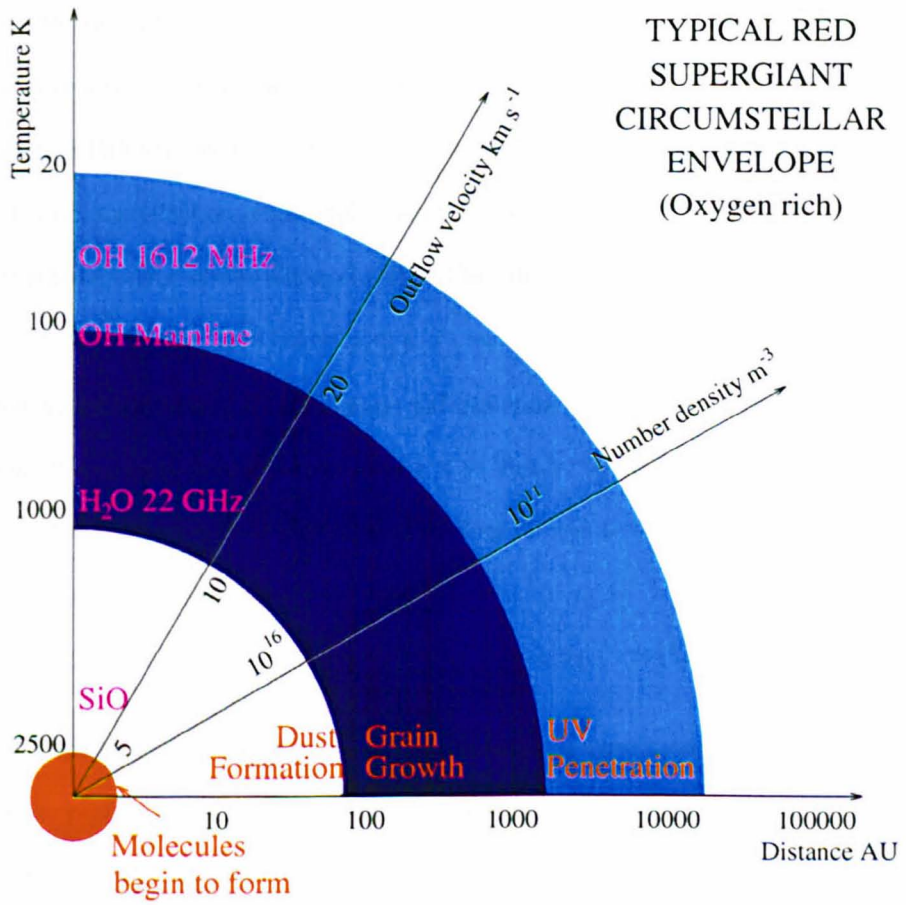


Figure 2.1: Schematic of a circumstellar maser source . SiO, $H_2O$ and OH maser emission is shown at various radii from the star. Temperatures and densities are given. Taken from Richards (1997).

the bipolar jets shock as they cross these boundaries. Such shocked regions are important for maser activity as here there is a mechanism for exciting the molecules. All four ground-state OH lines (1612, 1665, 1667, 1712 MHz) and one excited state at 715 GHz have been identified with H II regions. As discussed previously for circumstellar masers, $H_2O$ can be dissociated by UV radiation

creating OH molecules, and the H II regions provide sufficient radiation for this mechanism. Thus, conditions around the outflow are suitable for OH formation and excitation. As the H II regions expand beyond $\sim 0.1$ pc, the OH emission decreases, but the reason behind this is not clear. It is now thought that the OH emission spots are on the edge of the H II expansion, where the jets hit the ionisation edge.

$H_2O$ masers also exist in star-forming regions, but it is unclear where they originate. One suggestion is that of a disc around a young star in a "warm, dense concentration of molecular gas" (Cohen 1989).

### Extragalactic masers

A few extragalactic masers in the LMC and other nearby galaxies (in the Local Group) seem similar to Galactic masers. However most extragalactic masers (detected at $z \leqslant 0.5$) are freaks in one way or another. The infrared luminosity of these galaxies is huge, $L \sim 10^{12}\ L_\odot$, and is a major component of the luminosity of these galaxies. While most (if not all) Galactic masers are created by outflow, half of the extragalactic masers are associated with the in-fall of material, and appear to exist in thin discs around the central black hole, at very small distances from it.

*OH mega-masers* were detected by Baan et al. (1982) from IC 4553, with a high OH luminosity of $10^3\ L_\odot$. This is $\sim 10^6$ times higher than from Galactic sources, and so the phrase mega-maser was applied to these masers. OH mega-

masers have output powers $\sim 10^{29}$ W. By 1992, almost 50 OH mega-masers had been detected but only in near-by systems with red-shifts out to $z = 0.17$. The brightest OH emission is well explained by a simple model (Baan & Haschick 1984; Baan 1985) in which the nuclear continuum is amplified with a small gain by the intervening molecular material which is typically 100s pc from the nucleus. In IC 4553, the continuum and maser intensities are comparable, which leads to gains of only $e^{-\tau} \sim 2$, $\tau \sim -0.7$ (compared to $\tau = -25$ for Galactic OH masers). Owing to low column densities of OH, there is only modest inversion. In these cases, the amplifying material is in clouds rotating in a disc, usually close to edge-on, around the nucleus.

*$H_2O$ masers.* There are two classes of extragalactic $H_2O$ masers:

(a) Those in star-forming-like systems which are located outside the nucleus. These are the fainter of the two classes.

(b) Brighter systems ($\sim$ 100 times brighter than star-forming-like systems) and further away from us; these have high velocity spreads and exist very close into the nucleus.

A good example of a type-b maser is that in NGC 4258 (Miyoshi et al. 1995). Red and blue-shifted features have been discovered at $\pm$ 1,000 km $s^{-1}$ around the systemic velocity of the galaxy. These features are in Keplerian motion and arise in a disc 4–8 mas from the core, with a thickness of only 0.003 pc. This data is very well explained as emission from material in a region $<$ 0.13 pc in

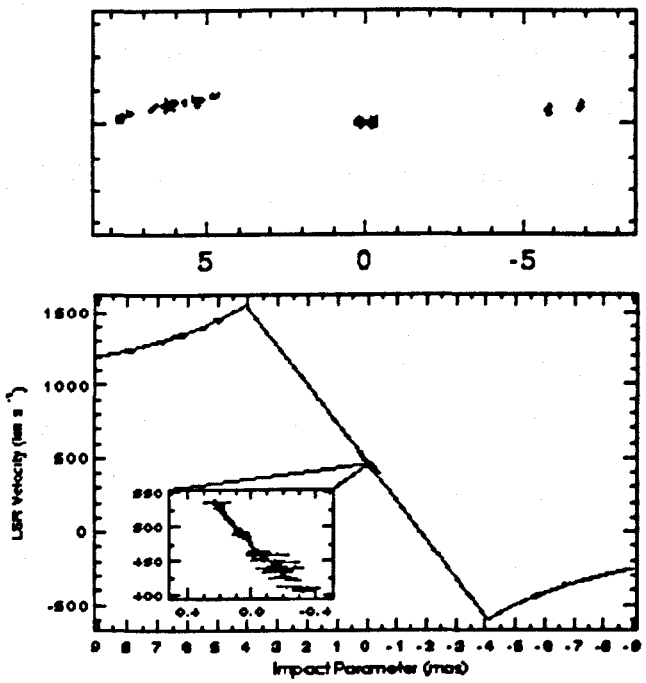


Figure 2.2: Velocity dispersion against angular separation from the core for the water masers in NGC 4258. The top panel is the spatial distribution and the bottom panel is the rotation curve. The line drawn is that of a disc in Keplerian rotation (Ho 1998 adapted from Greenhill 1997)

orbit around a black hole, with a mass of $3.6 \times 10^7$ $M_\odot$. Figure 2.2 shows the velocity dispersion in NGC 4258 against distance from the core. The line drawn is for Keplerian motion around the core, and is in very good agreement with the observational evidence. A vast majority (possibly all) $H_2O$ AGN are in systems which appear to have edge-on discs.

### 2.1.1 Maser Physics

The two criteria for maser emission are

1. population inversion and

2. stimulated emission.

Population inversion occurs when the molecules are forced out of their natural state – more molecules occupy higher energy states than lower ones – such that the gas is out of Local Thermal Equilibrium, having a non-Boltzmann population distribution. If $n_1$ and $n_2$ are the population numbers of energy levels 1 and 2 of a molecule, the ratio of the two levels normally follows a Boltzmann distribution of

$$\frac{n_1}{n_2} = \frac{g_2}{g_1} \exp\left(-h\nu_{21}/kT_{\rm ex}\right), \tag{2.1}$$

where 2 is the upper level, $g$ is the statistical weight of that level, $T_{\rm ex}$ is the temperature of the gas and $\nu_{21}$ is the frequency of a photon emitted following a transition between level 2 and level 1.

If the population becomes inverted, then the ratio of the population is greater than the statistical weights for these levels:

$$\frac{n_2}{n_1} > \frac{g_2}{g_1}. \tag{2.2}$$

The ratio of the statistical weights can be related to the Einstein coefficients of stimulated radiation:

$$\frac{g_2}{g_1} = \frac{B_{12}}{B_{21}} \tag{2.3}$$

where $B_{12}$ is the coefficient for stimulated *absorption* and $B_{21}$ is the coefficient for stimulated *emission*. The condition of the gas now becomes

$$B_{21} n_2 > B_{12} n_1, \tag{2.4}$$

and there are more photons from spontaneous emission than from spontaneous absorption.

Equations of radiative transfer show how this applies to the gas. The intensity of radiation, $I_\nu$, as it passes through a slab of gas of thickness, d$s$, is altered by a quantity, d$I_\nu$, given by

$$\frac{\mathrm{d}I_\nu}{\mathrm{d}s} = -\kappa_\nu I_\nu + \epsilon_\nu, \tag{2.5}$$

where $\kappa_\nu$ is the absorption coefficient of the gas, and the emissivity is $\epsilon_\nu$. The emissivity is a function of the spontaneous emission and is given by

$$\epsilon_\nu = n_2 A_{21} \frac{h\nu_{21}}{4\pi} f(\nu), \tag{2.6}$$

where $A_{21}$ is the Einstein coefficient for spontaneous emission, and $f(\nu)$ is a line-profile normalising parameter. The absorption coefficient, $\kappa_\nu$, is a measure of how the gas absorbs and emits stimulated radiation, and is described by

$$\kappa_\nu = (B_{12}n_1 - B_{21}n_2)\frac{h\nu_{21}}{c}f(\nu). \tag{2.7}$$

So for an inverted population, equation 2.4 forces $(B_{12}n_1 - B_{21}n_2)$ to be negative, which creates a negative absorption coefficient: the gas adds to the radiation rather than subtracting from it.

The absorption coefficient and optical depth are also related, and optical depth through a thickness of gas, $s$, is defined as

$$\mathrm{d}\tau_\nu = \kappa \mathrm{d}s \tag{2.8}$$

and radiation is attenuated by the optical depth of the gas by

$$I_\nu = I_\nu(0)\, e^{-\tau_\nu}. \tag{2.9}$$

So, for $\kappa_\nu < 0$, and $\tau_\nu < 0$,

$$\frac{I_\nu}{I_\nu(0)} > 1. \tag{2.10}$$

In fact for the most powerful masers optical depths can be as small as $-25$ thus creating gains of the order of $10^{11}$ in a single pass through the gas.

The masing condition is more easily attained at radio frequencies than optical frequencies because of the dependence of emission on frequency. The ratio of stimulated emission to spontaneous emission is

$$\frac{B_{21}}{A_{21}} = \frac{4\pi c^3}{2h\nu^3}, \tag{2.11}$$

so is $10^{18}$ times higher at radio wavelengths than optical wavelengths.

While these conditions of population inversion and stimulated emission are upheld the gas continues to emit maser radiation. However, such population inversion requires an input of energy, and such input is usually given to the gas by a *pumping mechanism*. Pumps include exciting the molecules by collision, or exciting them by radiation. Different pumps require different physical conditions. The collisional pumps generally occur in hotter, denser environments where the probability of a collision is high, and radiation pumps occur in the cooler environments where most of the input radiation is now at infrared wavelengths.

Maser amplification can be of a bright background source, or of the ambient radiation within the masing cloud. If the pump rate exceeds the de-excitation rate the maser is unsaturated and exponential amplification occurs. As the emission in the gas increases, the flux of photons increases to a point where

radiation is itself destroying the population inversion, and the maser now saturates and amplification is linear with path-length. Such a condition is common where the path length through the gas is high, or the optical depth is very low. Typical $H_2O$ masers are saturated when the flux reaches $\sim$ 100 Jy.

### 2.1.2 Why X-ray binaries?

The connection between energetic X-ray binaries and quasars has been established for a number of years, since the discovery of energetic radio jets displaying apparent superluminal motion (Mirabel & Rodríguez 1994). These radio jets are obviously energetic emitting synchrotron radiation far into the high frequency radio regime, and in the case of GRS 1915+105 into the infrared region of the spectrum. The obvious connection between the quasar and the X-ray binary is therefore established.

As discussed previously, maser emission has been observed in a variety of Galactic and extragalactic sources. Maser emission is therefore found in a wide variety of sources, the only requirements being a population of molecules which have been inverted, a source of radiation to form a seed, and sufficient gain length through which maser emission can be amplified in order to be observed.

It is useful to estimate the flux expected from an AGN with a mass of $10^{-6}$ $M_{\rm AGN}$ at a distance of 10 kpc. This puts the AGN on a comparable mass and distance scale to microquasars. The flux from a source is proportional to $LD^{-2}$, where $L$ is the luminosity and $D$ is the distance. So, if one assumes the

luminosity to scale as $L \propto M$ then one can write

$$\frac{S_X}{S_{AGN}} = \frac{M_X}{M_{AGN}} \frac{D^2_{AGN}}{D^2_X} = \frac{10^{-6}}{10^{-6}} \tag{2.12}$$

where we have assumed the AGN is at a distance of 10 Mpc where the X-ray binary is at a distance of 10 kpc. As one can see the flux from the two sources should be comparable.

The environment around both systems should be conducive for the formation of masers. This is achieved in the AGN case by the formation of a molecular disc around the central engine, within a distance of 0.1 pc. Again using the mass ratio to scale the two systems the distance from the binary of a molecular torus or disc would be within 20,000 AU. While this is too far out to be a Roche lobe over flow accretion disc, it could be formed by an outflow of material which creates a thin torus around the binary system.

## 2.2 Observations

I carried out a large number of observations at different observatories and frequencies to complete our maser programme. A summary of sources observed with date of observation is given in table 2.1.

With a large number of sources in the programme, details of the observations are best documented by telescope, rather than source. In chronological order, observations were carried out using:

| Source | Maser line | MJD | Date of observation |
|---|---|---|---|
| Cyg X-3 | $H_2O$ | 50136–50139 | 1996 February 23–27 |
| | $H_2O$ | 50240 | 1996 June 06 |
| GRS 1915+105 | $H_2O$ | 50136–50139 | 1996 February 23–27 |
| | $H_2O$ | 50240 | 1996 June 06 |
| | OH | 50676–50678 | 1997 August 16–18 |
| | $H_2O$ | 50844–50845 | 1998 January 30–31 |
| GRO J1655−40 | $H_2O$ | 50262 | 1996 July 28 |
| | OH | 50676–50678 | 1997 August 16–18 |
| V404 Cyg | $H_2O$ | 50136–50139 | 1996 February 23–27 |
| | $H_2O$ | 50185 | 1996 April 21 |
| SS 433 | $H_2O$ | 50136–50139 | 1996 February 23–27 |

Table 2.1: Sources observed in the maser programme, together with the line observed and dates in MJD and calendar standards.

1. Cambridge: *all sources except GRO J1655−40.* Part of the MERLIN array, which was used while MERLIN was off-line for maintenance. 5 sources, 7 spectra per source, giving a total velocity width of 420 km $s^{-1}$. $H_2O$ search on 1996 Feb 23–27.

2. MERLIN: *V 404 Cyg.* 108 km $s^{-1}$ spectral coverage, 0.84 km $s^{-1}$ resolution. Follow-up observations based on the Cambridge data. $H_2O$ search on 1996 April 21.

3. MERLIN: *GRS 1915+105 & Cyg X-3.* 53.9 km $s^{-1}$ spectral coverage, 0.42 km $s^{-1}$ resolution. Observations were interleaved, 30 minutes on one source, then 30 minutes on the other source. $H_2O$ search on 1996 June 06.

4. Parkes: *GRO J1655−40.* 2000 km $s^{-1}$ spectral coverage, 0.40 km $s^{-1}$

resolution. 5 spectra, each 400 km $s^{-1}$ wide. $H_2O$ search on 1996 June 28.

5. Compact Array: *GRS 1915+105 & GRO J1655–40.* 719 km $s^{-1}$ spectral coverage, 0.702 km $s^{-1}$ resolution. OH search on 1997 Aug 16-18.

6. MERLIN: *GRS 1915+105.* A followup observation to observation number 3 and identical to it. $H_2O$ search on 1998 Jan 30-31.

All observations, except those taken by the Australia Telescope Compact Array are of the $H_2O$ molecular line at 22.235 GHz. Compact Array observations were of the OH line at 1667 MHz. Each configuration presented is different, and individual techniques had to be applied to each set of observations, as given below.

### 2.2.1 All Northern Sources: Cambridge-telescope observations

While MERLIN was off-line for scheduled maintenance, A.M.S. Richards, R.E. Spencer, S.J. Newell, J.V. Smoker, R.J. Cohen and I started a search for maser emission in X-ray binaries using the single Cambridge telescope. One thing we were certain of was any possible emission could have a wide range of LSR velocities, just because we were not sure where any maser emission would originate from.

The observations used the old auto-correlation spectrometer, rather than the

MERLIN correlator in single-dish mode because the maintenance work on the MERLIN system prevented us from using that equipment. A large number of calibrator sources were used, and the first observations were of very bright (10–100 Jy) sources as a check that the correlator output was what we required. A total of 25 bright masers were observed, with LSR velocities which covered the majority of frequency space which we wanted to use with the X-ray binaries. A table of the sources observed, together with RA, Dec, Observing frequency, LSR velocity and 'band identifier' is given in table 2.2. The LSR velocity of the X-ray binaries was calculated from a catalogue of velocity and Galactic co-ordinates, assuming distances to the objects.

Strong calibrators were observed with a single 30-second integration time, to check for correlator or local oscillator problems, and when all problems were fixed all other sources were observed with an integration time of 2 minutes over a variable number of cycles. The strong calibrators were observed for a total of 8 minutes each. X-ray binary targets were observed for a total of 32 or 30 minutes in each frequency band.

There occurred a number of correlator-based problems during the observations, which were not satisfactorily sorted out. For most of the data only the left-hand circular polarisation was used as the RHC polarisation was corrupted.

A number of 'spikes' in the spectra of the calibrators were caused by the correlator also, and these had to be manually removed for high data quality. The noise diode for calibrating system temperatures was unavailable, and continuum

| Source | RA (1950) | Dec (1950) | $\nu_{obs}$ [MHz] | Vel [km s$^{-1}$] | Band |
|---|---|---|---|---|---|
| S Per | 02:19:16 | +58:21:20 | 22236.523 | −40 | C |
| W3B | 02:21:53 | +61:52:23 | 22236.941 | −44 | C |
| W3OH | 02:23:16 | +61:38:58 | 22236.927 | −44 | C |
| IK Tau | 03:50:46 | +11:15:42 | 22229.539 | +35 | E |
| IRC50137 | 05:07:20 | +52:48:54 | 22232.471 | +08 | D |
| ORION-KL | 05:32:47 | −5:24:23 | 22231.275 | +10 | D |
| U Ori | 05:52:51 | +20:10:06 | 22235.164 | −39 | C |
| VY CMa | 07:20:55 | −25:40:13 | 22231.597 | +20 | D |
| OH0739 | 07:39:59 | −14:35:44 | 22231.979 | +20 | D |
| IRC20197 | 09:42:57 | −21:47:54 | 22231.841 | +36 | E |
| RT VIR | 13:00:06 | +05:27:14 | 22235.708 | +17 | D |
| W Hya | 13:46:13 | −28:07:11 | 22234.281 | +40 | E |
| RS Vir | 14:24:45 | +04:54:07 | 22238.825 | −15 | D |
| S CrB | 15:19:21 | +31:32:47 | 22237.276 | +03 | D |
| WX Ser | 15:25:32 | +19:44:06 | 22237.372 | +06 | D |
| U Her | 16:23:35 | +19:00:15 | 22239.046 | −15 | D |
| VX Sgr | 18:05:03 | −22:13:56 | 22237.370 | +05 | D |
| OH12.8 | 18:13:53 | −18:16:09 | 22241.905 | −56 | C |
| W43A | 18:45:05 | −01:48:16 | 22234.800 | +50 | C |
| OH37.1 | 18:59:36 | +03:15:53 | 22231.035 | +87 | E |
| OH42.3 | 19:06:44 | +08:11:41 | 22230.563 | +57 | E |
| RR Aql | 19:55:00 | −02:01:17 | 22234.898 | +28 | D |
| Z Cyg | 20:00:03 | +49:54:07 | 22247.098 | −148 | B |
| W75N | 20:36:50 | +42:26:58 | 22235.407 | +08 | D |
| NML Cyg | 20:44:34 | +39:55:57 | 22235.979 | +00 | D |
| Cep A | 22:54:20 | +61:45:44 | 22235.480 | −10 | D |
| NGC7538 | 23:11:37 | +61:11:50 | 22239.002 | −59 | C |
| PZ Cas | 23:41:41 | +61:31:01 | 22237.335 | −39 | C |
| R Cas | 23:55:52 | +51:06:40 | 22232.047 | +29 | D |

| A | B | C | D | E | F | G |
|---|---|---|---|---|---|---|
| −180 | −120 | −60 | 0 | 60 | 120 | 180 |

Table 2.2: Calibrator sources for the Cambridge observations. Observation frequencies are given, as well as the corresponding LSR velocity in km s$^{-1}$. The band designators are given at the bottom of the table, and are 60 km s$^{-1}$ wide, centred on the velocities given.

calibrator sources such as CR21 were too weak to be detectable at 22 GHz. To calibrate the flux axis we scaled the spectra using the estimated $T_{sys}$ of the Cambridge antenna of 120 K at 5 Jy/K (the sensitivity of the Cambridge telescope), which gave reasonable fluxes for known circumstellar masers. Results of the observations are given below.

### V404 Cygni

While seven spectra per source were obtained, the most promising was that from V404 Cyg centred on 0 km $s^{-1}$. This spectrum given in figure 2.3. There was a possible feature at $-5$ km $s^{-1}$ at a brightness of 0.13 K, which corresponds to 1.6 Jy. This feature is not highly significant as the spectrum has a $1\sigma$ noise of 0.52 Jy, giving the 'feature' a $3\sigma$ significance. $H_2O$ emission lines have a FWHM of around 0.5 km $s^{-1}$, The width of this feature (3.5 km $s^{-1}$) suggested it could be real.

### Other X-ray binaries

The other sources: Cyg X-3, GRS 1915+105 and SS 433 produced spectra with either no discernable features, or correlator based faults / interference. Figure 2.4 shows the spectrum for Cyg X-3 centred on $-180$ km $s^{-1}$. Spectra like this one can be falsely identified, as the broad emission around $-20$ km $s^{-1}$ appears to be real (strong signal to noise, over many channels), but the inclusion in the spectrum of a single spike at 0 km $s^{-1}$, together with absorption features

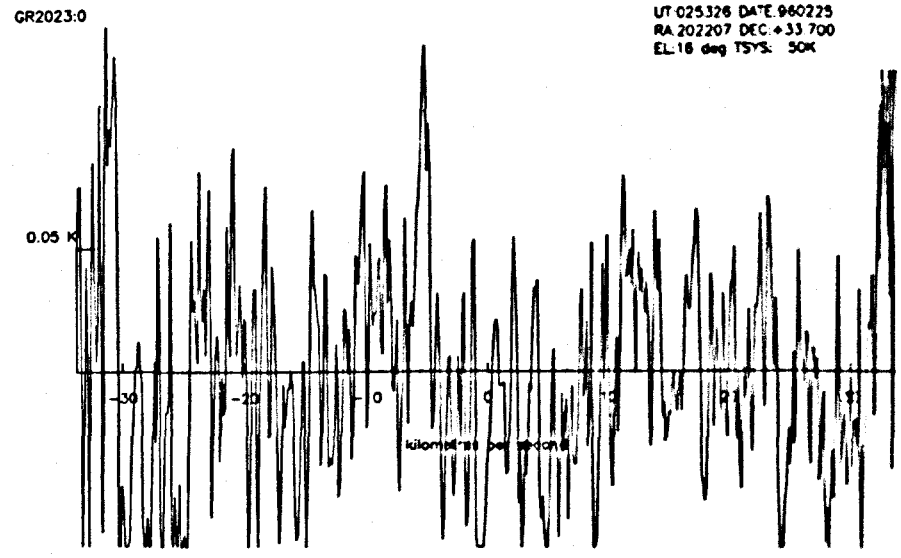


Figure 2.3: Cambridge observations of V404 Cyg. Output is in K, with a conversion of 12 J/K. We were alerted to a potential feature at $-5$ km s$^{-1}$ with a temperature of 0.1K. This corresponded to 1.2 Jy. The $1\sigma$ noise in this spectrum is 0.52 Jy.

in the neighbouring channels, indicates a correlator fault. This, together with a wide-band absorption feature around +20 km s$^{-1}$, would indicate that the complete spectrum has no real emission and is a fake. This spectrum looked promising as we were observing, so a shift was made by +10 km s$^{-1}$ to see if the feature was real. It disappeared on subsequent observations.

### Cambridge results

The results from the Cambridge observations gave us the possibility of emission from the single source V404 Cyg, and upper limits to emission from the other sources studied. The upper limits from the spectra at the $1\sigma$ level are given in table 2.3. Spectra of SS 433 have high upper-limits because the source was at

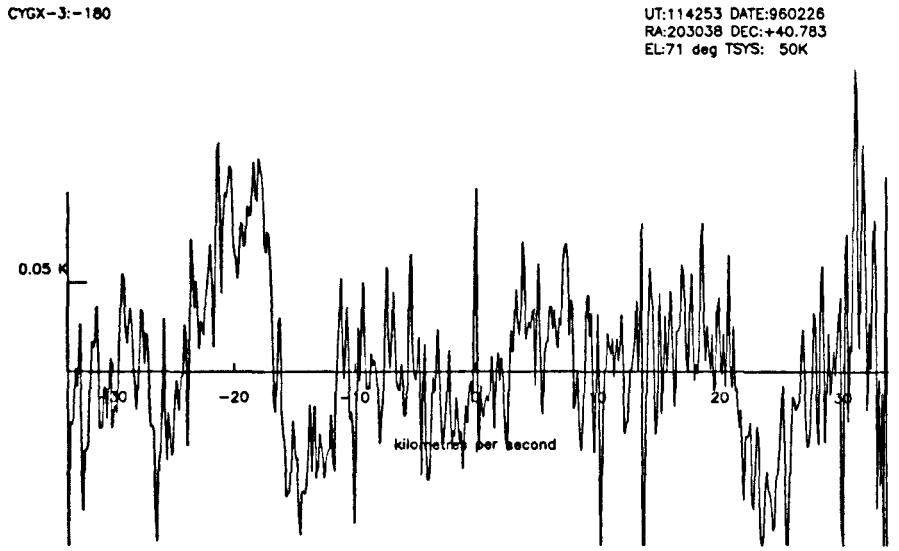


Figure 2.4: Cambridge observations of Cyg X-3, with the spectrum centred on $-180$ km s$^{-1}$. There appears to be a wide emission feature at $-20$ km s$^{-1}$, but this is mirrored by an absorption feature at $+20$ km s$^{-1}$, and a correlator based spike at 0 km s$^{-1}$, leading to the conclusion that the spectrum contains false data.

| | Central velocity (km s$^{-1}$) | | | | | | |
|---|---|---|---|---|---|---|---|
| Source | $-180$ | $-120$ | $-60$ | 0 | $+60$ | $+120$ | $+180$ |
| SS 433 | 0.90 | 0.54 | 1.29 | 1.54 | 0.34 | 2.09 | 0.96 |
| GRS 1015+105 | 0.62 | 0.37 | 0.64 | 0.66 | 0.58 | 0.31 | 1.05 |
| V404 Cyg | 0.66 | 0.48 | 0.44 | 0.52 | 0.43 | 0.32 | 0.31 |
| Cyg X-3 | 0.55 | 0.42 | 0.70 | 0.62 | 0.50 | 0.24 | 0.49 |
| GT 2318+602 | 0.44 | 0.86 | 0.36 | 0.37 | 0.36 | 0.52 | 0.88 |

Table 2.3: $1\sigma$ upper limits in Jy for the sources observed by Cambridge. Spectra of SS 433 are particularly noisy due to the source being at a low elevation at the time of observation.

low elevation (7 degrees for the $-60$ km s$^{-1}$ observations).

With this initial programme completed, we obtained 12 hours director's time for MERLIN to pursue the result from V404 Cygni, and wrote two proposals to

look at GRS 1015+105 and Cyg X-3 with MERLIN, based on these results.

### 2.2.2 V404 Cygni: MERLIN observations

We observed V404 Cyg (2022+337) on 21 Apr 1996 with 5 telescopes of MERLIN. A number of carefully chosen calibrators were also observed, and the telescope configuration was thus:

- 8 MHz, 128 channels for the source and 3C84,
- 16 MHz, 32 channels for the calibrators 3C84 and 2021+31

The higher bandwidth for the calibrators was needed because at 22 GHz signals would be weaker, and we needed high signal to noise to facilitate proper adjustment of the amplitudes and phases. The details of reduction of MERLIN data, the requirements and use of calibrators is documented in appendix A.1.1.

The quality of data for these observations was not very high. We were unable to obtain full Stokes coverage (MERLIN data usually records in LL, RR, LR, RL polarisations), and only the Left-Left polarisation was recorded. This loss of polarisation resulted in a $\sqrt{2}$ reduction in sensitivity; normally LL and RR are added. Phase information from the phase-calibrator was not used as the quality of data was rather poor. With low-quality data the final spectrum from the source is not overly impressive. Fig 2.5 shows the spectrum from the source. The mean flux from the continuum of the source over the 8 MHz bandwidth is $490 \pm 6$ mJy. If line emission is significant then the phase over the width of the

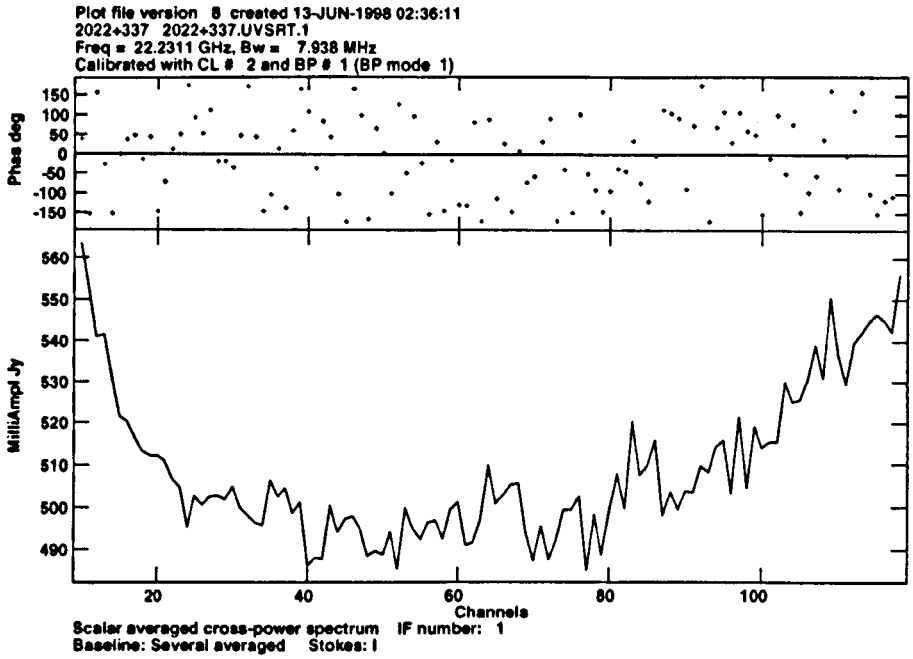


Figure 2.5: Spectrum from MERLIN for V404 Cyg. The spectrum covers a bandwidth of 8 MHz in 128 channels. This gives a 110 km $s^{-1}$ velocity coverage with channel 64 centred on the LSR velocity of the source.

line would be correlated, and follow a straight line.

### 2.2.3 Cygnus X-3: MERLIN observations

Cygnus X-3 was observed with MERLIN in semester 96A on 96 Jun 06 21:45 UT – 07 10:54 UT. The observations were combined with a related observing programme, to observe GRS 1915+105, and each source was observed in blocks of 30 minutes for 9.5 hours. The reason for the unusual schedule was to minimise the possibility of losing large quantities of data from weather or technical failures, and to obtain good hour angle coverage.

To increase signal to noise in the line a wide channel width was chosen of 0.42 km $s^{-1}$, which is comparable to the $H_2O$ line width. To achieve this a bandwidth of 4 MHz with 128 channels was chosen for the target source. As with most MERLIN observations of weak spectral-line sources, observations of the phase-calibrator requires a higher bandwidth to obtain strong enough signals for calibration. A bandwidth of 16 MHz with 32 channels was chosen for the phase-calibrator: 2005+403. The flux calibrator, 4C39.25, was therefore observed in both 4 and 16 MHz, as required in order to calibrate the phase difference between narrow and wide band inputs to the correlator. The details of why this is important and the methods used in practical calibration are given in the appendix A (section A.2.5). For the calibration of the flux, we used a value of 5.15 $\pm$ 0.24 Jy for 4C39.25 (based on Wiren et al. 1992). After proper calibration, figure 2.6 shows the spectrum of Cyg X-3 plotted against velocity.

Since no significant feature was observed in the spectrum, a $3\sigma$ upper limit of 579 mJy can be placed on any maser emission from Cyg X-3. While an absence of emission is disappointing, a map of the continuum can be made by averaging all the channels. The resulting image is given in figure 2.7.

### 2.2.4 GRS 1915+105: MERLIN observations

GRS 1915+105 was observed with the MERLIN array on two successive occasions. The first observations were taken concurrently with Cyg X-3 as part of a detailed search. Following some interesting results, GRS 1915 was observed

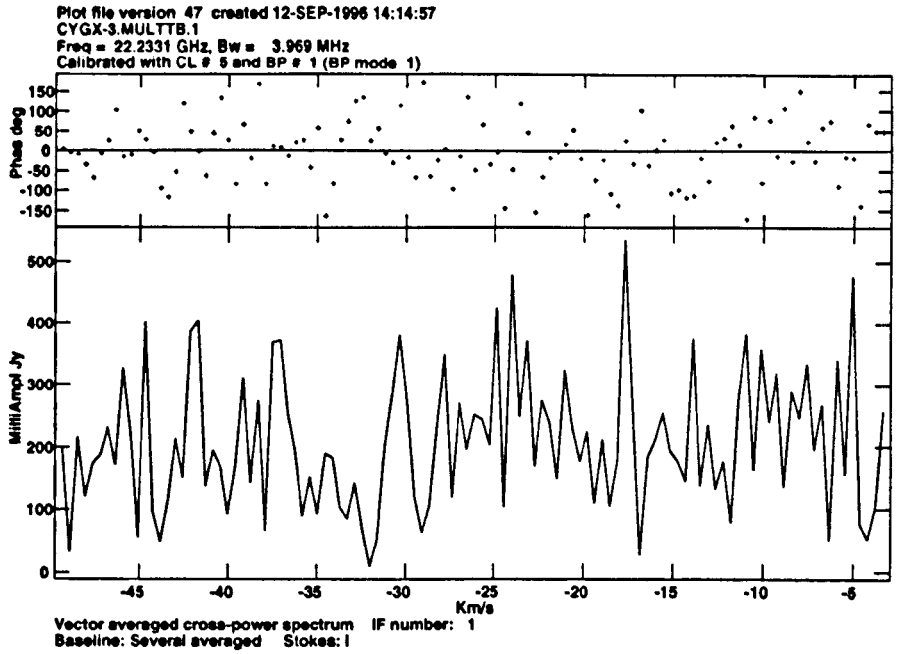


Figure 2.6: A spectrum of Cyg X-3. Data has been plotted against velocity over 128 channels with a channel resolution of 0.42 km $s^{-1}$. No correction for the LSR velocity of the source has been made. The top panel shows phase in degrees, and the bottom panel shows amplitude in mJy. The continuum flux is 240 mJy, and the RMS noise is 113 mJy. No features are visible above the noise level and so a $3\sigma$ upper limit of 579 mJy can be placed on any maser emission.

a second time, on 1998 January 30–31. Details of the observations and results are presented in two subsections: *Semester 96A* and *Semester 98A*.

### Semester 96A

These are the first observations of GRS 1915+105 with the MERLIN array. As with Cygnus X-3 (section 2.2.3), 4 MHz 128 channels were used for the source, and 16 MHz 32 channels were used for the calibrators. This was to obtain strong

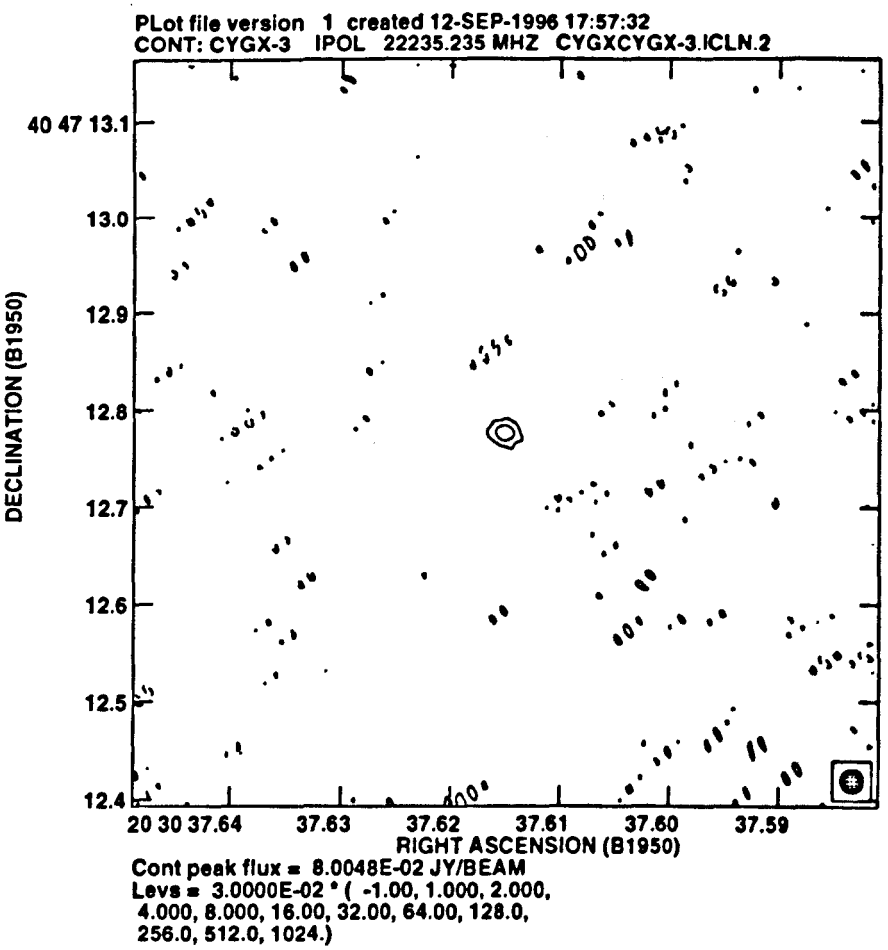


Figure 2.7: A map of the continuum at 22.235 GHz for Cyg X-3. The image has an RMS noise of 10 mJy and Cyg X-3 can be seen as a point source with a peak flux of 80 mJy/beam. The beam (shown in the bottom right corner) has been circularised with a diameter of 30 mas.

| Source | Calibrator | RA(2000) | Dec (2000) | Channels |
|---|---|---|---|---|
| 4C39.25 | Flux | 09 27 03.01 | +39 02 20.85 | 32 & 128 |
| 1920+154A | Phase | 19 22 34.70 | +15 30 09.73 | 32 |
| GRS 1915+105 | Target | 19 15 11.55 | +10 56 44.11 | 128 |

Table 2.4: Sources observed in the first MERLIN observation of GRS 1915+105.

amplitude and phase information for the calibrator sources so the spectral line data could be calibrated.

The flux calibrator used in the observations was 4C39.25, and a nearby phase-calibrator 1920+154A was also observed for 2.5 minutes every 10 minutes. Source details are given in table 2.4.

Data was calibrated according to the plan in appendix A.2.5. After phase and amplitude calibration of GRS 1915+105, and after averaging all the baselines together, a vector averaged spectrum was obtained. This is shown in figure 2.8. The top frame shows the phase and the bottom frame shows the amplitude. While the spectrum is fairly noisy (a total of 8 hours of data has been included), two emission features are present in channels 55 and 74. The continuum flux for GRS 1915 is 30 mJy, and the $1\sigma$ noise is 16 mJy. The two emission features are at a flux of 78 mJy, (just) at the $3\sigma$ level.

The data can be plotted by flux against velocity, as the maser line frequency of 22.235 GHz has been shifted to the LSR velocity of GRS 1915+105. A spectrum against velocity is given in figure 2.9. Only the inner region is shown.

The data has been taken using an interferometer, and as well as an increased

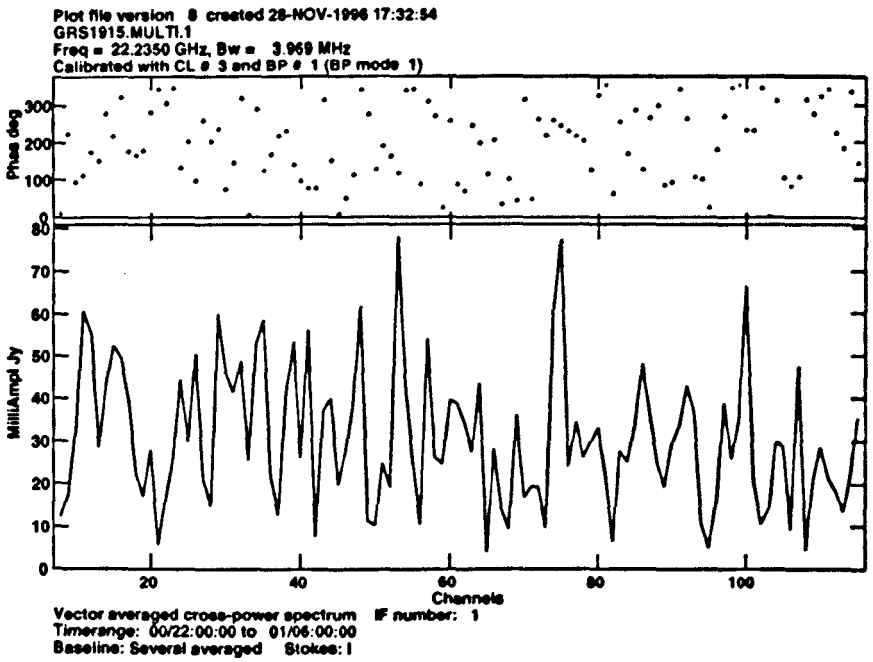


Figure 2.8: A spectrum of GRS 1915+105 for epoch 1 (1996). Data has been plotted against channel number where channels are 31.25 kHz wide. The top panel shows the phase in degrees, and the bottom panel shows amplitude in mJy. The continuum flux is 30 mJy, with an RMS noise of 16 mJy. There are two emission features at channels 55 and 74.

collecting area over a single dish telescope, the interferometer can re-create a map of the spectral line source. Channels 55 and 74 were selected, and maps of the brightest regions of emission in each of these channels was obtained. Channel 55, the blue-shifted feature is shown in figure 2.10, and the red-shifted feature in channel 74 is shown in figure 2.11.

The figures showing the positions of the maser emission in GRS 1915+105 are offset from the radio position of GRS 1915. The blue shifted feature has $x$

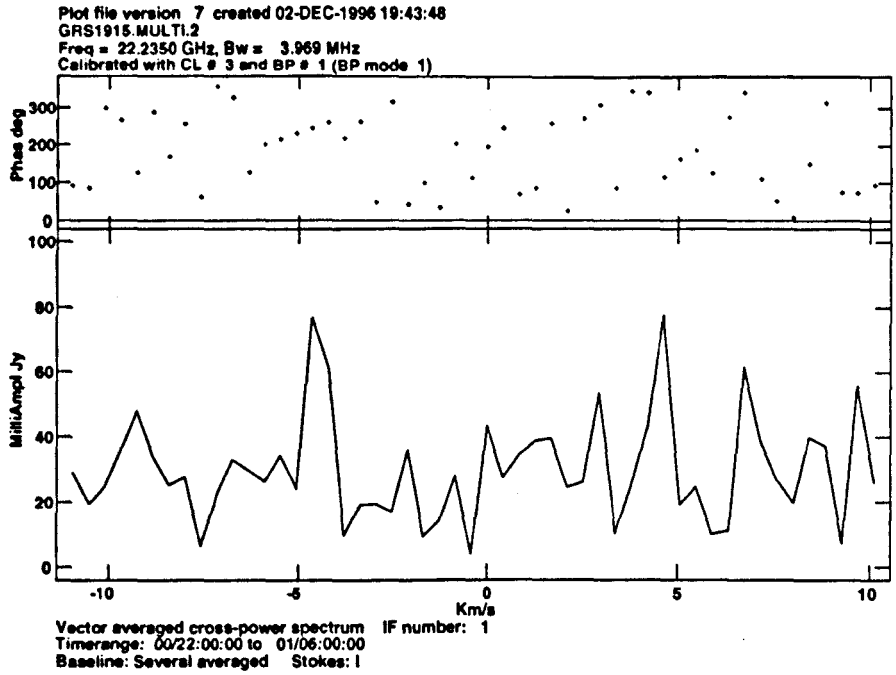


Figure 2.9: The spectrum of GRS 1915+105 shown in figure 2.8, but plotted against velocity in km $s^{-1}$. Data have been corrected to the LSR velocity of the source. The two emission features are rotating around the central source at ±5 km s−1.

and $y$ offsets from the centre of the map of +50, −190 mas and the red-shifted feature has offsets of +295, −130 mas from the centre. The beam size in both these images is 8 × 23 mas. A cartoon of the maser emission in relation to the centre of the binary can be drawn. This is shown in figure 2.12. If the emission originates from a ring rotating in the plane of the binary, and the spots are equidistant from the centre of the binary, then an accurate radio position for GRS 1915 can be obtained. The position of GRS 1915+105 would therefore be

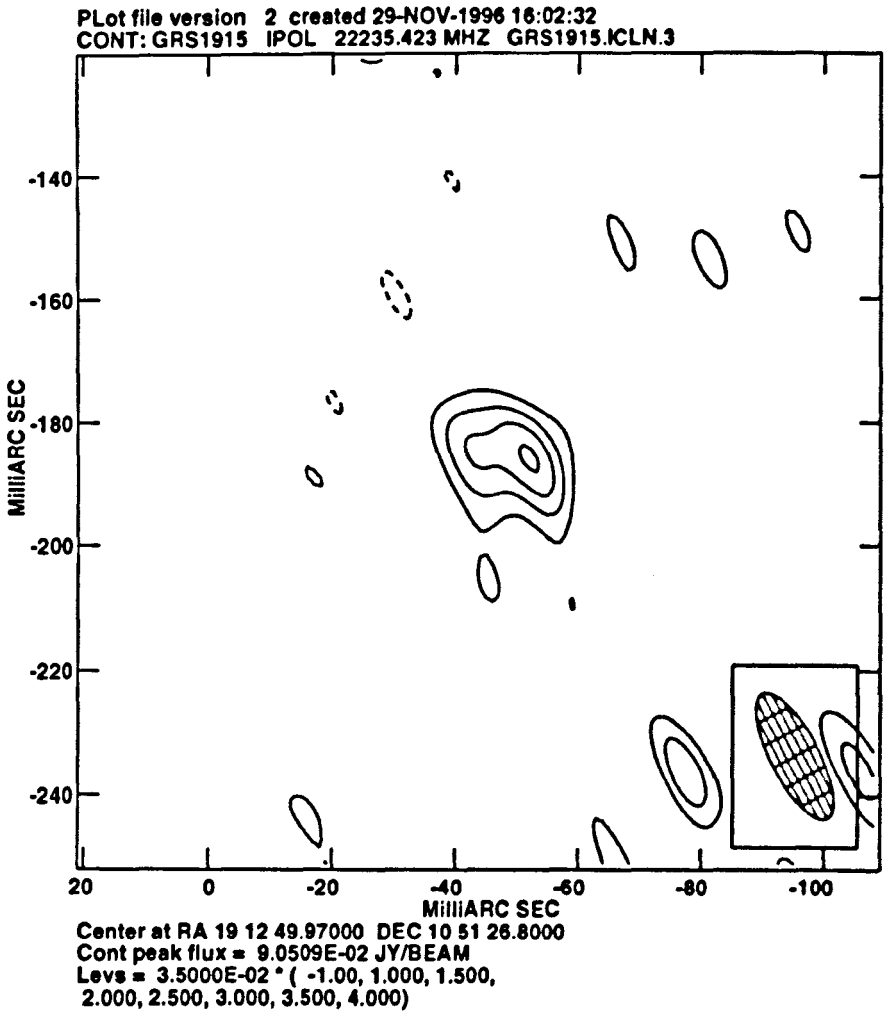


Figure 2.10: A map of the brightest feature in channel 55, corresponding to the blue-shifted feature in the spectrum for GRS 1915. The noise level in this map is 35 mJy, and the feature has a peak flux of 90 mJy/beam. The position of this image is offset by +50, −190 mas from the centre of the map.

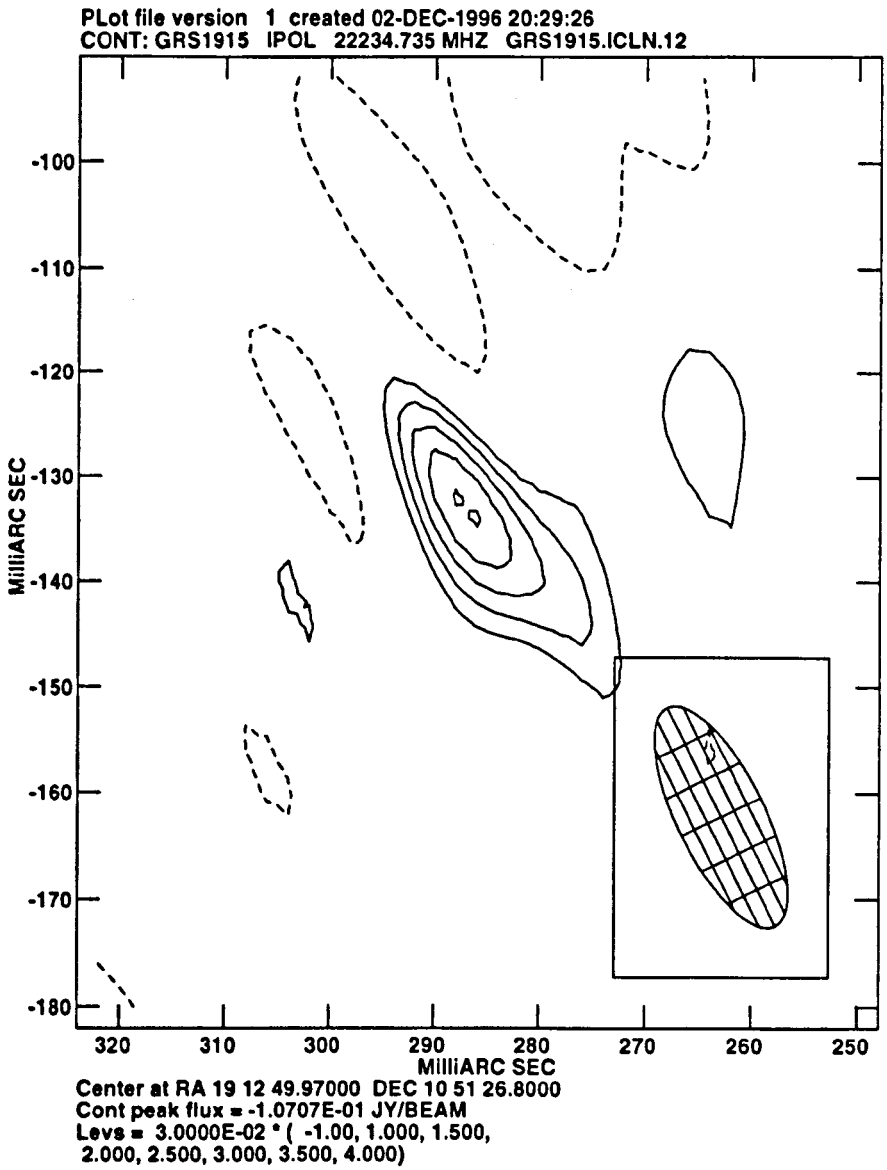


Figure 2.11: A map of the brightest feature in channel 74, corresponding to the red-shifted feature in the spectrum for GRS 1915. The noise level in this map is 30 mJy, and the feature has a peak flux of 90 mJy/beam. The position of this image offset by +295, −130 mas from the centre of the map.

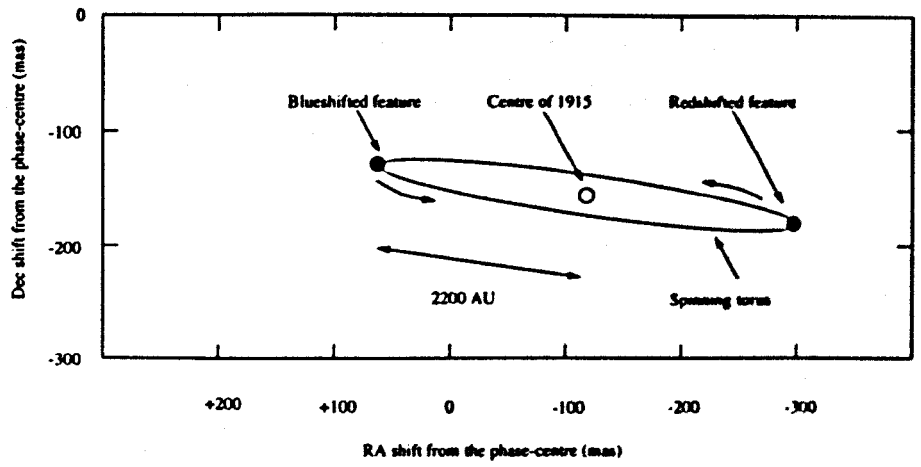


Figure 2.12: A cartoon showing the relative positions of the masers features for GRS 1915+105.

RA(2000) 19 15 11.72, Dec(2000) +10 56 43.950.

If these maser spots are orbiting the binary in Keplerian motion, then the combined mass for the binary can be obtained. The combined mass is

$$M_{1+2} = 1.12 \times 10^{-3}\, v^2_{\mathrm{km/s}} D_{\mathrm{kpc}} \theta_{\mathrm{mas}}\ \mathrm{M}_\odot \qquad (2.13)$$

where $v$ is the rotation of the maser spots in km s$^{-1}$, $D$ is the distance to the source in kpc and $\theta$ is the separation of the maser spots from the centre of the source in milli-arcseconds. Given the range of distances, velocities and measured separations in the data, the central mass has a value of $M_{1+2} = 41 \pm 17\ \mathrm{M}_\odot$, or a range between 24 and 68 $\mathrm{M}_\odot$.

**Semester 98A**

Following the apparent success of the above observations, we were awarded 24 hours of observation time in 1998 semester A to follow up the observations, and hopefully to confirm as well as reduce the noise in the data. A slightly different set of calibrators were used in the observations; the flux calibrator used was 3C273 with a 22.235 GHz flux of 39 Jy instead of the source 4C39.25. However, the technique of 128 channel 4 MHz bandwidth flux and target observations with 32 channel 16 MHz phase calibrator observations was used again in these observations.

When the data had been calibrated, a spectrum of all the data was produced. This is given in figure 2.13. The apparent emission features at $3\sigma$ shown in figure 2.8 for epoch 1 are not confirmed. Careful investigations showed there was intermittent interference at one telescope – Darnhall, which accounted for any significant emission features. The interference was faintly detected and correlated over other short baselines (the interference was probably The Home Office fixed data link!). This is also the conclusion of the emission features from epoch 1.

While no significant emission was detected or confirmed from GRS 1915+105, we can place a lower upper-limit to any water maser emission from this source. The $3\sigma$ upper-limit to emission in the velocity range of $-25 \rightarrow +25$ km s$^{-1}$ either side of the LSR velocity is 45.5 mJy.

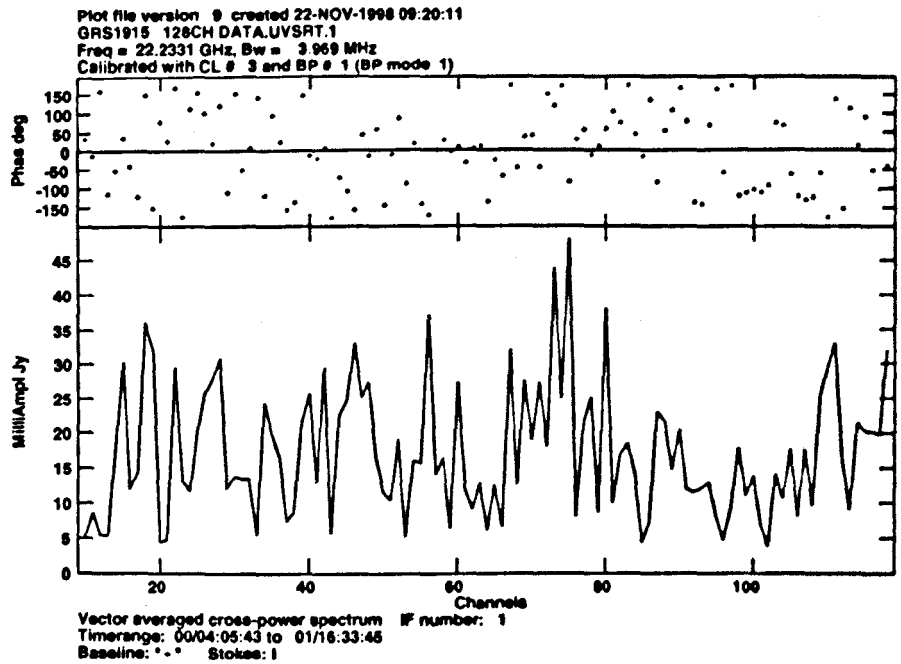


Figure 2.13: A spectrum of GRS 1915+105 for epoch 2 (1998). As before, data is plotted with phase and amplitude against channel number. The total bandwidth used in the observations is 4 MHz which corresponds to a channel resolution of 31.25 kHz or 0.42 km $s^{-1}$. The mean flux in the spectrum is 17.3 mJy with a 1 $\sigma$ noise level of 9.4 mJy. The emission features at channels 55 and 74 as observed in epoch 1 (figure 2.8) are not confirmed.

### 2.2.5 GRS 1915+105: Compact Array observations

To complement the water maser observations with MERLIN, time was awarded to look for OH maser emission from GRS 1915+105 (and GRO J1655−40, see section 2.2.7) in 1997 August 16–18. We decided to sandwich observations of GRS 1915 and GRO J1655 together for two complete days, in order that if observations were corrupted on one of the days, all the time on one source was

| Source | Type | RA(2000) | Dec (2000) | $t_{int}$ (hh mm) |
|---|---|---|---|---|
| VY CMa | Correlator | 07 22 58.56 | −25 46 03.79 | 01 30 |
| 0823−500 | Flux | 08 25 25.860 | −50 10 38.490 | 00 30 |
| 1934−638 | Flux | 19 39 25.026 | −63 42 45.630 | 01 30 |
| 1655−40 | Target | 16 54 00.200 | −39 50 45.000 | 13 30 |
| 1718−649 | Phase | 17 23 41.029 | −65 00 36.610 | |
| 1915+105 | Target | 19 15 11.550 | +10 56 44.110 | 09 15 |
| 1919+086 | Phase | 19 22 18.634 | +08 41 57.370 | |

Table 2.5: Source particulars for the Compact Array observations. Integration times are approximate to within 15 minutes, times for both targets include the times for the phase calibrators which take up about 3 minutes every hour.

not lost.

Five calibrators were used in total. Flux calibration was taken from the sources 0823−500 and 1934−638, depending on which source was above the horizon at the time of the observations. A correlator-calibrator was used to check the electronic setup; for this a bright known maser VY CMa was used. Two phase calibrators were also used, 1718−649 for GRO J1655−40, and 1919+086 for GRS 1915+105. Source particulars are given in table 2.5.

A central frequency of 1667 MHz was chosen for the maser frequency. The observations required a high channel resolution, and both lines were not observable in the same bandwidth, so the 1667 mainline was chosen. A bandwidth of 4 MHz with 1024 channels was used in the correlator, this allowed all 4 polarisations to be measured, as well as having a small channel resolution of 0.702 km $s^{-1}$. After focusing the array by observing a flux calibrator and automatically matching phases and delays for the telescopes, flux calibrators were

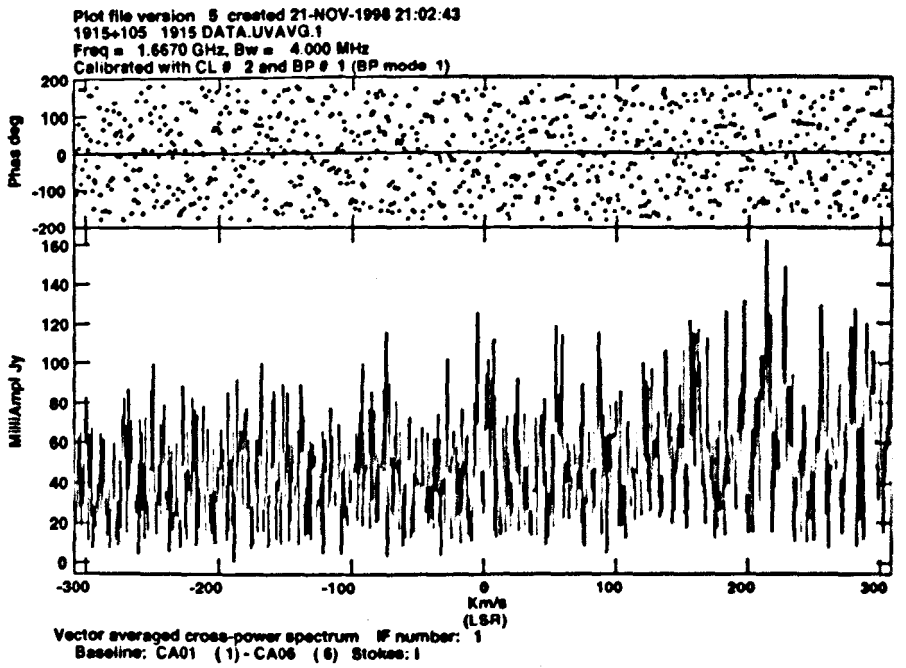


Figure 2.14: An OH maser spectrum of GRS 1915+105. Data is plotted against velocity over 900 channels. The top frame shows phase in degrees and the bottom frame shows amplitude in mJy. The mean flux is 49.2 mJy with a $1\sigma$ noise of 26.6 mJy.

observed and then the usual cycle of target, phase-cal, target, etc. was scheduled. Because of the stability of the array, and the small baselines used in the interferometer, the phase calibrators do not need to be as close spatially and temporally to the target as with MERLIN calibrators. Therefore phase calibration was performed for 3–5 minutes every 60 minutes.

After reducing the data, the spectrum for GRS 1915+105 at the OH maser frequency of 1667 MHz is given in figure 2.14. The data is plotted against LSR

velocity and has a mean flux of 49.2 ± 26.6 mJy.

### 2.2.6 GRO J1655−40: Parkes observations

The source GRO J1655−40 is too far south to be observed by MERLIN and we could not cover it in the wide frequency search with the Cambridge telescope. We carried out the wide search using the Parkes telescope of the Australia Telescope.

GRO J1655−40 was observed on 28 July 1996 for 11 hours at the $H_2O$ maser frequency. 5 spectra were obtained at 2 hours per scan, a total velocity coverage of 1350 km $s^{-1}$. The bandwidth chosen for each scan was 32 MHz, and 1024 channels. With a roll-off in the spectrum at the band edges, the total useable bandwidth was 20 MHz, which covers 270 km $s^{-1}$ in total. Spectra were offset by 20 MHz to cover a total of 100 MHz (1350 km $s^{-1}$).

Two known masers: R Crt and W Hya were observed to check correlator output. These two spectra are shown in figure 2.15.

While individual spectra for GRO J1655−40 are unimpressive, the velocity coverage is comprehensive. Figure 2.16 shows all five spectra stacked to give the full coverage.

RMS noise in each spectrum is given in table 2.6. Although the telescope and correlator are of the highest quality construction, weather played a large part in the data quality, and so noise levels are higher than usual.

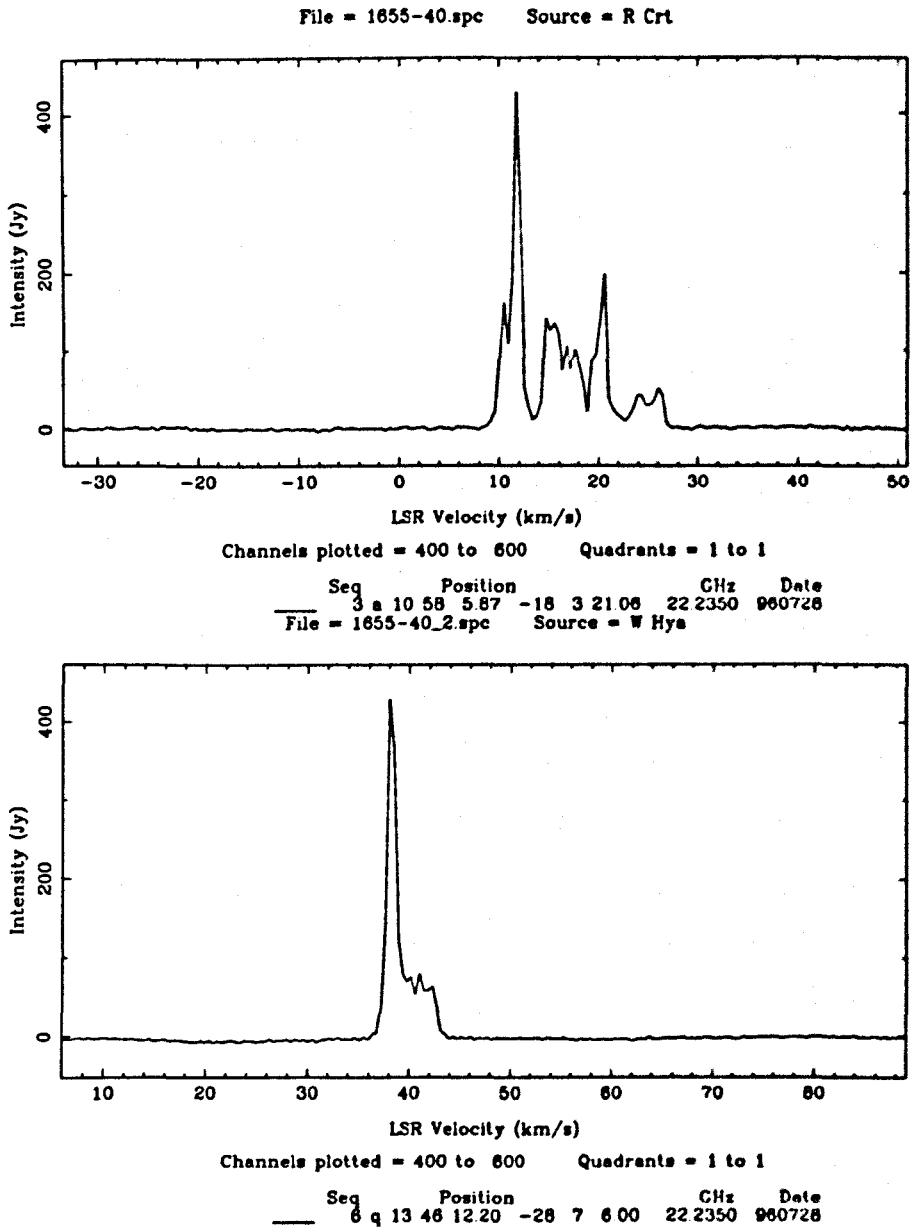


Figure 2.15: R Crt (top) and W Hyd (bottom) observed with Parkes.

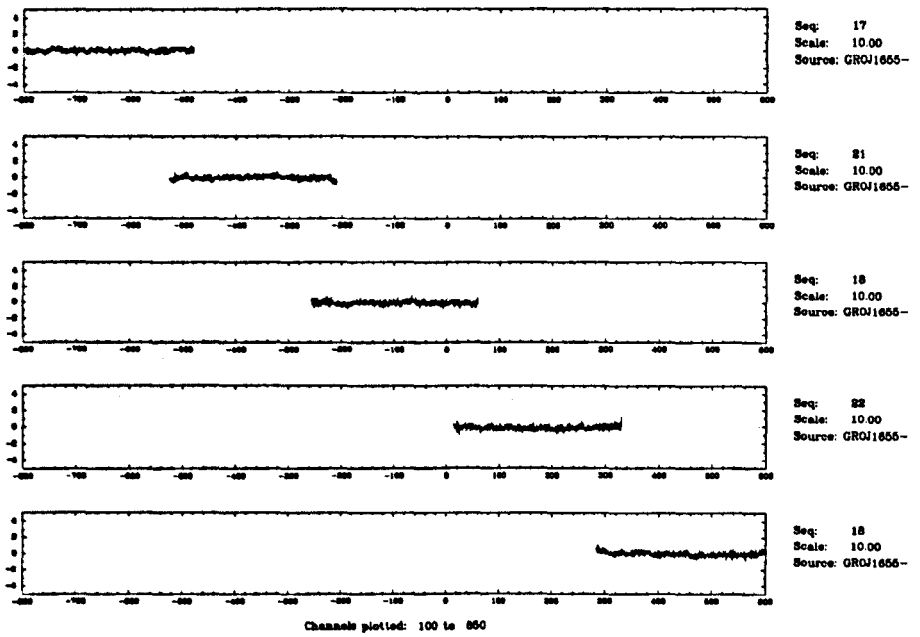


Figure 2.16: Parkes observation, GRO J1655−40 shown as five spectra stacked on top of each other.

| Velocity Range km s$^{-1}$ | RMS Flux [mJy] |
|---|---|
| $-800 \rightarrow -480$ | 390 |
| $-530 \rightarrow -210$ | 390 |
| $-255 \rightarrow +60$ | 460 |
| $+90 \rightarrow +330$ | 410 |
| $+280 \rightarrow +600$ | 433 |

Table 2.6: RMS flux values from the five spectra of the GRO J1655−40 observation made by the Parkes telescope.

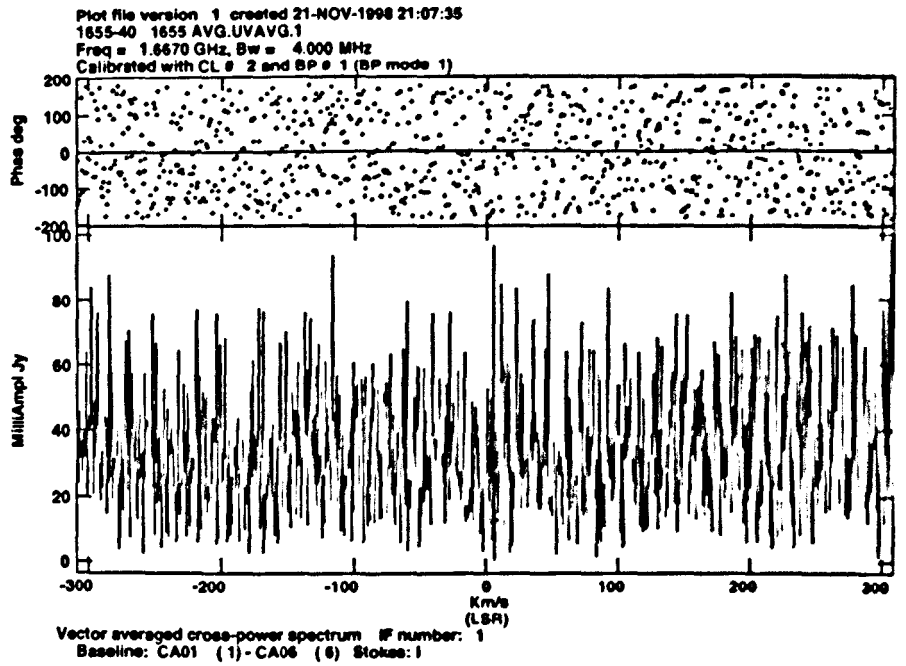


Figure 2.17: An OH maser spectrum of GRO J1655−40. Data is plotted against velocity over 900 channels. The top frame is phase in degrees and the bottom frame shows amplitude in mJy. The mean flux is 35 mJy with an RMS noise of 18 mJy. Again there are no significant emission features above $3\sigma$.

### 2.2.7 GRO J1655−40: Compact Array observations

Observations of GRO J1655−40 at the OH maser frequency of 1667 MHz were taken along side those of GRS 1915+105. The observational details for this source are identical to that of GRS 1915+105. See section 2.2.5 for information about the setup. A spectrum of the search is given in figure 2.17. One can see the flux of GRO J1655−40 at the time of these observations is 35 ± 18 mJy at the 1667 MHz frequency. As with all the previous observations, there is no

emission of any significance above a $3\sigma$ noise level.

### 2.2.8 Combined results for all sources

The results of all maser search programmes are collated in this section. All results presented are $3\sigma$ upper limits.

#### Water masers

The fluxes of the K-band water maser searches are presented in graphical form in figures 2.18 and 2.19. Plotted are individual sources with upper limits against LSR velocity. In figure 2.19, GRS 1915+105 is shown with a log flux scale because of the range of upper limits between the high Cambridge observations and the low MERLIN observations. The data are also presented in table 2.7.

#### OH masers

The OH maser searches cover less sources than the water maser searches and as there are less velocity bands to present, all results can be presented in tabular form, given in table 2.8.

## 2.3 Applications to X-ray binaries

While the physical conditions of masers and their astrophysical environments are well established, maser emission from X-ray binaries has never previously been investigated. By 1996 relativistic-jet X-ray binaries were becoming estab-

| Source | Telescope | Velocity range ($km\ s^{-1}$) | | | $3\sigma$ upper-limit (mJy) |
|---|---|---|---|---|---|
| | Parkes | −670 | → | −420 | 390 |
| | Parkes | −420 | → | −100 | 390 |
| GRO J1655−40 | Parkes | −100 | → | +170 | 460 |
| | Parkes | +170 | → | +440 | 390 |
| | Parkes | +440 | → | +710 | 460 |
| | Cambridge | −210 | → | −150 | 2700 |
| | Cambridge | −150 | → | −90 | 1620 |
| | Cambridge | −90 | → | −30 | 3870 |
| SS 433 | Cambridge | −30 | → | +30 | 4620 |
| | Cambridge | +30 | → | +90 | 1020 |
| | Cambridge | +90 | → | +150 | 6270 |
| | Cambridge | +150 | → | +210 | 2880 |
| | Cambridge | −210 | → | −150 | 1860 |
| | Cambridge | −150 | → | −90 | 1110 |
| | Cambridge | −90 | → | −53 | 1920 |
| GRS 1915+105 | MERLIN | −53 | → | +53 | 46 |
| | Cambridge | +53 | → | +90 | 1780 |
| | Cambridge | +90 | → | +150 | 930 |
| | Cambridge | +150 | → | +210 | 3150 |
| | Cambridge | −210 | → | −150 | 1980 |
| | Cambridge | −150 | → | −90 | 1440 |
| | Cambridge | −90 | → | −53 | 1320 |
| V404 Cyg | MERLIN | −53 | → | +53 | 508 |
| | Cambridge | +53 | → | +90 | 1290 |
| | Cambridge | +90 | → | +150 | 960 |
| | Cambridge | +150 | → | +210 | 930 |
| | Cambridge | −210 | → | −150 | 1650 |
| | Cambridge | −150 | → | −90 | 1260 |
| | Cambridge | −90 | → | −53 | 2100 |
| Cyg X-3 | MERLIN | −53 | → | +53 | 580 |
| | Cambridge | +53 | → | +90 | 1500 |
| | Cambridge | +90 | → | +150 | 720 |
| | Cambridge | +150 | → | +210 | 1470 |
| | Cambridge | −210 | → | −150 | 1320 |
| | Cambridge | −150 | → | −90 | 2580 |
| | Cambridge | −90 | → | −30 | 1080 |
| GT 2318+603 | Cambridge | −30 | → | +30 | 1110 |
| | Cambridge | +30 | → | +90 | 1080 |
| | Cambridge | +90 | → | +150 | 1560 |
| | Cambridge | +150 | → | +210 | 2640 |

Table 2.7: Water maser $3\sigma$ flux upper-limits for all the X-ray binaries searched.

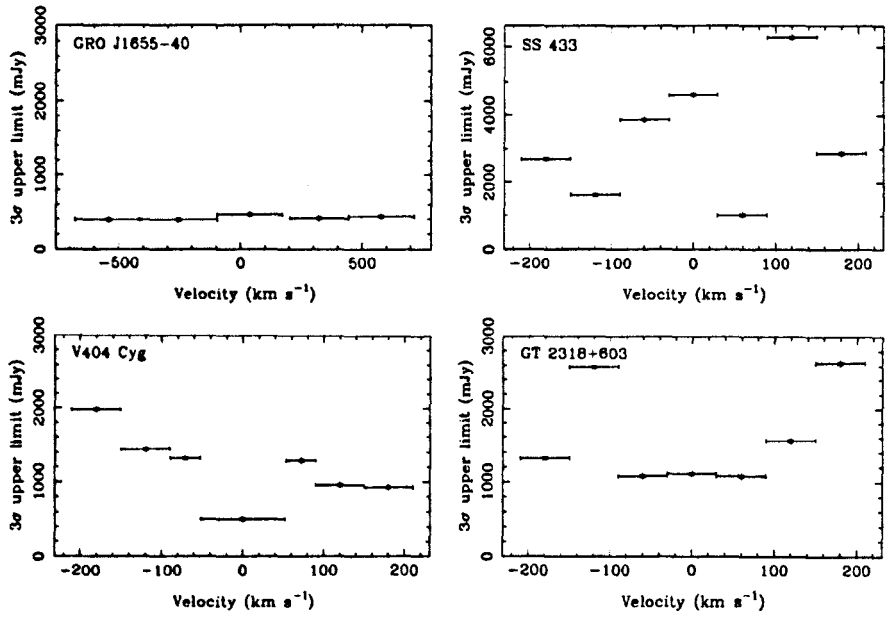


Figure 2.18: $3\sigma$ upper limits of water maser emission in frequency space for four X-ray binaries. All velocities are corrected to the LSR velocity of the source.

| Source | Velocity ($km\ s^{-1}$) | $3\sigma$ upper limit (mJy) |
|---|---|---|
| GRS 1915+105 | −300 - +300 | 129 |
| GRO J1655−40 | −300 - +300 | 89 |

Table 2.8: OH maser flux upper limits for GRS 1915+105 and GRO J1655−40.

lished as a separate class of X-ray binary, and the link with active galaxies was becoming apparent. Could relativistic-jet X-ray binaries emit maser radiation in the same way extragalactic sources do? To investigate this question, one needs to understand the processes of molecule creation and maser formation. The two main maser lines under investigation in this thesis are the water 22 GHz line

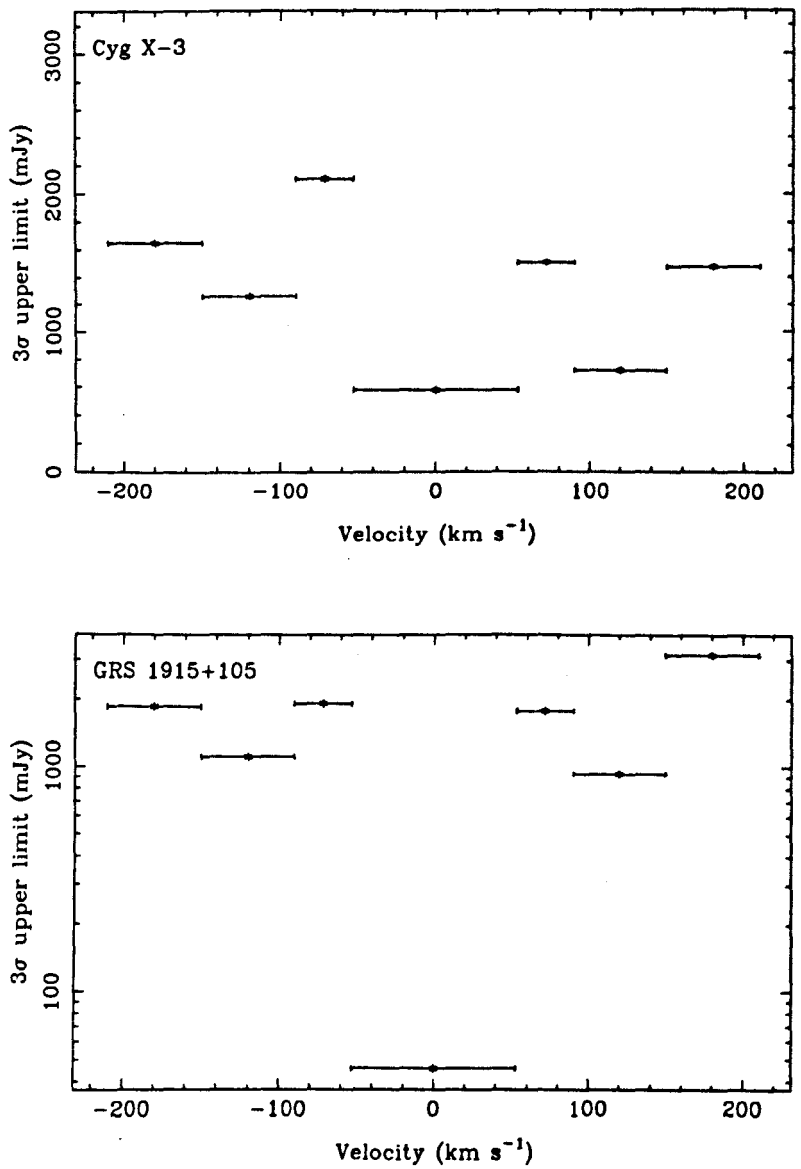


Figure 2.19: $3\sigma$ upper limits of water maser emission in frequency space for Cyg X-3 and GRS 1915+105. The y-axis in the GRS 1915+105 figure is given as a log scale due to the low upper-limit at a velocity of zero km s$^{-1}$. All velocities are corrected to the LSR velocity of the source.

and the hydroxyl main-lines at 1665 and 1667 MHz.

### 2.3.1 Creation of $H_2O$ masers

An $H_2O$ maser needs three things in order to emit radiation: (a) sufficient physical conditions for water to form; (b) densities in the right range so collisional excitation and shielding of molecules occurs; and (c) a sufficiently long path length for amplification to occur. If any one of these conditions is violated the maser emission will cease.

As seen in the sections above, water molecules are formed in temperatures between 1,000 and 100 K where number densities are of the order $10^{15}$–$10^{10}$ $m^{-3}$. If the temperature is too high the dust cannot form; if the number density is too high then the collisional rate exceeds the maser emission rate and the inversion is quenched, also if the number density is too low then the molecules are not excited sufficiently for inversion.

#### Cyg X-3

For the purposes of this argument I will assume Cyg X-3 behaves like a circumstellar maser source, with a wind outflow providing conditions for dust growth and water creation. While this does not follow the above arguments that microquasars should behave like AGNs with maser emission, Cyg X-3 is a special case of a microquasar[1]. The parameters of the wind in Cyg X-3 are not known

[1] With only 5 or 6 known microquasars, each could be their own special case, but Cyg X-3 is highly irregular, even among these select few.

with any certainty, but I will assume the following: the wind has a temperature at the surface of the star of $T_\star = 50{,}000$ K, it is flowing at a constant velocity of 1,600 km $s^{-1}$ and the mass lost in the wind is $1 \times 10^{-5}$ $M_\odot$ $yr^{-1}$, from a star of radius $r_\star = 5$ $R_\odot$.

For the formation of dust, the temperature in the wind has to drop to around 1,000 K. If one assumes a constant temperature decrease of the form

$$\frac{T}{T_\star} = \left(\frac{r}{r_\star}\right)^{-2/5} \tag{2.14}$$

(Cooke & Elitzur 1985), where $T$ is the temperature and $r$ is the radius, then a temperature of 1,000 K would occur at a distance of $r_{CE} = 90{,}000$ $R_\odot$ from the star. If one assumes a slightly different function of temperature with radius of

$$\frac{T}{T_\star} = \left(\frac{r}{r_\star}\right)^{-2/5} e^{-0.45(1-r_\star/r)} \tag{2.15}$$

which is applicable for dust growth in Mira variables (Collison & Nedoluha 1995) then the radius at which the temperature drops to 1,000 K becomes $r_{CN} = 30{,}000$ $R_\odot$. Any water molecule will form at distances beyond this radius from the central star.

Following the calculation of an inner radius, the density at that radius can be calculated. If the mass lost in the wind is not accelerated but has a constant velocity then the mass density, $\rho$, can be calculated at that radius. The density

of the wind has the form

$$\rho = \frac{\dot{M}}{4\pi r^2 v} \tag{2.16}$$

where $\dot{M}$ is the wind mass-loss rate and $v$ is the velocity of the wind. If the mass density for water is equal to $1.37\, m_{\rm H} n_{\rm H_2}$ where $n_{\rm H_2}$ is the number density then re-writing equation 2.16 with astronomical units, $n_{\rm H_2}$ can be expressed as

$$n_{\rm H_2} = 4.5 \times 10^{22} \frac{\dot{M}_5}{r^2 v_{\rm km/s}} \ {\rm m}^{-3} \tag{2.17}$$

where $\dot{M}_5$ has units of $10^{-5}$ $M_\odot$ yr$^{-1}$, $r$ is measured in metres, and $v_{\rm km/s}$ is measured in units of km s$^{-1}$. For the radii measured above, a radius of $r_{\rm CE}$ would imply a density of $n_{\rm CE} = 3.4 \times 10^9$ m$^{-3}$ and $r_{\rm CN}$ would imply a density of $n_{\rm CN} = 3.1 \times 10^{10}$ m$^{-3}$. Both of these densities are lower than is expected for water around circumstellar masers of $n \sim 10^{15} - 10^{12}$ m$^{-3}$. Or to use another approach, the temperature of the wind is too high at the expected densities for the creation of water molecules.

One can use these calculations for the density and radius to calculate upper limits to maser dimensions. A saturated maser requires the least pump power for a given output intensity because every pump photon results in a maser photon. We will therefore use the conditions of a saturated maser in our calculations.

For a cylindrical maser the output luminosity, $L$, is equal to

$$L = 2I\Omega A_{\rm m}\Delta\nu_{\rm m} \tag{2.18}$$

where $I$ is the intensity of the maser, $\Omega$ is the solid angle from which maser emission is beamed, $A_{\rm m}$ is the cross section of the cylinder and $\Delta\nu_{\rm m}$ is the maser line width. If we observe emission from the end of the cylinder, the luminosity of the maser is

$$L = \tfrac{1}{3}\Delta n_0 \Gamma h\nu V \tag{2.19}$$

where $\Delta n_0$ is the number density of inverted molecules, $\Gamma$ is the maser pump rate, $\nu$ is the maser output frequency and $V$ is the volume through which the maser is amplified (Elitzur 1992). The flux density measured on Earth is equal to

$$S = \frac{L}{4\pi D^2 \Delta\nu_{\rm m}}, \tag{2.20}$$

so the required population inversion number, $V\Delta n_0$ is equal to

$$V\Delta n_0 \leqslant \frac{12\pi D^2 S\Delta\nu_{\rm m}}{h\nu}. \tag{2.21}$$

In astronomical units, equation 2.21 becomes

$$V\Delta n_0 \leqslant 5.4 \times 10^{41} \frac{D^2_{\rm kpc}\Delta\nu_{\rm MHz}S_{\rm mJy}}{\Gamma\nu_{\rm GHz}} \ {\rm m^3 m^{-3}} \tag{2.22}$$

where quantities are measured in their subscripted units.

If the maser originates from a cylinder of cross section, $A_{\rm m}$ and length, $l$ then the maser volume can be written as $V = A_{\rm m}l$. The maximum maser amplification can occur over a gain-length between the radii at which the temperature is in the right range for water to form. This was calculated above using equation 2.14, so re-writing this equation for a path length $r_2 - r_1 = l$, where $r_2$ is the radius at a temperature $T_2$ and $r_1$ is a radius at which the temperature is $T_1$ then the maximum path length the maser can be amplified through is

$$l \leqslant 7 \times 10^8 \, r_\star T_\star^{5/2} \left(T_2^{-5/2} - T_1^{-5/2}\right) \ {\rm m} \tag{2.23}$$

The densities of inverted molecules, $\Delta n_0$ can be related to the population densities of $H_2$ and $n_1$ by the expression

$$n_{\rm H_2} = \Delta n_0 \frac{n_1}{\Delta n_0} \frac{n_{\rm H_2O}}{n_1} \frac{n_{\rm H_2}}{n_{\rm H_2O}} \tag{2.24}$$

and it is found that the fractions of water to hydrogen in various states are around $n_1/\Delta n_0 = 50$, $n_{\rm H_2O}/n_1 = 50$ (Richards 1997) and $n_{\rm H_2O}/n_{\rm H_2} = 3 \times 10^{-4}$ (Cooke & Elitzur 1985) so to a first approximation the density of $n_{\rm H_2}$ can be

related to the population inversion by the equation

$$n_{H_2} = 8.3 \times 10^9 \, \Delta n_0. \tag{2.25}$$

One can calculate the density of $H_2$ from equation 2.17 and therefore a number density of population inverted molecules is calculated by

$$\Delta n_0 = 2.7 \times 10^{30} \frac{\dot{M}_5}{r^2 v_{\mathrm{km/s}}} \ \mathrm{m}^{-3}. \tag{2.26}$$

One now has a set of approximations for various maser quantities, the maser inversion number, $V\Delta n_0$ can be calculated by equation 2.22, the maser gain length, $l$, can be calculated by equation 2.23, the number of inverted molecules can be calculated by equation 2.26 and therefore if the maser emission is emitted from a cylinder, one can calculate the cylinder cross section by the equation

$$A_m \leqslant 290 \frac{D^2_{\mathrm{kpc}} \Delta\nu_{\mathrm{MHz}} S_{\mathrm{mJy}} r_1^2 v_{\mathrm{km/s}}}{\dot{M}_5 \Gamma \nu_{\mathrm{GHz}} r_\star T_\star^{5/2} \left(T_2^{-5/2} - T_1^{-5/2}\right)} \ \mathrm{m}^2. \tag{2.27}$$

Using the above equations one can calculate the various maser upper and lower limits for Cyg X-3. Table 2.9 gives the assumed parameters for the system. Using these parameters, and equations 2.22, 2.23, 2.26 and 2.27 table 2.10 gives limits to various maser parameters. When the Cyg X-3 system is compared to a typical Mira variable at 10 kpc, the derived maser conditions are very different. The Mira maser source at 10 kpc has the same conditions as Cyg X-3 except for

| $D$ | $\Delta\nu$ | $r_1$ | $\dot{M}$ | $\Gamma$ |
|---|---|---|---|---|
| (kpc) | (MHz) | (m) | ($M_\odot$ $yr^{-1}$) | ($s^{-1}$) |
| 10 | 0.03125 | $6.3 \times 10^{13}$ | $1 \times 10^{-5}$ | 1 |
| $r_\star$ | $T_\star$ | $T_1$ | $T_2$ | $S$ |
| ($R_\odot$) | (K) | (K) | (T) | (mJy) |
| 5 | 50,000 | 1,000 | 100 | 570 |

Table 2.9: Assumed values for calculating the maser lower limits in the Cyg X-3 system.

| Source | $V\Delta n_0$ | $l$ | $\Delta n_0$ | $A_m$ |
|---|---|---|---|---|
| | ($m^3m^{-3}$) | (m) | ($m^{-3}$) | ($m^2$) |
| Cyg X-3 | $\leqslant 4.3 \times 10^{43}$ | $\leqslant 2.0 \times 10^{16}$ | $\leqslant 0.42$ | $\leqslant 5.2 \times 10^{27}$ |
| Mira at 10 kpc | $\leqslant 4.3 \times 10^{43}$ | $\leqslant 1.1 \times 10^{13}$ | $\leqslant 4.7 \times 10^{6}$ | $\leqslant 8.4 \times 10^{23}$ |

Table 2.10: Derived maser parameters. In calculating parameters for the maser at 10 kpc, the values for $D$, $\Delta\nu$, $\Gamma$, $r_\star$, $T_1$, $T_2$ and $S$ were the same as the Cyg X-3 system; however, quantities which differed were $\dot{M} = 10^{-7}$ $M_\odot$ $yr^{-1}$, $v = 5$ km $s^{-1}$ and $T_\star = 2500$K. These values represent a typical Mira variable.

a lower mass-loss rate of $10^{-7}$ $M_\odot$ $yr^{-1}$, a slower wind velocity of $v = 5$ km $s^{-1}$, but most importantly a lower surface temperature of $T_\star = 2500$ K. The lower temperature resulted in a much closer distance at which dust forms at 1000 K, and the number density of inverted water, $\Delta n_0$ is orders of magnitude higher. We can therefore conclude that the over-riding factor for the absence of maser emission in Cyg X-3 is the low density of inverted molecules, resulting from a high wind temperature.

### Other masers and systems

While the previous section details water maser creation in the Cyg X-3 system, this is not possible with the same depth of detail for the other sources, because less is known about their mass-loss and environment than for Cyg X-3. However, the limits presented for Cyg X-3 should be of the same order for the other sources.

## 2.4 Conclusions

The similarity between microquasars and the energetic active galactic nuclei prompted us to search for maser emission around the radio-jet X-ray binary systems. The searches included both water and hydroxyl masers from northern and southern hemisphere sources. Results were dissapointing as no maser emission was found from any source, but we have been able to place very low upper limits to maser emission on all sources.

The most promising observations were those of V404 Cyg and GRS 1915+105 with initial observations using the Cambridge telescope for V404 Cyg and the MERLIN array for GRS 1915+105. In both cases possible maser emission was detected; however on re-observation, the data included spurious emission due to correlator faults or in the rare case, localised interference.

Using the known environment for Cyg X-3, and the upper limit to any maser emission, upper limits to parameters such as the population inversion density

and gain lengths were calculated. Comparing the Cyg X-3 system with a Mira variable at 10 kpc, the extremely high temperature at the surface of the Wolf–Rayet in Cyg X-3 forces the molecules to travel to a larger distance than in the Mira variable before water molecules can form. At a larger distance from the source, the inverted molecules have a much lower density, preventing detectable maser emission.

# Chapter 3

# Superluminal motion in X-ray binaries

**Megene:** "Well it looks like he's got a firm grip of the reality of it now".

**Ataru Moroboshi:** "I... I... I'm a hippo!"

– *Urusei Yatura Movie 3*

## 3.1 General superluminal theory

Between November 1972 and February 1973 the first superluminal source was discovered. Wittels et al. (1975) found that two components of quasar 3C120 were separating at faster than the velocity of light, with a component in the

plane of the sky between 1.5 and 2.0 $c$. The most logical explanation for this, put forward by Blandford et al. (1977), is the superluminal motion is due to a projection effect combining a high jet velocity (though still $< c$) and a small angle between the jet's direction and the direction to the observer. These two requirements for classic superluminal motion can be easily created in massive galaxy systems, where there is a confinement mechanism to create a jet (presumably connected with the accretion onto a black hole), and there is also considerable energy available to accelerate material in the jets to highly relativistic velocities, and also to accelerate the electrons in the jets to sufficient energies to emit synchrotron radiation.

Given the large energies required to create superluminal motion, much interest surrounded the claim that, following an outburst, two synchrotron emitting blobs (*plasmons*) had been ejected from the centre of the Galactic source, GRS 1915+105, and given the expected distance to the source of 12.5 kpc, the southern plasmon had to be travelling at superluminal velocities (Mirabel & Rodríguez 1994). This observation which was followed by the discovery of the source GRO J1655−40 a year later, created a new class of objects, *microquasars*, Galactic sources with relativistic jets, which have outbursts producing plasmons at relativistic or mildly-relativistic velocities. Microquasars are all enigmatic binaries; the ones displaying superluminal plasmons, are all black-hole candidates.

Apparent superluminal motion occurs when a jet at a velocity of $\beta c$ is observed travelling at an angle $\theta$ to the line of sight, as illustrated in figure 3.1.

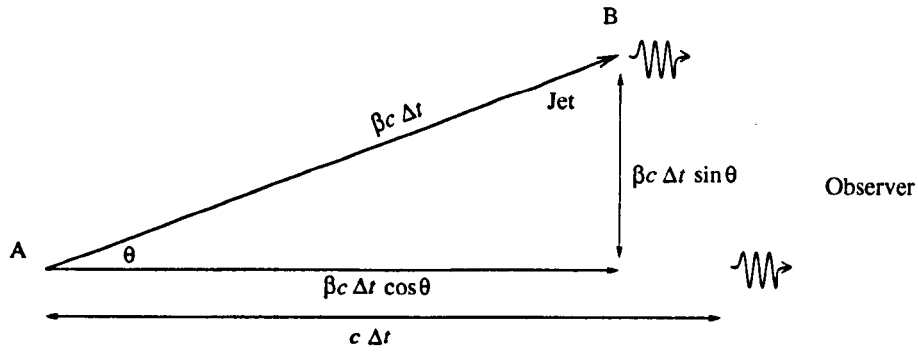


Figure 3.1: Explanation of classic superluminal motion. A jet travelling at a velocity $\beta c$ at $\theta$ to the line of sight emits bursts of radiation at positions $A$ at a time $t = 0$ and $B$ at a time $t = \Delta t$.

We consider two times in the jet's life; at a time $t = 0$ the jet is at position $A$ and emits a burst of radiation. After a time $\Delta t$, the jet has moved to position $B$ and emits a second burst of radiation. In the time $\Delta t$, the radiation from position $A$ and the jet have travelled distances

$$d_{\rm rad} = c\Delta t \tag{3.1}$$

$$d_{\rm jet} = \beta c\Delta t \tag{3.2}$$

so the jet is behind the radiation when it emits the second burst of radiation by a distance

$$d = c\Delta t - \beta c\Delta t \cos\theta \tag{3.3}$$

$$= c\Delta t(1 - \beta\cos\theta). \tag{3.4}$$

In the time-frame of the radiation, the time-difference between pulses is equal to $d/c$ or

$$\delta t = \Delta t(1 - \beta \cos\theta). \tag{3.5}$$

In the plane of the sky, in which the measurements are taken, the jet travels a distance $d_p$ where

$$d_p = \beta c \Delta t \sin\theta \tag{3.6}$$

which when measured from earth corresponds to a distance on a map. The time taken for the radiation to be measured is equal to $\delta t$, so the jet appears to travel in the plane of the sky at a velocity $v_{app} = d_p/\delta t$ where

$$v_{app} = \frac{\beta c \Delta t \sin\theta}{\Delta t(1 - \beta \cos\theta)}; \tag{3.7}$$

hence simplifying and writing $\beta_{app} = v_{app}/c$ gives the classic equation of superluminal motion as a function of true jet velocity and orientation angle:

$$\beta_{app} = \frac{\beta \sin\theta}{1 - \beta \cos\theta}. \tag{3.8}$$

The change of apparent velocity with angle is shown in figure 3.2. The apparent velocity diminishes to zero at zero angle because the velocity perpendicular

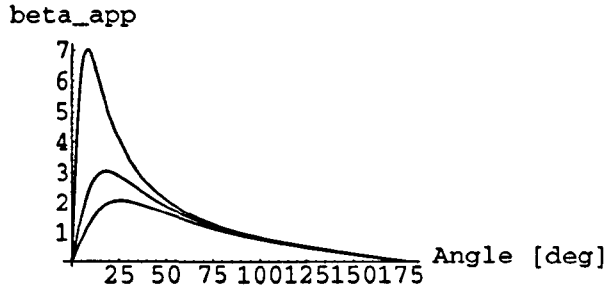


Figure 3.2: Variation of apparent superluminal velocity against jet angle. The velocity diminishes to zero at zero angle because what is measured is velocity perpendicular to the line of sight. Curves are for 0.90, 0.95 and 0.99$c$ jets.

to the line of sight will become zero as $\sin\theta$ becomes 0. The peak of figure 3.2 is found by setting the differential of equation 3.8 with angle, to zero.

$$\frac{\mathrm{d}\beta_{\mathrm{app}}}{\mathrm{d}\theta} = \frac{(1-\beta\cos\theta_{\mathrm{m}})\beta\cos\theta_{\mathrm{m}} - \beta^2\sin^2\theta_{\mathrm{m}}}{(1-\beta\cos\theta_{\mathrm{m}})^2} = 0 \tag{3.9}$$

which occurs when

$$\beta_{\mathrm{m}} = \cos\theta_{\mathrm{m}} \tag{3.10}$$

$$\theta_{\mathrm{m}} = \cos^{-1}\beta_{\mathrm{m}}. \tag{3.11}$$

The maximum apparent velocity can also be written as

$$\beta\mathrm{app(max)} = \gamma\beta \tag{3.12}$$

where

$$\gamma = \frac{1}{\sqrt{(1-\beta^2)}}. \tag{3.13}$$

## 3.2 Superluminal motion in GRS 1915+105 and GRO J1655−40

GRS 1915+105 was the first Galactic superluminal source to be discovered (Mirabel & Rodríguez 1994) and shows classic superluminal motion. It displays two jets at 180° to each other, the forward travelling jet is superluminal where as the backward travelling jet is sub-luminal. The apparent velocities of the jets are measured to be $1.25 \pm 0.15c$ and $0.65 \pm 0.08c$ where the source is at a distance of $12.5 \pm 1.5$ kpc. This motion can be created by two jets travelling at equal speeds of $0.92 \pm 0.08c$ at an angle of $70 \pm 2°$ to the observer's line of sight.

The second Galactic source discovered to be showing relativistic radio components was GRO J1655−40. Tingay et al. (1995) reported that its components moved with an angular speed of $65 \pm 5$ mas $d^{-1}$ so at a distance of 3-5 kpc, the emission would be moving with an apparent motion of $1.5 \pm 0.4c$.

While highly interesting sources in many aspects, these superluminal components can be understood in classical terms.

| Flare | Motion | Axis | $\beta_{app}$ | $\beta$ | $\gamma$ |
|---|---|---|---|---|---|
| 1 | Expansion | Major | $2.45 \pm 0.55$ | 0.920 | 2.56 |
| | | Minor | $0.84 \pm 0.09$ | 0.579 | 1.23 |
| | Contraction | Major | $2.97 \pm 0.33$ | 0.947 | 3.12 |
| | | Minor | $2.53 \pm 0.32$ | 0.926 | 2.65 |
| 2 | Expansion | Major | $4.75 \pm 0.42$ | 0.979 | 4.88 |
| | | Minor | $2.32 \pm 0.32$ | 0.914 | 2.46 |
| | Contraction | Major | $6.76 \pm 0.72$ | 0.989 | 6.86 |
| | | Minor | $2.53 \pm 0.54$ | 0.926 | 2.65 |

Table 3.1: Apparent and actual velocities along the axes of the ellipse from NGS. Values quoted for the variables $\beta$ and $\gamma$ are model dependent, based on a bipolar jet.

## 3.3 Superluminal motion in Cygnus X-3

It is curious that approximately a year separates the discoveries of GRS 1915+105 and GRO J1655−40, and that about a year later than the GRO J1655−40 result Newell, announced results of the third Galactic superluminal source, Cyg X-3 (Newell et al. 1998, hereafter NGS; see also Newell 1996). They announced that the results of VLBA observations indicated that Cyg X-3 increased in size at superluminal velocities, not in jets but as an ellipse, at velocities of 2.4 and 0.8 $c$ along orthogonal ellipse axes. The expansion was followed by superluminal *contraction* at increased superluminal velocities; later, another 'flare' produced faster expansion and contractions. A schematic of these expansions is given in figure 3.3 and the results are shown in table 3.1.

The Cyg X-3 data analysed by Newell et al. consisted of a quiescent flux of 50-100 mJy together with two minor flares. The quiescent flux agreed with Green Bank Interferometer (GBI) monitoring observations at 2 and 8 GHz, and

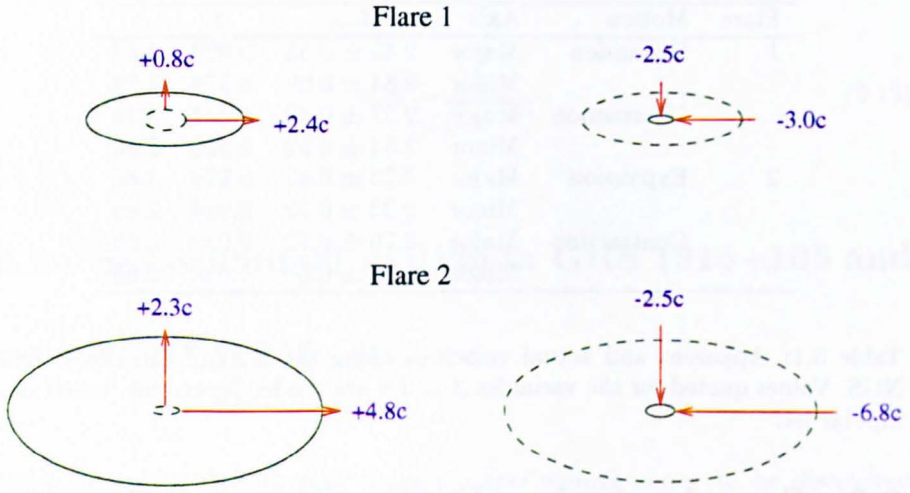


Figure 3.3: Schematic showing the results from Newell et al. (1998). Cyg X-3 starts off as expanding in two axes of an ellipse and contracting at higher velocities. Then a second 'flare' causes expansion and contraction with higher velocities still. To obtain these velocities the centre of the ellipse was deemed to be the centre of the expansions and contractions.

both GBI and Ryle telescopes observed minor flares similar to those shown in the VLBI data, and approximately simultaneously.

Newell et al. only saw flares on certain baselines. This relationship between baseline length and flare detection implied that a change in the structure of Cyg X-3 was observed, rather than just a brightening in the source (Newell 1998).

Newell et al. split the data into 20 minute scans, and mapped each length of data separately. They produced a number of maps where changes through intermediate sizes were observed in addition to the schematic shapes shown in figure 3.3. This indicated that a source structure change had occurred.

### 3.3.1 Model menagerie

The work in the following sections is an extension to a paper published in Monthly Notices of the Royal Astronomical Society (Ogley et al. 1997). In order to explain the motions seen in Cyg X-3 a number of models have to be investigated.

### 3.3.2 Bipolar jet model

The bipolar jet model is the standard explanation for superluminal motion and requires a core and jet, or a two-component jet. The apparent superluminal motion detected in Cygnus X-3 did not show emission resolved into discrete jet components which is typical of sources displaying classical superluminal motion. The VLBA images show an expanding ellipse of material. To measure the expansion a common centre was taken as the centre of the ellipse, distances were taken from the centre to the edge of the emission and velocities were measured as the distance change of this edge between subsequent epochs. If the VLBA maps are explained by a bipolar jet, with unresolved components, a number of problems arise.

#### The contraction problem

If the picture shown above is a true description of the source then in order to produce a contraction of the ellipse, the bulk motion has to be reversed. Such a large acceleration of the material is thought to be unrealistic especially

since the contraction is measured to be faster then the superluminal expansion. Superluminal contraction is not possible for a bipolar jet source.

If the jets are of similar construction to the jets in GRS 1915+105: the jets are formed of electrons-positron clumps (plasmons) with a mass of around $(1/3)M_{\rm moon}$ (Mirabel private communication). Each component of the bipolar jet is travelling at 0.92 $c$ with a gamma factor of $\gamma = 2.56$. Between one epoch and the next, the velocity of the jets changed from +0.92 $c$ to −0.95 $c$ in a time of 60 minutes in the observer's frame. A velocity change would require an acceleration on the jet of $-7,400$ km s$^{-2}$. The force on the jet to provide the acceleration would be $F = -1.9 \times 10^{29}$ N. It is difficult to see how such a system would arise.

### The elliptical problem

After the first expansion motion was detected orthogonal to the major axis of the ellipse at superluminal velocities. A simple jet system would require quadrature jets to be accelerated and decelerated in phase. Such a system is fanciful at the least. Difficult to arrange with a jet model.

### No red-shifted jet

In the original paper, NGS assumed that the centre of the ellipse was at the centre of the system which created the jets. This creates a problem in a bipolar model where one jet is blue-shifted and measured to have superluminal motion,

the other jet is red-shifted and has normal recession velocities. The bipolar jet model gives a two jet structure with the red-shifted and blue-shifted jets travelling at the same velocity. This violates the construction of superluminal jets so therefore the centre of the ellipse cannot be the core of a bipolar system. The section below deals with the construction of a model where the core is not in the middle of the ellipse.

The strength of evidence against a bipolar model discounts it for this source. However, in the other superluminal sources – GRS 1915+105 and GRO J1655–40 – it matches the observational evidence with high accuracy and therefore cannot be discounted for these sources.

### 3.3.3 Offset centre model

As discussed previously, a bipolar model cannot create both red and blue-shifted jets travelling at superluminal velocities, as reported in the NGS paper. The centre of the ellipse cannot be the core creating the bipolar emission. It is unfortunate that a consequence of hybrid mapping that NGS used in the reconstruction of the images is that absolute positional information is lost. It is not possible to accurately locate the ellipses relative to each other, or to the core of the system. NGS assumed that the bright core of each system represented the same feature.

If the superluminal expansion speeds along the major axis are caused by a bulk motion with a component towards the observer, then the speed in the

opposite direction must be sub-luminal, and the point from which the expansion takes place must be offset from the observed centre of the major axis. The same argument applies to the minor axis. The source of the expanding material is located at or near the rim of the ellipse, lying on neither its major or minor axis.

For the first flare, the expansion velocities on the major axis were $\pm 2.45\ c$. If one ignores the error on that velocity of $\pm 0.55\ c$, then a calculation of where the centre of expansion is can be made given a total expansion at $2 \times 2.45\ c$, and the red-shifted jet cannot display superluminal motion. An equation linking the measured velocity and the apparent velocities is given by

$$2\beta_{\rm app} = \frac{\beta_{\rm r} \sin\theta_{\rm r}}{(1 + \beta_{\rm r} \cos\theta_{\rm r})} + \frac{\beta_{\rm b} \sin\theta_{\rm b}}{(1 - \beta_{\rm b} \cos\theta_{\rm b})}, \tag{3.14}$$

where $\beta_{\rm app}$ is the measured velocity assuming the centre of the ellipse is the core and subscripts r and b are for the red and blue-shifted jet respectively. The angle of the jet can be assumed to be the same for both sides of the jet, so $\theta = \theta_{\rm r} = \theta_{\rm b}$. The true jet velocity is also the same for both jets which forces $\beta = \beta_{\rm r} = \beta_{\rm b}$. This makes equation 3.14

$$2\beta_{\rm app} = \frac{\beta \sin\theta}{(1 + \beta \cos\theta)} + \frac{\beta \sin\theta}{(1 - \beta \cos\theta)}. \tag{3.15}$$

Equation 3.15 can be solved for $\beta$ using the MATHEMATICA package and has

two roots:

$$\beta = \frac{\mp\xi\sec^2\theta - \sec^2\theta\sin\theta}{2\beta_{\rm app}}, \text{ where}$$
$$\xi = \sqrt{4\beta_{\rm app}^2\cos^2\theta + \sin^2\theta}. \tag{3.16}$$

The first root, corresponding to the $-\xi\sec^2\theta/(2\beta_{\rm app})$ factor, always produces values of $\beta < -1$ for all values of $\theta$ and $\beta_{\rm app}$. This root is therefore unrealistic. The second root, corresponding to the $+\xi\sec^2\theta/(2\beta_{\rm app})$ factor can be used if the angle to the line of sight is kept constant; as the jet velocity changes, the combined apparent velocity of expansion changes to give the observed values of $2\beta_{\rm app}$.

To observe this effect, a constant value of the angle to the line of sight needs to be taken. The choice of the angle is arbitrary, but when creating the observed apparent motion, the maximum superluminal effect occurs when $\mathrm{d}\beta_{\rm app}/\mathrm{d}\theta = 0$ which occurs at an angle $\cos\theta = \beta$. If the apparent velocity changes, and $\theta$ is kept constant, $\beta$ has to change to accommodate. The range of values for $\beta$ is lowest when $\theta$ is equal to $\cos^{-1}\beta(\max)$, where $\beta(\max)$ is the maximum jet velocity required to create the apparent velocity.

For example, the first flare gave an apparent expansion velocity of $\beta_{\rm app} = 2.45$. If the angle to the line of sight was equal to $\cos\theta = \beta$ for this jet, then the jet velocity would be $\beta = 0.92$ and $\theta = 23$ degrees. If one is assuming the angle to the line of sight is constant, then when the two jet model is constructed, as demonstrated by equation 3.15, the true jet velocity becomes $\beta = 0.997$ and

implies red and blue shifted apparent jet velocities of $\beta_r = 0.2$ and $\beta_b = 4.7$. However, as the observed expansion velocity $\beta_{app}$ increases, higher jet velocities are required to create the observed expansion. In this example, the high observed expansions of 3, 4 and 6 *c* require jet velocities greater than c *at an angle to the line of sight of* $\theta = 23$ *degrees.* If one uses a different initial value for $\beta$ in the equation: $\cos\theta = \beta$ where $\beta$ is now higher, the angle decreases and so at this lower constant angle to the line of sight, $\beta_r$ and $\beta_b$ also decrease.

The lowest fixed value for $\theta$ that can be used occurs at the maximum $\beta_{app}$ observed in the data. This is taken for the second flare contraction with $\beta_{app} = 6.76$, and so $\theta = 8.5$ degrees. Using equation 3.15, $\beta = 0.981$, $\beta_r = 0.074$ and $\beta_b = 4.826$. A lower value for the jet velocity now accommodates all observed apparent expansions and contractions.

Using the above values from the major axis of the second contraction: $\beta_{app} = 6.76$ and $\beta = 0.989$ so $\theta = 8.5$ degrees to the line of sight, equation 3.16 can now be used to calculate the jet velocity for any observed apparent velocity of expansion and contraction. Furthermore, the projected apparent velocities of the red and blue-shifted jets given by the two terms in equation 3.15 can be written as

$$\begin{aligned} \beta_{app,r} &= \frac{\beta \sin\theta}{(1+\beta\cos\theta)} = \frac{\beta\sqrt{1-\beta^2}}{1+\beta^2} \\ \beta_{app,b} &= \frac{\beta \sin\theta}{(1-\beta\cos\theta)} = \frac{\beta}{\sqrt{1-\beta^2}}. \end{aligned} \tag{3.17}$$

The projected velocities for the red and blue shifted jets are shown in table 3.2.

| Flare | Motion | Axis | $\beta_{app}$ | $\beta$ | $\beta_r$ | $\beta_b$ |
|---|---|---|---|---|---|---|
| 1 | Expansion | Major | 2.45 | 0.981 | 0.07 | 4.83 |
| | | Minor | 0.84 | 0.925 | 0.07 | 1.61 |
| | Contraction | Major | 2.97 | 0.986 | 0.07 | 5.86 |
| | | Minor | 2.53 | 0.981 | 0.07 | 4.99 |
| 2 | Expansion | Major | 4.75 | 0.995 | 0.07 | 9.43 |
| | | Minor | 2.32 | 0.979 | 0.07 | 4.57 |
| | Contraction | Major | 6.76 | 1.000 | 0.07 | 13.5 |
| | | Minor | 2.53 | 0.981 | 0.07 | 4.99 |

Table 3.2: Velocities of the red-shifted and blue-shifted jets which would create the observed apparent motions, assuming $\beta_{max} = \cos\theta$. A jet velocity of $\beta = 1.000$ for the second major contraction is due to rounding up and is not equal to 1.

The change in velocities changes the position of the centre by the ratio of the red and blue-shifted velocities. In most cases the jet centre shifts close to the edge of the ellipse.

If one ignores the problems in creating a source with emission over $2\pi$, the large deviations in values of $\beta$ make it seem unlikely that the source exhibits a variable speed jet. The logical argument used in contracting equation 3.15 from a three to a two variable problem was observations of the jet occurred at an angle where maximum superluminal effect occurred. If this assumption is relaxed and the jet velocity is held constant, then the jet can change its projection angle to produce the desired velocity excursions. This is a more plausible explanation than changing velocities.

For a bipolar jet source described by equation 3.15, the apparent superluminal velocity measured in the reference frame of one jet, rather than the reference

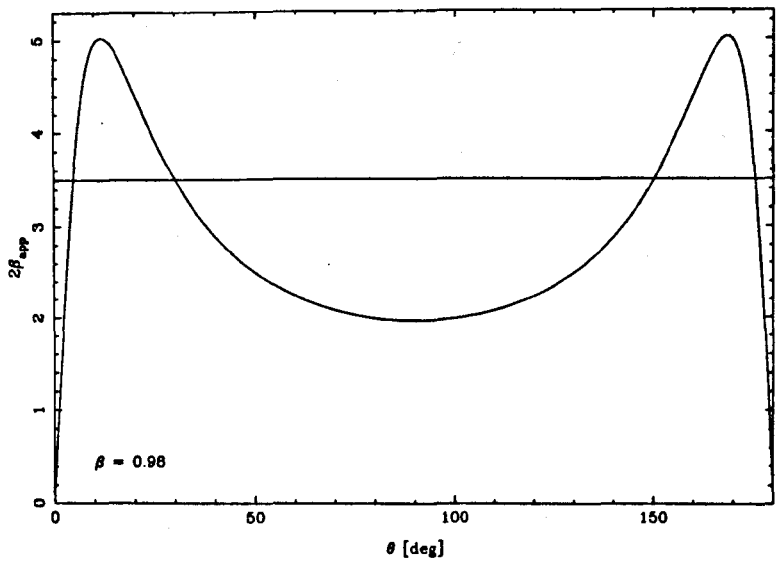


Figure 3.4: Variation of measured jet velocity for both jets combined, with angle to the line of sight. The curve is for two jets at 0.98 $c$, and the horizontal line shows the variation in angle to create an observed expansion of 3.5 $c$.

frame of the core[1], ($2\beta_{app}$ in equation 3.15) plotted as a function of angle to the line of sight is shown in figure 3.4.

For a fixed jet velocity $\beta$, angles between 0° and 180° give two maxima in apparent expansion velocity. The first maximum occurs when the blue shifted jet is at an angle $\cos\theta \simeq \beta$, and the second maximum occurs when the initial red shifted jet has been rotated in angle into our line of sight and replaces the blue shifted jet. The curve is mirror-symmetric about 90°. The curve reaches a

[1]Because no bipolar structure was resolved and velocities can only be measured from an assumed centre, a more robust definition is to measure the expansion from one side of the VLBA ellipse and to assume a blue and red shifted jet contribute to the measured velocities.

minimum at 90° and has a value of $2\beta$. No superluminal motion occurs as we are only observing the true expansion velocity of the two jets.

If a measured expansion velocity is less than the maximum expansion velocity (as indicated by a horizontal line in the figure) then for a fixed jet velocity, four angles to the line of sight produce the observed expansion velocity. Two angles to the line of sight are duplicated by mirror-symmetry in the equation.

Equation 3.15 can be solved for the angle to the line of sight using the MATHEMATICA package and produces the solutions

$$\cos\theta = \pm\left\{\frac{2}{\beta^2} - \frac{1}{\beta_{\rm app}^2\beta^2} \pm \frac{\left(1 - 4\beta_{\rm app}^2 + 4\beta_{\rm app}^2\beta^2\right)^{1/2}}{\beta_{\rm app}^2\beta^2}\right\}^{1/2}. \qquad (3.18)$$

For a given jet velocity, $\beta$, this equation produces either (a) four real roots corresponding to a slice as shown in figure 3.4 or, (b) two complex roots if the required expansion velocity is larger than the apparent superluminal velocity at an angle $\cos\theta \sim \beta$ (corresponding to the slice shown in figure 3.4 being at a larger value than the maxima in the figure).

Values of $\theta$ for $\beta = 0.997$ and $\beta_{\rm app} = 2.45$ are $\theta_1 = 0.87°$ and $\theta_2 = 24.3°$, which represents a deviation of $\delta\theta_1 = -3.57°$ or $\delta\theta_2 = 19.7°$ from the maximum jet-velocity angle of 4.44°. Table 3.3 tabulates jet angles and angle deviations from a maximum angle of 4.44°.

An outburst might produce an elliptical lobe with the central source lying at one end of the major axis of the ellipse, but it seems unlikely to do so for the

| Flare | Motion | Axis | $\theta_1$ | $\theta_2$ | $\delta\theta_1$ | $\delta\theta_2$ |
|---|---|---|---|---|---|---|
| 1 | Expansion | Major | 0.86 | 24.3 | −3.57 | 19.7 |
| | | Minor | 0.29 | 36.0 | −4.15 | 31.6 |
| | Contraction | Major | 1.08 | 19.2 | −3.36 | 14.8 |
| | | Minor | 0.91 | 23.4 | −3.54 | 18.9 |
| 2 | Expansion | Major | 1.95 | 10.4 | −2.50 | 5.91 |
| | | Minor | 0.83 | 26.0 | −3.62 | 21.6 |
| | Contraction | Major | 4.44 | 4.44 | −0.00 | 0.00 |
| | | Minor | 0.91 | 23.4 | −3.53 | 18.9 |

Table 3.3: Angles to the line of sight at which a red and blue-shifted jet would produce the observed expansion and contractions. $\theta_1$ and $\theta_2$ are possible angles to the line of sight. $\delta\theta_{1,2}$ are deviations of the angle to the line of sight from the angle at which maximum apparent velocity occurs; 4.44°.

central source offset from both the major and minor axes. In addition, while values for contraction have been tabulated, this model does not readily explain the superluminal contraction.

### 3.3.4 The Christmas tree model

If the superluminal effect is caused by a pattern of photons propagating, then relativistic bulk motion, and the reversal of relativistic bulk motion, may not be necessary. Equation 3.8 with $\beta = 1$ applies.

If an intense burst of radiation was emitted from the core of Cyg X-3, the observer might, in addition to seeing some of these photons directly, see either photons reflected or scattered off surrounding material, or secondary photons generated in this material following excitation by the burst of radiation. The size of the emitting patch would be governed by the extent of the distribution

of the material around the core of Cyg X-3, by the distance from the core that the burst of radiation had travelled, and possibly by the excitation time for the case of secondary photons.

It is possible to envisage an expanding patch of emission growing as the burst of radiation travels further out. The maximum size observed is determined by the duration of the burst, or by the extent of the surrounding material, or (less likely) by the optical depth of the surrounding material to the centrally emitted radiation. Note, however, that equation 3.8 is cylindrically symmetric about the line of sight, so that an isotropic burst of radiation into an isotropic distribution of surrounding material would give a circular patch of emission. The observed elliptical shape could be produced if either the burst of radiation or the surrounding material were confined to a disc inclined to the line of sight. Equation 3.8 requires that the total apparent expansion speed along any axis is $\geqslant 2\ c$, and the observations satisfy this. Along the axis of the ellipse that lies in the plane of the sky the total apparent expansion speed takes the minimum value of $2\ c$. With higher signal-to-noise ratio observations it should be possible to identify this axis and to determine the orientation of the disc in space.

The superluminal contraction, in this model, is most likely explained by a steady reduction in the effective extent of the photon pattern. Either the central intensity drops continuously and insufficient radiation reaches the outer areas to make visible the material there, or (less likely) a steady change of the central wavelength makes the optical depth gradually greater. It is unlikely that the

extent of the surround material shrinks superluminally. Another possibility is that we are seeing the cooling of an excited region after the central radiation has turned off. However, if the radiation ceases totally, the central parts of the patch cool first. This is not what is observed.

### 3.3.5 Off-axis beam

If a conical jet of high-energy photons or particles was ejected from the core of Cyg X-3 and there was a screen of material or a stationary spherical shell, then part of the shell would be excited and irradiated where illuminated by the jet. The observed emission is centrally peaked suggesting that the beam is more intense along its central axis. A diagram of an off-axis beam is shown in figure 3.5.

The apparent superluminal expansion and contraction can be produced by relatively small expansions and contractions of the opening angle for the cone. Observations at low radio frequencies ($\lesssim$ 5 GHz) show the existence of a scattering screen (Wilkinson et al. 1994), and observations in this thesis (chapter 5) and others (Waltman et al. 1996) show that radio emission following a flare becomes optically thin with increasing radius from the central source. Following Wright & Barlow (1975) and Waltman et al. (1996), a characteristic radius can be defined where the optical depth falls to 0.224, which can be written as

$$R = 2.8 \times 10^{26} \left(\gamma_e g Z^2\right)^{1/3} T^{-1/2} \left(\frac{\dot{M}}{\mu v_\infty \nu}\right)^{2/3} \text{ m}, \qquad (3.19)$$

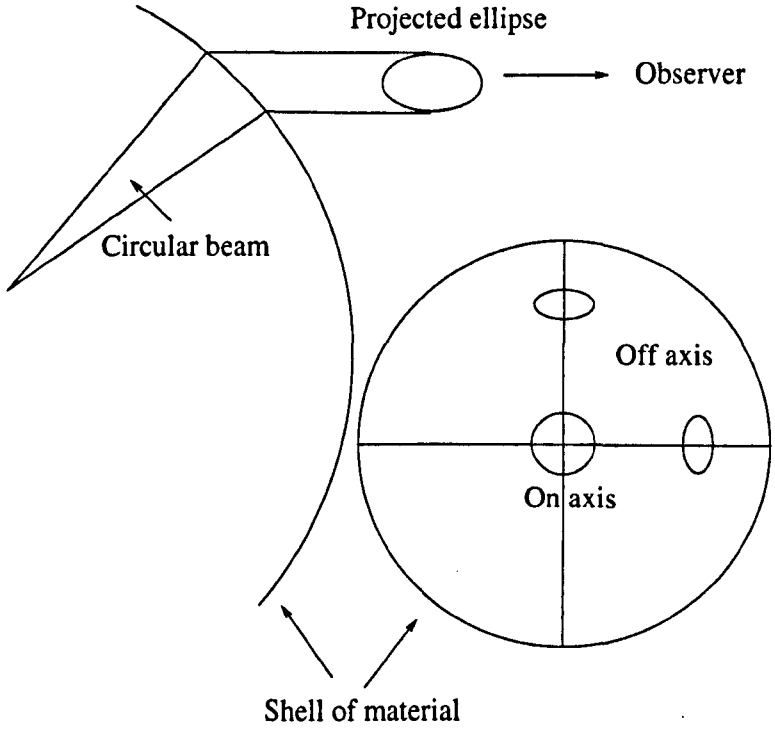


Figure 3.5: A diagram showing the projection of a circular beam offset to the line of sight, and illuminating a shell of material. Any orientation of an ellipse can be created by the beam offset from either axis.

where $\gamma_e$ is the mean number of electrons per nucleon, $Z$ is the ionic charge, $T$ is the temperature of the wind in K, $\mu$ is the mean atomic weight, $\nu$ is the frequency of radiation in Hz, $v_\infty$ is the velocity of the wind in km s$^{-1}$ and $g$ is the Gaunt factor which is equal to

$$g = 9.77 + 1.27 \log\left(\frac{T^{3/2}}{Zv}\right). \tag{3.20}$$

Numerically, Waltman *et al.* assumed the following values: $Z = 1$, $\gamma_e = 1$, $\mu = 4$, $T = 20{,}000$ K and $v = 2{,}000$ km s$^{-1}$. If one uses these values then the radius at which the wind becomes optically thin is equal to

$$R = 8.6 \times 10^7 \dot{M}^{2/3} \nu^{-7/10} \ \mathrm{R}_\odot \tag{3.21}$$

so for a mass transfer of $\dot{M} = 10^{-5}$ M$_\odot$ yr$^{-1}$, observing at a frequency of 1.6 GHz, a scattering screen would be at a distance $\gtrsim 29{,}000$ R$_\odot$. Using this distance to the scattering screen, the edge of the jet appears to travel at superluminal velocities if the jet opening angle changes at a rate of $\gtrsim 3$ arcsec s$^{-1}$. This rate of opening angle is minimised when the jet has an initial opening angle of zero degrees. With an average time interval over which the VLBA observations took place, the beam opening angle would have to expand at a rate of only 0.8 mas s$^{-1}$. Thus both superluminal expansion and contractions are within the bounds of this model. The requirement of this beam opening angle model is that the beaming and cooling time constants of the material are less than the time scales for the change of cone angle i.e. less than one hour. The confinement of the beam might be by a magnetic throat, with the opening angle in part governed by the flux in the beam, producing the observed correlation between size and intensity of the emission.

The observed elliptical shape of emission can be created by the beam striking the shell at an angle to our line of sight. For the expansion of flare two, the

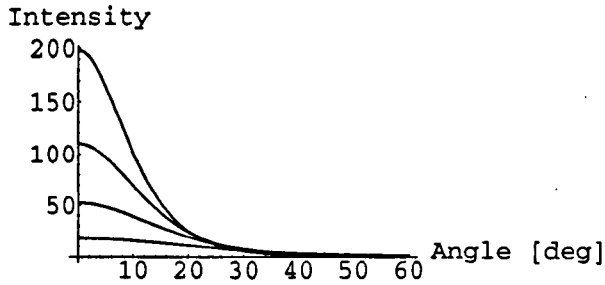


Figure 3.6: A plot of Doppler-boosted intensity against offset angle to the line of sight. The figures plotted are for $\gamma = 1.5, 2, 2.5, 3$.

axial ratio is 2.05. This can be created if the beam is inclined at an angle of 61° to our line of sight. If the inclination of the beam changes by $\sim 10°$ then the observed changes in eccentricity can be accommodated.

### 3.3.6 Superluminal shells

An alternative to a stationary shell as with the previous models is to have a shell of material moving at relativistic velocities. If one considers a shell moving at a velocity $V$ then emission from a region on the shell, at small angles to the line of sight, will have its intensity Doppler boosted according to the equation

$$I(\phi) = \frac{I'(\phi)}{\gamma^3 (1 - \beta \cos \phi)^3} \tag{3.22}$$

where $I$ is the boosted intensity, $I'$ is the rest-frame intensity, $\phi$ is the angle of the emission to the line of sight, $\gamma$ and $\beta$ are related to the shell's velocity (Rybicki & Lightman 1979). If $I'(\phi)$ is constant, the change of observed intensity with angle follows that shown in figure 3.6. The shell appears to have a bright

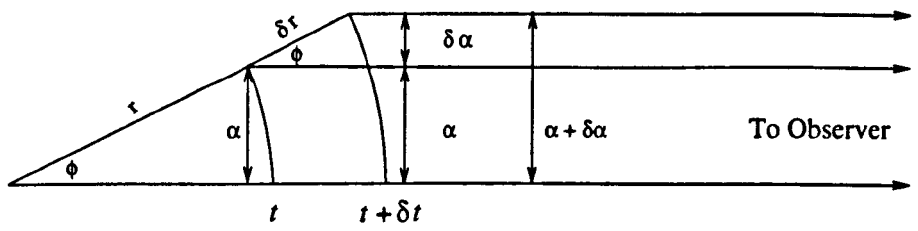


Figure 3.7: The geometry of a shell expanding at a velocity $V$. The radius of the shell is $r$ and $r + \delta r$. The shell subtends an angle $\alpha$ and $\alpha + \delta\alpha$ at times $t$ and $t + \delta t$.

spot centred on our line of sight which expands as the shell expands.

The expansion of the spot can be shown if one considers $r$ to be the radius of the spot with an angular diameter $\alpha$ at time $t$. At a time $t + \delta t$, the radius of the spot increases to $r + \delta r$ and the angular diameter increases to $\alpha + \delta\alpha$. This is shown in figure 3.7.

The shell is expanding at a velocity

$$V = \frac{\delta r}{\delta t} \tag{3.23}$$

and the observed expansion of the spot can be written as

$$v = \frac{\delta\alpha}{\delta t}. \tag{3.24}$$

Since

$$\sin(\phi) = \frac{\alpha}{r} = \frac{\delta\alpha}{\delta r} \tag{3.25}$$

then

$$\delta r = \frac{\delta \alpha}{\sin(\phi)} \tag{3.26}$$

and substituting $\sin(\phi) = \alpha/r$ gives

$$V = \frac{\delta \alpha}{\delta t} \frac{r}{\alpha} \tag{3.27}$$

which gives

$$V = v \frac{r}{\alpha}. \tag{3.28}$$

The VLBA images provide a limit to the size of emission from their dynamical range. As intensity drops with angle as shown in figure 3.4 and equation 3.22, for a dynamical range of 32 the maximum angle at which flux will be detected is 17.6°. This angle assumes values of $\beta$ and $\gamma$ consistent with the second flare expansion. At an angle of 17.6°, the value of $r/\alpha$ is 3.30. This implies that the observed expansion of the shell is a third of the true expansion of the shell. The adjusted velocities which correspond to shell velocities rather than observed velocities for both flares are shown in table 3.4.

In this model a spherical shell will produce a circular spot with circular expansion velocities. To simulate the elliptical shape observed, we postulate a shell distorted by expansion into an anisotropic dense medium.

| Flare | $\phi$ | Axis | $\beta_{app}$(spot) | $\beta_{app}$(shell) | $\beta$(shell) | $\gamma$(shell) |
|---|---|---|---|---|---|---|
| 1 | 36.7° | Major | 2.5 | 4.18 | 0.973 | 4.33 |
| | | Minor | 0.8 | 1.34 | 0.801 | 1.67 |
| 2 | 17.6° | Major | 4.8 | 15.8 | 0.998 | 15.8 |
| | | Minor | 2.3 | 7.58 | 0.991 | 7.63 |

Table 3.4: Adjusted velocities for a Doppler-boosted spot on an expanding shell. Values for $\phi$ are taken using a dynamical range for the VLBA maps of 32, thus intensity offset from our line of sight by more than $\phi$ is not boosted into our observing range.

A dense medium, sufficient to decelerate the shell, is required to explain the contraction. In this model the apparent contraction is due to a rapid reduction in intensity, lowering the emission from most of the spot area to below the detection threshold. The rapid reduction in intensity is due to the collapse of the Doppler boosting when the expansion velocity drops. To calculate the required velocity change, a reduction in Doppler boosting of the intensity of 1/32 is required. The fractional decrease in intensity can be written as

$$\mathcal{R} = \frac{(1-\Delta\beta^2)^{3/2}}{(1-\Delta\beta)^3} \tag{3.29}$$

which can be solved for $\Delta\beta$:

$$\Delta\beta = \frac{\mathcal{R}^2-1}{\mathcal{R}^2+1} - \frac{2.52\mathcal{R}^2}{(1+\mathcal{R}^2)\left(\mathcal{R}^2-\mathcal{R}^4+\sqrt{\mathcal{R}^4(1+\mathcal{R}^2)^2}\right)^{1/3}} + \frac{1.587\left(\mathcal{R}^2-\mathcal{R}^4+\sqrt{\mathcal{R}^4(1+\mathcal{R}^2)^2}\right)^{1/3}}{1+\mathcal{R}^2} \tag{3.30}$$

If $\mathcal{R} = 1/32$, a velocity change of $\beta = -0.819$ is required. If the deceleration occurs in $\sim$ 60 minutes (the typical time between contraction in the NGS observations), then the retardation is $\sim -70$ km s$^{-2}$ and the shell pushes back the retarding medium by $\sim 900$ R$_\odot$. If the shell's mass is approximately equal to the mass lost by the Wolf–Rayet in 60 minutes ($\dot{M}_{\rm WR} \sim 10^{-5}$ M$_\odot$ yr$^{-1}$), $M_{\rm shell} \sim 2.3 \times 10^{21}$ kg. The kinetic energy of the shell for the second flare is equal to $K \sim 3 \times 10^{39}$ J. This would represent a power loss of $8 \times 10^{35}$ W if the energy was lost in 60 minutes. Considerable energy would have to be transferred to the medium, presumably with detectable consequences.

### 3.3.7 Off-axis superluminal shells

This hybrid model, which combines the useful features of the off-axis beam and the superluminal shell models (sections 3.3.5 and 3.3.6), best addresses the difficult questions concerning the contraction and the elliptical shape of the emitting area. This model also addresses the difference in the speeds of the two shells.

The central source produces a series of expanding spherical shells, and a beam of energetic particles or photons. The beam, which is inclined to the line of sight, illuminates a patch on an expanding shell which is seen as an elliptical area of emission. As the shell expands the area expands superluminally, as set out in section 3.3.6, with the minor-axis expansion velocities apparently smaller than the major-axis ones. Doppler boosting of the intensity is not significant

here because of the large angle to the line of sight.

However, as the shell expands the illuminating beam intensity per unit area decreases, and so the emitted radiation falls. If the intensity of the emission across the area has a flat distribution (as is the case for Doppler-boosting at large angles) and is close to the detection threshold of the observer's equipment, then as the source fades its detectable area will rapidly shrink, simulating superluminal contraction.

Meanwhile, another shell has been produced and is expanding in the wake of the first. As emission from the first shell fades, the expanding spot on this second shell becomes visible. The difference in apparent speeds for the two flares can be explained if one imagines the flares to be running into some ambient medium and imparting momentum. A graph of the distance travelled by the shell against time is shown in figure 3.8. If both shells are expanding at the same initial rate, we would observe flare 1 to travel un-hindered, then run into an object that slows it down. After a time $t$ we would have observed it to have travelled a distance $A$ at an average velocity $v_1 = A/t$. During this deceleration, if the shell pushes back the ambient medium, it will have allowed flare 2 to expand a greater distance before being decelerated. For the second flare the initial speed is the same, but the shell travels further, to a distance $B$ before it is slowed down. On the same time-scale, $t$, the average speed will have increased to $v_2 = B/t$. The maximum shell expansion speed occurs when a previous shell has pushed the braking medium out far enough, so we do not see deceleration within the

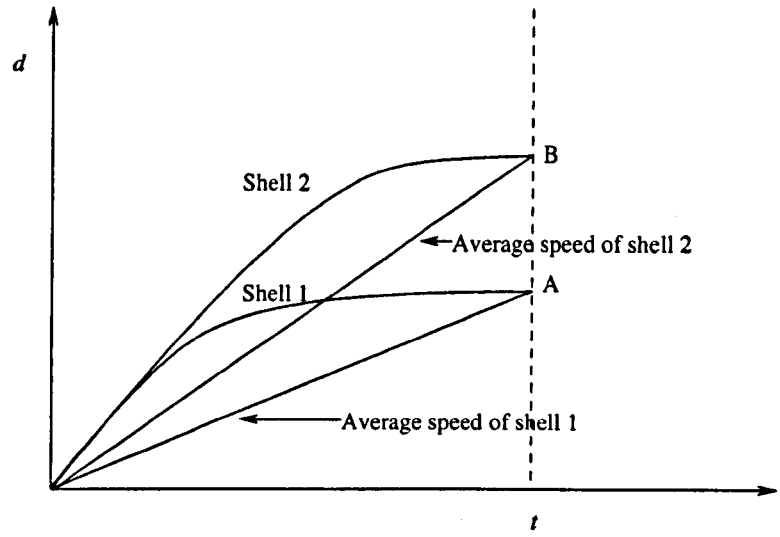


Figure 3.8: Shell expansions based on a constant initial speed for two shells. Shell 1 travels to a distance $A$ before it is halted by some braking medium. Flare 1 moves the braking medium back a bit, so shell 2 travels out further before being decelerated and thus has a higher average speed. The distance between A and B is approximately 900 $R_{\odot}$.

time-scale $t$. Is is then the true expansion velocity of the shell.

In this model a shell apparently expanding at 16 $c$ produces a superluminal expansion of an elliptical area which then fades and appears to contract superluminally. The model accounts for the elliptical shape and the lower minor-axis velocities. Illumination of a subsequent shell produces the next expansion and contraction phase. This shell is expected to travel further before retardation and have a higher average speed.

## 3.4 Conclusions

Superluminal motion is a fascinating phenomenon, the study of which is both rewarding and entertaining. Classical superluminal sources of which active galaxies and quasars are the progenitors serve as a good example of the massive energies required to accelerate jets to relativistic velocities. While classical superluminal sources hold problems themselves (for example how the jets are collimated over Mpc scales, and what provides the energy of the electrons for emission over millions of years), the explanation of the superluminal motion is well established.

While active galaxies and quasars utilise the gravitational potential of supermassive black holes as the power source to accelerate the jets, Galactic counterparts do not have such a high potential for acceleration, thus while jets can be accelerated to relativistic velocities such energy in the jets cannot be supported over millions of years. While Galactic superluminal sources came as a surprise, this shortness of energy provided the mechanism for a useful insight into energetic sources. As these Galactic microquasars only had stellar-size black holes, the timescales for energy release and transport was much shorter than for quasars. Microquasars are active on all time scales from seconds to years, and together with monitoring programmes, have provided much information about the formation of jets.

Jets from microquasars are well-established now to consist of discrete clumps of plasma. The transport of plasmons in the jets are a direct example of super-

luminal theory and this is established on the small scale now so that tests of the evolution of different plasmon ejections are now being undertaken.

The existence of apparent superluminal motion in Cygnus X-3 came as a surprise, not only since the underlying system in Cyg X-3 is different from that of other microquasars (Cyg X-3 is generally thought to contain a neutron star rather than a black hole as its compact object), but the mass transfer between the donor star and the compact object in Cyg X-3 is thought to be wind accretion, an unlikely environment in which to produce jets. While Cyg X-3 is a close binary, the gravitational energy in the system is much lower than that of GRS 1915+105 and GRO J1655−40. A closer analogy would be to SS 433.

Not only is the morphology different in Cyg X-3, but the observation of the superluminal motion is nothing like we have encountered before in any system. The main difference is the apparent superluminal *contraction*, although this could be a consequence of the limitations of the observations and not intrinsic to the binary itself. However, the contraction would not be possible without a major modification to how superluminal motion manifests itself in this system. The classical superluminal constructs fall down with this test.

With a major modification to superluminal theory necessary, two possibilities arise to explain the observed motion: (a) a pattern propagation of re-radiated photons creates the observed motion or; (b) an illumination of a shell – either moving or stationary – creates the expansions, while the contractions

are caused by the illumination at various angles dropping below detector limits thus creating apparent contraction. Both methods require further components to the system of Cyg X-3 and neither are satisfactory in their explanation.

The observation and theoretical explanation of superluminal sources is complete of the well-behaved sources, but far from satisfactory for Cyg X-3, where once again we are at a loss to explain it totally.

# Chapter 4

# Rapid radio photometry of Cyg X-3

"Please note that it is quite right to claim that mapping isn't a 'black art'. Mapping follows established physics and logical principles. It just *looks* like a black art".

– *MERLIN cookbook*

## 4.1 The state of Cyg X-3

Cygnus X-3 is a variable source both temporally and spatially. The system consists of a neutron star / Wolf–Rayet binary in close proximity. The interaction between the gravitational potential and magnetic fields of the neutron star

forms and accelerates relativistic jets that manifest themselves as synchrotron emitting plasma. See chapter 5 for a description of this emission.

### 4.1.1 The temporal variations

The Wolf–Rayet component in the system has a strong stellar wind. The density of the wind is not constant, but varies on random timescales. It is assumed that the consequence of increased wind density to the environment around the neutron star is that there are more electrons available for acceleration in the jet which increases the synchrotron luminosity. Radio photometry monitors the change in radio emission following a change in the Wolf–Rayet state and three distinct states of emission in an unresolved core of the system have been identified.

For the majority of the time the system is in a quiescent state with flux densities at GHz frequencies around 100 mJy. This is the normal state of the system and apart from the existence of a continuous flux from the source, is more or less uneventful.

When a large increase in the density of the Wolf–Rayet wind occurs, the system flares. From a quiescent flux of 100 mJy the flux can increase 10–100 times on a timescale of around a day. Major flares occur usually every 18 months, however more recently a larger number of flares have occurred. See section 1.3.2. A major flare episode is very energetic and lasts for days or weeks, exponentially decaying back to quiescence.

Identified immediately before a major flare is a period of quenching of the radio flux. The flux during quenching can drop to around 10 mJy and the period typically lasts for about a week, with a relaxation period between the quenching and the major flare. If the mass loss from the Wolf–Rayet star is constant over long timescales then there must exist a period of quenching before or after a flare.

There exists a third radio state which is more complex to interpret than quiescence or major flaring. This is a state of minor flaring in which there are small, short increases in flux up to 1 Jy (the arbitrary identification of a major flare event). These flares on the face of it are smaller counterparts to major flares. The flare strength is lower, and rise and decay times are shorter. However, unlike major flares which are one-off energetic events, minor flares exist during a flaring period. A minor flare period can last for up to a few weeks in which multiple daily or hourly flares can occur.

### 4.1.2 The spatial variations

Flux increases during major and minor flares have prompted observers to investigate the spatial nature of the source. Because the radio emission occurs from the jets in the binary (either resolved or unresolved), the plasmons[1] should be visible after a major flare. A well covered event in Cyg X-3's history was the 1986 flare. VLA and MERLIN observations at 5 GHz provided evidence that a

[1]Plasmons are discrete blobs of radio emitting plasma which are assumed to travel in ballistic trajectories from the core forming the jets.

bipolar jet had produced two plasmons travelling in a north–south direction at speeds of 0.35 $c$ (Spencer et al. 1986). This was good evidence of jet structure, and was only observed after the system had undergone a major flare.

Given the similarity between minor and major flares, plasmons in the jet produced by a minor flare should show similar structure to the major flare events, but with a decrease in intensity due to a decrease in the number of electrons available for emission. The apparently superluminal expansions and contractions of the source modelled in the previous chapter were observed following a minor flare by Newell et al. (1998) using the VLBA. Newell (1996) also investigated the decay of major and minor flare events and found there was a significant difference between the decays. Such evidence would indicate a difference in the creation of the two types of flares. However, when Newell observed Cyg X-3 with MERLIN after a minor flare, a bipolar jet structure was seen expanding at the previously observed velocity of 0.3 $c$. Either a deceleration of the jet occurs between the 1 mas scale of the VLBA where superluminal velocities are seen and the 300 mas scale of MERLIN, or a more complicated theory of jet formation needs to be established. However, note that we have found that a bipolar jet is the least likely scenario to explain the VLBA results and alternative models are required (see chapter 3).

Following plasmons as they travel from the source is of great interest for the determination of the jet velocity, and also for any identification of cooling or adiabatic expansion in the plasmons. Previous observations have had to rely on

the time delay between the onset of a flare event and the subsequent observation of plasmons some distance from the central source in order to determine the velocity of expansion. Mapping over a period of time resolves this problem of identifying a flare event – useful if multiple flares have occurred.

We were awarded 6 epochs of observing time with MERLIN at C-band (5 GHz) and also 2 epochs at L-band (1.6 GHz) to map the source during a minor flare period.

## 4.2 The Observations: C-band

Daily monitoring by both the Ryle telescope and the Green Bank Interferometer provided information about the state of Cyg X-3 and were used to trigger the MERLIN target-of-opportunity time to follow a minor flare. Figure 4.1 shows photometry at 15 GHz from the Ryle telescope; on MJD 50407 a minor flare occurred with a flux of 650 mJy. This was preceded by 4 days of quenching.

If the jets are travelling at 0.3 $c$ then to be resolved at 10 kpc the plasmons would have to have been travelling for 10 days, so their angular separation from the core is equivalent to the MERLIN beam size of $\sim$ 50 mas. The observations were therefore delayed for 12 days until MJD 50419. The expected separation of a plasmon and the core would then be 60 mas.

To follow any motion it was planned that observations should be sufficiently separated to allow the plasmons to move a distance of around 1 MERLIN beam

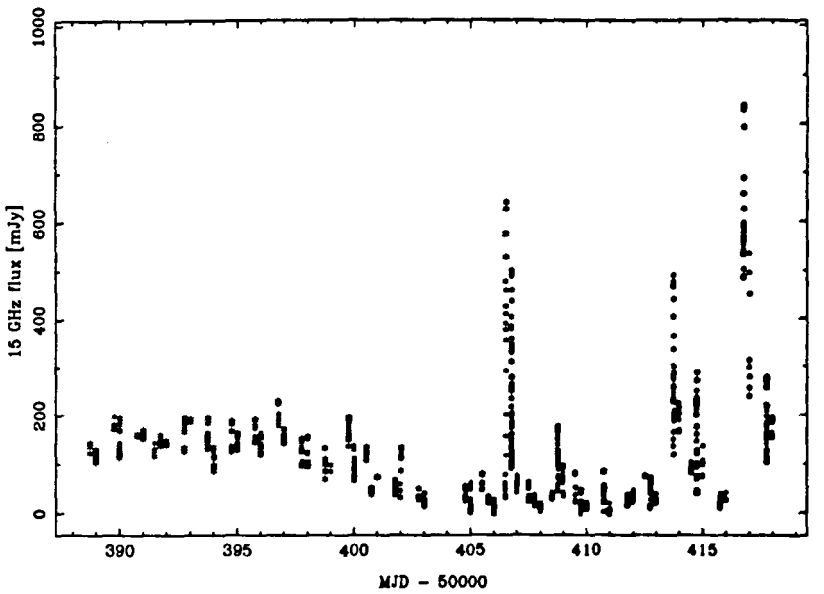


Figure 4.1: Flux monitoring of Cyg X-3 using the Ryle Telescope during 1996 November. A minor-flare occurred on MJD 50407 which triggered the MERLIN observations. The minor-flare followed a period of quiescence with a short burst of quenching.

width between epochs; this would be ideal for interpretation. The additional 5 epochs were separated by around one week from each other. Observations occurred on the dates MJD 50419, 50425, 50433, 50438, 50446 and 50459. Figure 4.2 shows the photometry at 15 GHz for the time of the first 5 epochs. Observations were taken at positions marked by the arrows. One can see that the source was not constant over the time of the observations.

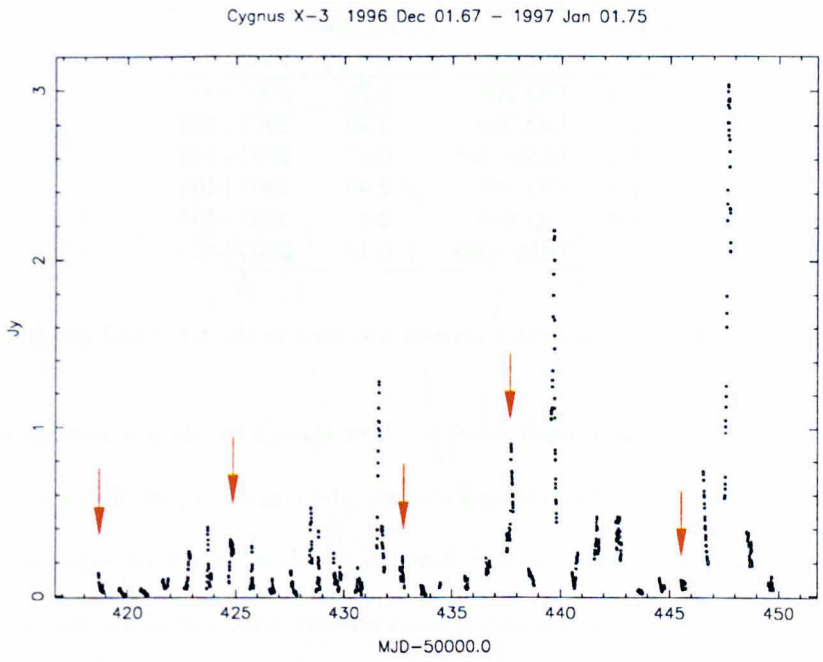


Figure 4.2: Flux monitoring at 15 GHz of Cyg X-3 while MERLIN data was being taken. This plot shows data during 1996 December and the start of January. Dates of MERLIN observations are marked by the arrows.

### 4.2.1 MERLIN data

Reduction of the MERLIN data followed standard techniques for calibration of a weak source with external phase referencing, as documented in appendix A.1.1. The calibrators used, and their flux densities[2] for all 6 C-band epochs are given in table 4.1.

A plot of flux against *uv* distance for first epoch of data shows that the source

[2]The observed flux densities for the point-source calibrators are not constant in time, and have to be calibrated with a source with a known constant flux. However, this constant flux source is resolved on all but the shortest MERLIN baselines and therefore cannot be used as a flux calibrator over longer baselines. For a proper discussion see section A.2.2.

| Epoch | Calibrators | | |
|---|---|---|---|
| MJD | Point source | $S$ [Jy] | Phase |
| 50419 | OQ 208 | 2.29 | 2005+403 |
| 50425 | OQ 208 | 2.39 | 2005+403 |
| 50432 | 0552+398 | 6.07 | 2005+403 |
| 50438 | OQ 208 | 2.43 | 2005+403 |
| 50446 | OQ 208 | 2.41 | 2005+403 |
| 50459 | 0552+398 | 6.19 | 2005+403 |

Table 4.1: Table of calibrator sources observed in the 6 C-band epochs

is unresolved out to the longest baseline. Even though the data is variable (see figures 4.4–4.9) and the flux changes over the observation, a plot of flux against $uv$ distance does not show a $\mathrm{sinc}^2$ function profile as would be expected for a resolved source, the plot shows a constant flux with variations due to the variable nature of the source. The plot of flux against $uv$ distance is given in figure 4.3. Because the source is unresolved over all the baselines, the longer baselines can be used in any photometry giving a lower noise level than for just the single shortest baseline. Photometry of the 6 epochs are given in figures 4.4 to 4.9. Note that the vertical scales vary and that the zero has been suppressed.

Data have been averaged into time bins of 2.0–4.0 minute duration to reduce noise and a number of features are visible in the plots. Points to note in the data are:

- In all but the MJD 50445 (28 Dec 1996) data, the flux is variable on timescales shorter than a couple of hours. This caused problems in the mapping of the source as the first assumption that flux is constant over

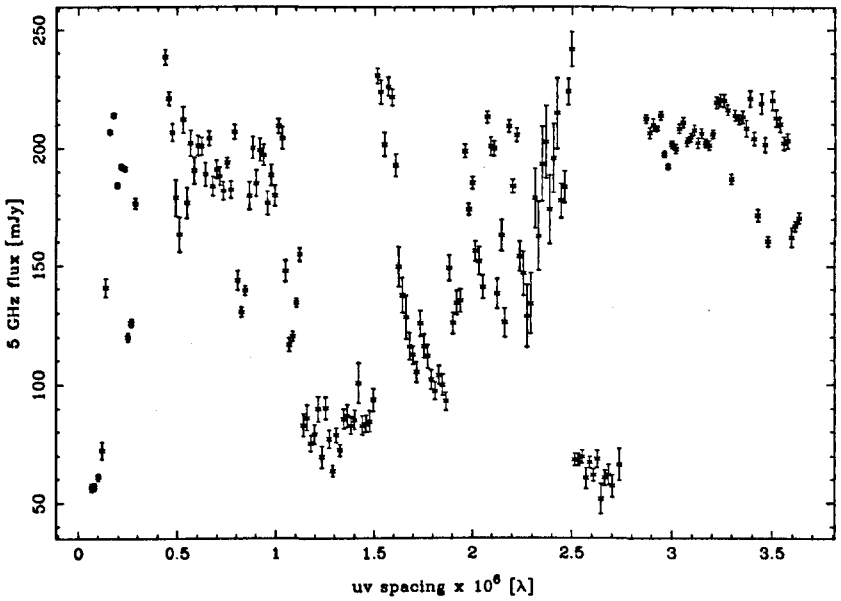


Figure 4.3: A plot of flux against *uv* distance for the first epoch. Even though there are flux changes as shown, the source does not display a $\text{sinc}^2$ profile of a resolved source. Cyg X-3 is therefore unresolved over all the MERLIN baselines.

the timescale for aperture synthesis is then invalidated.

- A number of flares occurred, however the timescales involved are not constant or correlated by flare strength or length of time in quiescence preceding a flare.

- Sudden jumps in the data, both increases and decreases, are apparent. Note the small jumps at MJD 50432.54 and 50445.66; and the large jumps at MJD 50438.46 and 50445.77. These steps downward are extremely

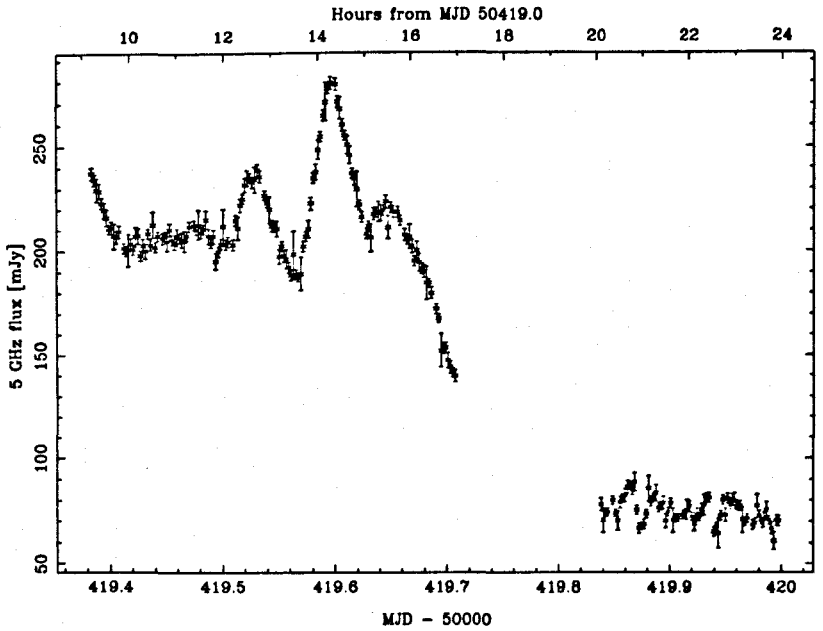


Figure 4.4: Cyg X-3 photometry at C-band on 01 December 1996. Time bins are 3.4 min.

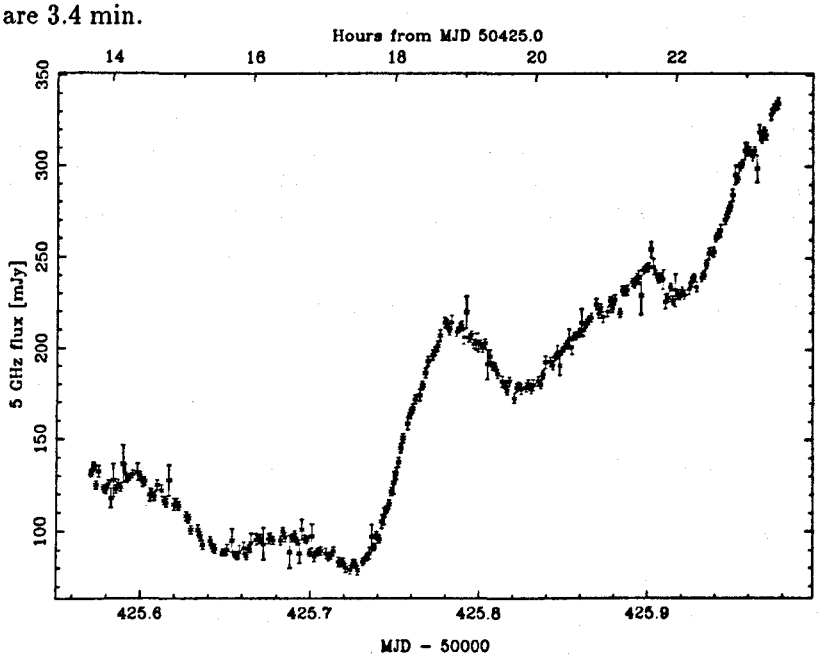


Figure 4.5: Cyg X-3 photometry at C-band on 07 December 1996. Time bins are 2.2 min.

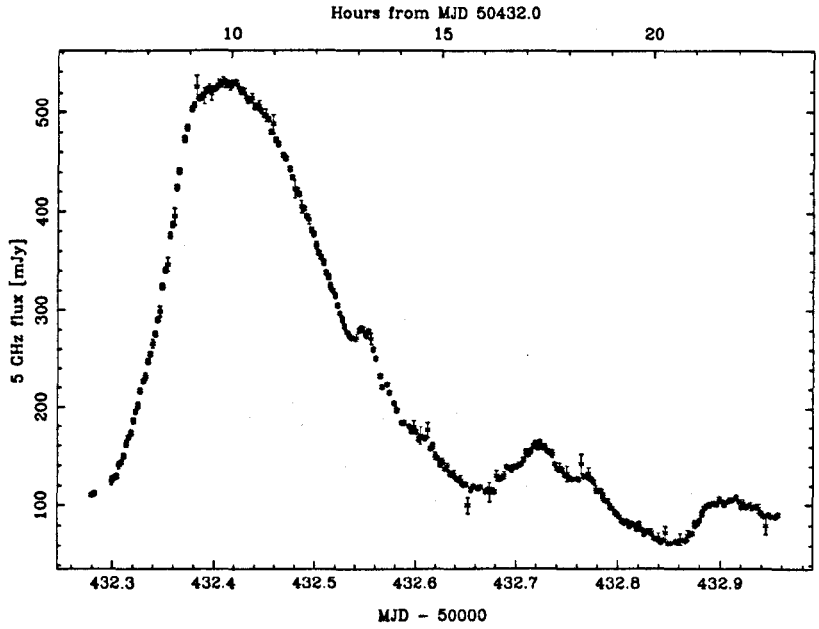


Figure 4.6: Cyg X-3 photometry at C-band on 15 December 1996. Time bins are 3.8 min.

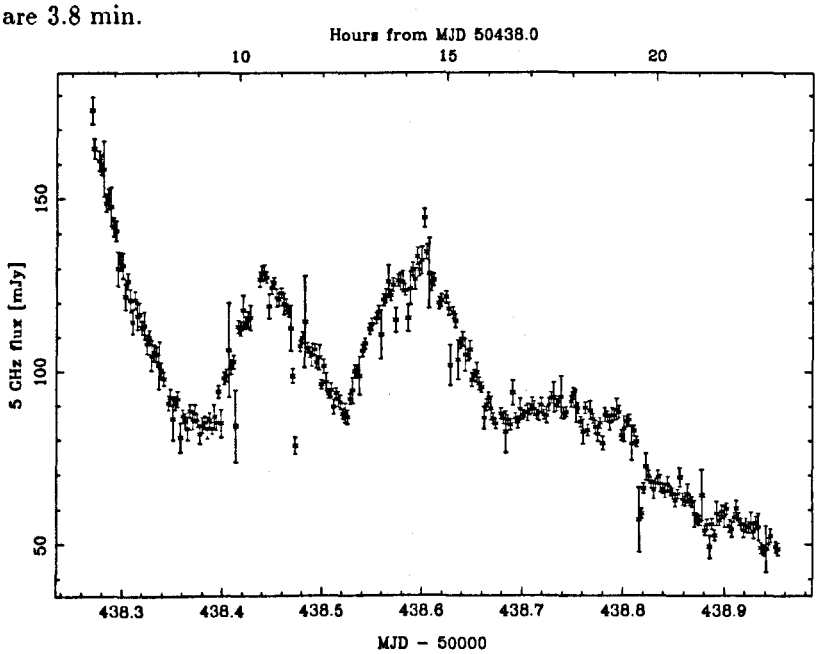


Figure 4.7: Cyg X-3 photometry at C-band on 21 December 1996. Time bins are 4.0 min.

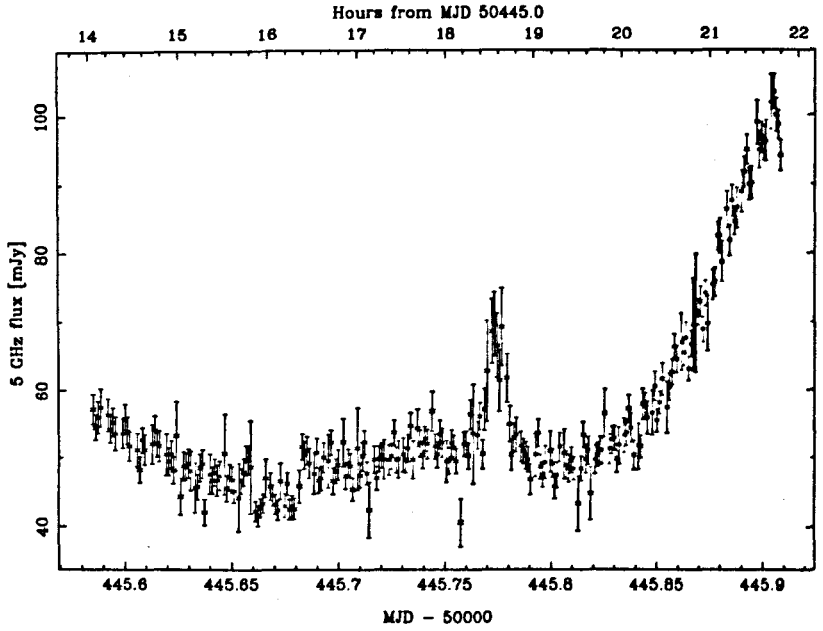


Figure 4.8: Cyg X-3 photometry at C-band on 28 December 1996. Time bins are 2.0 min.

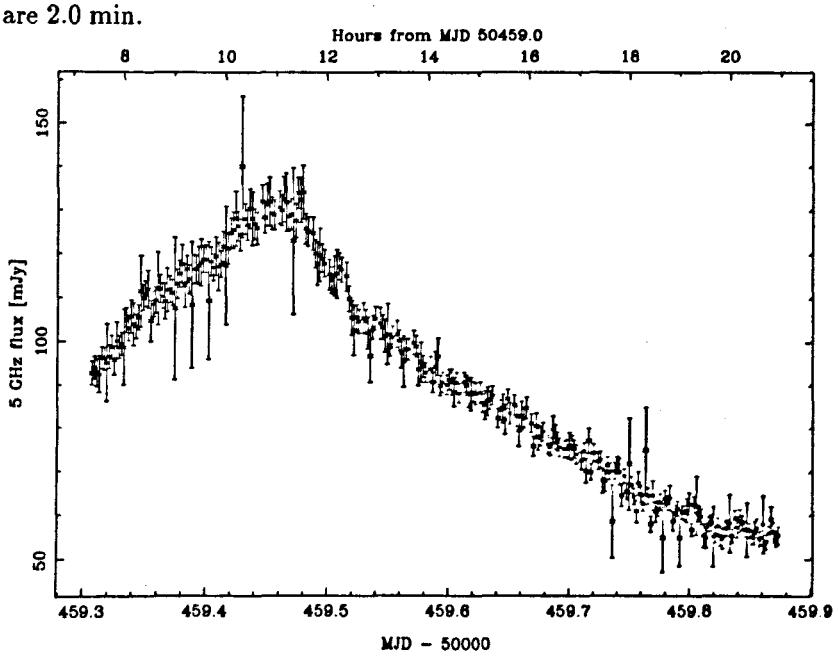


Figure 4.9: Cyg X-3 photometry at C-band on 11 January 1997. Time bins are 3.4 mins.

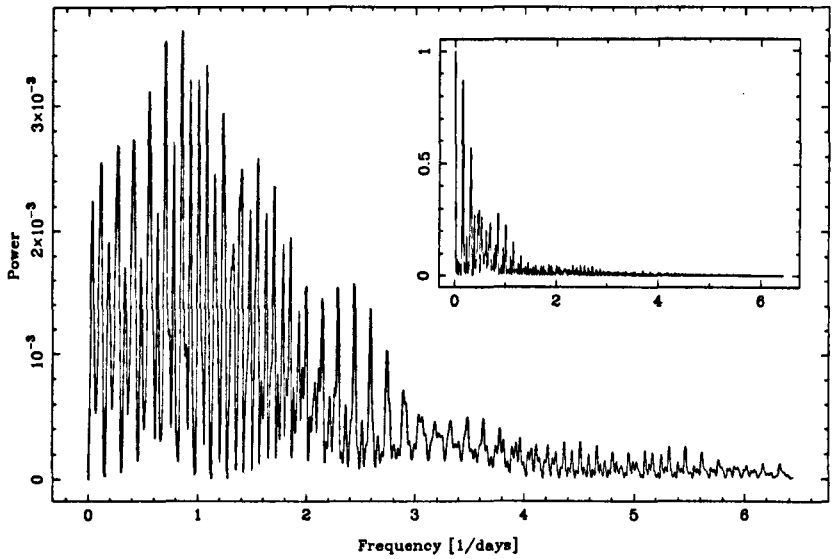


Figure 4.10: Dirty power spectrum

difficult to explain.

### 4.2.2 Power spectra

To search for any periodic signals in the data, photometric points from all 6 epochs were concatenated into a file, then the Fourier spectrum was found of the data. This is shown in figure 4.10. The main part of the figure is the power spectrum or direct Fourier transform of the data; the insert is the Fourier transform of the windowing function. The direct Fourier transform is the time-domain equivalent of a dirty map and the windowing function is equivalent of the dirty beam in 2-D interferometer Fourier transforms. In the same way as one can re-create a clean map from a dirty map and dirty beam, the power

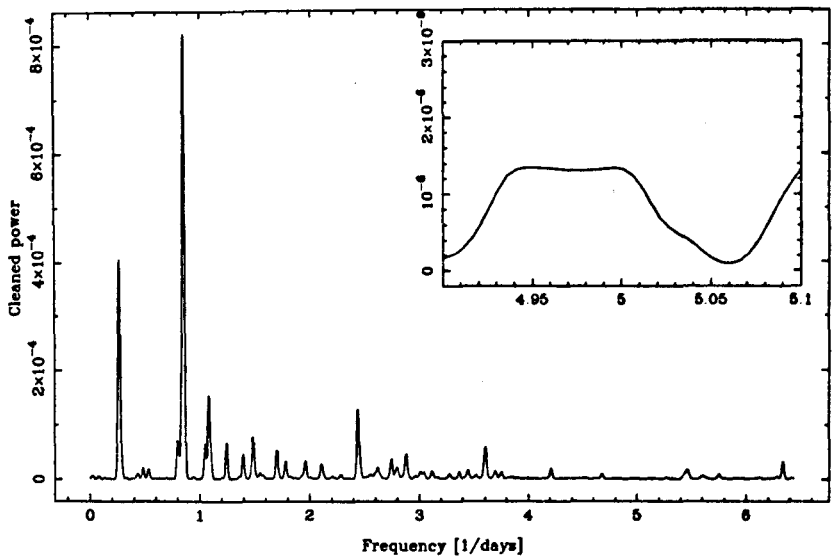


Figure 4.11: A Cleaned spectrum. An insert shows the power at a period of 4.8 hours. There is no evidence for any periodic signal at the binary period.

spectrum can be cleaned by an iterative subtraction of the window function. The result of this procedure is shown in figure 4.11. There are a number of very strong peaks in the cleaned spectrum. The strongest occur at periods of 3.8 days and 1.2 days. There is no evidence for periodicity at the 4.8 hour orbital period, shown by the insert.

To check whether these periodicities are spurious, the first three epochs were analysed separately from the last three epochs. The cleaned spectra are shown in figure 4.12. As there is no correlation between the two halves of the data sets, analysed and cleaned separately, we can conclude that there are no stable

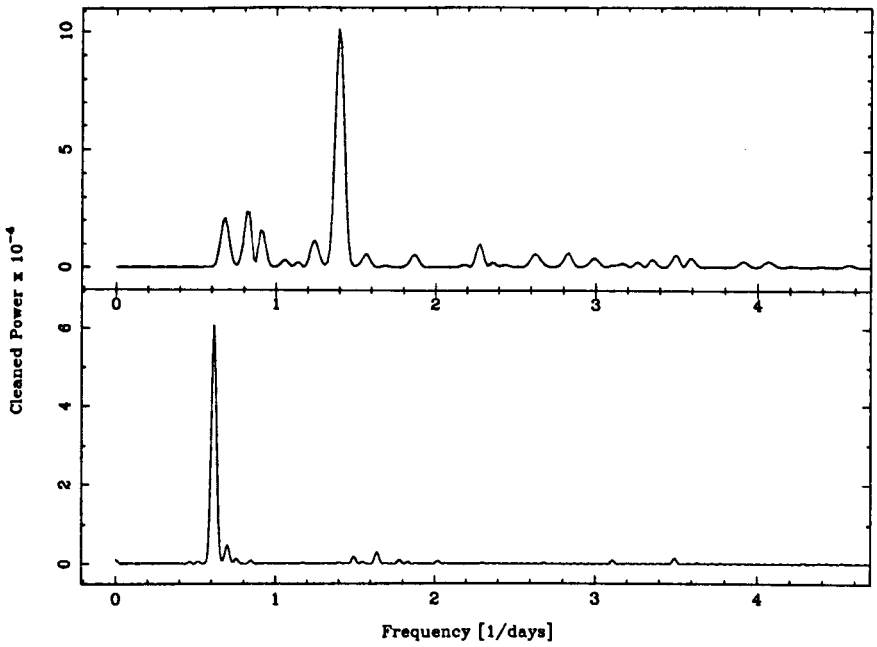


Figure 4.12: C-band data cleaned as shown in figure 4.11, but split into two halves. The top panel shows the first three epochs, and the bottom panel shows the last three epochs. There is no correlation in the periods found in the two halves of the data, indicating that the system is chaotic in nature, and any periodicity is spurious.

periodicities and any periodicity shown is due to spurious features or quasi-periodic oscillations.

### 4.2.3 Mapping and model fitting

While the photometric data generally invalidate the first assumption of interferometric mapping, that the flux of the source is constant, there is a small range of data which is constant. The flux of the source at MJD 50445 is ap-

proximately constant at 50 mJy for 6 hours. Unlike the VLA, MERLIN does not have the spatial coverage of telescopes and therefore is more dependent on rotation synthesis for a completely sampled aperture (See Appendix, section A.3 for *uv* coverage and aperture synthesis). An observation of 6 hours at a declination of 40° is approaching the limit of imaging a source with MERLIN.

Mapping the constant flux region of the data gives the map shown in figure 4.13. The synthesised beam shown in the bottom left of the map is 69 × 36 mas. The map has a $1\sigma$ noise level of 260 μJy and contour levels are logarithmic at -3, 3, 6, 12, 24, 48 times the noise. The core of Cyg X-3 has a peak flux of 36 mJy/beam and the map shows what appears to be two blobs of emission north-east and south-west from the core. However, with the noise in this image, it is difficult to tell with any certainty whether these features are real.

To investigate the effect of a change in flux, a similar map was produced which included all the data from MJD 50445. The map is shown in figure 4.14 and includes the following differences. The beam size has increased despite the extended *uv* coverage. The new beam is now 69 × 41 mas. The noise has also increased to 430 μJy and the NE and SW features in the previous map are now shown to be artifacts due to the changing flux.

As the mapping of the sources is contaminated by flares, a direct observation of any jet structure cannot be obtained. An alternative approach is to take small time intervals in which the flux of the source is approximately constant and to model fit the data in the *uv* plane. This removes any necessity of having a long

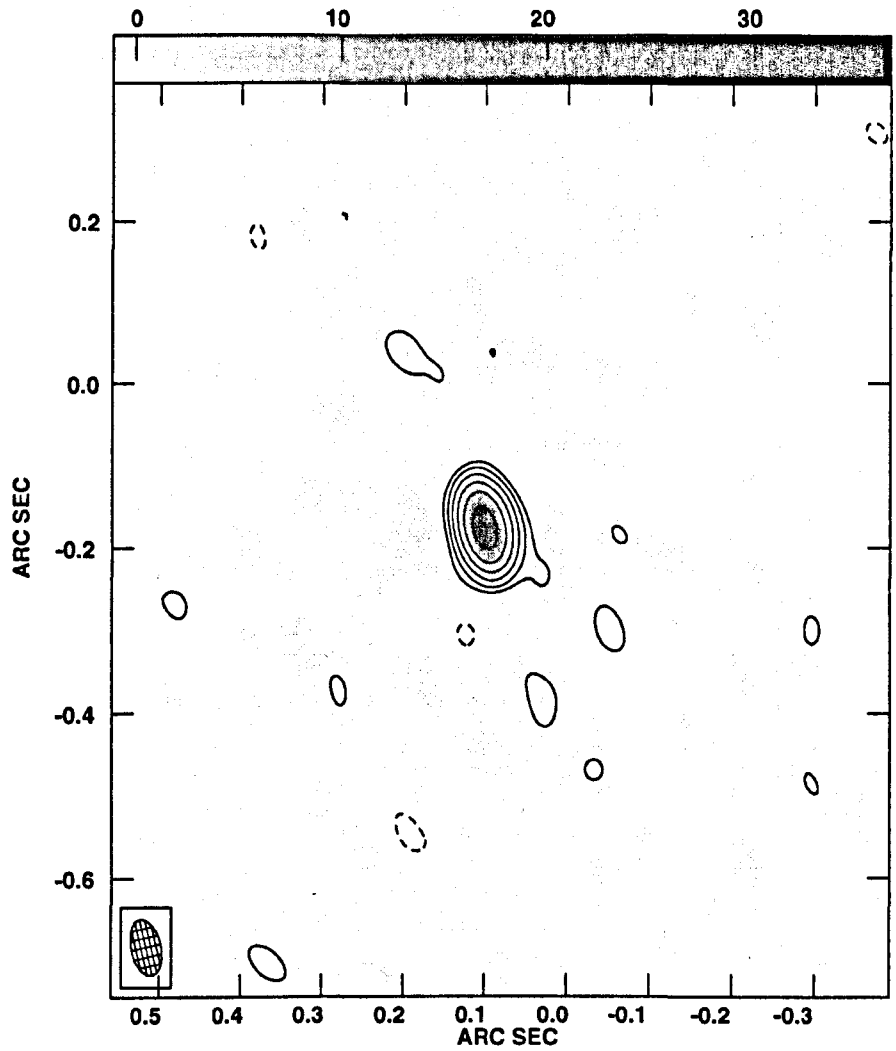


Figure 4.13: A map using 6 hours of data where flux is constant. The map has a beam size of 69 x 36 mas and has a $1\sigma$ noise of 260 μJy. Contours are -3, 3, 6, 12, 24 times the noise and the peak is 36 mJy. At this level of noise, it is uncertain whether the 'jet' like features are real.

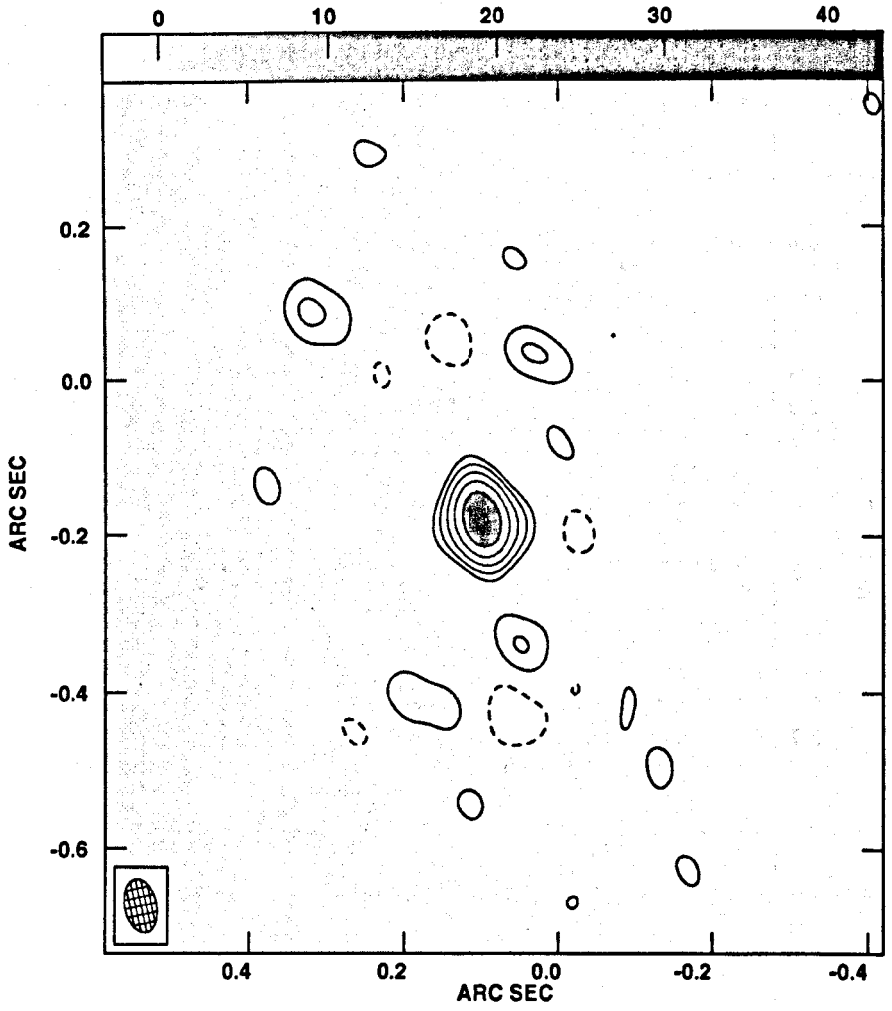


Figure 4.14: A map using all the data, including the time-varying components. The map has an increased beam size of 69 × 41 mas and has a $1\sigma$ noise of 430 μJy. Contours are -3, 3, 6, 12, 24 times the noise and the peak is 43 mJy. Features on the map are due to amplitude errors and not to any jet structure.

| $S$ (mJy) | $R_\phi$ (mas) | $\theta$ (deg) | $R_{\rm Maj}$ (mas) | Ratio | $\phi$ (deg) | $\chi^2_{\rm r}$ | d.o.f |
|---|---|---|---|---|---|---|---|
| 43.5 | 0.601 | 165 | 14.27 | 0.499 | −34.8 | 0.00619 | 1366 |
| 42.7 | 0.538 | 162 | 14.56 | 0.499 | −21.52 | | |
| 1.52 | 232 | 23 | 51.52 | 0.000 | −86.44 | 0.005995 | 1354 |
| 1.65 | 233 | −163 | 45.62 | 0.000 | −2.494 | | |

Table 4.2: Two models fitted in the $uv$ plane for the MJD 50445 data. The first model consists of a single core component and the second model consists of a core with two components 230 mas from the core. Parameters have been iterated to reduce the $\chi^2$ value.

constant flux for aperture synthesis.

Data were calibrated in a standard way using the AIPS package then exported to the Caltech difference mapping package: DIFMAP. The user can then specify components at a position, flux and size which are then Fourier transformed into the $uv$ plane. Given an initial model, the programme then varies any components specified by the user to minimise a $\chi^2$ fit to the $uv$ data.

To test the MJD 50445 data, two models over the stable 6-hour time range were investigated. The core of Cyg X-3 was shifted into the phase centre to counter an arbitrary shift by the MERLIN operators in observations. The first model consisted of a core-only source whereas the second model consisted of a core with two components at the approximate positions shown in the figure 4.13. The parameters fitted to the model were a flux, $S$, radius from the phase centre, $R_\phi$, at a given position angle, $\theta$, a source size, $R_{\rm Maj}$, axial ratio and major axis position angle, $\phi$. The two models together with the values for the reduced $\chi^2$ and degrees of freedom are given in table 4.2. While the models

presented in table 4.2 would seem to indicate a source with two components, it has been shown that the apparent plasmon structure is due to amplitude errors in the data.

At a speed of 0.35 $c$ at a distance of 10 kpc, plasmons ejected following a flare event travel around 7 mas per day. If the flare on MJD 50407 produces two components then by MJD 50445, the components should have travelled an angular distance of 268 mas. If the absence of components shown in these images is due to the plasmons fading below the noise level, then data taken while the components are closer to the core and brighter in flux can be modelled.

Observations on MJD 50425 provide an intermediate observation with a semi-stable flux to model fit from. If the plasmons travelled at 7 mas per day they would have separated by 85 mas from the core by the time the data was taken. One can approximate the flux to 100 mJy for 4 hours at the start of the observations. Using this data and allowing the parameters to vary, table 4.3 shows that the minimised $\chi^2$ fits to the $uv$ data with one component and three components are equivalent. The fitted parameters to the second model have produced large and unrealistic values for the major axis of the components. This could be due to the still large variation in flux within the 4 hour sampling interval used in the modelling. However, reducing the sampling time did not produce significantly different results from the ones shown in table 4.3. Similar modelling of the data at other epochs produced either no difference in the fit to either 1 or 3 component models, or the 3 component model had a worse

| $S$ (mJy) | $R_\phi$ (mas) | $\theta$ (deg) | $R_{\rm Maj}$ (mas) | Ratio | $\phi$ (deg) | $\chi^2_{\rm r}$ | d.o.f |
|---|---|---|---|---|---|---|---|
| 106 | 3.32 | 121 | 20.8 | 0.21 | 85.7 | 0.00472 | 35124 |
| 104 | 3.33 | +121 | 20.6 | 0.000 | +85.8 | | |
| 3.1 | 84 | +23 | 2132 | 0.000 | −65.22 | 0.00471 | 35116 |
| 8.42 | 84 | −163 | 450 | 0.82 | −4.46 | | |

Table 4.3: Two models fitted in the *uv* plane for the MJD 50425 data. The first model consists of a single core component and the second model consists of a core with two components 230 mas from the core. Parameters have been iterated to reduce the $\chi^2$ value. The large major axes for the fitted components are unrealistic and should be discounted from the analysis. The low $\chi^2$ values and high number of degrees of freedom calculated by the DIFMAP package are significantly different from expected values and therefore both are unreliable.

fit to the core-only model. The values of the $\chi^2$ fits to all of these models are all too close to zero. We believe that the number of degrees of freedom have been over-estimated consequently reducing the $\chi^2$ value. The number of degrees of freedom for points on the *uv* plane is approximately $2n(n-1)t_{\rm tot}/t_{\rm int}$ where $n$ is the number of telescopes, $t_{\rm tot}$ is the total observation time, $t_{\rm int}$ is the integration time, and each baseline contributes to 4 degrees of freedom. For MERLIN observations with 5 baselines and a 2.5 minute integration time over 4 hours would provide 3800 degrees of freedom. To obtain 35000 degrees of freedom for table 4.3, 36 days of observations are required. However, with this modified number of degrees of freedom, the $\chi^2$ values are still significantly low, and hence neither the $\chi^2$ nor the number of degrees of freedom are reliable. I suspect there is a major 'bug' in this bit of the DIFMAP programme.

We can conclude that either the components decay at a rate which lowers

them below the noise in the data, which would make any fitting indistinguishable, or no plasmons were produced after the flare on MJD 50407. Given the previous observations of plasmons, we would favour the first conclusion.

### 4.2.4 Brightness temperature of the flares

A brightness temperature increase can be calculated associated with the flux change from the source. The brightness temperature of a source with intensity $I_\nu$ emitting at a frequency $\nu$ is equal to

$$T_b = \frac{c^2 I_\nu}{2k_B \nu^2} \tag{4.1}$$

where $k_B$ is Boltzmann's constant. A flux change of $\Delta S$ will increase the source's intensity thus increase the brightness temperature by a factor

$$\Delta T_b = \frac{c^2 \Delta S}{2k_B \nu^2 \Omega} \tag{4.2}$$

where $\Omega$ is the source solid angle. For a flux change to be coherent, emission must occur within a sphere whose diameter is less than the light-travel time for the flare. The diameter of the emission region must be $d \leqslant c\Delta t$ and so by assuming small angles, the angular diameter of the emission region can be

equated to the timescale of the flare by

$$\theta \leqslant 2.06 \times 10^{-3} \frac{\Delta t}{D_{\rm kpc}} \text{ mas} \tag{4.3}$$

where $D_{\rm kpc}$ is the distance to the source in kpc. Since the solid angle of a source can be approximated to the angular diameter of the source by $\Omega \simeq \pi\theta^2/4$ where $\theta$ is measured in radians then the change in brightness temperature increase is equal to

$$\Delta T_{\rm b} \geqslant 1.16 \times 10^{11} \frac{\Delta S_{\rm mJy} D_{\rm kpc}}{\nu^2_{\rm GHz} \Delta t^2_{\rm min}} \text{ K} \tag{4.4}$$

where $\Delta S$ is measured in mJy, $\nu$ is measured in GHz and $\Delta t$ is measured in minutes. While not in standard units, equation 4.4 has been chosen to match typical values in the observations.

The equation 4.4 is only valid while the size of the emission region is smaller than the beam size used in the observations. For observations using MERLIN, this is true while the product $\Delta t_{\rm min}\ \nu_{\rm GHz} < 20200$. For our observations at 5 GHz, the condition that $\Delta t_{\rm min} < 3360$ is valid for all flares.

For a typical flare at MJD 50419.56, the flux increase is measured at $\Delta S =$ 80 mJy, $\Delta t = 46$ min and so the brightness temperature increase is $\Delta T_{\rm b} \geqslant 1.8 \times 10^{10}$ K. It is interesting to note that for the large flare on MJD 50432, the timescale is much longer, but because the flux increase is so large, the change in brightness temperature is similar at $\Delta T_{\rm b} \geqslant 1.3 \times 10^{10}$ K. This is repeated for

many of the flares over hour timescales with brightness temperatures of $10^9$–$10^{10}$ K. However, the brightest flare occurred on MJD 50438.6 and if the change within 1 integration bin is believable then for a flux increase of $\Delta S = 10$ mJy over 4.0 minutes, the increase in brightness temperature is $\Delta T_b \geqslant 2.9 \times 10^{11}$ K.

## 4.3 The Observations: L-band

After the C-band observations at 5 GHz were taken, we were awarded 2 epochs of data at L-band (1658 MHz) to follow a minor flare period. A major flare was detected by the Ryle telescope at 15 GHz and the GBI at 2.25 and 8 GHz on MJD 50611 and MERLIN operators scheduled the first of our two observations approximately 7 days after the flare, and the second observation 14 days after the flare. As shown in figure 4.15, the source was still recovering from the 3.5 Jy flare during our first epoch, and this created the same problems of variable source mapping as detailed in section 4.2. By the time the second epoch was observed, the source-flux-changes put Cyg X-3 in the minor-flare category. Photometry of Cyg X-3 at 2.25 GHz from the GBI together with the positions of our observations is shown in figure 4.15. Detailed plots of the data around the two epochs are given in figures 4.16 and 4.17 and the times of the MERLIN data is shown by the arrows.

Figure 4.18 shows photometry from the MERLIN data set for the first epoch: MJD 50613, 15 Jun 1997. The data shows the recovery from the major-flare.

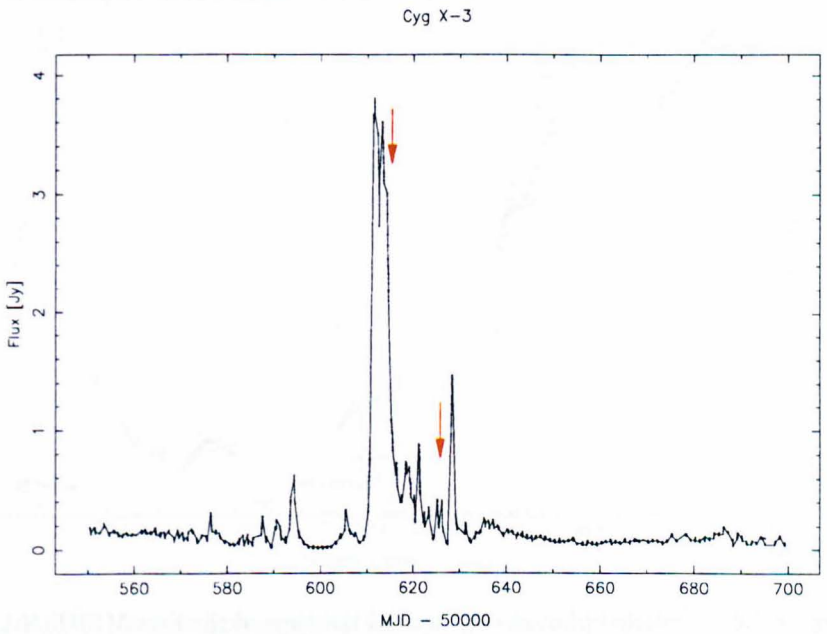


Figure 4.15: Green Bank Interferometer data at 2.3 GHz around the time of the MERLIN L-band observations in June 1997. A major flare occurred on 10 June 1997, MJD 50611. Our two epochs of L-band data are shown with two arrows.

At time 50615.05, the flux from the source is constant, which could be due to a second flare erupting and counteracting the decay. This flux then decays for the rest of the observation.

Figure 4.19 shows photometry from the MERLIN data set for the second epoch: 27 Jun 1997. The system is not as active as in the first epoch. For the majority of the observation Cyg X-3 was in a quiescent mode with flux densities of $\sim$ 50 mJy. We have observed the beginning of the flare shown in figure 4.17 which reaches a maximum at MJD 50628.4.

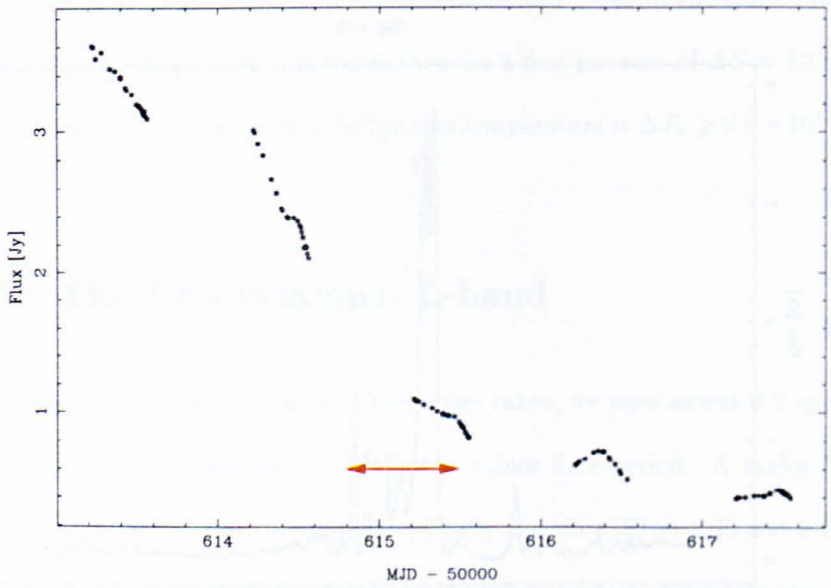


Figure 4.16: Detailed photometry around the time of the first MERLIN L-band data. Data is from the Green Bank Interferometer at 2.3 GHz

Even though for the second epoch the flux was roughly constant, the beam size for MERLIN maps at 1.6 GHz is $\sim$ 150 mas. If the jets travel at 9 mas per day, then 17 days after the flare the jets will have only travelled one beam width from the core, and due to the quality of data, any jet will be indistinguishable from the noise. Mapping at this frequency, soon after a flare is not possible.

## 4.4 Conclusions

Cyg X-3 is variable! The aim of these observations was to observe individual jet plasmons at consecutive epochs and confirm a jet structure, with a speed

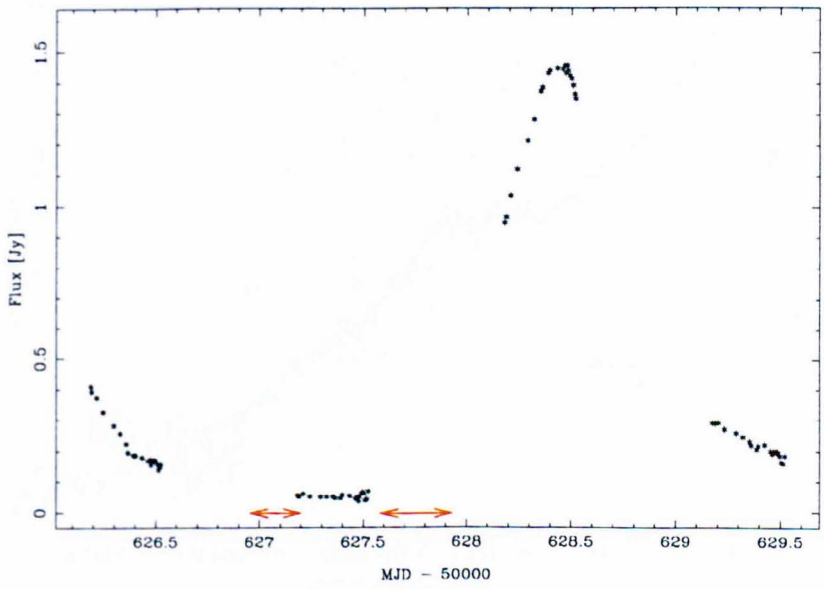


Figure 4.17: Detailed photometry around the time of the second MERLIN L-band data. Taken from the Green Bank Interferometer at 2.3 GHz.

of 0.3 $c$. The inability of MERLIN to be used in a 'snapshot' mode and a variable flux over the timescale required for aperture synthesis prevented reliable mapping of the source. The one data set that provided a constant flux so a map could be produced gave results consistent with a single point source, and no jet structure. Either no jets were produced, or more likely the jet had faded by the time the observations had been taken. Differences between a core-only and core-jet modelling of the $uv$ data were not statistically significant.

Photometry over all epochs show a rich variety of structure, both in the rapid rise and decay of flares, and also the range of strength of flares. These MERLIN observations are the most detailed photometric observations of Cyg X-3, and

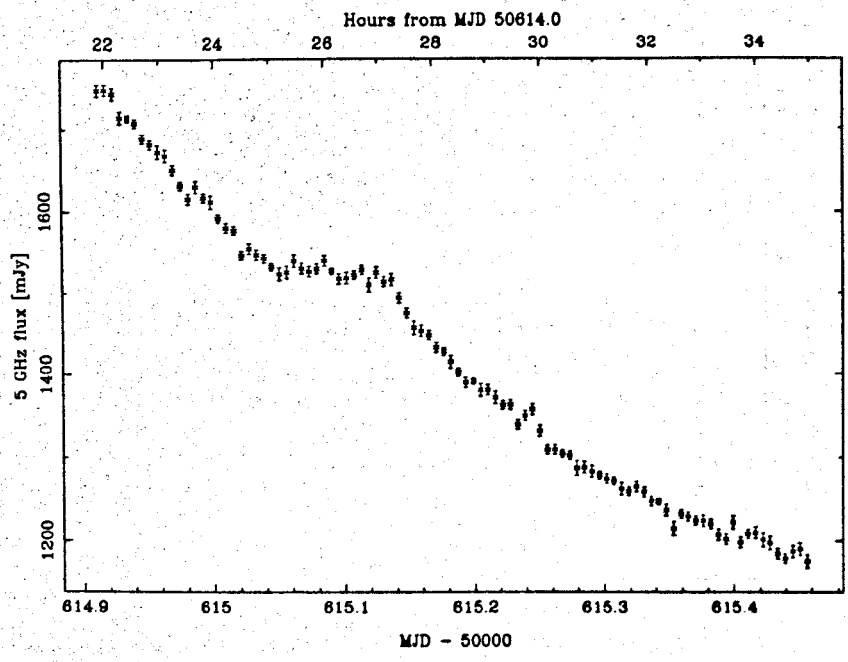


Figure 4.18: Cyg X-3 photometry at L-band on 15 June 1997. Time bins are 8.3 min. The system was recovering from a major flare of 3.5 Jy at 2.25 GHz on 10 Jun 1997 (MJD 50609). A slight flattening of the flux from the exponential decay could be due to the emergence of a second smaller flare.

due to the large collecting area of MERLIN represent the best obtainable data within the limited bandwidth of MERLIN. Improvement can be made to the time resolution using a higher bandwidth or larger collecting area. Because of the short time resolution, flares can be identified in a region of typically 10 light minutes across, with a diameter of around 260 $R_\odot$ However, to be visible at a frequency of 5 GHz these plasmons would be situated at a distance of 13,000 $R_\odot$ from the core (see section 5.2.2). A cartoon of the emitting region is shown in figure 4.20. The flares from a region of this size imply brightness temperature

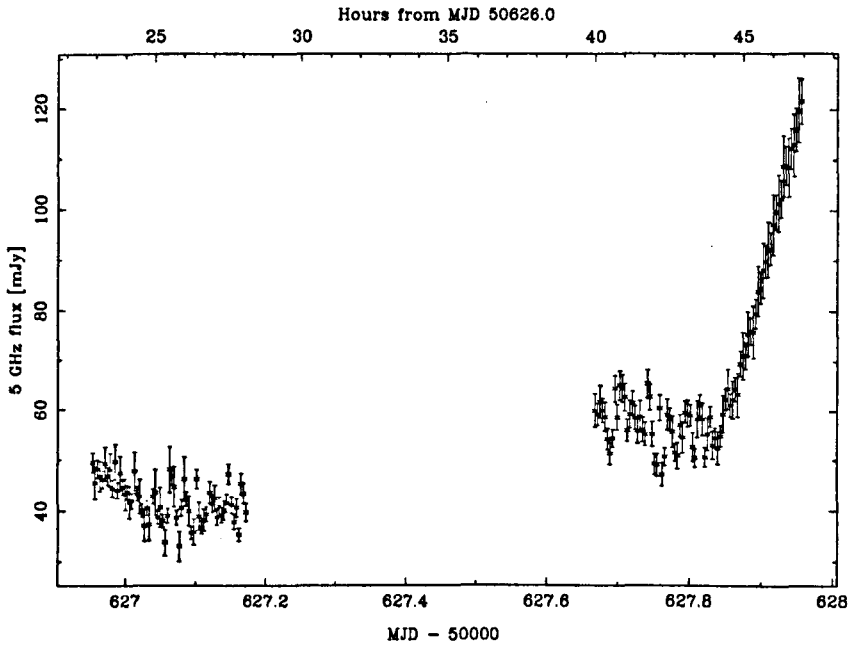


Figure 4.19: Cyg X-3 photometry at L-band on 27 June 1997. Time bins are 5.1 min.

increases of typically $10^9$–$10^{10}$ K, with some temperature increases of a few $\times 10^{11}$ K.

An analysis of the power spectrum over all epochs show that no recurrent periodicities are present, and there is a very small probability of a periodicity at the 4.8 h binary orbit. Analysing the 6, 5-GHz epochs separately show that the system either behaves chaotically or quasi-periodic oscillations occur in the system with periods between 1 and 4 days.

Further observations at 1.6 GHz provided no additional clues to the true nature of the source.

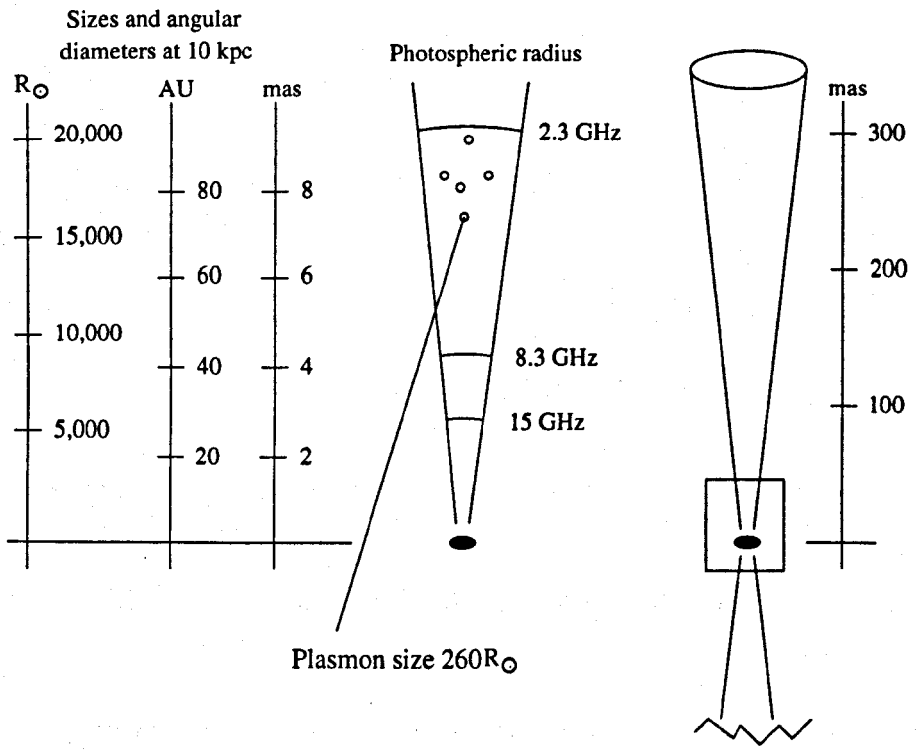


Figure 4.20: A cartoon showing the position and size of plasmons producing the flux changes in the multi-epoch MERLIN observations. The plasmons have to be outside the 5 GHz photosperic radius to be observed, but flux changes on 10 minute timescales would require a maximum plasmon size of 260 $R_\odot$.

# Chapter 5

# Sub-mm observations of Cyg X-3 – an estimate of the magnetic field

" 'To Start Press Any Key'. Where's the ANY key? I see Esk, Catarl, Pig-up. There doesn't seem to be any ANY key. Woo! All this computer hacking is making me thirsty. I think I'll order a TAB. Awp...no time for that now, the computer's starting".

– Homer Simpson, *King size Homer*

## 5.1 Sub-mm radio emission

The radiation from radio-jet X-ray binaries can split into two regimes: radio to infrared and X-rays to $\gamma$ rays. The optical and UV radiation is usually heavily obscured because sources are in the Galactic plane and therefore obscured by dust. One would expect two different emission mechanisms to dominate over these two observational bands, and that is generally the case. In the X-ray band, the dominant emission has a power law shape superimposed with numerous emission lines; while vital in investigating the region of space around the black hole or neutron star, it only partially influences the emission in the radio regime. The radio and (for the very energetic sources) infrared emission is dominated by synchrotron emission which is perfectly represented by the energetics of the sources.

### 5.1.1 Cyclotron radiation

Cyclotron emission is the low-velocity counterpart to synchrotron emission. Both emission mechanisms follow the same physical processes and occur when an electron is in orbit (either circularly or helically) around a magnetic field. The Lorentz force on the electron is equated to the centrifugal force of the electron's motion; thus,

$$\boldsymbol{F} = -e\,\boldsymbol{v} \wedge \boldsymbol{B} = \frac{m_e v^2}{r}\hat{r} \tag{5.1}$$

and as the electron orbits the magnetic field, it describes a radius (*gyro radius*), $r_g$, given by

$$r_g = \frac{m_e v}{Be}. \tag{5.2}$$

As the electron orbits the magnetic field, a precise frequency of radiation is emitted. This gyro-frequency is given by

$$\nu_g = \frac{Be}{2\pi m_e} \tag{5.3}$$

which depends linearly on the magnetic field strength perpendicular to the direction of motion of the electron. For example a pulsar magnetic field of $10^9$ Tesla would create cyclotron radiation at 115 keV. The radiation pattern of a cyclotron-emitting electron is a dipole pattern, and measured in the electron's rest-frame the radiation pattern is shown in figure 5.1.

### 5.1.2 Synchrotron radiation...

#### ...from a single electron

As the velocity of the electron is increased, in the relativistic limit cyclotron emission becomes synchrotron emission. The radiation pattern, frequency of emission and intensity are all significantly altered. Instead of emitting radiation in a dipole pattern, radiation is beamed in the direction of the electron thus

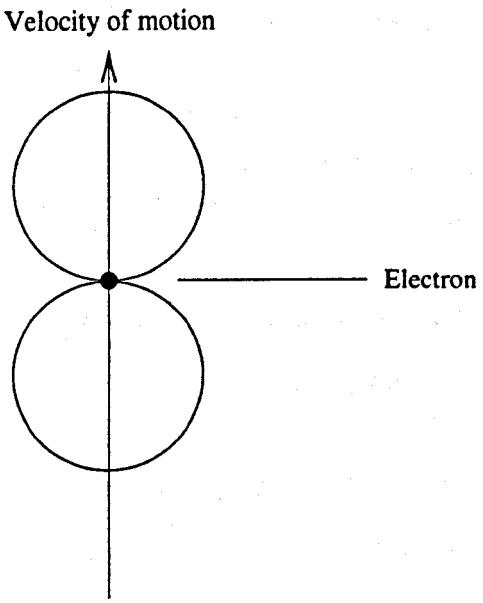


Figure 5.1: The radiation pattern of a cyclotron-emitting electron, measured in the electron's frame of reference.

creating a cone of emission at increased intensity. The radiation pattern is shown in figure 5.2. Because the radiation is beamed, an important variable to consider is the electron pitch angle. This is defined as the angle, $\phi$, between the magnetic field and the velocity vector of the electron, $v$. The pitch angle can be written as $\sin\phi = v_\perp/v$, where $v_\perp$ is the velocity component perpendicular to the magnetic field vector. Relativistic velocities change the gyro-frequency from the classical value, and it is now equal to

$$\nu_{g'} = \frac{1}{\gamma}\frac{eB\sin\phi}{2\pi m_e} \tag{5.4}$$

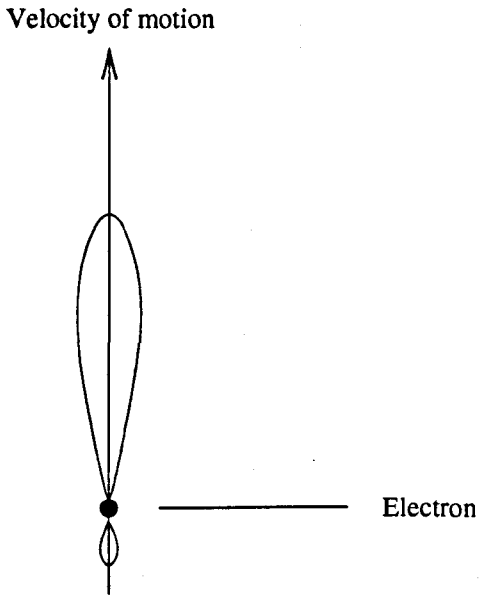


Figure 5.2: The radiation pattern of a synchrotron-emitting electron, measured in the electron's frame of reference. Photons from the sides of the electron are beamed into a cone of opening angle $\sim 1/\gamma$, and the radiation is boosted.

where $\gamma$ is the electron gamma factor ($\gamma = 1/\sqrt{1-\beta^2}$). The power radiated by this single electron can be calculated and is equal to

$$P_s = \frac{8\pi}{3}\frac{c}{\mu_0} r_0^2 \gamma^2 B^2 \sin^2\phi, \text{ where}$$
$$r_0 = \frac{e^2}{4\pi\epsilon_0 m_e c^2} \tag{5.5}$$

and is the classical radius of the electron. If the pitch angles are isotropically distributed then the value $\sin^2\phi = 2/3$. For magnetic fields measured in Tesla, the gyro-frequency now becomes $\nu_{g'} = 22.8\,|B|\,\gamma^{-1}$ GHz.

The frequency of radiation is determined by the gyro-frequency of the elec-

tron, but it is modified by the cone opening angle and the difference between the times of emission and arrival of pulse. The frequency at which most radiation is emitted is is equal to

$$\nu_s = \frac{\gamma^2 eB \sin\phi}{2\pi m_e} = \gamma^2 \nu_g. \tag{5.6}$$

The power radiated by the electron over a frequency interval $\nu + \Delta\nu$ is

$$P(\nu)\mathrm{d}\nu = \frac{\sqrt{3}e^3 cB\sin\phi}{8\pi^2\eta_0 m_e}\,\frac{\nu}{\nu_s}\int_{\nu/\nu_s}^{\infty} K_{5/3}(\eta)\,\mathrm{d}\eta\,\mathrm{d}\nu \tag{5.7}$$

(Lang 1980), where $K_{5/3}(\eta)$ is a modified Bessel function. A graph of normalised power is shown in figure 5.3 adapted from Hughes & Miller (1991) and peaks at a frequency $\nu = 0.29\nu_c$ where $\nu_c$ is a critical frequency given by

$$\nu_c = \frac{3\gamma^2 eB\sin\phi}{4\pi m_e}. \tag{5.8}$$

The electron looses energy by radiating at a rate of $\mathrm{d}E/\mathrm{d}t$ where

$$\begin{aligned}\frac{\mathrm{d}E}{\mathrm{d}t} &= -\int_0^{\infty} P(\nu)\,\mathrm{d}\nu \\ &= -1.58\times10^{-14}\,\gamma^2\,B^2\sin^2\phi\ \ \mathrm{W}.\end{aligned} \tag{5.9}$$

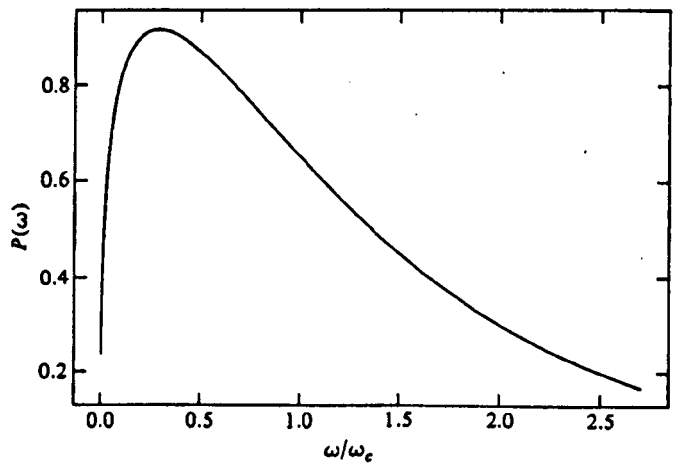


Figure 5.3: The normalised power radiated by a synchrotron electron as a function of frequency (adapted from Hughes & Miller 1991). In this figure $\omega = 2\pi\nu_g$, and $\omega_c$ is a critical frequency given in frequency form by equation 5.8

The energy loss as a function of time can be re-written as

$$E(t) = \frac{E_0}{(1 + t/t_{1/2})} \tag{5.10}$$

where $t_{1/2}$ is the half-life for the electron which is equal to

$$t_{1/2} = 13470 \frac{\gamma}{B_\perp^2} \text{ s} \tag{5.11}$$

and $B_\perp$ is measured in T.

**...from an ensemble of electrons**

Most astrophysical synchrotron sources do not consist of a single electron, but a collection of electrons with different energies, so the power distribution and spectrum will deviate from the form above. The distribution of electron energies in such an ensemble is usually a power-law with index $-\delta$:

$$N(E)\,\mathrm{d}E = KE^{-\delta}\,\mathrm{d}E \tag{5.12}$$

where $K$ is a constant. For a collections of electrons with a power-law distribution of energy in a homogeneous magnetic field, the intensity of radiation, $I(\nu)$ can be written as

$$I(\nu) = Kla(\delta)\frac{\sqrt{3}}{8\pi}\frac{e^3c}{m_e}\left[\frac{3e}{4\pi m_e^3c^4}\right]^{(1+\delta)/2} B_\perp^{(1+\delta)/2}\nu^{(1-\delta)/2} \tag{5.13}$$

(Lang 1980) where $l$ is the dimension of the radiating material along the line of sight and $a(\delta)$ is a dimensionless function of $\delta$ given by

$$a(\delta) = 2^{(\delta-3)/2}\frac{7/3+\delta}{1+\delta}\Gamma\left(\frac{3\delta-1}{12}\right)\Gamma\left(\frac{3\delta+7}{12}\right), \tag{5.14}$$

where $\Gamma$ is the Euler gamma function.

*It follows from equations 5.10 and 5.12 that the total electron energy, $U_e$, is* given by

$$U_e = 4.22 \times 10^{-5} \frac{L}{B_\perp^2} \frac{3+\delta}{2+\delta} \left( \frac{E_2^{(2-\delta)} - E_1^{(2-\delta)}}{E_2^{(3-\delta)} - E_1^{(3-\delta)}} \right) \text{ J} \qquad (5.15)$$

where $E_1$ and $E_2$ represent the lowest and highest electron energies and $L$ is the luminosity from synchrotron radiation. The intensity of radiation is a power-law function of frequency, with a power-law index of $\alpha$ where $\alpha = (1-\delta)/2$. If the energy distribution index $\delta \neq 2$ or 3 then the luminosity of the source can be written as

$$L = 4\pi d^2 \frac{S_{\nu_r}}{\nu_r^\alpha} \int_{\nu_1}^{\nu_2} \nu^\alpha \, \mathrm{d}\nu \qquad (5.16)$$

where $S_{\nu_r}$ is the flux density at a frequency $\nu_r$ and $\nu_1$ and $\nu_2$ are the lower and upper frequencies at which radiation is emitted (for a given spectral index). If each electron radiates at its critical frequency then the total electron energy can be written as

$$U_e = 10^5 \frac{L}{B_\perp^{3/2}} \frac{\nu_2^{1/2+\alpha} - \nu_1^{1/2+\alpha}}{\nu_2^{1+\alpha} - \nu_1^{1+\alpha}} \frac{(2\alpha+2)}{(2\alpha+1)} \text{ J}. \qquad (5.17)$$

**...from a plasma**

The discussion above deals with radiation from an optically thin medium. Most radio-jet X-ray binary synchrotron emission is embedded in a plasma, the opac-

ity of which changes as a function of time as the cloud expands after it has been ejected from the core of the system.

As the frequency of the emitted photons decreases, the plasma progressively becomes optically thick to the radiation. For an optically thin plasma the kinetic energy of the electrons is less than the energy of the incident radiation so the radiation is brighter than the electrons can absorb. However, as the brightness temperature decreases, the radiation becomes self-absorbed by the electrons. Since any incoherent system cannot radiate more efficiently than a black body, in the optically thick frequency regime the plasma is radiating as a black body and the spectrum turns over when it becomes optically thin. The energy of the electrons in the optically thin part of the spectrum is equal to the radiative energy of the gas, or

$$\gamma m_e c^2 = 3 k_B T \tag{5.18}$$

where $k_B$ is Boltzmann's constant[1]. The intensity of radiation from the gas is equal to the black body intensity in the Rayleigh-Jeans limit,

$$I_\nu = \frac{2\nu^2 k_B T}{c^2} \tag{5.19}$$

and since the energy of the electrons $\gamma m_e c^2 \propto \nu^{1/2}$ then the intensity in this

[1]The energy of the gas is not $E = \frac{3}{2} k_B T$ as is the standard result in kinetic theory because we are dealing with a relativistic gas which has a different value for the ratio of the specific heats than a classical gas.

region is

$$I_\nu \propto \nu^{5/2}. \tag{5.20}$$

The spectral change between the optically thick and thin regions can be found by equating the electron energy to the radiative energy of the gas as in equation 5.18, and substituting

$$\begin{aligned} k_B T &= \frac{c^2 I_\nu}{2\nu_b^2} \\ &= \frac{4c^2 S_b}{2\pi\theta^2 \nu_b^2} \end{aligned} \tag{5.21}$$

and

$$\gamma = \left(\frac{\nu_b}{\nu_g}\right)^{1/2}, \tag{5.22}$$

where $\nu_b$ is the self-absorption frequency, $S_b$ is the flux density of radiation at the self-absorption frequency, $\theta$ is the angular diameter of the source, and $\nu_g$ is the gyro frequency of the electron. The flux density of the source does not need to be measured at the self-absorption frequency since the spectrum in the optically thin regime is known, the substitution $S_b \nu_b^\alpha = S_2 \nu_2^\alpha$ can be made, as long as a flux density $S_2$ can be obtained at a frequency $\nu_2$. This allows the

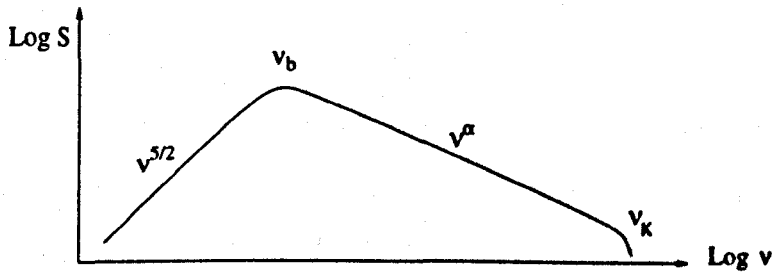


Figure 5.4: The spectrum of a synchrotron source in a plasma. At the low frequencies the plasma is optically thick to the radiation, synchrotron self-absorption occurs and the plasma emits with a spectral index of 5/2. The change in the spectrum occurs at $\nu_b$ as discussed in the text. Intermediate frequencies have a spectral index of $\alpha$ and at the highest frequencies radiation losses occur.

self-absorption frequency to be calculated by

$$\frac{4c^2 S_2 \nu_2^{\alpha}}{2\pi\theta^2 \nu_b^2 \nu_b^{\alpha}} = \left(\frac{\nu_b}{\nu_g}\right)^{1/2} \frac{m_e c^2}{3} \tag{5.23}$$

so

$$\nu_b = \left[\frac{6 S_2 \nu_2^{\alpha} \nu_g^{1/2}}{\pi\theta^2 m_e}\right]^{2/(5+2\alpha)} . \tag{5.24}$$

A typical synchrotron spectrum is shown in figure 5.4.

### Radiation losses from a synchrotron plasma

High energy electrons loose their energy at a greater rate than low energy electrons therefore the spectrum of the radiation will steepen over time. This is the phenomenon of spectral ageing. Electrons with a power-law energy index of $-\delta$

will develop a spectrum with an index of $\alpha = (4\delta - 3)/3$ for frequencies higher than a cut-off frequency of $\nu_K$ where

$$\nu_K = 3.4 \times 10^5 \, t^{-2} B_\perp^{-3} \text{ GHz} \tag{5.25}$$

where $B \perp$ is measured in mT and $t$ is measured in seconds (Kardashev 1962).

### Spectra examples

Examples of emission from different sources are shown in figure 5.5. These spectra are from a variety of different emission mechanisms, not just synchrotron. Cas A shows a typical optically thin synchrotron spectrum. The emission from the Orion nebula is thermal free-free and shows an optically thick $\nu^2$ spectrum together with an optically thin $\nu^{-0.1}$ spectrum. 3C 84 has peculiar high frequency emission and P1934-63 and P2134+004 show low frequency absorption which could be due to ionised hydrogen between the source and the observer, or from synchrotron self absorption due to an optically thick medium with a variable brightness temperature (Kellermann 1966).

## 5.2 Synchrotron emission from X-ray binaries

The radio emission from radio-jet X-ray binaries comes from the jets associated with the source, and is purely synchrotron. The radio flux of those sources so far detected in quiescence is typically 5 mJy at 15 GHz. If the source emits at

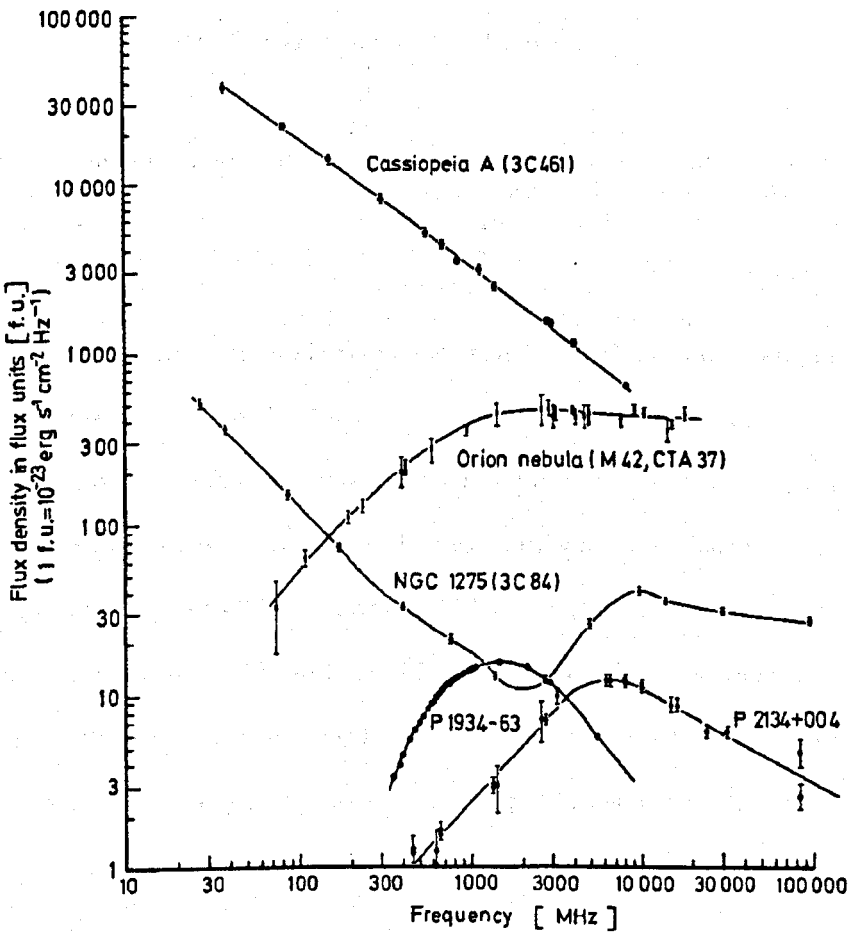


Figure 5.5: Spectra from a variety of sources showing differences in spectra and emission mechanisms (see text). Adapted from Lang (1980).

frequencies between 1 to 20 GHz, has a flat ($\alpha = 0$) spectral index and is at a distance of 10 kpc, then using equation 5.16 the luminosity will be $1.1 \times 10^{24}$ W. If a magnetic field of 10 mT is used in creating the emission, at 15 GHz the electrons will have a gamma factor ($\gamma = \{1 - \beta^2\}^{-1/2}$) of $\gamma = 23$, and the total energy in the electrons is $U_e = 3.9 \times 10^{28}$ J. The energy required to accelerate the electrons is perfectly feasible from an accretion powered black hole.

Radio observations of the sources in quiescence have shown emission consistent with the picture above. There is one vital quantity needed for the evaluation of synchrotron sources and that is the strength of the magnetic field required to support the emission. Single observations in the frequency regime of an optically thin plasma do not reveal the magnetic field as any distribution of electron energies can create an observed spectral index; as the magnetic field strength increases then the electron energies required to match the observed spectrum decrease. In order to unambiguously determine the magnetic field strength, observations of a spectral change – either due to synchrotron self-absorption, or spectral ageing – is required.

The source under investigation in this chapter is Cygnus X-3 and it has the following characteristics:

- High flux variability (see chapter 4) which is probably due to a change in density of the wind accreting onto the neutron star.
- Synchrotron emission observed through a modified Wolf–Rayet wind (Waltman et al. 1996); we only observe emission when the region becomes op-

tically thin, at some radius from the core of the system.

- Low-frequency synchrotron emission which is scattered by a foreground screen (Wilkinson et al. 1994).

- At infrared wavelengths the emission is no longer dominated by synchrotron but is thermal emission from a modified black body (Fender et al. 1995) and chapter 6 in this thesis).

As was shown above there will exist two spectral breaks in the synchrotron emission, the first from self-absorption, and the second from ageing; the latter occurs at a frequency between the radio and the infrared. Astrophysical implications of these spectral changes are now investigated.

### 5.2.1 Synchrotron self-absorption

To calculate the magnetic field from synchrotron self-absorption both the self-absorption frequency and a measurement of the size of the source are required. Substituting the equation for the gyro-frequency into equation 5.24, the magnetic field is

$$B_{\perp} = \frac{\pi^3 \nu_b^{(5+2\alpha)} \theta^4 m_e^3}{18 e S_2^2 \nu_2^{2\alpha}}, \tag{5.26}$$

for Cyg X-3. If $\alpha = 0$ (see section 5.3) then

$$B_\perp = \frac{\pi^3 \nu_b^5 \theta^4 m_e^3}{18 e S_2^2} \tag{5.27}$$

or

$$B_\perp = 0.043\, \nu_{b,\mathrm{GHz}}^5 \theta_{\mathrm{mas}}^4 S_{2,\mathrm{mJy}}^{-2} \ \mathrm{T}. \tag{5.28}$$

Since with today's radio telescopes Cyg X-3 is a diffraction-limited point source, the apparent angular size of the source should vary with a single power of frequency. However at frequencies below $\sim 5$ GHz a screen of material between Cyg X-3 and Earth scatters radiation and it is found that the size of the apparent source varies as $\theta = j\nu^{-2.06}$ (Wilkinson et al. 1994) where $j$ is a conversion factor which depends on the telescope used. For MERLIN observations, if the angular size varies as

$$\theta = 442\, \nu_{\mathrm{GHz}}^{-2.06} \ \mathrm{mas}, \tag{5.29}$$

then the magnetic field is

$$B_\perp = 1.64 \times 10^9 \frac{\nu_{b,\mathrm{GHz}}^{(2\alpha - 3.24)}}{S_{2,\mathrm{mJy}}^2 \nu_{2,\mathrm{GHz}}^{2\alpha}} \ \mathrm{T}. \tag{5.30}$$

The magnetic field can be calculated exactly if there is a direct observation

of the flux from the source either side of the self-absorption frequency. However, since no observations of this frequency have been obtained, only an upper limit to the magnetic field can be calculated. As the dependence on self-absorption frequency is $B_\perp \propto \nu_b^{-3.24}$, from equations (5.28,5.29), a lower frequency observation is not useful in obtaining a lower upper-limit to the magnetic field because the scattering screen increases the angular size of the source at low frequencies. The best example is with MERLIN; at 1.6 GHz, the angular size is 160 mas. A quiescent flux of 100 mJy and a flat spectrum provides the two other unknown variables to the equation, hence $B_\perp \leqslant 36$ kT. One can consider this a rather high upper limit to the magnetic field.

### 5.2.2 High-frequency losses

The evaluation of the magnetic field using a self-absorption argument gives a high estimation which cannot be improved by observations at a lower frequency. The other alternative is to look for the high-frequency spectral break from ageing arguments. Observations with *ISO* (chapter 6 this thesis) and UKIRT (Fender et al. 1995) show the emission at these wavelengths is dominated by a modified black body. Between the radio observations of synchrotron emission and the infrared observations of thermal emission, the losses from the high energy electrons responsible for the synchrotron emission are considerable. At some intermediate frequency there will be a steepening of Cyg X-3's spectrum away from the flat $\alpha = 0$ spectral index at low frequencies.

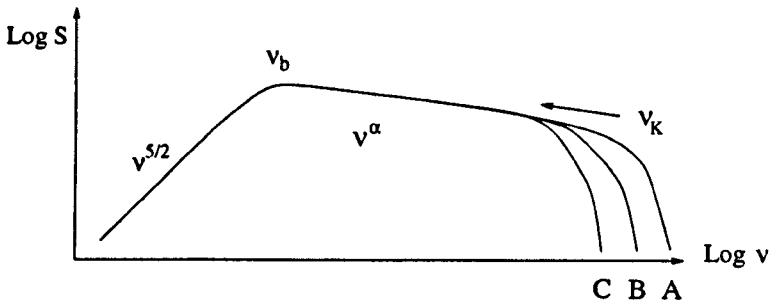


Figure 5.6: The change in Kardashev-frequency with time as a consequence of high energy electrons losing energy faster than the low energy electrons. Times shown are at arbitrary times A → B → C.

The dominant process in changing the spectral index of a synchrotron source at high frequencies is spectral ageing. This is a consequence of high-energy electrons losing energy faster than the lower energy electrons, thus the spectrum steepens and a characteristic cut-off frequency, $\nu_K$ (equation 5.25), moves to lower frequencies with increasing time. A diagram of this process is shown in figure 5.6. The spectrum is shown at times A, B and C and the frequency at which a deviation from the $\nu^{\alpha}$ spectrum occurs moves in time. A full calculation of $\nu_K$ requires the age of the source to be determined. The spectral break can be used to calculate the magnetic field and equation 5.25 can be re-written as

$$\nu_K = \frac{9c_7 B}{4\left(B^2 + B_{MB}^2\right)^2 t^2} \tag{5.31}$$

(Leahy 1991) where $c_7$ is Pacholczyk's constant (Pacholczyk 1970) and $B_{MB}$ is the field which gives an energy density equivalent to that of the microwave

background radiation. This equation is only valid for a constant magnetic field and that justification will most probably be violated by the adiabatic expansion of the plasmon as it travels out from the core. If one defines expansion factors $\mathcal{R}_\perp = \sqrt{A_2/A_1}$ and $\mathcal{R}_{||} = l_2/l_1$ for an element with cross section $A$ and length $l$, then the evolution of the magnetic field for adiabatic expansion follows

$$\begin{aligned} B_{||} &\propto \mathcal{R}_\perp^{-2} \\ B_\perp &\propto \mathcal{R}_\perp^{-1}\mathcal{R}_{||}^{-1} \\ B_T &\propto \mathcal{R}^{-2} \end{aligned} \tag{5.32}$$

where $B_{||}$ and $B_\perp$ are the parallel and perpendicular magnetic fields, $B_T$ is a tangled magnetic field and $\mathcal{R}$ is an average scale length, $\mathcal{R} = (\mathcal{R}_\perp^2 \mathcal{R}_{||})^{1/3}$. If one considers a steady flow in a jet with a constant opening angle, the perpendicular scale factor $\mathcal{R}_\perp^2 \propto \Omega^{-1}$, where $\Omega$ is the beam solid angle, and $\mathcal{R} \propto \Omega^{-1/3}$. As the parallel field expansion is zero, the perpendicular and tangled magnetic fields expand as

$$\begin{aligned} B_\perp &\propto \Omega \\ B_T &\propto \Omega^{2/3}. \end{aligned} \tag{5.33}$$

It is debatable at this point which field orientation to use. Previous observations of the jets in Cyg X-3 determine an angle between them and the line of sight of around 90° (Spencer et al. 1986; Newell 1996) which would make the projected

perpendicular field zero. It is unlikely that the magnetic field confines the jets in this example, and so one would expect the magnetic field to be tangled within the plasmon.

There is another aspect to the question of whether the field change by adiabatic expansion is applicable to this determination of the cut-off frequency. There must be some expansion correction as discussed above, but major work into the investigation of synchrotron spectra was undertaken via observations of radio galaxies, where the conditions are different from Cyg X-3. For radio galaxies (for example the investigation of 3C234 by Alexander (1987)), observations of the radio lobes and hotspots provide the data for the spectral break. To determine the break frequency, $\nu_K$, a measurement of both the electron age and the magnetic field are required. In observations of radio galaxies, these quantities are measured in different places in the system and a modification to the magnetic field is required. Electrons flow from the jet in the system and enter the hotspot. It is at the hotspot that the electron age is determined. Between the hotspot and the lobe, electrons and magnetic fields are adiabatically expanded, and it is from equipartition arguments that the magnetic field in the lobe is measured. If one just uses derived quantities for the electron age and magnetic field in this example, the break frequency would be incorrect due to the different conditions between the hotspot and lobe regions. Expansion has to be taken into account. For the case of Cyg X-3, the electron age and break frequency are both measured in the same physical environment; even though the

assumption that the field is constant is violated, no expansion (or contraction) of the field has to be taken into account. However, if one calculates the magnetic field in the optically thin region, equation 5.33 can be applied to calculate the magnetic field at the origin of the jet.

Together with $B_T$, the constants $c_7$ and $B_{\rm MB}$ in equation 5.31 can be evaluated to provide a complete function for the break frequency. $c_7$ and $B_{\rm MB}$ are equal to

$$\begin{aligned} c_7 &= \frac{27\pi m_e^5 c^2}{\mu_0^2 e^7} = 1.12 \times 10^{12}\ \mathrm{T^3\ s^2\ Hz} \\ B_{\rm MB} &= \sqrt{2\mu_0 u_{\rm MB}} = 0.138(1+z)^2\ \mathrm{nT}. \end{aligned} \tag{5.34}$$

Since we are observing Galactic sources, the energy density of the microwave background radiation causes a minimum magnetic field, $B_{\rm MB}$, and $z = 0$ will be assumed in all further work. If one assumes $B \gg B_{\rm MB}$ then $(B^2 + B_{\rm MB}^2)^2 \simeq B^4$ and one can substitute numerical values into equation 5.31 and re-write so the magnetic field required to create the break in the spectrum is

$$B_\perp = 13.4\, \nu_{\rm K,GHz}^{-1/3} t^{-2/3}\ \mathrm{T}. \tag{5.35}$$

with $\nu_{\rm K}$ measured in GHz and $t$ measured in seconds. If the frequency $\nu_{\rm K}$ can be found and a lifetime of the electrons can be determined, the magnetic field can be calculated.

The jets of Cyg X-3 are the source of relativistic electrons emitting the

synchrotron radiation. If the jets are travelling at a constant speed and the ambient medium around the jets is becoming optically thin as the jets travel to greater distances, then the time at which we see the emission can be used as an lower limit to the lifetime of the electrons. The lifetime of the electrons in the jets, $t_j$, is a function of the radius at which the medium becomes optically thin, $R_v$, and the jet velocity, $v$, thus

$$t_j = \frac{R_v}{v}. \tag{5.36}$$

For the determination of $R_v$ the characteristic radii for Wolf–Rayet winds is used as this is thought to be the main component of the surrounding medium for the jets. Wright & Barlow (1975) applied a profile of a stellar wind and derived a characteristic radius at which the optical depth is 0.244. This radius is

$$R = 2.8 \times 10^{26} \left(\gamma_e g Z^2\right)^{1/3} T^{-1/2} \left(\frac{\dot{M}}{\mu v_\infty \nu}\right)^{2/3} \text{ m} \tag{5.37}$$

where $\gamma_e$ is the mean number of free electrons per nucleon, $g$ is the Gaunt factor, $Z$ is the mean ionic charge, $T$ is the temperature of the wind in K, $\dot{M}$ is the mass loss rate in $M_\odot$ yr$^{-1}$, $\mu$ is the mean atomic weight per nucleon, $v_\infty$ is the velocity of the wind at infinity in km s$^{-1}$ and $\nu$ is the frequency at which emission is observed in Hz. The assumed parameters for Cyg X-3 are

| Frequency (GHz) | Wavelength (cm) | $R_v$ ($\times 10^{12}$ m) | $R_v$ ($R_\odot$) | $t_s$ (min) | $t_f$ (min) |
|---|---|---|---|---|---|
| 2.25 | 13 | 15 | 20,000 | 3,000 | 900 |
| 8.3 | 6 | 6 | 9,000 | 1,000 | 400 |
| 15 | 2 | 4 | 6,000 | 700 | 200 |
| 150 | 0.2 | 0.8 | 1,000 | 140 | 50 |
| 352 | 0.085 | 0.5 | 700 | 90 | 30 |
| 666 | 0.045 | 0.3 | 400 | 60 | 20 |

Table 5.1: Radii and travel times at which the opacity of the Wolf-Rayet wind becomes a characteristic value of 0.224 (Wright & Barlow 1975), based on the Waltman model. Lifetimes are presented for slow (0.3 $c$ jets) and fast (0.92 $c$ jets).

that the wind is Wolf-Rayet-like[2] consisting of hot He II nuclei accelerated to velocities $\simeq 1,700$ km s$^{-1}$; and the secondary star has a mass loss of around $\dot{M} \simeq 10^{-4}$ M$_\odot$ yr$^{-1}$ (van Kerkwijk et al. 1996).

While this model for the secondary works well for most cases, to explain the intermediate radio frequencies (1-15 GHz) for example, Waltman et al. (1996) discovered that a modified Wolf-Rayet wind fitted the observed flux measurements better. To fit the data they proposed the following changes: a reduced mass-loss rate of $\dot{M} \leqslant 1.0 \times 10^{-5}$ M$_\odot$ yr$^{-1}$, a temperature of 20,000 K and a wind velocity of 2,000 km s$^{-1}$. Waltman et al. (1996) also assumed values of $\gamma_e = 1$, $Z = 1$ and $\mu = 4$. Characteristic radii taken from Waltman et al. (1996) for frequencies below 20 GHz and our extrapolation to high frequencies are given in table 5.1. The function of the radius, $R_v$, with frequency is therefore

[2] A Wolf-Rayet-like secondary star is used for most arguments. However, I have seen papers using Cyg X-3 as the archetypal Wolf-Rayet (Cherepashchuk & Moffat 1994) which it certainly is not!

$$R_\nu = 4 \times 10^4 \, \nu_{\rm GHz}^{-0.7} \ {\rm R}_\odot \tag{5.38}$$

with $\nu$ measured in GHz. Using equations 5.36 and 5.38, the lifetime of the electrons has a lower limit of

$$t_{\rm j} \geqslant 90,000 \, \nu_{\rm GHz}^{-0.7} v_c^{-1} \ {\rm s} \tag{5.39}$$

where $v_c$ is the jet velocity is in units of $c$. The corresponding magnetic field required to create a spectral break at the frequency $\nu_{\rm K}$ for electrons with a lifetime $t_{\rm j}$ using equation 5.35 and 5.39 is

$$B_\perp \leqslant 6.7 \, v_c^{2/3} \nu_{\rm K}^{2/15} \ {\rm T} \tag{5.40}$$

with $\nu_{\rm K}$ measured in GHz.

## 5.3 Sub-mm observations

Observations of Cyg X-3 were taken using the SCUBA instrument on the JCMT on 1997 September 29 0557–1115 UT. To complement these observations radio photometry at 15 GHz was obtained with the Ryle telescope (Cambridge), and at 8.6 and 2.3 GHz with the Green Bank Interferometer (W. Virginia). X-ray observations in the 2–10 keV energy range with the Proportional Counter Array (PCA) instrument on *XTE* were also obtained. This provided a full

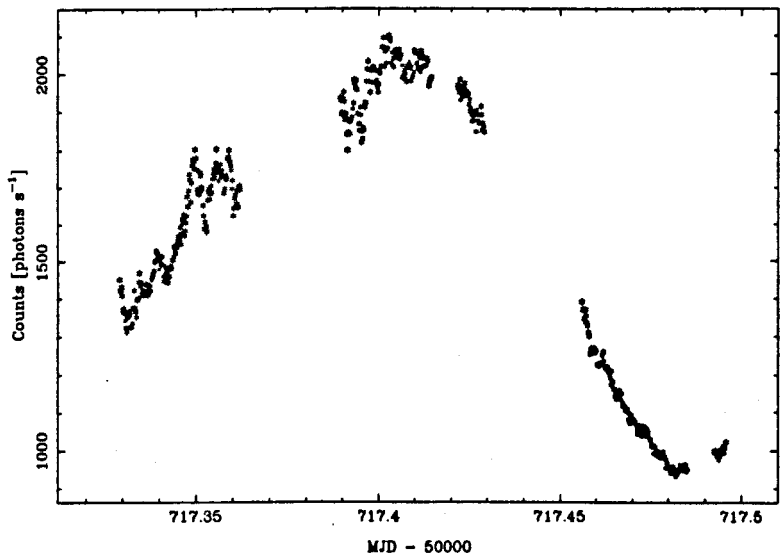


Figure 5.7: XTE photometry of Cyg X-3 taken simultaneously with the sub-mm SCUBA photometry.

complement of energy bands over the time-scale of the observations, so the relationship between the different emission mechanisms could be investigated properly. The X-ray observations were reduced by Drs Fender and Ford at the University of Amsterdam. The photometric data in the 2–10 keV range is given in figure 5.7, and shows a 4.8 hour modulation

SCUBA (Sub-mm Common User Bolometer Array) is a hexagonally packed array of bolometers operating in the 2–0.45 mm wavelength range. The instrument can operate in either array mode where individual bolometers are combined to form an image of the source, or in photometric mode where either

the central bolometers from each array can be used to provide simultaneous observations at 450 and 850 μm, or single observations can be obtained using one of three dedicated bolometers at 1.1, 1.35 or 2.0 mm. Our observations used the telescope in photometric mode in order to obtain as wide coverage in frequency as possible.

The observational strategy is to observe a pointing, focusing and flux calibrator source, and to regularly take sky dip measurements interleaved with target observations. Our primary calibrator used for the pointing, focusing and flux calibration was Mars; secondary pointing sources used were a BL Lac object, Uranus and W75N. Table 5.2 gives the calibration times, modes and sources observed. Times and bolometers used for observation of Cyg X-3 are given in table 5.3.

Each integration consisted of 10-cycles of 9 seconds on and 9 seconds off source. Individual integration times of 9 seconds can be retained for analysis if the source is strong enough, however most observations will use an average flux over each 10-cycle integration. Observations were halted at 06:42 UT for 1h 35m and 10:05 UT for 0h 37m when fog prevented reliable detection. For times after 11:00 UT when the fog cleared and calibration had been completed, the atmospheric opacity was too great for short wavelength observations and the single 2000 μm mode was used.

| UT | Obsmode | Source | Bolometer |
|---|---|---|---|
| 05:07 | Skydip | Sky | 450:850 |
| 05:12 | Pointing | Mars | 450:850 |
| 05:17 | Focus | Mars | 450:850 |
| 05:20 | Align | Mars | 450:850 |
| 05:26 | Pointing | Mars | 450:850 |
| 05:28 | Photom | Mars | 450:850 |
| 05:31 | Photom | Mars | P2000 |
| 05:34 | Map | Mars | 450:850 |
| 05:40 | Skydip | Sky | 450:850 |
| 05:46 | Pointing | CygX-3 | 450:850 |
| 05:54 | Pointing | BL Lac | 450:850 |
| 06:42 | Skydip | Sky | 450:850 |
| 08:22 | Pointing | Uranus | 450:850 |
| 08:28 | Pointing | Uranus | 450:850 |
| 08:30 | Focus | Uranus | 450:850 |
| 08:33 | Skydip | Sky | 450:850 |
| 08:39 | Pointing | Uranus | 450:850 |
| 08:42 | Photom | Uranus | 450:850 |
| 08:46 | Photom | Uranus | P2000 |
| 08:51 | Pointing | W75N | 450:850 |
| 09:37 | Skydip | Sky | 450:850 |
| 09:46 | Pointing | W75N | 450:850 |
| 10:42 | Skydip | Sky | 450:850 |
| 10:48 | Pointing | W75N | 450:850 |
| 11:04 | Pointing | W75N | 450:850 |
| 11:20 | Skydip | Sky | 450:850 |

Table 5.2: Calibrators used in the observations and the calibration mode used. The observation at 05:46 UT of Cyg X-3 was an initial test of whether the source could be used to calibrate the pointing, but it was too weak and a BL Lac object was used instead.

| UT | Obsmode | Source | Bolometer |
|---|---|---|---|
| 05:57 | Photom | CygX-3 | 450:850 |
| 06:02 | Photom | CygX-3 | P2000 |
| 06:07 | Photom | CygX-3 | 450:850 |
| 06:12 | Photom | CygX-3 | P2000 |
| 06:17 | Photom | CygX-3 | 450:850 |
| 06:22 | Photom | CygX-3 | P2000 |
| 06:27 | Photom | CygX-3 | 450:850 |
| 06:32 | Photom | CygX-3 | P2000 |
| 06:36 | Photom | CygX-3 | 450:850 |
| 06:46 | — | — | — |
| 08:56 | Photom | CygX-3 | 450:850 |
| 09:01 | Photom | CygX-3 | P2000 |
| 09:05 | Photom | CygX-3 | 450:850 |
| 09:15 | Photom | CygX-3 | 450:850 |
| 09:22 | Photom | CygX-3 | P2000 |
| 09:27 | Photom | CygX-3 | 450:850 |
| 09:32 | Photom | CygX-3 | P2000 |
| 09:51 | Photom | CygX-3 | 450:850 |
| 09:55 | Photom | CygX-3 | P2000 |
| 10:00 | Photom | CygX-3 | 450:850 |
| 10:05 | — | — | — |
| 11:00 | Photom | CygX-3 | P2000 |
| 11:06 | Photom | CygX-3 | P2000 |
| 11:11 | Photom | CygX-3 | P2000 |
| 11:15 | Photom | CygX-3 | P2000 |

Table 5.3: Times and photometric modes for the Scuba Cyg X-3 observations. At times indicated by the dashes fog prevented observations.

### 5.3.1 Calibration

Some of the observing modes given in table 5.2 provide automatic calibration of the telescope while other modes provide data which can be used in secondary calibration. The available observing modes are:

**Align** This mode sets the X and Y positions of the secondary mirror. The reduction software currently does not support any calibration for bad

alignments. The telescope is presumed to have been corrected for any mis-alignment by the observing software.

**Focus** This mode sets the Z axis position for the secondary mirror. As with the align mode, focus calibration is not supported by the data reduction software.

**Map** This is the main image mode. The secondary mirror is jiggled to provide a minimal redundancy image of the source.

**Photom** This mode uses either the central bolometer of the arrays (at 450 and 850 μm) or dedicated bolometers (at 1.1, 1.35 and 2.0 mm). The mode provides chopping and nodding of the array to reduce sky noise, together with jiggling the array to reduce the effects of seeing.

**Pointing** This mode is used in observations of a bright source at a known position to align the array.

**Skydip** This mode measures the sky brightness temperature as a function of elevation to calculate the zenith sky opacity.

The tasks used, and the procedure followed, in the calibration of SCUBA photometry data is shown in the descriptions below (Jenness & Lightfoot 1997).

**Nod compensation** This step subtracts the off-source position from the on-source position and divides the signal with an internal calibration signal to provide a source signal strength.

**Extinction correction** This step applies an extinction correction from the skydip measurements of the zenith opacity. The optical depth is linearly interpolated as a function of time to find the correction that should be applied to each observation.

**Scuphot** This step takes the jiggled signal and determines the average signal for each bolometer and integration time.

**Scucat** This step concatenates the individual bolometer integration times into one file which is in a format of counts against time. This file can then be calibrated from the photometric observations of known flux sources to provide a flux / time photometric result.

The results from the skydip measurements give zenith opacities at 450 and 850 μm at various LST times which can be interpolated for every photometric observation. Table 5.4 gives the opacities, array wavelengths and times for the 450 and 850 μm data together with the 2.0 mm data which is extrapolated from the 1.3 mm data provided by the Caltech Sub-mm Observatory. After interpolating these opacities to the times of the photometric data, the reduction software provided photometric signals in volts for the central bolometer.

To convert the voltages to a flux, photometric observations of Mars were used, together with a skydip around the time of the Mars observation. The flux of Mars was 69.45 Jy/beam at 2.0 mm, 371.61 Jy/beam at 850 μm and 1171 Jy/beam at 450 μm.

| UT | LST | 450 μm | 850 μm | 2.0 mm |
|---|---|---|---|---|
| 05:42 | 19 39 14 | 2.731 | 0.376 | 0.113 |
| 06:44 | 20 40 37 | 2.622 | 0.485 | 0.094 |
| 08:35 | 22 32 04 | 2.412 | 0.311 | 0.076 |
| 09:41 | 23 39 03 | 2.654 | 0.336 | 0.086 |
| 10:44 | 00 41 50 | 2.452 | 0.341 | 0.093 |
| 11:21 | 01 19 33 | 3.016 | 0.355 | 0.093 |

Table 5.4: Zenith sky opacities for the three wavelength observations listed by UT and LST. 450 and 850 μm data are taken from skydip measurements. 2.0 mm data is approximated from the 1.3 mm data provided by the Caltech Sub-mm Observatory.

### 5.3.2 Photometric results

The individual 9 second bins for the data were not long enough to provide detections with reliable signal to noise, so each 10 cycles were averaged, and scaled from voltage to mJy/beam using the Mars calibration. Table 5.5 gives the 850 μm and 2.0 mm data in mJy with UT. The 450 μm data were too noisy to provide a reliable flux on a 1.5 minute integration time, so 450 μm data were averaged over all the cycles to provide a $3\sigma$ upper limit of 231 mJy. A plot of flux against MJD − 50000 is given in figure 5.8 for all the data except the short wavelength datum.

To complement the SCUBA observations, a number of other observatories took observations as close to simultaneously as possible. The Green Bank Interferometer (GBI) monitors a number of variable radio sources at 2.25 and 8.3 GHz. The Ryle telescope monitors some X-ray binaries during gaps in their CMB experiments, and provides radio data at 15 GHz. The *XTE* telescope had

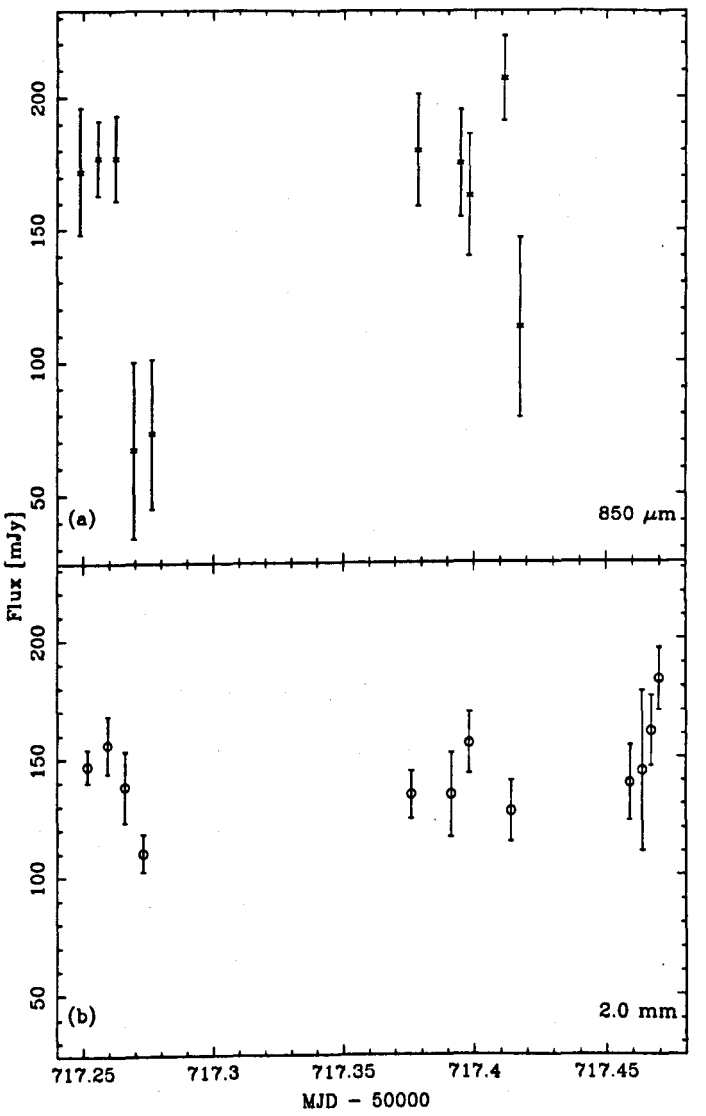


Figure 5.8: Photometry at 850 μm (panel a) and 2.0 mm (panel b) against MJD − 50000.

| UT (850, 2000 μm) | 450 μm flux (mJy) | 850 μm flux (mJy) | 2.0 mm flux (mJy) |
|---|---|---|---|
| 05:57, 06:02 | | 172 ± 24 | 132 ± 6 |
| 06:07, 06:12 | | 177 ± 14 | 143 ± 11 |
| 06:17, 06:22 | | 177 ± 16 | 128 ± 13 |
| 06:27, 06:32 | | 67 ± 33 | 101 ± 7 |
| 06:36 | | 73 ± 28 | |
| 08:56, 09:01 | | 180 ± 21 | 119 ± 9 |
| 09:17, 09:22 | $\leqslant 231$ | 163 ± 23 | 119 ± 16 |
| 09:27, 09:32 | | 175 ± 20 | 138 ± 11 |
| 09:51, 09:55 | | 207 ± 16 | 111 ± 11 |
| 10:00 | | 113 ± 34 | |
| 11:00 | | | 117 ± 13 |
| 11:06 | | | 120 ± 28 |
| 11:11 | | | 134 ± 12 |
| 11:15 | | | 148 ± 10 |

Table 5.5: Fluxes averaged over each integration cycle of 180 seconds, referenced by time of observation. The 450 μm datum, provided by averaging over all observing time, is a $3\sigma$ upper limit.

an override programme scheduled for Cyg X-3 and observed the source with the PCA instrument to give photometry in the 2–10 keV band.

The radio variability at 2.25 GHz from the GBI is shown in figure 5.9 for a number of months either side of this programme. An insert in the figure shows the variability close to the time of our observations. More detailed radio photometry is given in figure 5.10 for a period of two days around the time of the SCUBA observations. In this figure, the upper panel shows the 15 GHz data from the Ryle telescope and the lower panel shows the 8.3 and 2.25 GHz data from the GBI. The arrow on both panels shows the time of the SCUBA coverage.

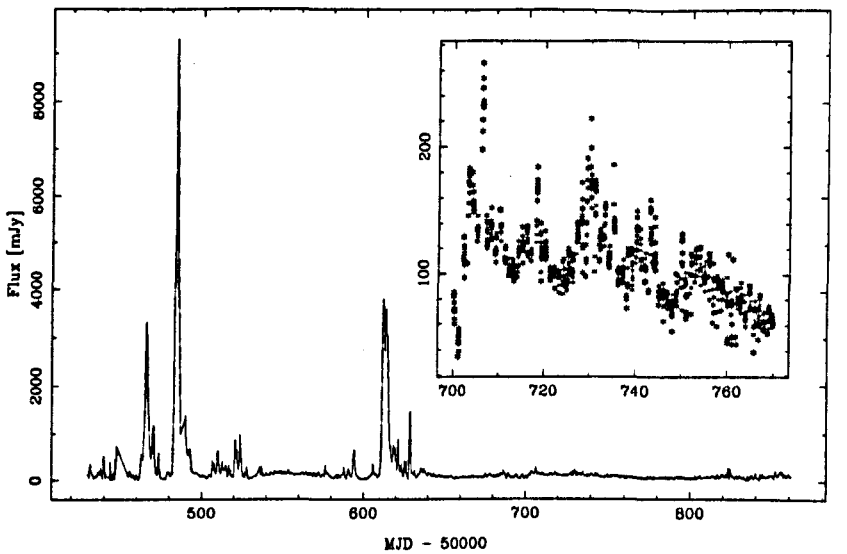


Figure 5.9: The radio variability at 2.25 GHz around the time of our SCUBA observations, provided by the Green Bank Interferometer. An insert shows the variability close to the time of our observations at MJD 50717.

As one can see the source is highly variable at all wavelengths. Figure 5.9 shows typical variability of the source which includes a number of major flares ($S > 1$ Jy) and while no major flare occurred just before the observations at MJD 50717, the system was in a variable state with a number of minor flares occurring at daily intervals. Because of this variability, any calculation which uses a flux measurement has to be either robust in its definition, or careful in its application. To resolve this problem we have averaged the flux over the time-interval shown in figure 5.10. This alleviates any problem in using a flux for a calculation which was either biased by a flare, or suppressed by quenching. The

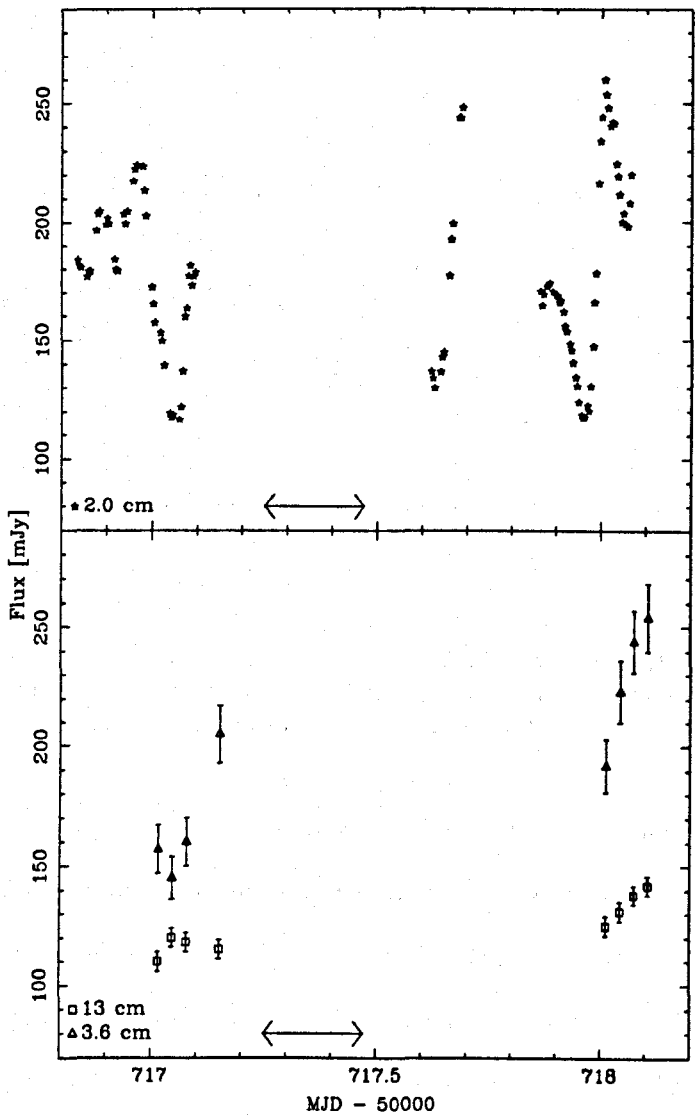


Figure 5.10: Photometry at 15 GHz from the Ryle telescope (upper panel), and 8.3 and 2.25 GHz from the GBI (lower panel) for two days around the SCUBA observations. The arrow in both plots show the coverage at mm and sub-mm.

| $\nu$ (GHz) | 2.25 | 8.3 | 15 | 150 | 352 | 666 |
|---|---|---|---|---|---|---|
| $\lambda$ (cm) | 13 | 3.6 | 2.0 | 0.2 | 0.085 | 0.045 |
| $S$ (mJy) | $120 \pm 10$ | $200 \pm 40$ | $186 \pm 32$ | $144 \pm 18$ | $150 \pm 46$ | $\leqslant 231$ |

Table 5.6: Average fluxes for all wavelengths over the time-scale shown in figure 5.10. Errors are $1\sigma$ deviations from the mean. The 450 μm datum is not statistically significant and I provide it as a $3\sigma$ upper limit.

averaged fluxes at all wavelengths are given in table 5.6.

A spectrum of the source can be presented using the average fluxes in table 5.6 and this is shown in figure 5.11. The figure shows two best-fit lines to the data. The solid line is calculated from all data points (except the 666 GHz datum) and has a gradient of $\alpha = 0.04 \pm 0.03$. The dashed line is a best-fit line using only the 8, 15, 150 and 352 GHz data points and has a gradient of $\alpha = -0.1 \pm 0.06$. Goodness of fits can be calculated for these lines using a $\chi^2$ fit. The $\alpha = 0.04$ fit has a reduced $\chi^2_r = 14.18$ with 4 degrees of freedom. Discounting the 2.25 GHz datum the $\alpha = -0.1$ fit has a reduced $\chi^2_r = 0.6$ with 3 degrees of freedom. The low-frequency point has been dismissed from the second Chi squared analysis because it could be a genuine spectral change.

### 5.3.3 Spectral analysis and interpretation

The data presented in table 5.6 and figure 5.11 present some challenges. The standard interpretation of radio data is that the quiescent flux is due to the superposition of flares caused by synchrotron emission from electrons in the jets. Minor and major flares are due to an increase in the number of electrons in the

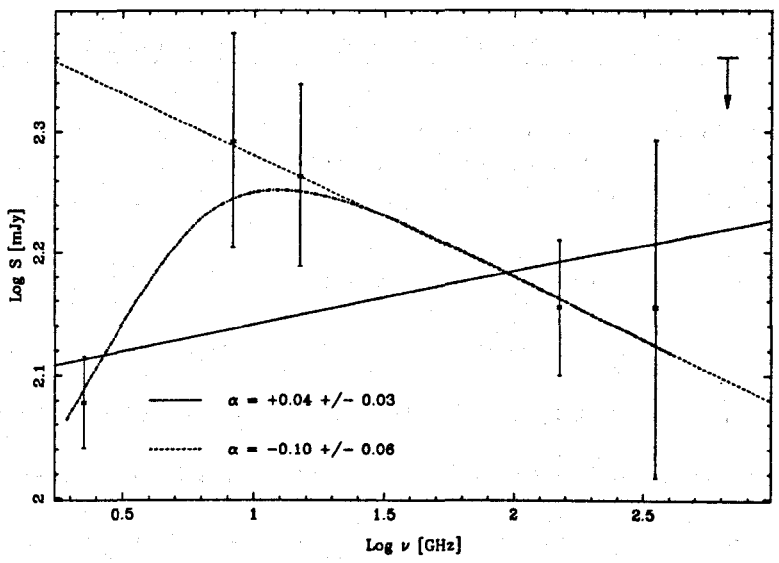


Figure 5.11: A spectrum using the averaged fluxes given in table 5.6. The datum at 450 μm is shown as an upper limit at $3\sigma$. Using a single power law a best fit line to the spectrum using all data points is shown by the solid line, whereas the best fit line using only the 8, 15, 150 and 352 GHz data is shown by the dashed line. A bold dot-dashed line is shown as a two component best fit through all the data points.

jets, and all radio emission comes from the same source. As one increases in frequency out of the radio regime and into the infrared, the source stops emitting synchrotron radiation and the emission is dominated by modified black body thermal emission. It is assumed that at infrared wavelengths one is observing the wind component of the source and not the tail end of the synchrotron emission from the jets. At some point in the spectrum, the emission changes from one type to the other.

Very few sources are powerful enough and have environments which can produce radiation of the same flux density from 1 to hundreds of GHz, no matter what the emission mechanism is. The flux densities in table 5.6 from the radio to sub-mm regimes are all comparable in magnitude and so one would expect extreme physical conditions to exist around Cyg X-3.

If synchrotron emission is the dominant emission mechanism then Cyg X-3 has to be very powerful in order to eject electrons at high velocities in the jets and with enough energy to emit radiation at 350 GHz. A source with similar parameters to Cyg X-3, GRS 1915+105, emits synchrotron radiation from radio to infrared frequencies (Fender et al. 1995) so this mechanism cannot be ruled out for Cyg X-3. However, the spectrum presented in figure 5.11 gives a good fit for frequencies above 5 GHz to a power-law spectrum with $S \propto \nu^{-0.1}$ spectral fit. Further analysis of the slope between the 2.25 and 8.3 GHz data points show that in that region the spectrum obeys a $S \propto \nu^{1.9}$ law. This is very similar to a spectrum of free-free emission becoming optically thick at lower frequencies. Caution must be observed here to avoid over interpretation of the data; the highly variable nature of the source gives rise to added complications in flux determination. For the rest of the discussion I will apply a synchrotron spectrum with a spectral index of zero. Because of the similarity of this source to GRS 1915+105 a synchrotron emission explanation is more probable.

### Sub-mm synchrotron emission

As mentioned above, the spectrum of emission from Cyg X-3 changes from synchrotron emission in the radio to modified black-body emission in the infrared. At some point in the spectrum a change in emission mechanisms occurs. These observations in the sub-mm regime show a spectrum consistent with a zero spectral index from 2 GHz to 350 GHz indicating that at the higher frequencies the electrons are not undergoing any appreciable losses and are still emitting synchrotron radiation.

Section 5.2.2 presents the theory of electron ageing for high frequency synchrotron emission. A lower age limit for the electrons was found by assuming radio emission was only observed when the plasmons had travelled from the core and through the dense stellar wind, and out to an optically thin region as given by equation 5.38. A magnetic field required to support electrons at a given age emitting at high frequencies is given in equation 5.40 and one can use this equation to calculate an upper limit to the magnetic field given that the spectrum has not appreciably turned over due to electron losses at the high frequencies observed by SCUBA.

At a frequency of 350 GHz, the electrons responsible for the emission will have travelled a distance of 700 $R_{\odot}$. The time that these electrons take to travel that distance depends on the velocity of the jet transporting the electrons out from the core. If the jet velocity is 0.3 $c$ as reported by radio observations following a major flare (Spencer et al. 1986) then the electrons have an age of

60 minutes. Alternatively if the jets are of the form seen in GRS 1915+105 and GRO J1655−40, and the speed is 0.92 $c$, then the electron age shortens to 20 minutes. However the energy released in these other superluminal sources is much greater than in Cyg X-3 due to the compact object being a black hole rather than a neutron star and so a 0.3 $c$ jet velocity is favoured for Cyg X-3. Alternatives to this simple picture are discussed in chapter 3 of this thesis.

Using equation 5.39 together with a cut-off frequency of $\nu_K = 350$ GHz and a jet velocity of 0.3 $c$, the magnetic field in the plasmons must be $B \sin\phi \leqslant 6.5$ T at 700 $R_\odot$ to support emission without appreciable ageing. This is the first reliable estimate to the magnetic field in the jets of Cyg X-3. With a magnetic field, and an upper and lower emission frequencies, equation 5.16 provides a synchrotron luminosity for the source. Given a distance of 10 kpc and a spectral index of 0, the total synchrotron luminosity is $L_s = 6.3 \times 10^{26}$ W, which would give a total electron energy of $U_e \geqslant 5.9 \times 10^{24}$ J.

### Comparison with GRS 1915+105

The 'microquasar' GRS 1915+105 is the other energetic X-ray binary for which detailed observations of the synchrotron emission have been carried out. Fender et al. (1997b) and Fender & Pooley (1998), following observations by Chaty et al. (1996) and Mirabel et al. (1996), observed GRS 1915 with the infrared telescope UKIRT together with radio observations with the Ryle telescope to monitor radio and infrared photometric changes from the source. They discov-

| Source | Synchrotron luminosity (W) | Magnetic field (T) | Electron energy (J) |
|---|---|---|---|
| GRS 1915+105 | $\geqslant 10^{29}$ | $\sim 8 \times 10^{-4}$ [a] | $6 \times 10^{27}$ [c] |
| Cyg X-3 | $7 \times 10^{26}$ | $\leqslant 7$ [b] | $\geqslant 6 \times 10^{24}$ [d] |

Table 5.7: Comparison of derived quantities for GRS 1915+105 (Fender et al. 1997b; Fender & Pooley 1998) and Cyg X-3 (this thesis). Notes: (a) magnetic field derived from equipartition arguments: electron cloud volume = 5 light minute radius sphere, filling factor of unity; (b) $B \sin \phi$ from spectral ageing arguments at a distance 700 $R_{\odot}$; (c) energy required to produce synchrotron emission at 2.2 μm; (d) total electron energy over all frequencies. Since the spectrum is flat, the electron energy at the highest frequencies is a reasonable approximation to the total energy.

ered that infrared flares were closely correlated with radio flares a number of hours later. The conclusions were that infrared flares were a consequence of repeated injections of synchrotron emitting electrons into the jets.

Fender et al. (1997b) and Fender & Pooley (1998) used the radio and infrared flux, assumed a spectral index and distance to the source to derive a synchrotron luminosity. They also used equipartition arguments to calculate the magnetic field in the source and used this value to derive properties of the source: the minimum energy in each ejection event and the minimum power into particle acceleration. For our observations we cannot determine an energy and power for ejections because the SCUBA observations did not observe a statistically significant flare, just variability from the source. However, one can compare the other derived quantities for GRS 1915+105 and Cyg X-3. These values are summarised in table 5.7. The derived examples are not exactly equivalent between the two sources. The magnetic field derived in GRS 1915+105 is taken from

equipartition arguments between the particle energy and magnetic field energy. The volume used in Fender's model is a uniform electron cloud of a sphere of radius 5 light minutes, corresponding to the rise time of the flare events. An equivalent volume cannot be calculated from the Cyg X-3 SCUBA observations because no flare occurred which could be identified with the certainty of Fender *et al.*'s observations, and so no particle energy density and thus equipartition magnetic field can be calculated. One other compared quantity, the electron energy, is not directly equivalent because the GRS 1915+105 energy is what is required to create synchrotron radiation at 2.2 μm with a magnetic field of 0.8 mT, whereas the Cyg X-3 energy is the total electron energy over all frequencies. However, since the spectrum is flat for both these sources the electron energy at the highest frequencies is a reasonable approximation to the total energy.

*Conclusions based on a tangled magnetic field*

The observations and conclusions in this thesis have used the magnetic field perpendicular to the direction of motion, $B_\perp$, or the magnetic field multiplied by the pitch angle of the electron, $B \sin \phi$. To put this into context, if the pitch angles are isotropically distributed then the value of $\sin^2 \phi = 2/3$, and $B_\perp = 0.82B$. This would be the case if a tangled magnetic field is frozen into the plasmon. The perpendicular magnetic field from the upper limit derived above in this case is $B_\perp = 5.7$ T, and using equation 5.3 the gyro-frequency for cyclotron radiation is $\nu_g = 160$ GHz. The magnetic field used in this calculation is derived for a distance of 700 $R_\odot$ and a frequency of 350 GHz. To emit

synchrotron radiation at 350 GHz, from equation 5.6, the gamma factor $\gamma \geqslant 1.5$.

The jets are moving through photospheres of varying radius so the higher frequency radiation is observed at an earlier time than the lower frequency radiation. If one compares emission at two different frequencies then the distance from the core at which the emission is observed is different. Because the jets are expanding, then the environment from which the radiation is emitted is different. The expansion of a plasmon with a tangled magnetic field is documented by equation 5.32 and at two radii, $R_1$ and $R_2$, the magnetic field is compressed or expanded by $B_1/B_2 = R_2^2/R_1^2$. Between 700 $R_\odot$ and 20,000 $R_\odot$ (corresponding to emission at 350 and 2.3 GHz), the magnetic field reduces in strength to $B_2 \leqslant 7$ mT at 20,000 $R_\odot$ (still assuming a tangled field). The gyro-frequency at this distance is now 200 MHz (due to the reduced field) and the gamma factor for the electrons is now $\gamma \geqslant 3.3$. This is the typical radius at which 2.25 GHz radiation is emitted (see equation 5.38 and table 5.1). There is no reason why radiation at higher frequencies cannot be emitted at this radius and any frequency up to the Kardashev frequency can be accommodated by increasing the electron energy factor $\gamma$.

For a comparison with other well known sources, if the magnetic field were extrapolated from a radius of $5 \times 10^{11}$ m (700 $R_\odot$) to the neutron star radius of $10^4$ m, the magnetic field would increase to $B_{ns} \leqslant 10^{16}$ T. While this is orders of magnitude larger than pulsar or magnetar magnetic fields, the compression of a plasmon down to surface of a neutron star is not robust in this scenario.

## 5.4 Conclusions

From the observations of Cyg X-3 with the SCUBA instrument on the James Clerk Maxwell Telescope, together with quasi-simultaneous radio observations, the flux densities measured at radio wavelengths and sub-mm wavelengths are comparable, and no change in emission mechanism has occurred up to a frequency of 350 GHz. Photometry also indicates the same degree of variability occurs in both frequency bands.

The spectrum taken using the average fluxes shows a flat spectrum with a spectral index of $\alpha = 0$ within errors. If spectral ageing of the electrons has not occurred at the higher frequencies, this places an upper limit on the magnetic field at the distance at which the high-frequency emission becomes optically thin. Adiabatic expansion of the plasmon responsible for the emission out to distances at which the low-frequency radiation becomes optically thin lowers the magnetic field, but the relativistic energy of the electrons at all distances in the jet are comparable.

The total synchrotron luminosity in Cyg X-3 is approximately $1000^{\text{th}}$ of that of GRS 1915+105 which is expected as GRS 1915+105 emits synchrotron radiation at infrared wavelengths whereas Cyg X-3 does not. However, this is still very high for a Galactic source.

# Chapter 6

# Wind emission in the mid infrared

> "The truth about things is like a bowl of fish hooks: you try to examine one little truth and the whole lot comes out in a black and vicious bunch".
>
> – Stephen Fry, *Making History*

## 6.1 Background

While the radio and sub-mm emission from Cygnus X-3 comes from relativistic jets hundreds of solar radii from the binary, the infrared emission is very much different, both in emission mechanism and emission region. One signifi-

cant feature of Cyg X-3 is the 4.8 hour period observed in the X-ray emission (Brinkman et al. 1972). With the absence of any similar period in the radio data, where the emission comes from far out in the binary, the most common interpretation is that we are seeing an orbital modulation in the X-ray data. As X-rays are generally produced close to the compact object in these systems, this interpretation is not unrealistic.

When van Kerkwijk et al. (1992) took a high-resolution infrared spectrum of Cyg X-3 using UKIRT, in addition to as an overall modulation of the intensity by a 4.8 hour period, they observed strong ionised He and N lines. The orbital modulation (which has been observed before – (Mason et al. 1986)) indicated that the infrared emission came from a region close to the binary, possibly from the companion star. However, strong He and N lines together with the observed line ratios are indicative of a Wolf–Rayet star of the WN7 class. A star of that type would have a supersonic, dense wind which would shroud the neutron star, accretion disc and the base of the jets.

We have now three different tools for studying different regions in Cyg X-3. Emission at radio wavelengths comes from the relativistic jets. The jets are produced from the centre of the binary close to the compact object, but the radio emission is not observed until the jets travel past an optically thick radio photosphere in the Wolf–Rayet wind. The radio emission is therefore well separated from the rest of the binary. At the other extreme is emission at X-ray wavelengths. The X-ray emission comes from the central region surrounding the

compact object at the inner edge of the accretion disc. The interesting (or energetic) components of the binary are enclosed in a dense, hot Wolf–Rayet wind, and it is from this region too that the infrared emission originates. Extending the radio and sub-mm picture that emission is only observed from outside a photosphere, the radius of the photosphere is $R_\nu = 4 \times 10^4 \nu_{\rm GHz}^{-0.7}$ $R_\odot$ (equation 5.38), and for infrared radiation at 100,000 GHz (3 μm) the corresponding photosphere is at only 13 $R_\odot$.

The importance of the *ISO* observations is that they fill part of the gap between the sub-mm observations taken by SCUBA (see section 5.3.2) and the infrared observations taken by UKIRT at 2 μm. The sub-mm observations show that the spectrum is dominated by synchrotron emission from the jets, but this high-energy emission cannot continue for many more decades of frequency than is currently observed. At the few micron wavelengths, synchrotron emission is so weak that thermal emission dominates. Fender (1995) and Fender et al. (1995) showed that the spectrum of the UKIRT emission at the short wavelengths has a spectral index of $\alpha = 2.3$[1], but at the longer wavelengths, around 3 μm, the spectrum was getting flatter. Two interpretations are possible: either the spectrum is due to free-free emission becoming optically thick at 2 μm (Molnar et al. 1988), or the spectrum is a power law with index $\alpha = 1.4$ (van Kerkwijk et al. 1996).

An important question is, what does the spectrum do at the longer wave-

[1] In this thesis the convention $S \propto \nu^\alpha$ is used.

lengths, before the sub-mm synchrotron emission dominates? This question can be partially answered by the Infrared Space Observatory.

## 6.2 The Infrared Space Observatory

### 6.2.1 Satellite capabilities and observational setup

Observations were taken using the CAM instrument on the Infrared Space Observatory (*ISO*). ISOCAM consists of a number of short and long-wavelength filters operating in the 2.5–18 μm wavelength range. The satellite has a 32 × 32 pixel CCD and 4 lenses allow different pixel field of views of 1.5, 3, 6 and 12″ for each pixel. There are three main modes of operation for the array, which include:

**CAM01:** general observations, single pointing, raster, micro-scanning;

**CAM03:** beam switching;

**CAM04:** spectrophotometry.

It is recommended that for simple photometry, either a single pointing or raster imaging be used.

The aim of our observations was to obtain photometry of Cyg X-3 at longer wavelengths than those previously observed by UKIRT (Fender et al. 1995). We therefore utilised the long-wavelength (LW) filters to obtain six separate observations between 4.5 and 18 μm. The filters used, together with the wavelength

| Filter | $\lambda$ (μm) | $\lambda_{ref}$ (μm) | Mode |
|---|---|---|---|
| LW1 | 4.00–5.00 | 4.5 | stare |
| LW4 | 5.50–6.50 | 6.0 | stare |
| LW5 | 6.50–7.00 | 6.8 | stare |
| LW6 | 7.00–8.50 | 7.7 | stare |
| LW10 | 8.00–15.0 | 12.0 | 3×3 raster |
| LW3 | 12.0–18.0 | 14.3 | 3×3 raster |

Table 6.1: Filters used in the *ISO* observations.

| Filter | LW1 | LW4 | LW5 | LW6 | LW10 | LW3 |
|---|---|---|---|---|---|---|
| $t_{int}$ (s) | 161 | 161 | 119 | 144 | 321 | 311 |

Table 6.2: Integration times for the observations

reference, wavelength range and observation mode are given in table 6.1. Since no structure is expected to be visible at any of the resolutions of ISOCAM for Cyg X-3 at 10 kpc, a pixel field of view of 6″ was chosen in order that a number of field stars could also be observed. For the stare modes this gave a total field of view of 3.2′×3.2′. The raster observation modes were taken in a 3 by 3 grid with a 24″ offset giving a total field of view of 4.4′×4.4′.

Observations were taken on 1996 April 07 (MJD 50180) for a total of 2895 seconds. The observations were centred on Cyg X-3 (RA(2000) 20 32 25.699, Dec(2000) +40 57 28.01); the orientation of the spacecraft gave an offset between the $y$-axis and north of 99.17 degrees. The integration time for individual frames was 2.1 seconds, and the total integration times for all the filters is given in table 6.2.

As is true for any astronomical observation, there exist a large number of auxiliary data sets together with the primary observation which provide calibration data and information about the status of the instrument. *ISO* is no exception, however many of the spacecraft files and instrumental files are automatically incorporated into a final 'raw-data file' with all the satellite housekeeping data included, from which the secondary calibration can be performed. Much of the initial calibration is very much standard and includes steps like calculation of filter wheel positions, on-off imaging states, detector identifications, black-body voltages and currents, gain and so on.

What is provided for the astronomer in order to obtain a calibrated data set are either observations or libraries which include:

**CISP:** CAM image standard processed data (raw data),

**DARK:** dark current exposures,

**DFLT:** detector flat field library,

**OFLT:** optical flat field library and

**SPEC:** engineering units to Jy conversion.

These files provide a complete set of calibration and image data in order that a final image can be produced.

### 6.2.2 Data analysis

The data analysis technique is relatively simple. It consists of taking the image data cube in the CISP file, splitting this into individual filter observations and performing the following on each filter:

1. dark correction,
2. de-glitch the data to remove transients,
3. stabilisation of pixels due to memory effects,
4. flat-field correction,
5. jitter correction,
6. average integration times into a stare image or raster map,
7. field of view distortion correction,
8. convert engineering units of adu gain$^{-1}$ s$^{-1}$ to Jy.

Each of the calibration steps is now covered in detail.

#### Dark subtraction

The dark subtraction accounts for a signal variation between odd and even detector lines in the image. There are a number of ways to do this, and these include the use of a library dark field, the estimation from a linear transform law (van Buren & Kong 1996) based on the library dark field, using the maximum

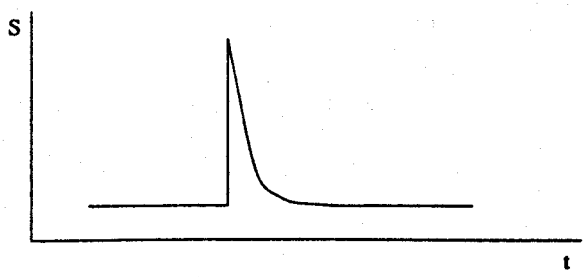


Figure 6.1: Schematic of a cosmic ray glitch. Plotted are flux against time for a stylised glitch. Typical glitches last for around 10 seconds, or a few integration times.

entropy method and using a time variation in Fourier space to suppress the effect. In the majority of observations the library dark field is sufficient, which was the case for our observations.

### De-glitching transients

When cosmic rays hit the detector, they alter the current in the detector in the pixels they encounter, for a few integration times. A schematic of a glitch is shown in figure 6.1. The de-glitching algorithms need to identify a glitch for a given pixel over the noise level, and subtract it. The techniques for de-glitching the data are:

**Manual:** data is identified by hand (and eye). This takes a long time, but is robust.

**Spatial and temporal:** for each frame of data (one integration time) neighbouring pixels are compared. Those pixels with deviations over a certain

standard deviation from the mean are flagged as glitched. This is relatively efficient, but can fail if long glitches occur or the when the same pixel is hit twice in quick succession.

**Multi-resolution Median Transform,** uses a non-linear technique to identify time-resolved variations which occur on a timescale which is shorter than the total integration time for an observation. All significant structure on the small scale should be a glitch, and should be removed. This technique is the slowest of the automatic de-glitching routines, but works best for most data.

Of all the techniques, the MMT routine gave the best results for our data.

### Stabilisation

A problem that became apparent when it was too late to correct it was that on ISOCAM all pixels exhibit a memory of previous incident radiation. This memory effect can be caused by a filter change as when the filter wheel rotates there will be a time when the pixels have no incident radiation. The memory effect can also be caused by a brighter or fainter previous observation, a cosmic ray incident on a pixel, or a mosaic observation when the pattern of incident radiation shifts by a number of pixels. All of these effects create an incorrect output for a given pixel, and the stabilisation routines either suppress this effect, or model an ideal pixel response.

Due to the differences in how memory effects are created, each effect requires

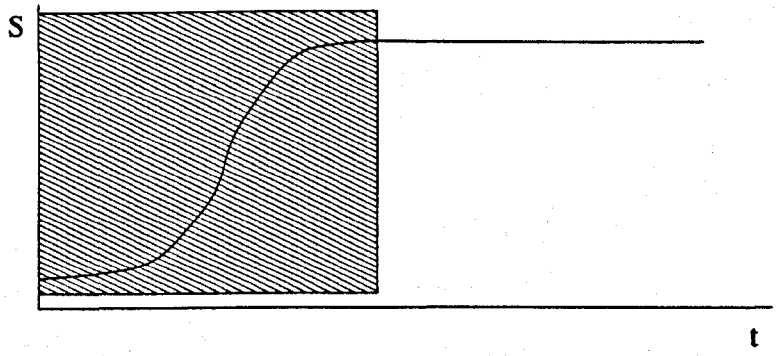


Figure 6.2: The change in pixel output for a bright source with time after a filter change, or an observation change. The shaded region is the amount of data that is masked out.

a different technique to correct the data. Memory effects which are due to observing changes like filter changes, or source changes can be corrected by masking the first $x\%$ of the observation until the source or background pixels have had time to adjust to a different level of incident radiation. Figure 6.2 shows how the pixels covering a bright source behave after a filter change , and how they can be corrected. The exact cut-off used for the masking of the pixels is dependent on the filter used in the observation, and the percentage of the total integration which is masked out can vary wildly. For our observations this initial mask was created when the observations were scheduled and proved to be perfectly acceptable for all the observations.

Memory effects due to the shift of a field in a mosaic creates a similar effect. When the bright source in the field shifts to another position, a number of pixels in the background retain a residual image which creates a cross shape of

extended emission in the final mosaic. The technique to remove this is simple yet clever. The pixels with the memory problem are systematically masked out as the mosaic is built up, creating a slight over-correction to the field. However, for point sources this over-correction is of the order of the noise level, and as it removes spurious extended emission it is considered an acceptable correction.

The most difficult memory effect to remove is that due to transients such as the cosmic ray glitches. Glitches are automatically removed in the de-glitching process, but the memory effect still exists which usually raises the noise level in the background. Rather than just suppressing below 90% of the peak, or the first 10% of an observation (as is done in the filter stabilisation), these memory effects need to be modelled. As with any modelling process, the results could become problematic and the application of such an algorithm should be used with caution.

The method which produced the lowest background and highest dynamical range with the least spurious features was the 90% stabilisation method where pixels outside the 90% of their average value were suppressed.

### Flat-field correction

The detector response over the entire field is not flat as a consequence of differences in the detectors themselves and the optics in the instrument. There exists a library of two flat fields and, to correct for any difference in pixel response over the array, the processed data is divided by the product of these fields.

There are two techniques to correct for the flat-field. The first is a direct use of the library flat-fields, but unfortunately due to differences in the filter wheel position, this technique does not work all the time, and the detector output at the edges of the fields can change quite significantly between two observations with different filters. The second technique is more successful with raster observations than stare observations, and uses only the background pixels as an observed flat field. Raster observations of point sources in a non-crowded field usually have the majority of the pixels in the array observing the background at one time or another, therefore a flat-field response can be calculated. However, if there is any gradient in the background or memory / transient effects have altered the background then this technique can fail.

Out of all the data reduction steps, this correction gave the least satisfactory results. The library flat-fields were used in the stare modes of the shorter wavelength observations, and as one can see in the maps below, the flat fielding is less than perfect. The raster observations at the two long wavelengths gave better results using the background-observed flat-field method, but could not be employed in the stare observations.

### Jitter correction

Jitters of the order 0.5″ have been reported for the satellite. However, as our observations had pixel resolutions of 6″, no jitter correction needed to be performed.

### Field of view distortion correction

The optics of the larger pixel fields of view is distorted at the edges, and while this affects the 12″ pixels to a large degree, at 6″ resolution, the effects are important only at the 3% level. However, corrections are simple to apply and no complications occurred in the process.

### Detector output to flux conversion

The detector levels after flat-field gain correction, and summation are in ADU (Analogue Digital Units) per gain per second and require the conversion to the more astronomical units of Jy. This was achieved by using standard internal conversion tables for each filter, and were assumed not to be in serious error.

At this stage, the reduction is complete and a 32×32 or 44×44 pixel image in mJy was obtained for all six filters.

## 6.3 *ISO* results

### 6.3.1 Imaging

Following the data reduction stage described above, six images were produced at 4.5 to 18 μm with a field of view of either 3.2′ × 3.2′ or 4.4′ × 4.4′ depending on whether stare or raster mode was used. Figures 6.3 to 6.8 show the infrared images in contours.

There is a known problem with CAM data in that the absolute celestial posi-

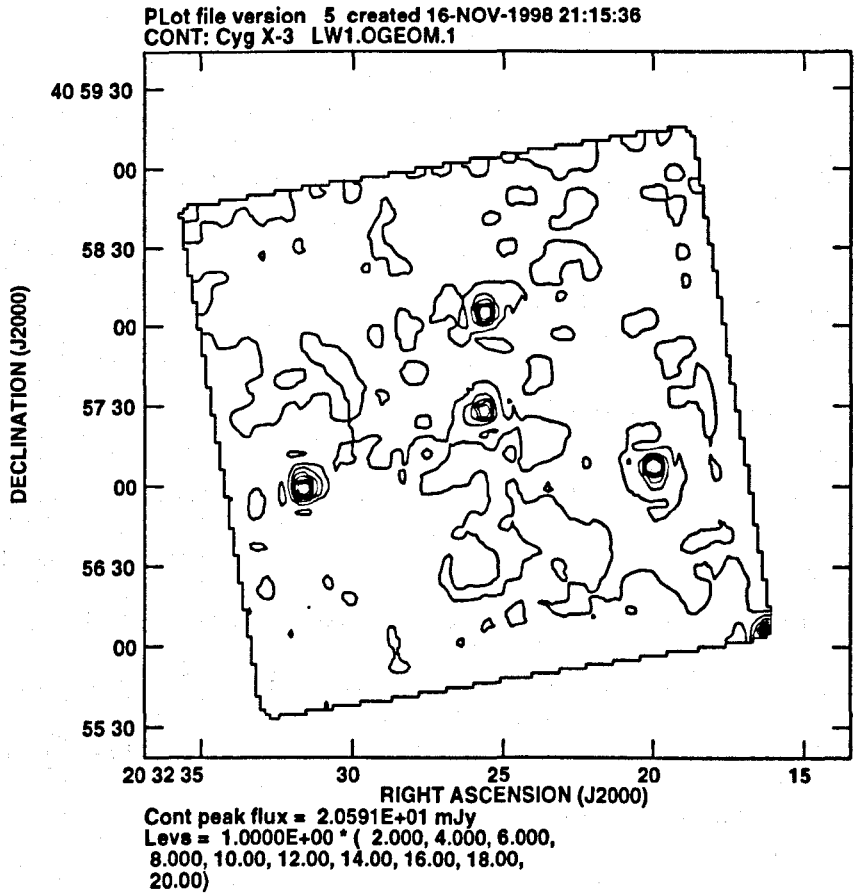


Figure 6.3: Cyg X-3 image with the LW1 filter, 4.5 μm. Cyg X-3 is at the centre of the image, other sources are identified in figure 6.11.

tion of the pixels is not known to any degree of accuracy. When the filter wheel rotates and stops in the correct position the star trackers can be misaligned with the CCD array by as much as two pixels, or in our case 12″. The consequence of this is that a previously measured position for one of the objects in the field is required, and the positions of other sources can be obtained from that.

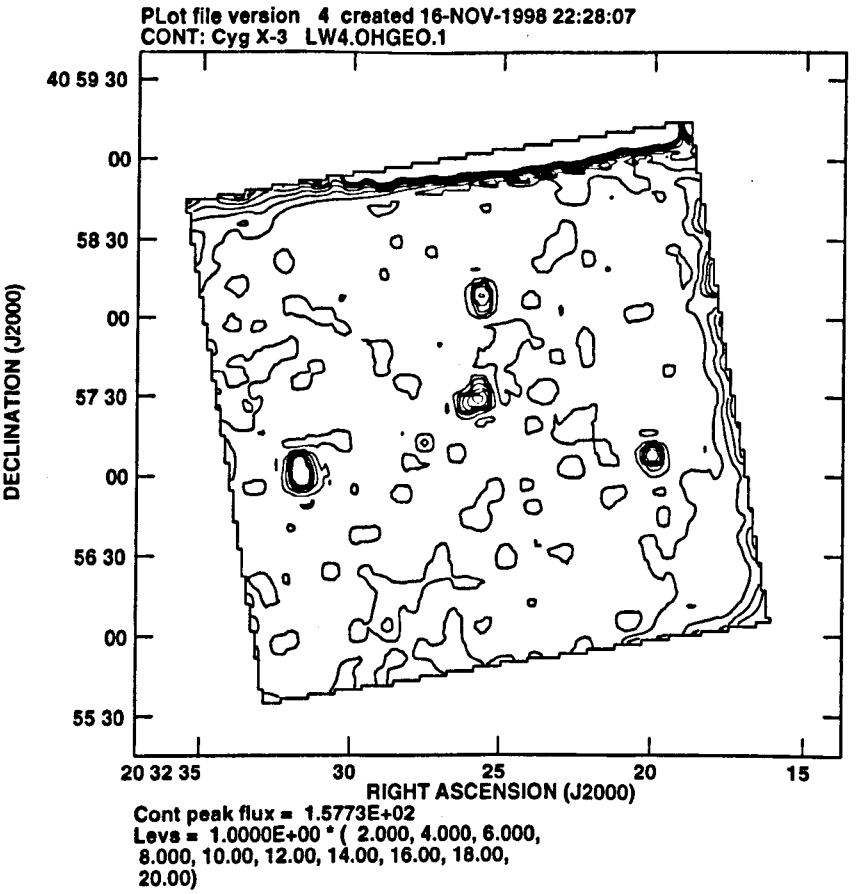


Figure 6.4: Cyg X-3 image with the LW4 filter, at 6.0 μm. There are serious, steep flux gradients at two edges due to a misaligned filter wheel affecting the flat-fielding. The background near the sources of interest is unaffected.

An optical image from the Digitised Sky Survey can be used to check the alignment of the infrared sources with any optical counterparts. Figure 6.9 shows the DSS image for the Cyg X-3 region.

To align the infrared sources, accurate positions for them needs to be established. Positions can be calculated from phase-referenced radio images, optical

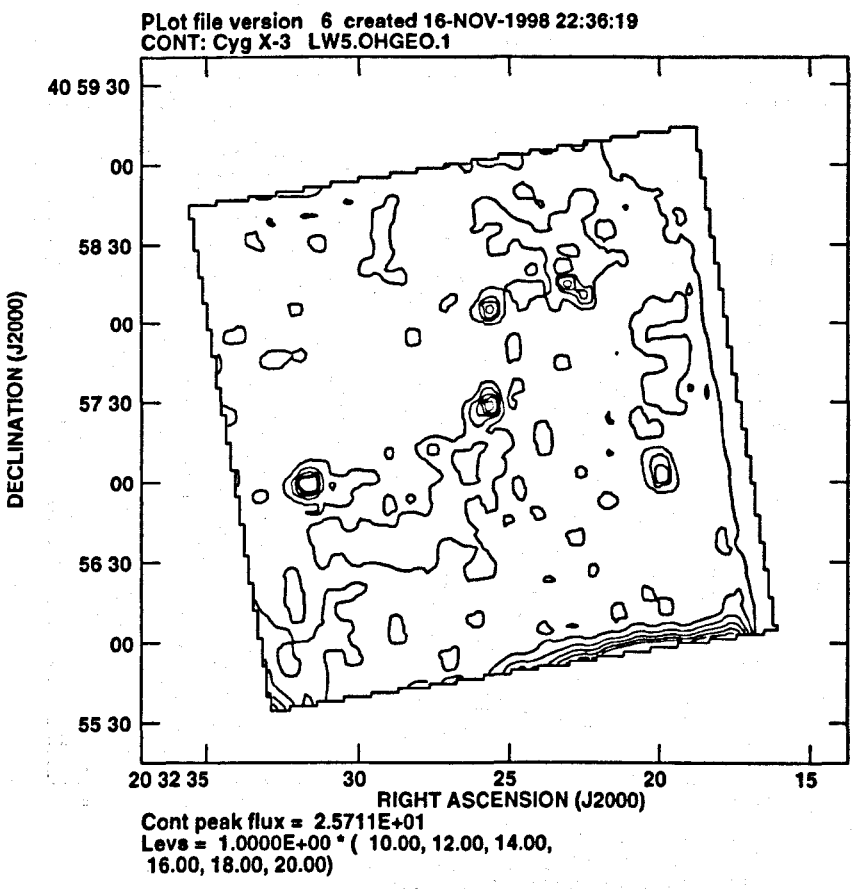


Figure 6.5: Cyg X-3 image with the LW5 filter, at 6.8 μm. Flat-fielding errors are observed in this filter as well as in the LW4 filter in figure 6.4.

sources with known infrared counterparts or catalogued sources.

The only known radio position we have with any certainty is from our observations at 22 GHz of Cyg X-3 (see section 2.2.3). The source has been phase-referenced and so the absolute position is known to a high degree of accuracy. The radio position for Cyg X-3 is RA(2000) 20 32 25.712 Dec(2000) +40 57 28.21. If the infrared emission comes from the wind around the Wolf-Rayet

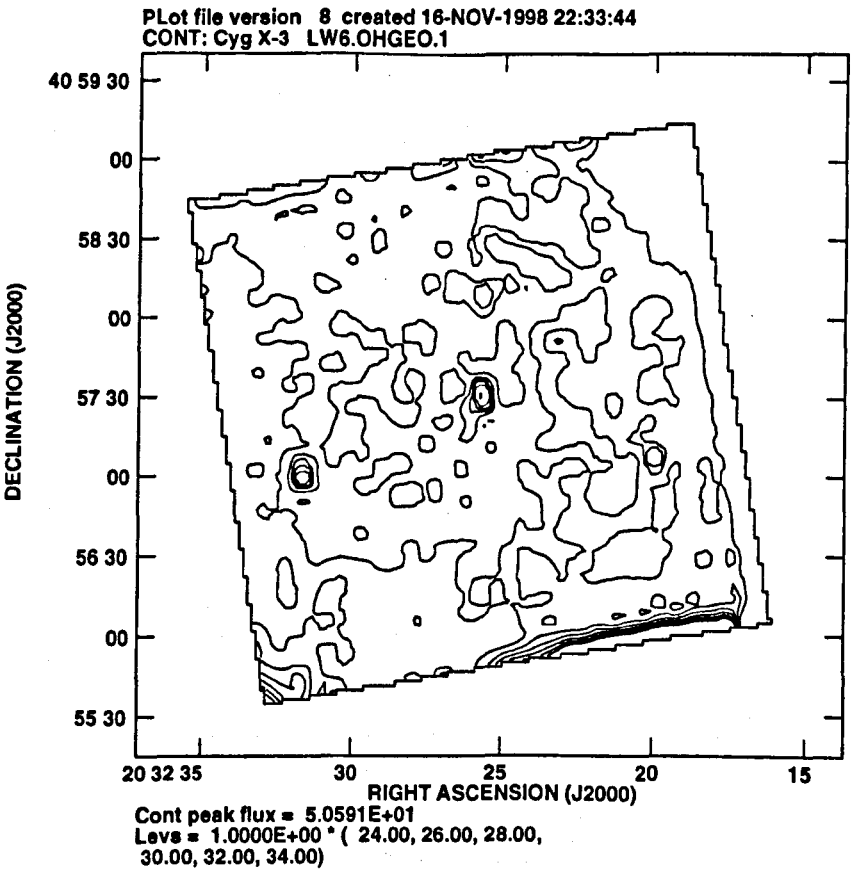


Figure 6.6: Cyg X-3 image with the LW6 filter, at 7.7 μm. As with the LW4 and LW5 filter images, this image shows flat-fielding problems. However, in all the affected fields, the central sources are unaffected.

(see section 6.4) then, because the radio emission is synchrotron, the radio and infrared emission do not come from the same place in the system. The infrared emission should come from the inner 100 $R_\odot$, and the radio at 22 GHz is outside the relevant photosphere (see section 5.2.2) $\gtrsim$ 5000 $R_\odot$. However, at 10 kpc, both regions are within a few mas of each other, and on the scale of the *ISO*

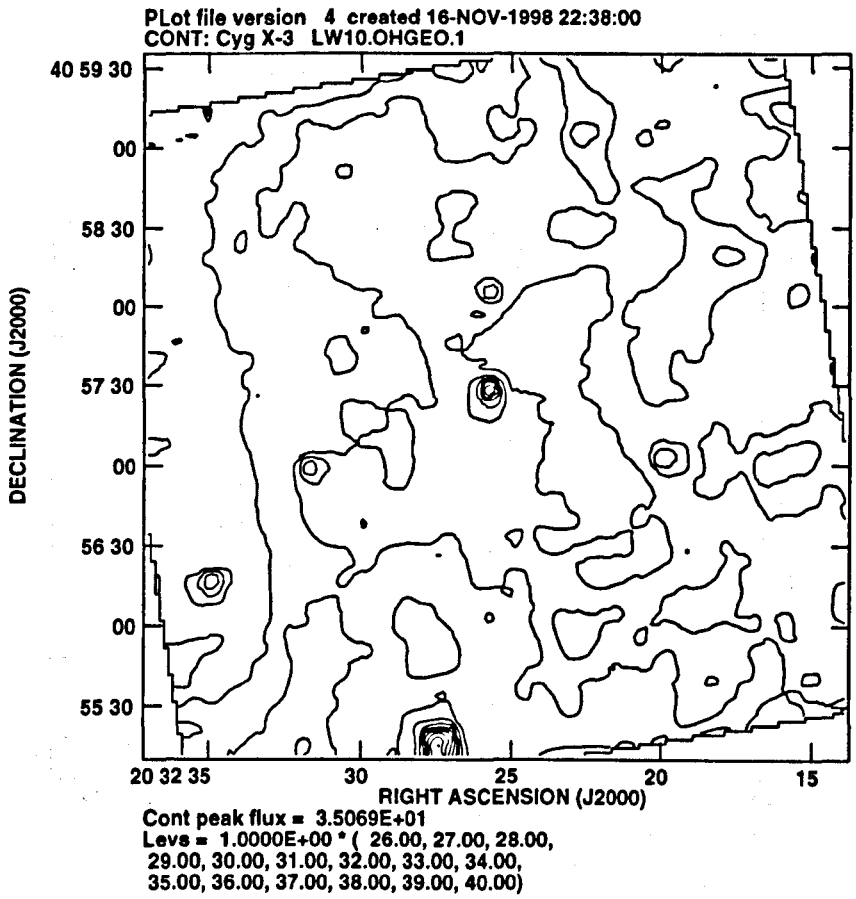


Figure 6.7: Cyg X-3 mosaic with the LW10 filter at 11.5 μm.

pixels this is thousands of times smaller than the resolution of *ISO*. For our argument here both emission regions are co-incidental.

The catalogue position for sources can be taken from the SIMBAD catalogue of astronomical sources. I have found in the past that SIMBAD co-ordinates can be significantly in error.

After correcting for the misalignment of the *ISO* satellite with the known

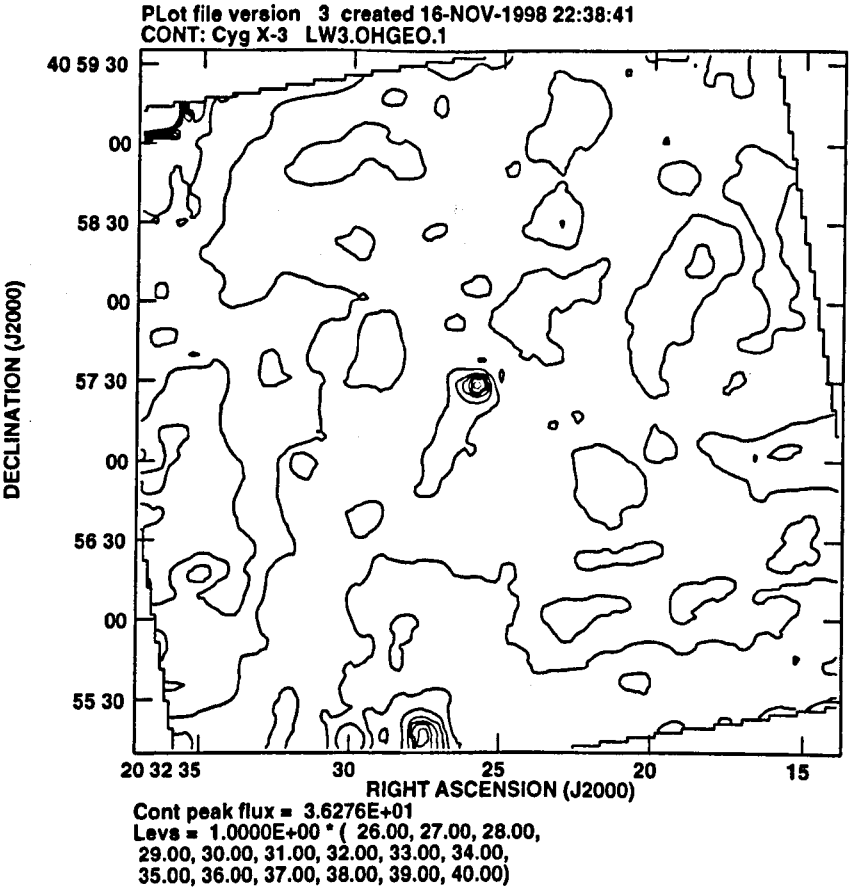


Figure 6.8: Cyg X-3 mosaic with the LW3 filter at 15.0 μm.

radio position, Figure 6.10 shows an overlay of the grey-scale DSS optical image with a contour *ISO* image using the LW1 filter at 4.5 μm.

The alignment of the surrounding stars is good, but not perfect, and no rotation, or linear shift could position all of the objects to an exact alignment. As Cyg X-3 is the only star in the field to have both known radio and infrared emission, the alignment of the *ISO* field with the known radio position aligns

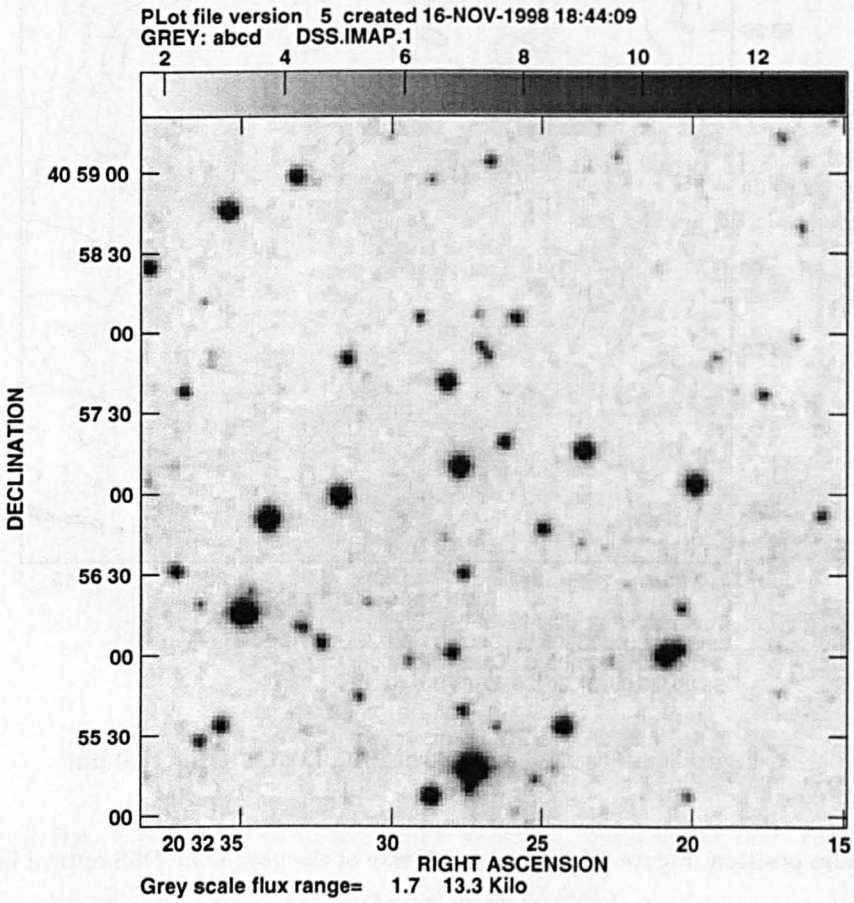


Figure 6.9: A Digitised Sky Survey image of the Cyg X-3 region.

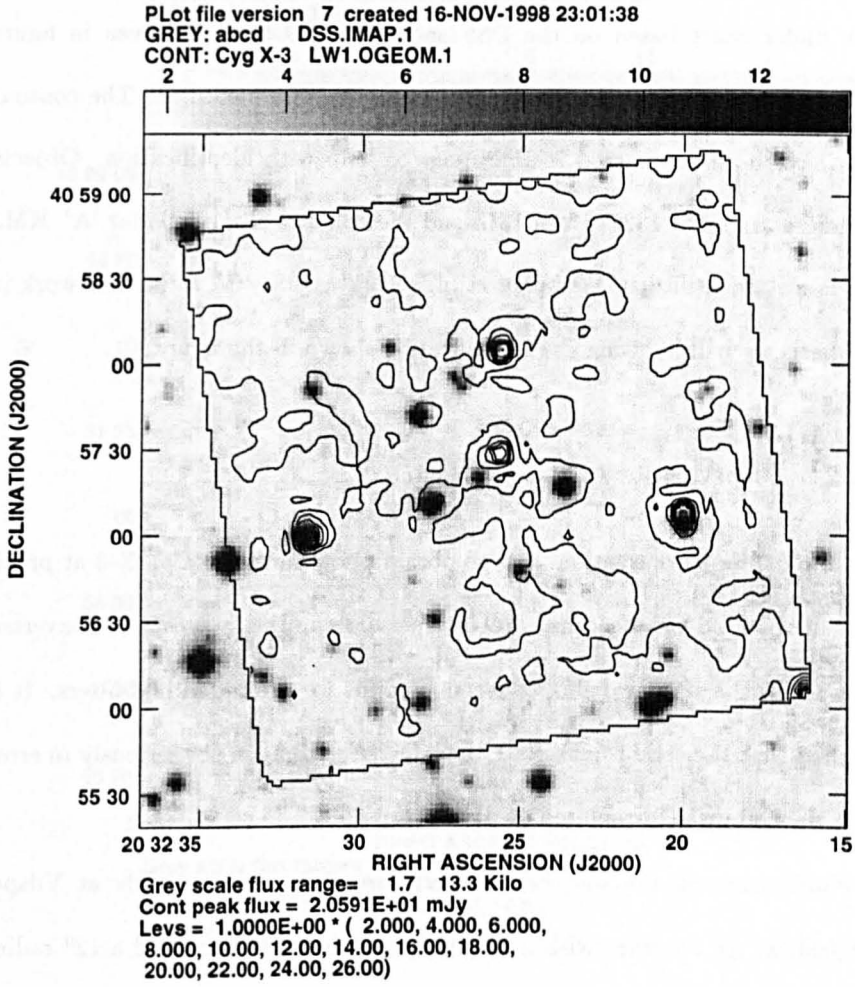


Figure 6.10: A composite image of the optical DSS frame in grey-scale with the infrared LW1, 4.5 μm, image in contours.

the images with the optical image as shown. While some stars could have been used to align the optical and infrared images, an exact correlation between any optical and infrared emission is unknown.

A finder chart based on the DSS and LW1 *ISO* image is given in figure 6.11. The bright sources in the *ISO* images have been identified. The contour levels have been suppressed in the image to help with identification. Objects of interest are KMJ 1327, 1328, 1315 and Westphal et al. (1972) star 'A'. KMJ 1328 is also identified in Westphal et al.'s work as star 'C'. In further work in this thesis we will be using the identification shown in the figure.

### 6.3.2 Photometry

The aim of these observations was to obtain photometry for Cyg X-3 at previously unobserved wavelengths. *ISO* internal units in the images were converted to Jy using the standard flux conversion ratios for the individual filters. It is assumed that the code to calculate the ADU/G/s to Jy is not seriously in error when the code was formulated on 1998 April 05.

Photometry on the sources was performed using private code at Vilspa, Villafranca. An aperture with a 24″ diameter, then a 6″ gap, and a 12″ radius annulus for the background was used. This is shown in figure 6.12.

To correct for the size of the point spread function used in the observations, an idealised point spread function model was taken at all the filters used in the observation, and photometry was performed on the PSF to calculate the

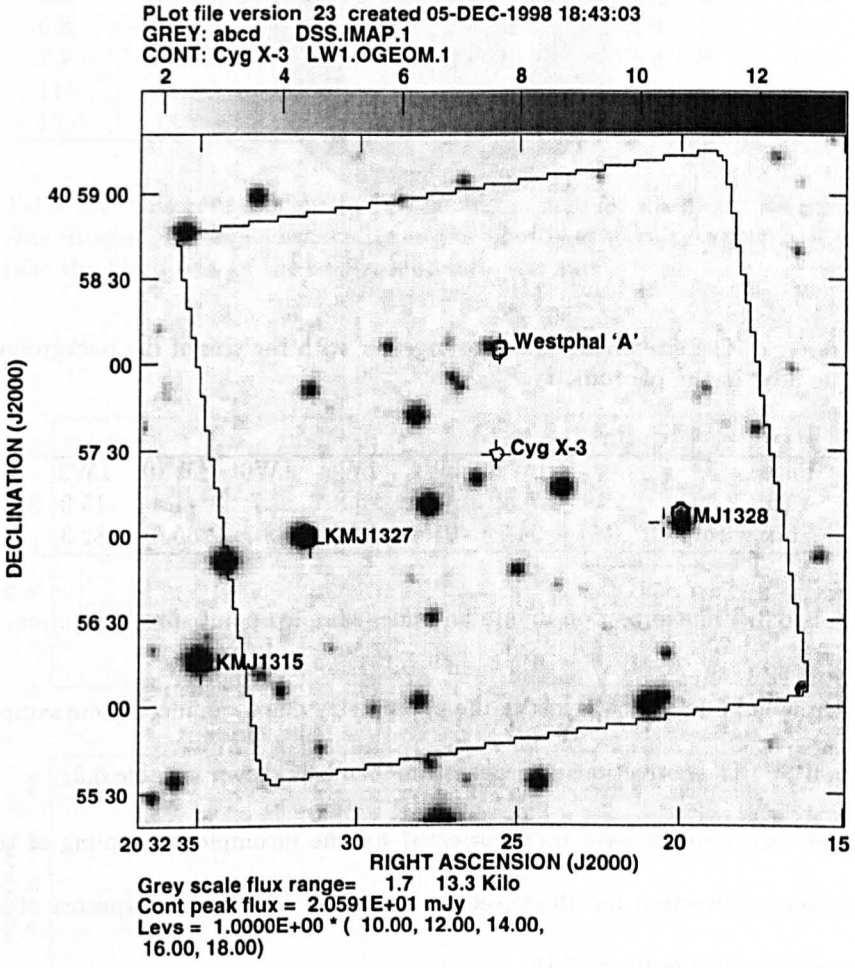


Figure 6.11: A finder chart based on the grey-scale DSS image and *ISO* LW1 contours. Contours are suppressed so objects can be identified more clearly. Westphal et al. (1972) star 'A' is identified, and object KMJ 1328 is also known as Westphal et al. (1972) star 'C'.

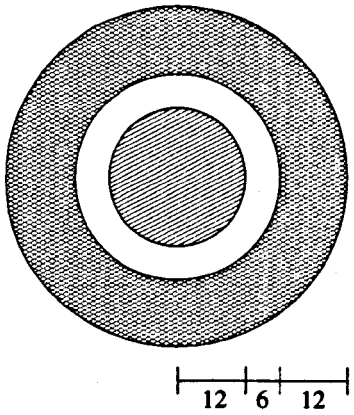


Figure 6.12: The size of the aperture together with the size of the background sample used in the photometry.

| Filter | LW1 | LW4 | LW5 | LW6 | LW10 | LW3 |
|---|---|---|---|---|---|---|
| $\lambda$ ($\mu$m) | 4.5 | 6.0 | 6.8 | 7.7 | 11.4 | 15.0 |
| Flux within 12″ (%) | 94.7 | 91.6 | 90.3 | 88.7 | 85.0 | 82.3 |

Table 6.3: Flux correction due to an under-sampled point spread function.

percentage of flux that was lost in the photometry due to an incomplete sample of the PSF. The corrections for each of the bands is shown in table 6.3.

The fluxes which have been corrected for the incomplete sampling of the point spread function for all objects are given in table 6.4 and spectra of all sources are given in figure 6.13.

All fluxes in table 6.4 are reddened. To de-redden the data, a value for the extinction at the different wavelengths needs to be calculated. It is preferable to express extinction at a given standard wavelength band, for example visual, $A_V$, or the infrared J-band, $A_J$. At other wavelengths this extinction coefficient

| λ (μm) | Cyg X-3 | KMJ 1328 | 'A' | KMJ 1327 | Background |
|---|---|---|---|---|---|
| 4.5 | $18.2 \pm 2.5$ | $26.0 \pm 1.8$ | $21.0 \pm 2.2$ | $35.4 \pm 2.2$ | 2.0 |
| 6.0 | $31.1 \pm 4.1$ | $28.0 \pm 3.6$ | $22.2 \pm 3.2$ | $50.2 \pm 3.6$ | 8.5 |
| 6.8 | $20.6 \pm 4.9$ | $22.0 \pm 5.7$ | $14.2 \pm 4.9$ | $30.9 \pm 5.1$ | 11.4 |
| 7.7 | $24.3 \pm 3.9$ | $17.6 \pm 6.8$ | $22.4 \pm 4.9$ | $30.6 \pm 4.9$ | 24.4 |
| 11.5 | $15.2 \pm 1.6$ | $8.0 \pm 2.6$ | $7.0 \pm 1.6$ | $8.9 \pm 3.0$ | 27.1 |
| 15.0 | $18.7 \pm 1.8$ | $3.9 \pm 2.0$ | $4.3 \pm 1.5$ | $6.5 \pm 2.7$ | 30.4 |

Table 6.4: Observed reddened flux densities in mJy for the bright sources in the *ISO* images. Errors shown are from the photometric calculations and do not take the brightness of the background into account.

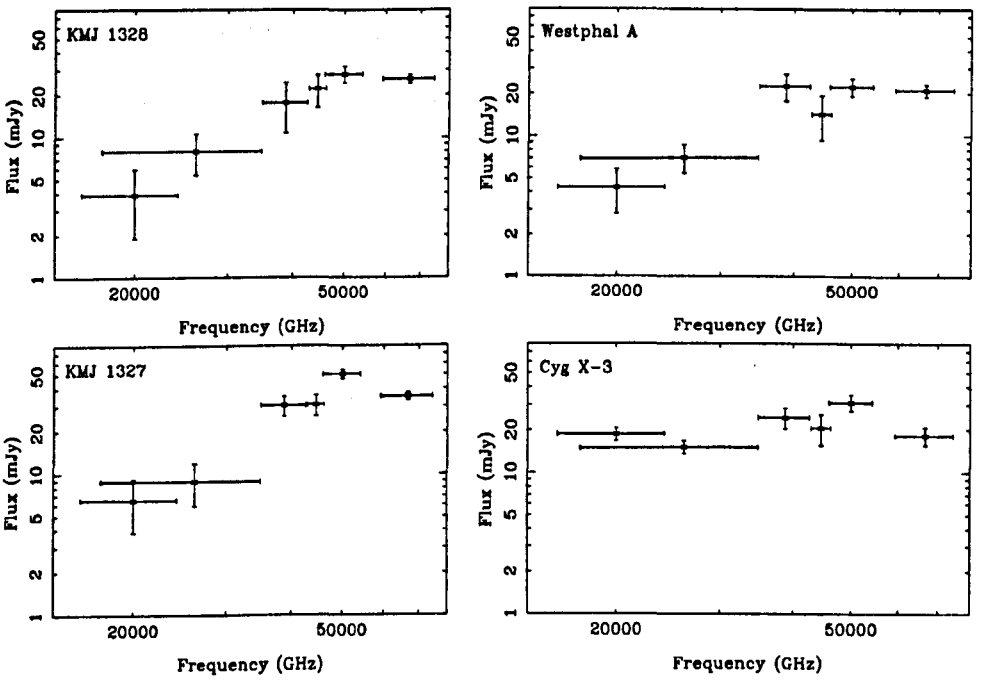


Figure 6.13: Basic spectra of the stars in the *ISO* fields. No source has been de-reddened. Even without de-reddening the data, one can see that Cyg X-3 is significantly different from the other three sources which are normal stars.

has a different value, and its appropriate form needs to be calculated. The variation of extinction with wavelength can be expressed as $A \propto \lambda^{-1.76}$ (Rieke & Lebofsky 1985). The extinction at a given wavelength can be related to the extinction at J-band which has a wavelength of 1.25 μm by the expression

$$A = A_J \left( \frac{\lambda}{1.25\ \mu\text{m}} \right)^{-1.76}. \tag{6.1}$$

The extinction coefficient represents the number of magnitudes by which a source has its flux reduced due to the presence of dust. One can relate the flux of a source to its magnitude by the equation

$$2.5 \log \left( \frac{S}{S_0} \right) = (M_0 - M) \tag{6.2}$$

where $S$ is the flux of a source at a magnitude $M$, and $S_0$ is the flux at a magnitude $M_0$, measured in the same band. When extinction is present, this alters the magnitude of a source and the observed reddened source can be related to the de-reddened source by the equation

$$2.5 \log \left( \frac{S'}{S} \right) = M - M'. \tag{6.3}$$

The primed quantities refer to the observed reddened source. If the reddening

at the wavelength concerned is $A$ magnitudes then

$$M = M' - A \tag{6.4}$$

so

$$\begin{aligned} 2.5 \log\left(\frac{S'}{S}\right) &= M' - A - M' \\ &= -A. \end{aligned} \tag{6.5}$$

The un-reddened and observed fluxes of an object can therefore be written as

$$\log\left(\frac{S}{S'}\right) = \frac{A}{2.5}. \tag{6.6}$$

Equation 6.6 is still wavelength dependent, both for the extinction co-efficient, $A$, and the fluxes, $S$ and $S'$. This expression can be related to the extinction at a given wavelength band, which is constant for a given source. Equation 6.1 can be used to relate the magnitude of extinction with a standard extinction coefficient to obtain

$$\log\left(\frac{S_\lambda}{S'_\lambda}\right) = \frac{A_J}{2.5}\left(\frac{\lambda}{1.25\ \mu\text{m}}\right)^{-1.76}. \tag{6.7}$$

The value for the extinction co-efficient at J-band for each object is a difficult question. Cyg X-3 must have a high co-efficient for it to be an infrared source

| Star | $V$ (Mag) | $B-V$ (Mag) | $U-B$ (Mag) |
|---|---|---|---|
| KMJ 1328 | 15.03 | +1.37 | +1.70 |
| 'A' | 15.05 | +0.98 | +0.43 |

Table 6.5: The optical characteristics for two of the field stars in the ISO images as measured by Westphal et al. (1972).

but not an optical source. As it is at a distance of 10 kpc in the Galactic plane, this is not surprising. In his analysis of infrared data of Cyg X-3 from UKIRT, Fender (1995) used a value of $A_J = 6$ which, while high ($A_V = 30$), this is not unreasonable and is the value which we will adopt here.

Stars KMJ 1328 and Westphal's star 'A' have optical characteristics measured by Westphal et al. (1972) which can be used to calculate the extinction co-efficient. Quantities for the visual magnitude, together with $B-V$ and $U-B$ colours have been measured for both stars. The values are shown in table 6.5. van Kerkwijk et al. (1996) took a spectrum of Westphal's star 'A' using the CGS4 spectrograph on UKIRT as part of an observation to measure the spectrum of Cyg X-3 in the infrared. They identified star 'A' as an F5 to G0 star with a temperature of 5900–6400 K. If star 'A' is a main sequence star then its intrinsic colours would be $(B-V) = 0.51 \pm 0.08$ and $(U-B) = 0.06 \pm 0.06$ (Johnson 1966). From the observed and intrinsic colours for this star, a value of $A_J = 0.41 \pm 0.07$ is inferred for the extinction at J-band.

For star KMJ 1328 its spectral type has not been determined and so the intrinsic colours are unknown. However, from the observed colours, if the star

| Star | $A_J$ | $A_{4.5}$ | $A_{6.0}$ | $A_{6.8}$ | $A_{7.7}$ | $A_{11.4}$ | $A_{15.0}$ |
|---|---|---|---|---|---|---|---|
| Cyg X-3 | 6 | 0.62 | 0.38 | 0.30 | 0.24 | 0.12 | 0.08 |
| KMJ 1328 | 6[a] | 0.62 | 0.38 | 0.30 | 0.24 | 0.12 | 0.08 |
| 'A' | 0.4 | 0.04 | 0.03 | 0.02 | 0.02 | 0.01 | 0.01 |
| KMJ 1327 | 6[a] | 0.62 | 0.38 | 0.30 | 0.24 | 0.12 | 0.08 |

[a] An upper limit to the extinction

Table 6.6: Coefficients of extinction for the *ISO* wavelengths. The coefficients of extinction for the star KMJ 1328 is unknown, but a value of zero is the most probable based on the optical colours and magnitude.

is at a distance of zero and therefore un-reddened then it will be a K3/K4 supergiant or giant. With a V magnitude of 15, KMJ 1328 must be at a distance which is significantly greater than zero, and therefore will be reddened by some amount.

For stars KMJ 1327 and 1328 we have used an extinction co-efficient of $A_J = 6$ as an upper limit. The true value must be less than this otherwise KMJ 1328 would have an intrinsic V magnitude of $-20$. While this is unrealistic for the visible wavelengths, large changes in the value of $A_J$ only effect the 4.5 and 6.0 μm fluxes to a small degree, and for wavelengths longer than 6 μm the change in flux is less than the error bars in the *ISO* data.

From the extinction co-efficient at J-band, extinction co-efficients can be calculated for the *ISO* bands from the application of equation 6.1. Table 6.6 gives the extinction co-efficient at the *ISO* bands together with $A_J$ for all known stars. If one applies these corrections to the fluxes given in table 6.4 then the de-reddened photometric fluxes increase. De-reddened fluxes are given in table 6.7 for the three stars with known co-efficients and spectra for the stars are

| λ (μm) | Cyg X-3 | KMJ 1328 | 'A' | KMJ 1327 |
|---|---|---|---|---|
| 4.5 | 32.2 ± 4.4 | 46.0 ± 3.2 | 23.0 ± 2.4 | 63.2 ± 2.9 |
| 6.0 | 44.1 ± 5.8 | 39.7 ± 5.1 | 23.8 ± 3.4 | 71.2 ± 3.6 |
| 6.8 | 27.2 ± 6.5 | 29.0 ± 7.5 | 14.9 ± 5.1 | 41.1 ± 6.1 |
| 7.7 | 30.3 ± 4.8 | 22.0 ± 8.5 | 23.5 ± 5.1 | 38.2 ± 6.8 |
| 11.5 | 17.0 ± 1.8 | 8.9 ± 2.9 | 7.2 ± 1.6 | 10.7 ± 5.1 |
| 15.0 | 20.0 ± 1.9 | 4.2 ± 2.2 | 4.4 ± 1.5 | 7.0 ± 3.9 |

Table 6.7: De-reddened flux in mJy for the four sources with known or assumed extinction co-efficients.

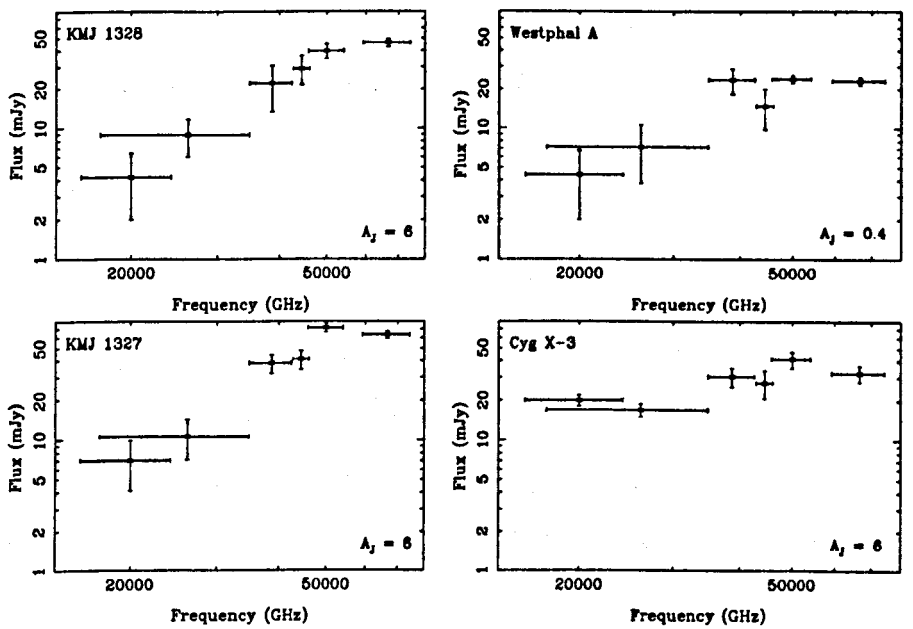


Figure 6.14: Spectra of the field stars in the *ISO* images with fluxes de-reddened by $A_J$'s shown in the figure. Star KMJ 1328 shows a smooth spectrum where as stars 'A', KMJ 1327 and Cyg X-3 all show emission features at 38,700 and 50,000 GHz (6.0 and 7.7 μm). An interesting feature of the spectrum of Cyg X-3 is the turn-up at 20,000 GHz which is unobserved in the other sources.

given in figure 6.14.

Star KMJ 1328 shows a smooth spectrum which turns over at the high

frequencies. Both stars 'A' and KMJ 1327 show features in the spectrum in the 38,700 and 50,000 GHz (6.0 and 7.7 μm) bands. It is unclear whether these are emission lines similar to Cyg X-3, or an absorption dip in the spectrum. Star 'A' is relatively cool ($T = 6,000$ K) and so absorption lines will be present in its spectrum, however such absorption features will have a narrow width and the drop in the spectrum over the wide *ISO* bands will be small. The flat spectrum for Cyg X-3 becomes very clear when compared to the other sources. An interesting feature in the spectrum of Cyg X-3 is the turn-up in the spectrum at 20,000 GHz.

These data for Cyg X-3 can be combined with photometry from UKIRT (Fender 1995) to create a composite infrared spectrum. This is shown in figure 6.15. It is very reassuring that the *ISO* data taken at a different epoch fits with the UKIRT data by a continuous, smooth spectrum. The gradual flattening in the spectrum shown in the UKIRT data is extended in the *ISO* part of the spectrum, and therefore is most likely to be from an extension of the wind emission. The interpretation of wind emission is discussed in section 6.4.

The infrared data presented in figure 6.15 can be combined with radio and sub-mm photometry presented in section 5.3.2. Figure 6.16 shows the complete spectrum with data in the radio at 2.3–15 GHz, sub-mm SCUBA at 150–353 GHz, *ISO* and UKIRT. This spectrum shows two completely different emission mechanisms. The low-frequency radio and sub-mm emission is due to synchrotron emission from the relativistic electrons in the jets. By the higher

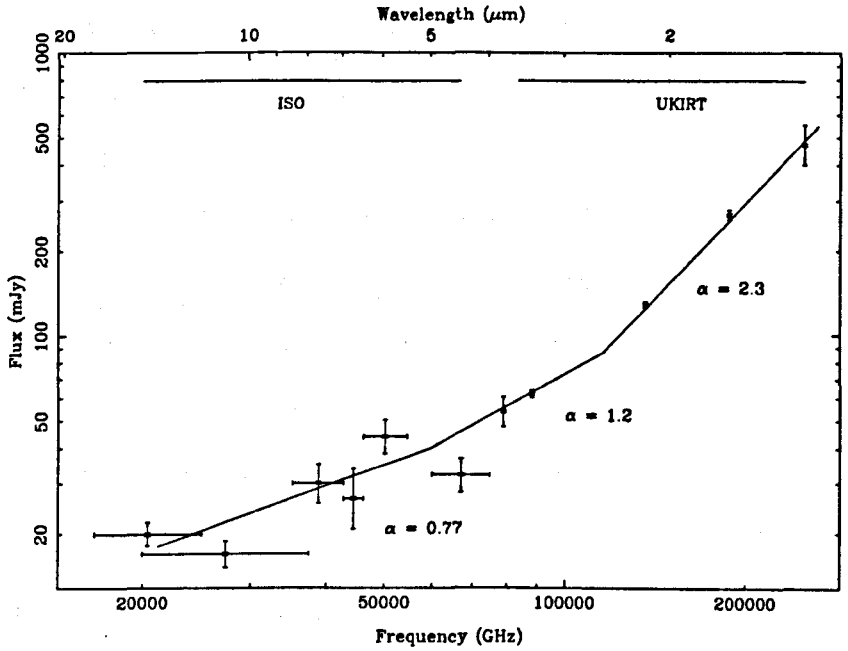


Figure 6.15: An infrared spectrum for Cyg X-3 with photometric data from *ISO* (this thesis) and UKIRT (Fender 1995). Both data sets have been de-reddened using an extinction co-efficient of $A_J = 6$. The data is clearly split into two sections, the UKIRT data with a steep spectrum, and the *ISO* data with an underlying flatter spectrum. Lines drawn represent best-fits to the data.

frequency infrared regime the relativistic electrons do not have enough energy to emit synchrotron radiation at 10,000 GHz and the most dominant emission comes from the thermal wind in the system.

## 6.4 WR emission in the IR

It has been established that the infrared emission from Cyg X-3 comes from the companion star. While not universally accepted, it is generally assumed that

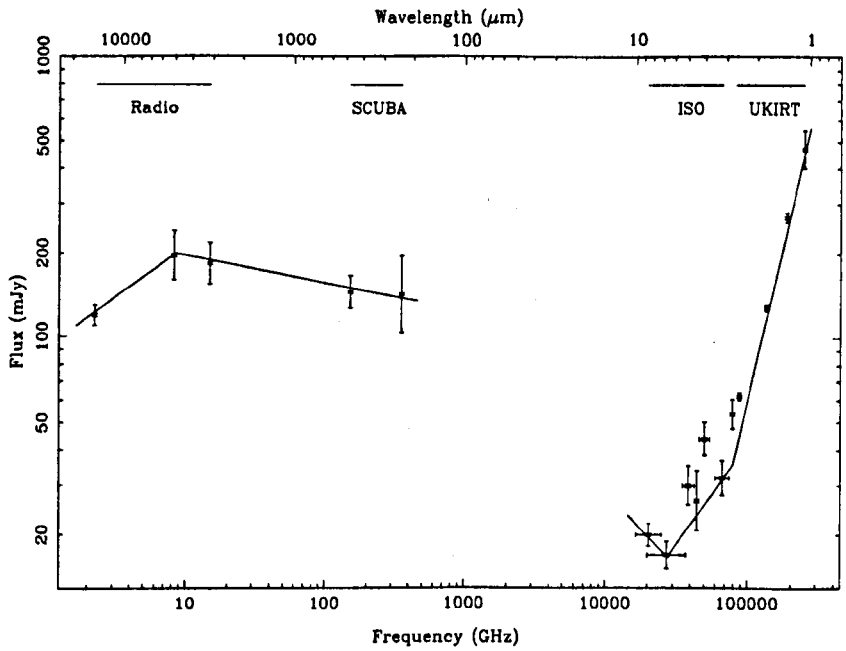


Figure 6.16: A composite spectrum presenting data from the radio and sub-mm (section 5.3.2) together with the infrared data presented in this section. Two different mechanisms are responsible for the observed emission.

the emission lines seen by van Kerkwijk et al. (1992) come from a Wolf-Rayet, WN7, class star. The assumed parameters for such a star are its mass which can range between 5 and 40 $M_\odot$ (Terasawa & Nakamura 1995; Schmutz et al. 1996), a partially or fully ionised stellar wind with a temperature between 10,000 and 50,000 K (van Kerkwijk et al. 1996; Waltman et al. 1996) being ejected at a velocity of 1,200–1,800 km $s^{-1}$ (van Kerkwijk et al. 1996; Cherepashchuk & Moffat 1994) which removes around $10^{-5}$ $M_\odot$ $yr^{-1}$ from the companion star. As one can see, the particulars of the Wolf-Rayet are not certain, although, a general picture can be used in any analysis.

The flux at the *ISO* wavelengths can be used as a tool for investigating the mass lost from the system. Wright & Barlow (1975; from hereafter WB) modelled the radio and infrared free-free emission from a star with mass-loss in the form of a wind. Their initial analysis which will be used here deals with a uniform wind at constant velocity. WB identified three cases: (a) at long infrared wavelengths (e.g. *ISO*) the flux of the source should vary as $S \propto \nu^{2/3}$ for a uniform wind. This is the case we shall be considering in the analysis; (b) at radio wavelengths the spectrum should be slightly shallower due to the long wavelength dependence of the Gaunt factor, which is approximated as 1 at infrared wavelengths. This changes the radio dependence to $S \propto \nu^{0.6}$; (c) at the shortest infrared wavelengths where one is observing deep into the wind, the constant velocity assumption for the wind is not valid as in this region the wind should be accelerating. The acceleration causes a steepening in the spectrum, which is observed in the UKIRT work by Fender (1995) and van Kerkwijk et al. (1996).

In the long wavelength *ISO* regime of Cyg X-3, we can use the infrared case, (a), above. The free-free flux of a wind at a given frequency can be expressed as

$$S = \frac{0.0232}{D_{\rm kpc}^2} \left( \frac{\dot{M}}{\mu v_\infty} \right)^{4/3} \left( \nu_{\rm GHz} \gamma_e g Z^2 \right)^{2/3} \ {\rm mJy} \qquad (6.8)$$

where $D$ is the distance to the source in kpc, $\dot{M}$ is the mass lost in $M_\odot$ yr$^{-1}$, $\mu$

is the mean atomic weight per nucleon, $v_\infty$ is the velocity of the wind at infinity, $\nu$ is the frequency in GHz, $\gamma_e$ is the number of free electrons per nucleon, $g$ is the Gaunt factor and $Z$ is the ionic charge (WB).

We can use our *ISO* observations to constrain wind parameters. However, in the above equation only the flux, distance, frequency and gaunt factor are constant and five variables remain unknown. We have to rely on previous observations or educated guesses to obtain realistic values. van Kerkwijk et al. (1996) observed Cyg X-3 using a high resolution spectrograph on UKIRT. Their observations were scheduled over a range of orbital phases and from this they were able to obtain a wind velocity of $v_\infty = 1,600 \pm 300$ km s$^{-1}$. We believe this is a reliable estimate for the wind in the system, and is consistent with a typical WN6/7 star's wind (Eenens & Williams 1994). To find a mass loss rate for the system, the other three variables which are unknown are $\mu$, $\gamma_e$ and $Z$ – which are all related to the wind's composition. One can test a range of ionised winds to obtain a range of mass loss rates.

Three scenarios can be tested. These include:

(a) A WN7-type wind. In this case a classical WR wind is used. The wind is partially ionised with values of $\mu = 1.5$, $\gamma_e = 1.0$, $Z = 1.0$. From the flux at 44,400 GHz the mass loss rate is $\dot{M}_1 = 7.3 \times 10^{-5}$ M$_\odot$ yr$^{-1}$.

(b) A partially ionised wind responsible for radio photospheres (see Waltman et al. 1996). This wind has the parameters of $\mu = 4$, $\gamma_e = 0.5$, $Z = 0.5$ and a mass loss rate of $\dot{M}_2 = 5.5 \times 10^{-4}$ M$_\odot$ yr$^{-1}$.

| Paper | $M_1$ | $M_2$ | $M_3$ |
|---|---|---|---|
| | $\times 10^{-5} M_\odot$ yr$^{-1}$ | | |
| Waltman *et al.* | 0.25 | 1.65 | 2.7 |
| This thesis | 7.3 | 55 | 6.8 |
| van Kerkwijk *et al.* | - | - | 12 |

Table 6.8: The mass loss rate for the Wolf-Rayet star given the various models discussed in the text.

(c) A fully ionised wind used in the infrared interpretation at UKIRT wavelengths (van Kerkwijk et al. 1996). This wind has the parameters of $\mu = 4$, $\gamma_e = 2$, $Z = 2$ and a mass loss rate of $\dot{M}_2 = 6.8 \times 10^{-5}$ M$_\odot$ yr$^{-1}$.

We have shown that for a single temperature non-accelerating wind with a variety of ionisation states, the free-free emission causing the infrared fluxes in the *ISO* wavelengths is due to a standard WR wind with a mass loss rate of (6.8–55) $\times 10^{-5}$ M$_\odot$ yr$^{-1}$. This figure is dependent on the particular type of wind.

This value for the mass loss rate is slightly higher than that predicted by Waltman et al. (1996) to be responsible for the delay between radio emission at a range of frequencies. However, it is slightly lower than is predicted by van Kerkwijk et al. (1996) for their interpretation of the short wavelength infrared fluxes. Given the amount of uncertainty in all these interpretations, we do not believe our analysis is seriously in error. Results from both papers, together with our analysis are given in table 6.8.

## 6.5 Conclusions

We have observed Cyg X-3 at long infrared wavelengths for the first time. The *ISO* observations have partially filled the gap between observations at short infrared wavelengths with UKIRT and other telescopes, and the very long wavelengths of sub-mm and radio observations. These observations are very important in determining the spectral characteristics of the system, and in particular investigating the Wolf-Rayet counterpart.

Observations in the radio and sub-mm regions show synchrotron emission from the jets in the source. It was known that the near infrared emission displayed a Wolf-Rayet-like spectrum with ionised He and N emission lines. It was known that the infrared spectrum was definitely not synchrotron (unlike GRS 1915+105) and so the gap between the two emission mechanisms is very important.

We have discovered that the slight flattening in the infrared spectrum at long wavelengths continues into the 5–15 μm wavelengths, and the spectrum is beginning to look more like a typical wind spectrum of Wright & Barlow. The spectrum displays emission features at 6.0 and 7.7 μm which are also displayed in two of the field stars. This has been tentatively interpreted as PAH emission.

Our spectrum forms the missing link between the radio and the infrared, and shows a slight turn-up at the longer wavelengths, in line with an expected rise in flux towards the sub-mm. Further investigations are required to determine whether this is the cross-over between the free-free emission of the wind and

the synchrotron emission of the jets. It will be very interesting to see what the results from the FIRST satellite show for this source.

The *ISO* data can be used to determine the mass-loss rate from the Wolf–Rayet, and using different models for the ionisation of the wind, we find the mass loss rate is around $10^{-4}$ $M_{\odot}$ $yr^{-1}$, in line with other WR winds.

# Chapter 7

# Conclusions and future work

"We have given this specimen a careful and detailed examination, and regret to inform you that we disagree with your theory that it represents 'conclusive proof of the presence of Early Man in Charlston County two million years ago'. Rather, it appears that what you have found is the head of a Barbie doll, of the variety that one of our staff, who has small children, believes to be the 'Malibu Barbie'. It is evident that you have given a great deal of thought to the analysis of this specimen, and you may be quite certain that those of us who are familiar with your prior work in the field were loath to come to [a] contradiction with your findings".

– Apparent letter from the Paleoanthropology Division, Smithsonian Institute. via e-mail

## 7.1 The scene

The work in this thesis investigates aspects of the radio-jet X-ray binaries, in particular Cygnus X-3. The astrophysics behind these objects is exceptional; the physics behind neutron stars and black holes is interesting enough, but even the relatively mild processes (in comparison!) behind distorting a companion, creating a disc and producing high energy radiation is of huge interest. This is taken a step further in radio-jet X-ray binaries when highly relativistic electrons, capable of emitting infrared synchrotron radiation, are accelerated from the system. This behaviour has captivated researchers for a number of years, but with the advent of long-term monitoring a lot of the subtle details which were missed before are being discovered.

Cygnus X-3 is no exception to the group of enigmatic sources. Since Giacconi et al. (1967) discovered it to be a bright X-ray source, radio and infrared measurements have shown the system to be highly unusual. The system appears to be a high-mass binary with a mass of 10 + 1.4 $M_{\odot}$, but the binary is far too small to behave as a typical high-mass system. There is apparently an accretion disc around the compact object to accelerate radio jets, but unlike the simple picture of SS 433 or GRS 1915+105, the wind from the companion star obscures the central system and the radio jets until they are far from the binary system. This has the consequence that radio monitoring is not a true representation of what is happening at the base of the jets, which confuses the picture of the system.

Both the infrared and the radio emission are highly variable. The radio emission is synchrotron in origin, and little was known about its properties, or in fact the environments of the jets which produce the radiation. The radio emission shows a number of distinct states including major and minor flare events, a general quiescence and also a quenching state. The flare events are thought to be due to jet production, but again the details are not well known.

Two of the microquasars show highly relativistic jets with velocites of 0.92 $c$, and the explanation of the superluminal motion in these sources is well understood. When the apparent relativistic motion in Cyg X-3 was reported, the situation was completely (some may say hopelessly) different. The motion was not in terms of a bipolar jet, but of ejection at superluminal velocities with an elliptical shape. What made this discovery highly unusual was the report of superluminal contraction from the source. This makes for a very strange system.

The final mystery I will report on is the composition of the binary. As mentioned above, a compact object is required for the emission of X-rays and relativistic electrons to form the jets. The second binary component is generally assumed to be a Wolf–Rayet WN7 which makes it a windy companion and highly active in the infrared. The infrared emission does not show a spectrum typical of the synchrotron emission as in the radio regime, but rather a modified black body, which is indicative of emission from a wind. The spectral change-over between these two emission mechanisms is of key importance in investigating

the physics of this source, but Sod's law will dictate this will lie in the region of the spectrum which is most difficult to observe.

This thesis investigated these problems.

## 7.2 The magnetic field

The radio jets emit synchrotron radiation. This is simple enough in itself, but the physics of the jets are relatively unknown unless a spectral break is found, which would indicate how the emission behaves. With the introduction of the SCUBA array on the JCMT, low-noise sub-mm photometry could be carried out for the first time. Our observations detailed in chapter 5 were the first photometric observations with the SCUBA instrument, and together with complementary radio and X-ray observations extended the synchrotron spectrum from 2 GHz to 350 GHz. The interpretation of the photometry which gave the most statistically significant result was that the spectrum was flat from 8 GHz to 350 GHz, with a slight turnover between the 2 GHz and 8 GHz data points.

The shape of the spectrum is due to optically thin synchrotron emission in the mid part of the spectrum, with a low-frequency self-absorption. Here we had discovered one spectral break in the spectrum, but unfortunately if one used this low-frequency break to calculate the physics in the jet we could only obtain a high upper-limit, partly due to the low angular resolution of our observations.

When the spectrum was extended to the high frequencies, this gave us an

idea of where another spectral break occured. Over time the higher energy electrons lose energy and a spectral break occurs. While we did not observe this break directly it must fall between the sub-mm and ISO waveband. Thus a lower limit to the age of the electrons, together with a lower limit to the frequency at which the spectral break occurs, gave us the lowest estimate to the magnetic field in the jet for Cyg X-3. This also allows some other physical parameters of the system to be investigated, namely energetics and luminosity – previously uninvestigated work.

## 7.3 The plasmons

The initial idea for the work presented in chapter 4 was to use MERLIN in order to map plasmons as they travelled from the core following a flare period. Together with the work on the magnetic field, and the high frequency radiation emitted by the jet, how plasmons move is of equal interest.

We showed that Cyg X-3 lives up to the name of a variable source, with a variety of flare activity over a minor flare period. The variability, which was vital in the investigation of the plasmons, prevented MERLIN obtaining a map of the source because it cannot work as a snapshot instrument. The images that were produced did not show any jet structure and the likely explanation of this was that the jets had faded from the time of ejection to the time of observation.

While no individual plasmon was imaged, the photometry provided by the

observations was very useful. We obtained fast radio photometry with a time resolution of a few minutes. From this we postulated that the increase in flux causing a flare would have to originate from a plasmon of a few light minutes in size, which in turn gave values for the brightness temperature of the flares.

The photometry revealed a large amount of structure in the radio emission, probably the most interesting was a complete minor flare over a number of hours, and also very short duration drops in flux. Given the current technology, collecting area and available bandwidth, we believe these are the best possible photometric observations of Cyg X-3.

## 7.4 The superluminal

The third, and most unusual, Galactic superluminal source to be discovered was Cyg X-3. Instead of following the usual observation of a bipolar jet at an angle close to the line of sight as in the quasars and microquasars, Cyg X-3 did not have a resolved jet, but showed an elliptical superluminal expansion effect together with superluminal contraction.

A number of models were investigated to explain this observation, and there are only three which are unrealistic enough to be discounted. The problems that the models had to overcome were expansion *and contraction* on both major and minor axes of an ellipse, for two consecutive flares. This obviously could not be explained by a bipolar jet model.

The most successful ideas were the introduction of either (a) a propagating pattern of re-radiated photons, or (b) an illumination of a shell of material. The pattern propagation theory used a central source which varied in brightness with photons being scattered into our line of sight at various distances depending on the intensity of the central source. As the central brightness altered, contraction was achieved as less photons reached the outer regions. This theory did not need any relativistic motion which is the possible downfall of the other theories. The second model uses a shell being illuminated by a jet, but the shell is moving at relativistic velocities and the combination of the two produce the superluminal expansion. Contraction is produced by either the shell running into some ambient medium and decelerating, or the spot emission dropping below our detector threshold as it moves out. Either scenario requires a fast moving shell of material. The final model is one in which a jet of radiation or particles illuminates a stationary shell - in a similar way to the models above - but the beam is offset to our line of sight which produces an elliptical shape. Here the superluminal expansion and contraction is produced by small changes in the opening angle of the jet producing the illuminating radiation. This model is the most satisfactory of all suggested as it does not require ideas which overreach the limits of physical reality.

Whichever model is closest to the true nature of the source, Cyg X-3 in this instance provided the astronomer with a puzzling observation, the solutions of which are not immediately obvious.

## 7.5 The masers

The application of quasar and active galactic nuclei models to the Galactic sources was the subject investigated in chapter 2 of this thesis. It has been known for a decade that some AGN emit maser radiation. Maser emission has proved to be an excellent tool for the investigation close in to the AGN nucleus. We undertook a comprehensive study of maser emission from the radio-jet X-ray binaries in both water and hydroxyl emission lines. Despite a hopeful false result from GRS 1915+105 none of our observations show maser emission.

Despite the disappointing result of no emission, the subsequent upper limits to any maser emission were used to put limits on the maser properties in these systems. Cyg X-3 was used as an example, mainly because the enviroment around this system is the best known of the X-ray binaries studied in detail.

We found that the conditions around Cyg X-3 are far too harsh for molecular creation and inversion. The consequence of a hot, dense Wolf–Rayet wind prevents water and grain growth until the molecules are so far out from the system that there is insufficient density of molecules for maser emission to be observed. These systems are just too hot and energetic for maser emission.

## 7.6 The wind

The enviroment of the secondary star is the subject of my last chapter, and one which on its own looks moderately impressive, but when put with other work

become a superlative result. The far infrared emission is one which has been ignored in earlier work, mainly due to an absence of available instrumentation.

If the secondary star is a Wolf–Rayet, as is generally believed, then it should show wind-like emission in the infrared. Previous observations with UKIRT have shown that this emission is best described by a modified black body of the sort which looks similar to, but not quite like, standard wind emission. Our observations used the long wavelength imaging capabilities of the *ISO* satellite. When the infrared data from *ISO* is included with the previous UKIRT photometry, the spectrum continues to fall towards longer wavelengths, but also shows a flattening at the long wavelengths which looks very similar to standard wind emission.

While this result is interesting in its own right, when the data are combined with the previous radio and sub-mm photometry then a link between the two emission mechanisms is made. As mentioned previously, the synchrotron emission appears to show a spectral break between the sub-mm emission at 350 GHz and the infrared emission at 10000 GHz. The last data point in the *ISO* spectrum shows a slight turn-up which could be due to the synchrotron emission from the jets becoming important. The complete spectrum covers a full 5 decades of frequencies and is the most satisfactory result in this thesis.

## 7.7 The future

When Cyg X-3 was discovered over 30 years ago it signalled the start of a baffling and exciting area of astronomy: the microquasars. I may be biased, but I believe Cyg X-3 is the most entertaining of this class of objects and will continuously give both the observational and the theoretical astronomer new surprises. In the long term I could never predict where the future lies for this object, but in the short term things are much easier. A number of observations need to be made of Cyg X-3 in particular, and the other microquasars in general, that will provide us with more information about these sources.

The nature of the jets in these sources is of great interest, and not much work has been done in investigating this. My observations using SCUBA have helped to provide an upper limit to the magnetic field in the jets, but until we can properly investigate the exact position of the spectral breaks in the synchrotron spectrum, our knowledge of the jets in these sources is far from complete. To do this we need to extend what is available observationally and this requires satellite observations; the ESA far IR and sub-mm telescope (FIRST) will help.

Monitoring at all wavelengths is extremely useful for these sources, but radio monitoring can be used as triggers for flare observations so with luck a couple of maps of the plasmons from the jets can be obtained. The variability of Cyg X-3 on the very short timescale requires a snapshot instrument to map the plasmons. Once the plamons have been imaged successfully, the magnetic field in the plasmons is of equal importance. This will allow the structure to be

investigated, and hopefully provide information about the jet creation.

Following down into the centre of the system, much work is being done close to the compact object with X-ray monitoring and infrared measurements, but unfortunately the identification of either components to the binary remains unknown. An enormous leap forward in our knowledge of Cyg X-3 will come when we know exactly what we are dealing with. At the moment the best estimate of object and mass is far too broad for detailed theories about what is happening in the system. It would have been invaluable to have observed spatially resolved maser spots from Cyg X-3, but perhaps that was far too much to ask.

In conclusion – the future is uncertain but exciting.

## 7.8 The acknowledgements


- The Green Bank Interferometer is a facility of the National Science Foundation operated by the NRAO in support of NASA High Energy Astrophysics programs.

- MERLIN in a national facility operated by the University of Manchester on behalf of PPARC.

- The James Cleark Maxwell Telescope is operated by The Observatories on behalf of the Particle Physics and Astronomy Research Council of the United Kingdom, the Netherlands Organisation for Scientific Research and the National Research Council of Canada.

- ISO is an ESA project with instruments funded by ESA Member States (especially the PI countries: France, Germany, the Netherlands and the United Kingdom) and with the participation of ISAS and NASA.

- The ISOCAM data presented in this thesis was analysed using 'CIA', a joint development by the ESA Astrophysics Division and the ISOCAM Consortium. The ISOCAM Consortium is led by the ISOCAM PI, C. Cesarsky, Direction des Sciences de la Matiure, C.E.A., France.

- The Australia Telescope is funded by the Commonwealth of Australia for operation as a National Facility managed by CSIRO.

# Appendix A

# Radio interferometry

## A.1 What is an interferometer

An interferometer is a collection of telescopes which allows the astronomer to measure smaller spatial resolutions without the necessity of building a single dish with an impracticably large diameter. The resolving power of a telescope follows the diameter of the dish, and the wavelength of radiation by the Raleigh criterion of

$$\theta = 1.22\frac{\lambda}{D} \tag{A.1}$$

where $\theta$ is the angular separation of two – just resolved – sources, $\lambda$ is the wavelength of radiation and $D$ is the diameter of the telescope. For the largest

steerable telescopes with a diameter $\simeq$ 75 m, observing at a wavelength of 21 cm, the resolving power is around 10 arcminutes.

Because radiation can be collected and focused from all parts of a single dish, this is a completely sampled aperture. The aim of an interferometer is to use separate dishes to sample a larger aperture as completely as possible, providing an effective area much larger than is physically possible. Radio interferometers provide angular scales from the arcsecond, through milliarcsecond to sub-milliarcsecond resolutions (e.g. VLA, MERLIN and VLBI/VSOP).

The aim of any astronomical telescope is to measure the sky brightness distribution of sources, and while optical and infrared telescopes have developed CCD arrays from which an image can be easily obtained, radio interferometers employ a slightly different technique than direct imaging. This can be demonstrated by analysing a two-element interferometer.

Each receiver outputs a voltage from a time-varying electromagnetic wave;

$$\begin{aligned} O_{\mathrm{i}} &= A_{\mathrm{i}} e^{\mathrm{i}(\nu t - \phi_{\mathrm{i}})} \\ O_{\mathrm{j}} &= A_{\mathrm{j}} e^{\mathrm{i}(\nu t - \phi_{\mathrm{j}})}, \end{aligned} \tag{A.2}$$

where $O$ is the voltage detected by receiver i and j, with an amplitude $A$, at a frequency $\nu$ and phase $\phi$. Because the EM radiation is from the same source, the phase measured by receiver j is the same as the phase measured by receiver i, but with an additional component due to a time delay from the geometric difference

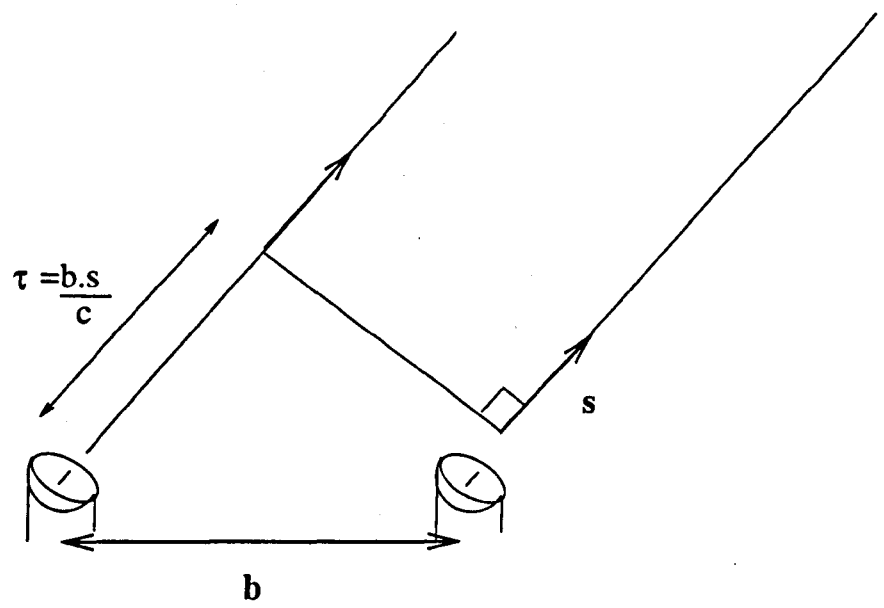


Figure A.1: A two element interferometer with a baseline $\boldsymbol{b}$ detecting radiation from a source with wavefronts along a unit vector $\boldsymbol{s}$. Between the two receivers, there is a time delay $\tau$ due to the geometry of the baseline and source vectors.

between the two receivers. This is shown in figure A.1.

The phase measured by receiver j is $\phi_j = \phi_i + \phi_\tau$. This is the same as receiver i, but delayed by $\phi_\tau = \nu\tau = \nu\boldsymbol{b}\cdot\boldsymbol{s}/c$. The correlation of these voltages produces a fringe effect with a response $R = A_i A_j e^{i\phi_\tau}$; this complex response is best described by sine and cosines representing an amplitude and phase. The projected baseline changes as the source moves across the sky, so the response of the telescope varies with zenith angle as $R = A_i A_j \cos\left(2\pi\nu b \sin(\theta)/\lambda\right)$. A more convenient unit for the baseline is the number of wavelengths, $b_\lambda = b/\lambda$, which sets up a condition with the two telescopes creating a fringe pattern on the sky

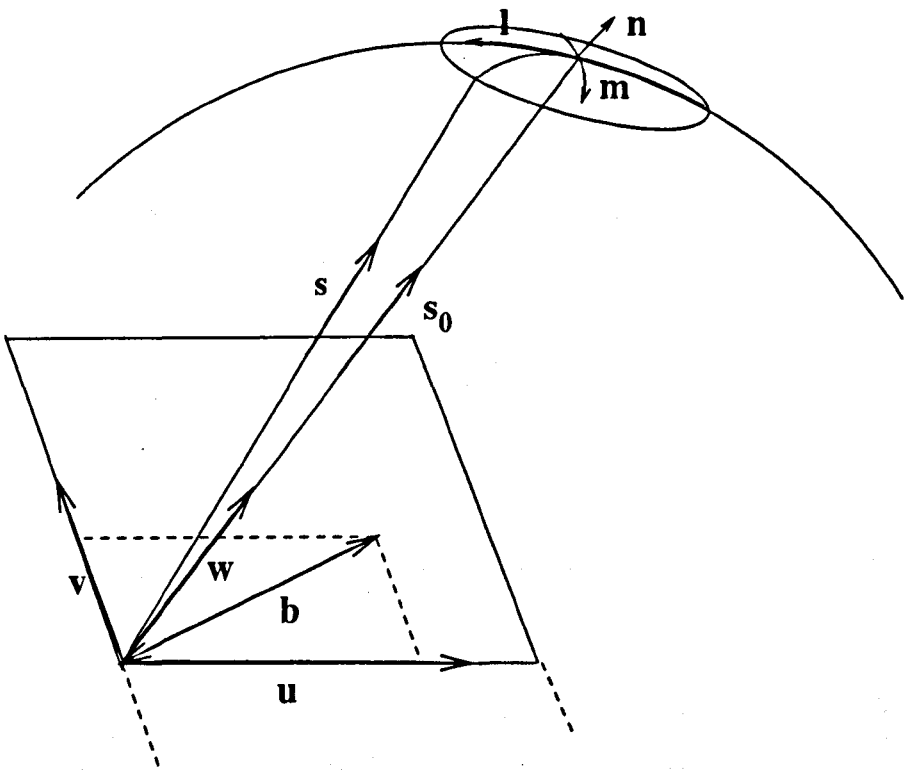


Figure A.2: The relationship between sky co-ordinates $l$, $m$, $n$ and baseline projected co-ordinates $u$, $v$ and $w$.

with fringe spacing $\sim 1/b_\lambda$, and a correlator output of $R = A_i A_j e^{i(2\pi b_\lambda \cdot s)}$.

When one considers an extended source, centred on the geometrical, or phase centre, one can set up a co-ordinate system as shown in figure A.2. The unit vector towards the phase-centre is $s_0$, the vector to the region of interest is $s$, and one can describe a co-ordinate system with $l$, $m$ and $n$ being co-ordinates centred on the phase-centre, $l$ - north, $m$ - east and $n$ in the direction of $s_0$. The baseline $b$ is then projected on a plane with co-ordinates $u$, $v$, $w$, with

$w$ co-incident with $s_0$. This then becomes the widely used $uv$ plane, and the correlator response, or *complex visibility* then becomes

$$V = \iint I(l,m) e^{i\left(2\pi(ul+vm+wn)\right)} \, d^2\Omega \tag{A.3}$$

with $u$, $v$, $w$, $l$, $m$ and $n$ all measured in wavelengths, $I(l,m)$ is the intensity of radiation, and $\Omega$ is the solid angle of the source. One can usually approximate to small angles from the phase-centre, and in this small angle approximation, $w = 0$, and the co-ordinates $x$ and $y$ replace the directional cosines $l$ and $m$. In this approximation, the visibility function now becomes

$$V(u,v) = \iint I(x,y) e^{i\left(2\pi(ux+vy)\right)} \, dx \, dy \tag{A.4}$$

and it can be easily seen that the correlator response is the Fourier transform of the sky brightness, with the full intensity recovered by a complete sampling of the $uv$ plane.

For a single baseline, one value of this complex visibility is measured. With more than one baseline, more points on the $uv$ plane can be sampled; figure A.3 shows the instantaneous coverage with the VLA. Each point on the $uv$ plane is a single visibility from a baseline and the $uv$ plane is symmetrical about the $u$ axis[1]. Coverage of the $uv$ plane could be obtained by making measurements by

[1]The VLA consists of 27 telescopes giving $N(N-1)/2$ baselines. The $uv$ plane coverage is symmetrical about the $u$ axis because baseline $b$ is equivalent to $-b$.

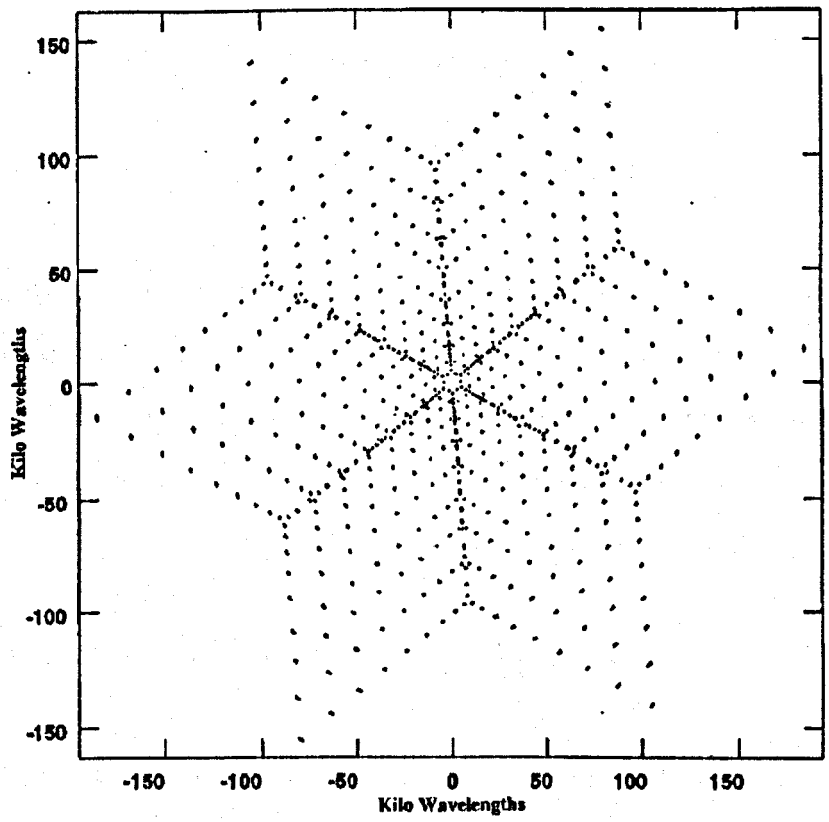


Figure A.3: *uv* instantaneous coverage with the VLA for an object at the zenith. Each point represents measurement by a single baseline.

moving telescopes to form different baselines, but the more usual technique is to allow the Earth's rotation to alter the projection of the baseline as the source rises and sets. This can be shown by the transformation matrix between sky

co-ordinates $(lmn)$ and interferometric co-ordinates $(uvw)$:

$$\begin{pmatrix} u \\ v \\ w \end{pmatrix} = \begin{pmatrix} \sin H_0 & \cos H_0 & 0 \\ -\sin\delta_0 \cos H_0 & \sin\delta_0 \sin H_0 & \cos\delta_0 \\ \cos\delta_0 \cos H_0 & -\cos\delta_0 \sin H_0 & \sin H_0 \end{pmatrix} \begin{pmatrix} l \\ m \\ n \end{pmatrix} \tag{A.5}$$

where $H_0$ is the hour angle, and $\delta_0$ is the declination of the phase-centre. As the hour angle of the source changes, the projected baselines trace out an ellipse on the $uv$ plane. The major, $a$, and minor, $b$, axes of the ellipse are

$$\begin{aligned} a &= b_\lambda \cos d \\ b &= b_\lambda \cos d \sin\delta_0 \end{aligned} \tag{A.6}$$

with a centre at $(u, v) = (0, c)$ where $c$ is given by

$$c = b_\lambda \sin d \cos\delta_0 \tag{A.7}$$

where $d$ is the declination of the baseline.

It is the aim of aperture synthesis to sample the $uv$ plane to a sufficient level to reconstruct the sky brightness distribution. For normal interferometric observations the reconstruction is not straightforward, which is mainly due to both the incompleteness in the $uv$ plane, and gridding the data so computations can be carried out. The direct transform of the visibilities, $V(u, v)$, multiplied by a sampling function, $\mathcal{S}(u, v)$ reproduces a modified image, known as the *dirty*

*map*, $\mathcal{D}(x,y)$. The sampling function can be inverted to form what is commonly known as a *dirty beam*, $\mathcal{B}(x,y)$, and the true dirty map is the convolution of the sky image with the dirty beam. This can be expressed as

$$\begin{aligned} \mathcal{S} &\Longleftrightarrow \mathcal{B} \\ V \times \mathcal{S} &\Longleftrightarrow \mathcal{D} \\ V \times \mathcal{S} &\Longleftrightarrow I \otimes \mathcal{B}. \end{aligned} \tag{A.8}$$

The sampling function, $\mathcal{S}$, arises from gaps in the $uv$ plane together with a tapering function to reduce aliasing, and a gridding function which places the data on an $n \times n$ grid. Non-linear techniques, like the CLEAN algorithm, are used to recover the sky image from the dirty map.

### A.1.1 MERLIN

The MERLIN (Multi-Element Radio-Linked Interferometer Network) system consists of 6 telescopes distributed over the north and central England, connected by microwave link. This creates a unique instrument with a maximum baseline of 215 km giving a resolution between that of the VLA and VLBI systems, together with an instantaneous correlation between telescopes[2]. While the work in this section is applicable in general to all radio interferometers, some particular sections which give examples of calibration are specific to the

[2]The VLBI system requires amplitude and phase of each telescope to be recored on magnetic tape, and then correlated at a later date

MERLIN system.

## A.2 Calibration

The amplitudes and phases measured by a receiver need some level of calibration to be usable in making a radio map. The flux needs to be calibrated so the amplitudes are equal to a flux standard. The atmospheric corrections to the phase need to be calculated, and to a small extent, the gains of the telescope need to be corrected in both time and elevation. It is the general job of calibration to correct for all the effects above, so any amplitude and phase changes are due to the interferometer response to the source, and not due to anything else.

### A.2.1 Reason for calibration

The true complex visibility, $V$, is corrupted by instrumental and atmospheric effects to create a modified visibility, $V'$. A complex gain for each telescope at a given baseline can be altered to recreate the true visibility. If a visibility $V'_{ij}$ is measured from a baseline $b_{ij}$, there is a contribution from the complex gains, $G_{ij}$, noise, $n_{ij}$, and a baseline dependent complex offset, $e_{ij}$. This is expressed as

$$V'_{ij} = G_{ij}V_{ij} + n_{ij} + e_{ij}, \tag{A.9}$$

which can be expressed as measured amplitudes and phases:

$$V'_{ij} = A'_{ij} e^{i\phi'_{ij}}. \tag{A.10}$$

Noise ($n_{ij}$) is assumed to be constant, and the baseline offset from MERLIN observations is small and only affects data at frequencies below 2GHz. Writing the gains for individual baselines gives

$$G_{ij} = g_i g_j^*, \tag{A.11}$$

and the gains for a particular telescope can be expressed as an amplitude and phase error so

$$g_i = \mathcal{A}_i e^{i\varphi_i}. \tag{A.12}$$

So the measured visibility amplitude and phase is a sum of all these corrections:

$$A'_{ij} e^{i\phi'_{ij}} = A_{ij} \mathcal{A}_i \mathcal{A}_j e^{i(\phi_{ij} + \varphi_i - \varphi_j)}. \tag{A.13}$$

The formation of *closure amplitudes* and *closure phases* cancels out the errors $\mathcal{A}$ and $\varphi$. A closure phase if formed by the summation of raw phases on three

independent baselines,

$$\begin{aligned}\phi'_{ij} + \phi'_{jk} + \phi'_{ki} &= (\phi_{ij} + \varphi_i - \varphi_j) + (\phi_{jk} + \varphi_j - \varphi_k) + (\phi_{ki} + \varphi_k - \varphi_i) \\ &= \phi_{ij} + \phi_{jk} + \phi_{ki}, \end{aligned} \tag{A.14}$$

and closure amplitude is formed by the product on four independent baselines,

$$\begin{aligned}\frac{A'_{ij}A'_{kl}}{A'_{ik}A'_{jl}} &= \frac{A_{ij}\mathcal{A}_i\mathcal{A}_jA_{kl}\mathcal{A}_k\mathcal{A}_l}{A_{ik}\mathcal{A}_i\mathcal{A}_kA_{jl}\mathcal{A}_j\mathcal{A}_l} \\ &= \frac{A_{ij}A_{kl}}{A_{ik}A_{jl}}. \end{aligned} \tag{A.15}$$

### A.2.2 Flux calibration

For a point source at the phase centre, the closure phases should be zero (with scatter from noise), and the closure amplitude should be equal to unity, so observing a known flux point source can recover the phase and amplitude errors on all baselines. In practice this is complicated by the point sources being variable, and the constant flux sources being resolved on the longer baselines. The calibration can proceed if one either knows the brightness distribution of the resolved source, or observes a 'boot-strapping' source together with a variable flux point source. The 'boot-strapping' source has a known flux, but is usually only a point source on the shortest baselines, so one can use that to calculate the flux thus:

- as the resolved source is a point-source on the shortest baseline, the measured amplitude on the shortest baseline, $A'_{(12),r}$, is an estimate of the source flux. This gives a flux to scale the point-source by, $S'_{(12),r}$.

- the flux of the point-source is variable, but the measured amplitude on the shortest baseline of the point-source can be compared to the resolved source, giving a flux estimation for the rest of the baselines.

$$S'_{(12),p} = S'_{(12),r} \frac{A'_{(12),p}}{A'_{(12),r}}.$$

- as the point-source is unresolved on all baselines, $S'_{(12),p}$ can be used as the source flux on all baselines.

- the true source flux can be calculated by solving for the closure amplitudes.

- any other calibrators (phase, polarisation) can use this calibrated flux to estimate their flux, under the calibration procedure.

The amplitude scale is therefore initially calibrated to a known flux.

### A.2.3 Phase calibration

Any source structure offset from the phase-centre will produce a non-zero closure phase. The phase is very important in re-creating the original brightness distribution. However, changes in the atmospheric opacity will rotate the phase recorded by a single telescope, and noise will contribute to phase changes also.

If the source is sufficiently strong, so that phase-changes due to source structure are larger than the phase-changes due to noise and atmospheric contamination, then the reconstruction of the phase after atmospheric contamination can be performed by self-calibration. This is done by minimising the telescope gains between the measured visibility and a model visibility. If the calibration is for phase only, then a function $S(\Phi)$ needs to be minimised for $\varphi_1 \ldots \varphi_n$ where

$$S(\Phi) = \left( \sum_{1 \le i < j \le n} w_{ij} \left| V'_{ij} - e^{i(\varphi_i - \varphi_j)} V^{\mathrm{m}}_{ij} \right|^p \right)^{1/p}, \qquad \text{(A.16)}$$

$V'$ is the measured visibility, $V^{\mathrm{m}}$ is a model visibility, $w$ is a weighting function, and $p$ is a parameter where $p = 1$ for a weighted sum, and $p = 2$ for a least-squares solution. This minimisation can be performed because there are only $N$ solutions to the phase that need to be found, where there are $N(N-1)/2$ observations. There is a factor of $(N-1)/2$ redundancy in the solutions.

To self-calibrate the phase, a model of either (a) a point source, (b) a map of from a previous observation or (c) a map created by inverting the original data is used. It is usual to use either a) or c) in the self-calibration process. With this set of model visibilities, the phases $\varphi$ can be altered to minimise $S(\Phi)$. When self-calibrating the phases, the telescope gains, $g$, are solved for, but the amplitude gains are fixed at unity, and just the phase component is varied. With these modified gains, a second round set of visibilities can be used as the input visibilities and the calibration cycle is repeated. This process can

be repeated as many times as necessary until the observed visibilities closely match the source visibilities, or as close as can be determined.

The process of phase self-calibration is summarised as:

1 Choose a model for the source, either:

   - a point source,
   - a previous map of the source, or
   - an inverted map from the observed visibilities,

2 Minimise the function $S(\Phi)$ by comparing the model and observed visibilities and modifying the phase-gains $\varphi$.

3 Form a new set of visibilities: $\overline{V} \Leftarrow V'$ by applying the gains $\varphi$ to the visibility set $V'$.

4 Minimise the function $S(\Phi)$ by comparing the new visibilities $\overline{V}$ to the model visibility set $V^{\mathrm{m}}$, and form a new visibility set $\overline{\overline{V}}$.

5 Repeat steps 3 and 4 until satisfied. The modified visibility set will be as close to the true visibility set as possible, based on the input model.

If the target source of interest is weak, any source structure evident in non-zero closure phase would be indistinguishable from noise. In this case, the observations need to include short observations of a point-source phase calibrator, which is close to the target source in both space and time, to minimise the errors from a spatial distribution of phase-errors, and also the slowly-varying

temporal phase-errors. With an external phase-calibrator, phase-gain solutions can be found by self-calibration, and these gain solutions are directly applicable to the target source, as the errors originate from the same patch of atmosphere which is responsible for the corruption. The gains can then be applied to the target visibility set, and any true source structure will be evident after sufficient integration[3].

The phase-calibrator is usually a variable source and so amplitude calibration using a known non-variable point source is done. The flux-calibrator needs to be unresolved on the shortest baselines otherwise some flux is not measured and an accurate calibration is missed. The flux-calibrator cannot be used as a phase-calibrator for the following reasons: sometimes it is resolved on the longest baselines and therefore the point-source approximation for some baselines fails; and because it is generally too far from the target to have the same atmospheric transfer function as the target.

Calibration of the phase-calibrator is the most important part of interferometric mapping. The image quality, based on the dynamic range[4] of the map, is not only dependent on the density and coverage of the $uv$ plane, but also on the phase fluctuations in the source. To first order, the dynamic range $D$ can

[3]Solution intervals to calculate the gain solutions have to be shorter than the period over which the phase varies by $\pi/2$. If the phase-calibrator is too weak, then the phase-change over this integration time would be less than the noise in the data. For a weak target, a map created to show the source structure will have a longer integration time than the solution interval for the phase-gains, so after phase-calibration the phase will look random, but will have source structure over a long integration time.

[4]Dynamic range is measured as the peak flux divided by the RMS noise in an image. A dynamic range of 1000 is good for MERLIN without any self-calibration of a phase-reference/target source observation.

be calculated from the phase errors, $e_\phi$, over a time scale, $t_\phi$, for an observation with $N$ telescopes over a total time $T$ by

$$D \sim \left(\frac{N^2 T}{e_\phi^2 t_\phi}\right)^{1/2} \tag{A.17}$$

(Thomasson et al. 1994). For example phase errors of 15° on a time scale of 5 minutes in a 12 hour observation would give rise to a map with a dynamic range of 300.

The most involved part of the calibration process is application of the different telescope gains at various stages. This is done by the storage and application of calibration and solution tables. The next section details a typical application of these tables to a simple interferometer observing a continuum source.

### A.2.4 Practical calibration – continuum observations

Most radio interferometer data is analysed by the Astronomical Image Processing System, or AIPS package. Over many years this has evolved into a comprehensive suite of calibration and analysis packages, applicable to both single dish, interferometric, continuum or spectral line data. It is also useful in calibrating VLBI data, and the new VSOP programme, which includes a complex time-variable baseline from the HALCA satellite. While other radio packages exist (for example; OLAF, MIRAID), this section will detail the AIPS processes, as this is the most wildly used set of programmes.

Central to the AIPS processes are data tables. These store time or frequency variable data which are applied to the observed visibilities. Many tables exist, but for the calibration process there are three main ones: SU – a source flux table which provides a zero-spacing flux estimate for each source, CL – a calibration table which contains a time series of antenna gains, and SN – solution table which contain corrections to the complex gains at a particular calibration cycle. The tables are referenced by a number, with higher numbers produced by the later calibration cycles.

Together with calibration tables, data from connected sources are usually combined into a multi-source file, with data arranged in time-baseline order irrespective of source (sources are still referenced, but data is contiguous). The consequence of this is that calibration from one source (say the phase-calibrator) can be applied to the target source, by interpolating the solutions in time. This makes a multi-source observation easily calibrated. A typical observation would consist of four sources, described in time order by figure A.4. Because the phase-calibration needs to include time variable solutions, there are three time-scales which are important: $t_\phi$, the time observing the phase-calibrator, $t_t$, the time observing the target, and $t_c$ the time between successive observations of the phase-calibrator (or target). For MERLIN observations the typical timescales are $t_\phi = 2.5$ min, $t_t = 7.5$ min and $t_c = 10$ min.

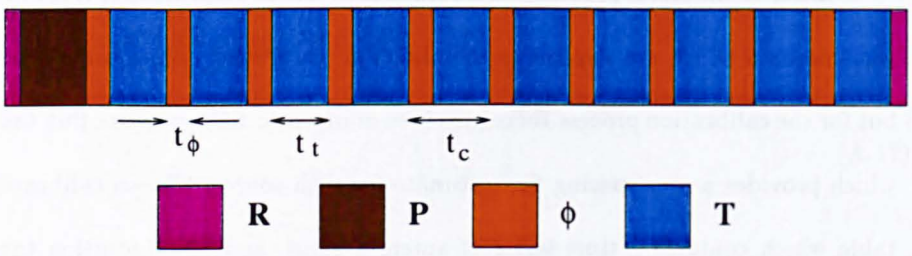


Figure A.4: A typical observing programme in time order. The programme consists of a resolved flux calibrator: **R**, an unresolved point source flux calibrator: **P**, a phase calibrator: $\phi$, and the target source: **T**. Observations can also include a polarisation calibrator observed at a similar time to the flux calibrators.

**Initial flux calibration**

From first-order flux calibration of the point-source flux calibrator (**P**, hereafter called the flux-calibrator), and from the resolved flux calibrator (**R**), the zero-spacing flux estimate is input as a model into the SU or source table.

The antenna gains for both amplitude and phase are solved for the flux-calibrator based on a point source of given flux at the phase centre. In effect, the ratio of the amplitudes for all sources are compared, and the gains for all telescopes for each source are used as an initial zero-space flux estimate for all sources. This is similar to comparing the resolved and unresolved flux calibrators in the initial calibration step. All sources then have their zero-spacing flux recored in the SU tables, and from that, the phase calibration can commence.

**Phase calibration – phase-target setup**

To calibrate phases, it is usual to observe a separate phase-calibrator, and use the solutions obtained from that source, interpolating them to the target source. Because the phase-calibrator and the target are close together in the sky, any atmospheric calibration will be common to both sources, and calibration can commence.

Initial calibration of the zero-spacing fluxes of both sources will have been carried out in the flux calibration stage, and so phase calibration can continue. It is usual to observe a point source as the phase-calibrator, so closure phases will be zero (as long as the phase-calibrator is at the phase centre). Any observations of an extended phase-calibrator will only usually occur if the maximum baseline is long. In practice this only happens with a small number of MERLIN calibrators, and those observed with VLBI interferometers. If an extended source is observed, one can use a map of the source as a model for the visibilities, and the phases can still be recovered. With either a point source, or an extended source, an initial point source is used as the model – for the first round of calibration.

All calibration starts with an unmodified visibility set, or CL (calibration table) with all phase and amplitude corrections set to 0 and 1 respectively. This table is CL(1), and any calibration can be reset by applying CL(1) to the visibility set. To calculate the first round of calibration, from the point-source model, the visibilities are compared to the model over a time interval $t$. To

obtain a good model of the atmosphere, if the calibrator is bright enough, a solution interval over the integration time $\tau_{\rm int}$ is used. This creates a set of closure phase corrections which are stored in the solution table SN(1) with a model of the short-timescale variations of the atmosphere.

With an initial set of corrections, corresponding to corrections on a small time-scale, the initial solution table data set is smoothed and interpolated to create a new calibration table, CL(2) The smoothing interval is taken to be the cycle time between phase calibration and target observations, $\tau_{\rm c}$.

Figure A.5 shows: the raw, un-calibrated amplitudes; the solution tables for a point source model; and the modified visibility set from the application of these solutions. The modified visibility set is achieved by interpolating the SN(1) table in time across the data to create a CL(2) table.

With the calibration applied to the visibilities a second (and even a further third) cycle of calibration can be applied to the phase calibrator, in order to improve the calibration. When determining closure solutions for the second calibration cycle, a calibration switch is set true and the CL(2) table is applied to the visibilities before solutions are found. This ensures that solutions found are taken from the corrected visibilities. The solution interval used here should be the time at which the phase changes by $\pi/2$. Instead of the previous phase corrections of up to $\pm 180°$, the new solution table SN(2) consists of corrections of around a few degrees to the zero phase solution of a point source. Also, these solutions are usually obtained by averaging the data over a longer time

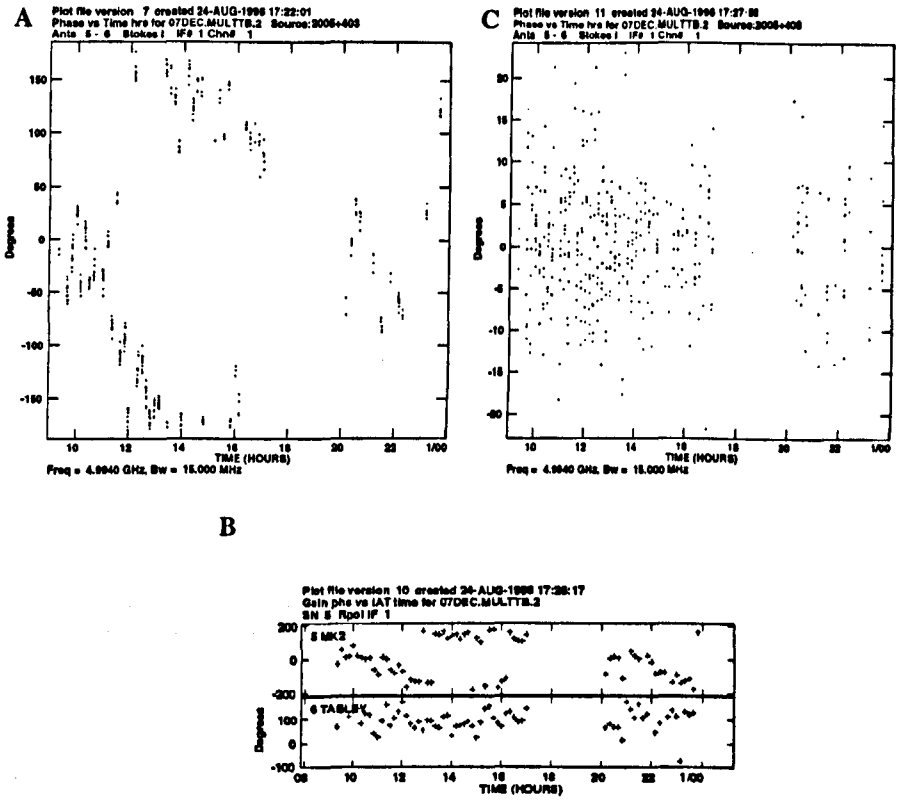


Figure A.5: (A) is the raw, un-calibrated data shown for the phase-calibrator on the shortest baseline. (B) is the solutions to a point source at the phase centre as phase corrections to the two telescopes making the shortest baseline ($\varphi_i$ and $\varphi_j$). (C) is the modified visibility phases after this calibration.

interval than previous calibration, as the phase changes are not as severe and a small solution interval may include noise into the solutions as well as confusing genuine source structure, if the model is not a point source. As before, the solution table is interpolated in time between phase and target observations to provide a calibration table CL(3), which consists of small order corrections to both the phase calibrator and the target sources. Examples of this round of

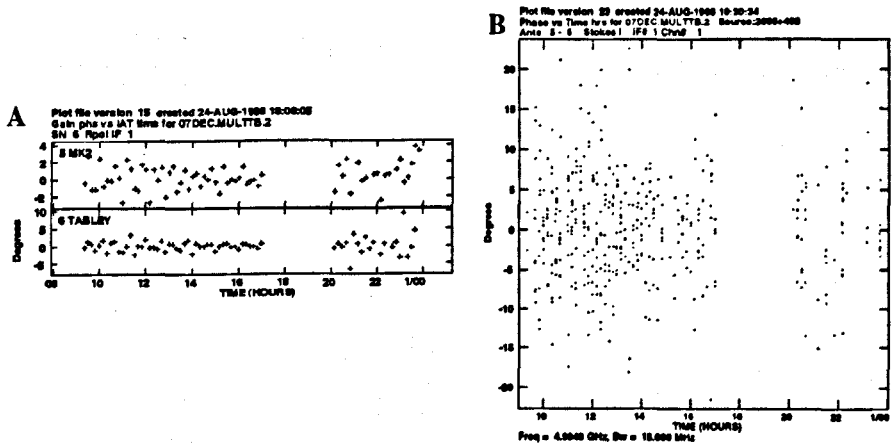


Figure A.6: (A) Solution tables for the telescopes making up the shortest baseline for a second round of calibration, after the CL table has been applied from the first calibration cycle described in figure A.5. (B) The modified phases for the shortest baseline after both rounds of calibration have been applied. There is little change in the calibrated phases implying we are at the noise limit of calibration. An improvement can be made by lengthening the averaging time over the calibration process.

calibration are shown in figure A.6 in the frames (A) and (B).

After this second round of calibration the phase calibrator's observed visibilities are close to the true visibilities. Since the interpolation step of the SN tables to the CL tables corrected both the phase-calibrator and target's visibilities, by interpolating in time between the two observations both the phase-calibrator and target sources can be mapped. If the phase-calibrator showed any structure at this stage it is wise to delete the second calibration and use the inverted map as a model for the source, rather than a point source. The second stage of calibration can be continued as long as necessary until any calibration was including noise in the solutions and phases did not improve.

| Calibration cycle | Phase error [degrees] | Dynamic range |
|---|---|---|
| 0 | 180 | 10 |
| 1 | 5 | 375 |
| 2 | 2 | 940 |

Table A.1: Dynamical range against calibration cycle with observations made with 8 telescopes, a time scale for the phase error of 4 minutes and a total integration time of 67 minutes.

The quality of maps can be calculated as an indication of the quality of calibration. Inversely, the quality of calibration as measured by phase errors in the data determines the dynamical range of the map, as described by equation A.17. If one uses as an example a noisy data set with observations by 8 telescopes, an integration time of 67 minutes, then the phase error is the typical phase change in an integration time of 4 minutes and for each round of calibration the phase errors and dynamic range of a map is given in table A.1. Cycle 0 is pre-calibration and subsequent calibration is shown. One can see that calibrating out the phase errors dramatically increases the quality of images that can be produced.

### Phase calibration – self-calibration

If the source is strong enough to self-calibrate then the process of phase-calibration is similar to that presented above. The only difference is that solution tables are not interpolated between phase-calibrator and target, and the shortest baselines are progressively tapered in to the calibration process.

The practical application of phase calibration depends on whether the target source is strong enough that self-calibration can be performed, or whether a separate phase-calibrator is required.

### A.2.5 Practical calibration – spectral-line observations

#### Bandpass calibration

Spectral-line observations require that the full bandwidth is split into a large number of spectral channels. Bandpass calibration corrects amplitude differences in the channels of the pass-band in spectral-line datasets. A bright point source with a flat spectrum is generally used for this calibration.

The bandpass is calibrated by observing the flux calibrator and recording the spectral change over the pass-band. This results in a scaled bandpass with the response of individual channels recorded over the entire bandwidth. To use this as a template for the other sources, the bandpass is divided by the average flux taken from the inner 75% of the bandpass. This normalises the bandpass for further use.

#### Phase-calibration of weak calibrators

When making spectral line observations, the calibrators need to be strong enough that they are detected with the smaller bandwidth used. The noise

in the observations increases as

$$\sqrt{\frac{\Delta\nu_c}{\Delta\nu_s}} \tag{A.18}$$

where $\Delta\nu_c$ is the bandwidth in continuum mode, and $\Delta\nu_s$ is the bandwidth in spectral line mode – usually the channel width. So for a continuum observation at 16 MHz, and a spectral line observation with 4 MHz spread over 1024 channels, the noise increases by a factor of 64. If the calibrators are fairly weak (as is usual with phase calibrators, especially at 22 GHz), then a dual configuration is needed, with the phase calibrator being observed in continuum mode, the target being observed in spectral-line mode, and the flux-calibrator being observed in both modes. The flux calibrator is used to align any phase-offsets which are due to instrumental effects between the two correlator configurations.

The matching of phases between the two modes is carried out as in the following example. The phase on one telescope is measured to be 128 degrees in the spectral-line mode ($\phi_s = 128$), and the phase is 32 degrees for measurements in the continuum mode ($\phi_c = 32$). Calibration of the spectral-data is performed and a solution table SN(S1) is created. This consists of phase solutions of $\Delta\phi = -128$. This solution table is copied to the continuum data set to make SN(C1), and this is then interpolated and smoothed with a long solution interval to create CL(C2). The continuum data has an offset of $32 - 128 = -96$ degrees to that of the spectral-line data. This is shown in figure A.7 which shows the

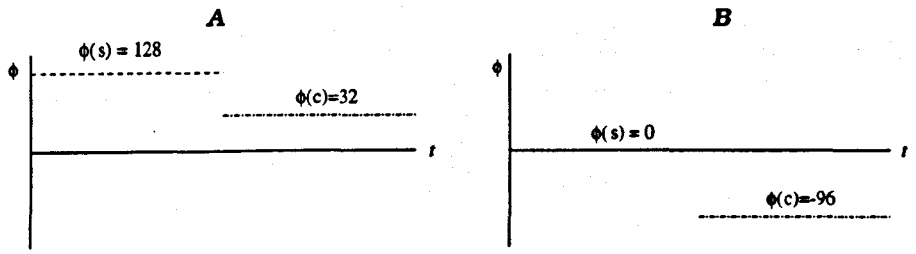


Figure A.7: (A) Phases of the initial visibility set for the flux calibrator in spectral-line mode and continuum mode. The phase in spectral-line mode is 128° and in continuum is 32°. (B) phases after the calibration of the spectral line data set. Here there is a shift of −128°, and the continuum data is offset from zero by −96°.

initial and new visibilities.

The calibration of the continuum visibilities requires a shift of +96 degrees so the calibration of the phases using the continuum phase-calibrator can be applied correctly to the spectral line data set. This offset of +96 degrees represents a shift in phase from configurations between the spectral-line data and the continuum data.

Figure A.8 shows the phases in time from a telescope, with an overall drift due to atmospheric contamination. The continuum observations of the phase-calibrator need to be shifted to align them with the phases from the target. The first frame (A) of figure A.8 shows the un-corrected data, and the second frame (B) shows the corrected data and from this stage, normal phase-calibration can be carried out, as the phases between the target and phase-calibrator can be interpolated properly.

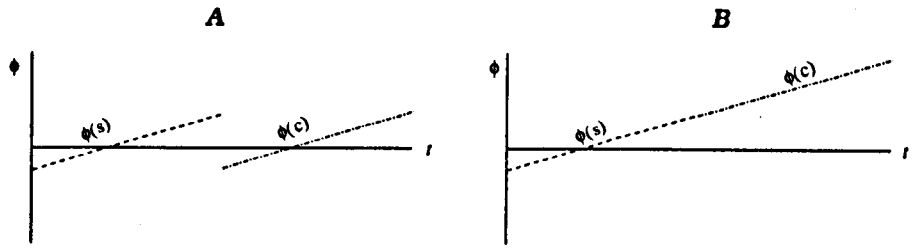


Figure A.8: (A) A phase-time plot of the observations showing the continuum observations of the phase-calibrator and the spectral-line observations of the target. The phase-calibrator phases need to be shifted by the same amount as is measured by the flux-calibrator observations. (B) The phases of the phase-calibrator have been shifted (here by +96°) and any solutions for the phase in normal calibration can now be applied to the target.

### A.2.6 Calibration example from a data set

An example of the complete calibration process is given in this section. The observations were of the X-ray binary Cyg X-3, in spectral-line mode with 4 MHz, 128 channels for the target source. All observations were at the water maser line frequency of 22.235 GHz. A phase-calibrator 2005+403 was also observed but since it is rather weak at this frequency, the phase calibrator was observed in continuum mode of 16 MHz and 32 channels. The flux calibrator 4C39.25 was observed in both 16 and 4 MHz configurations and is distinguished in this example by 4C39.25(128) and 4C39.25(32) for the 4 MHz 128 channel data and 16 MHz 32 channel data respectively. SN refers to the solution tables, and CL refers to the calibration tables as explained above.

**Flux-calibration**

- 4C39.25(32), phase-cal, map, and continue this cycle until get a good model (if not a point source)
- Write SN(1) table using no other calibration, just a good model
- Copy SN(1) table to 4C39.25(128) and use this to write CL(2)
- Edit based on CL(2), delete CL(2) and re-write CL(2)
- Apply CL(2) to create in phase-cal only, SN(2)

**Phase-calibration**

- Concatenate 4C39.25(32) and 2005+405
- INDXR & SETJY on this file. These are AIPS tasks which create virgin calibration tables and set the zero-spacing flux for the source
- Copy SN(2) to this data set and write to CL(2) using 4C39.25 as the cal-source
- Edit 2005+405 and if necessary delete and re-create a new CL(2) table
- Use 4C39.25(32) to do a bandpass table with Stokes parameter I[5], dividing by channel zero, no calibration, scalar averaging[6]

[5] Polarisation of radio data comes in Left and Right circular polarisations. The cross-correlation (as default by MERLIN) of the polarisation between two pairs of telescopes creates the polarisation pairs: $L_1L_2$, $R_1R_2$ and the cross pairs $L_1R_2$ and $L_2R_1$. Stokes parameter, I, is the total power in all of the polarisation pairs, LL + RR + LR + RL.

[6] When creating the bandpass table, one can either scalar or vector average the data. Scalar

- Delete SN tables
- Calibrate again, amplitude and phase, use the 4C29.25(32) model applying this bandpass correction → CL(3)

**Mapping and fine tuning of the phase calibrator**

- Use CL(3), phase cal, to calibrate 2005+405 again
- Map and 'pray' for a point source
- Look at phase and continue calibrating 2005+405 until happy
- We would then have a 32-channel well-calibrated phase reference source. Use the best model to make a solution table SN(4) from CL(1) with amplitude and phase corrections

As an example of real calibration tables and solutions I provide a noisy calibrator and its solutions. Figure A.9 shows the closure phases with a noise cutoff of $3\sigma$. Many solutions were rejected due to the noise being higher than the pre-determined cutoff.

With a relaxation in the cutoff, more solutions can be found. Figure A.10 shows the closure phases for the calibrator with a cutoff of $0.5\sigma$. Here many more solutions are found, but the validity of the solutions are brought into question.

---

averaging takes the amplitude over the whole time period and calculates the average in each channel from that. Vector averaging uses the phase, but since the phase at that stage was un-calibrated (by the step above), vector averaging would have produced spurious results.

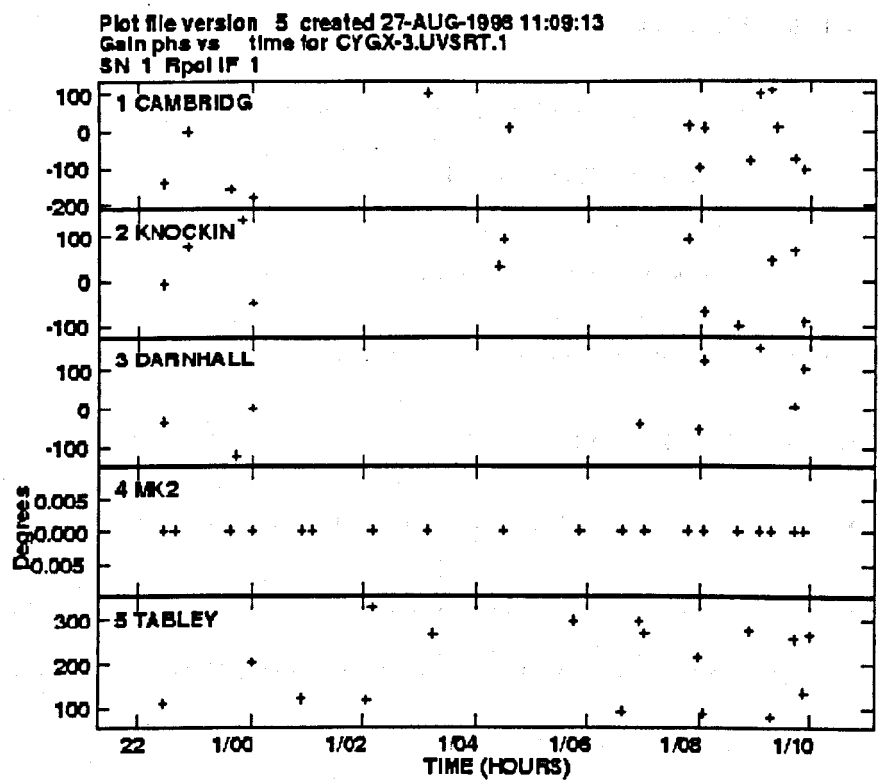


Figure A.9: The Solution table for a noisy calibrator. The S/N cut-off for these solutions was set at $3\sigma$ which caused many solutions to be rejected.

Using the phase offsets for the target after, I then calibrated the phase using the model above. The phase-solutions are shown in figure A.11.

To believe the phase solutions the phase jumps between one point and the next have to be small, otherwise interpolation may lead to wrong results. For much of the time the phase cannot be accurately followed, so it is best to reject these solutions. In effect, we were attempting to self-calibrate the data on a very weak source, which is not possible in practice. This was undertaken with

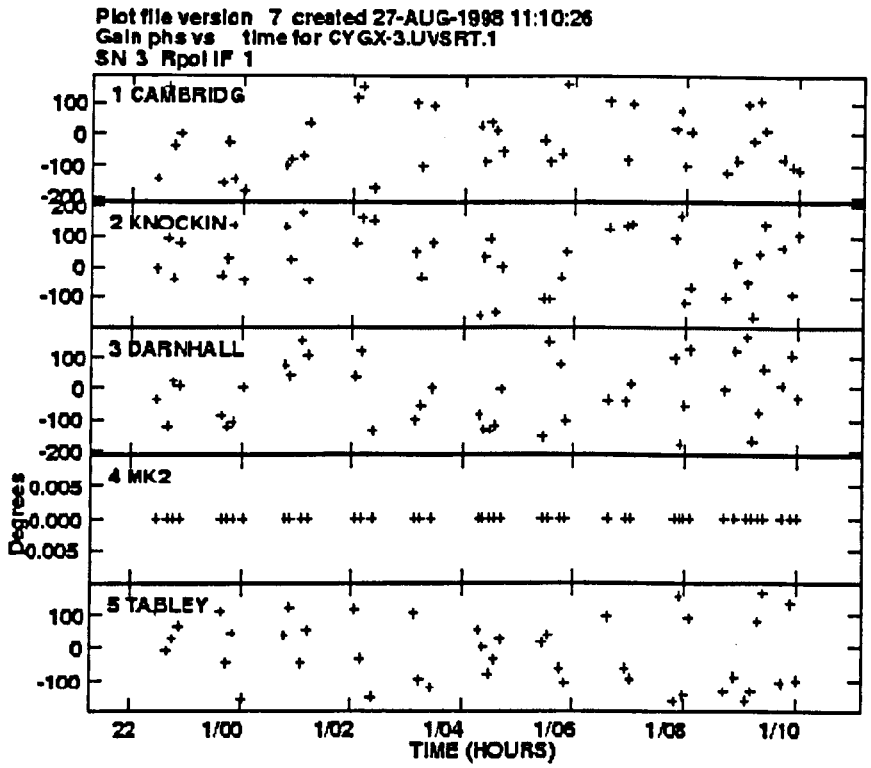


Figure A.10: The Solution table for the same calibrator, but with a S/N cut-off of $0.5\sigma$. Although the weaker constraint resulted in more solutions, one has to be very careful that the given solutions are genuine and can be used in further calibration.

this data to provide an example of noisy solutions.

## A.3 Mapping

With a well calibrated amplitude and phase visibility set for the target source, the most interesting interferometry stage is to map the source. As described in

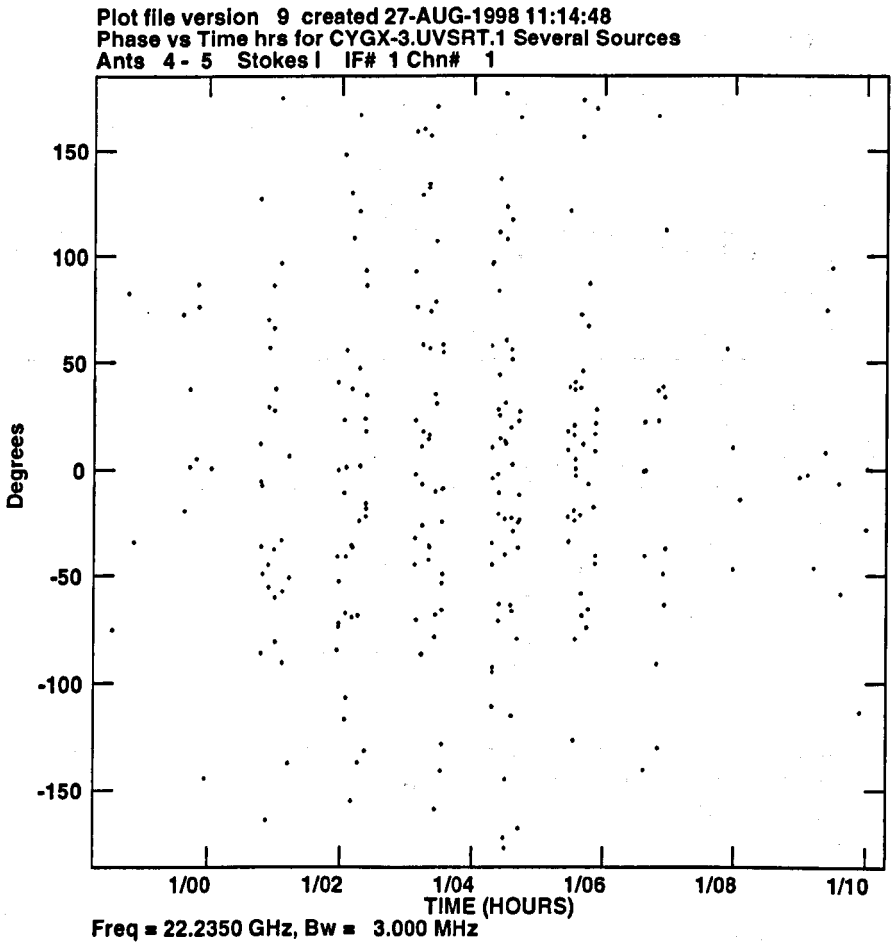


Figure A.11: Calibrated phases for the target based on the model used in the previous figure. One can see that the data is too noisy to provide calibration and the coherence time is less than the integration time. Data is either un-calibrated, or an alternative phase reference is needed.

equation set A.8, a direct Fourier inversion of the sampled visibilities does not produce the sky brightness distribution, but instead produces what is called the dirty map, $\mathcal{D}$. The true sky brightness distribution is convolved with the dirty beam, and the dirty beam can be recovered from a Fourier transform of the $uv$ sampling function. This can be represented by $V \times \mathcal{S} \Leftrightarrow I \otimes \mathcal{B} = \mathcal{D}$.

A non-linear restoration technique is used to recover the sky brightness distribution (herein after called *map*). It is usual to use the Högbom clean (CLEAN) algorithm for that task. The CLEAN algorithm is generally simple, but has grown in complexity to include reducing the effects of aberrations (such as the 3D sky approximation or bandwidth smearing).

Since the only observed quantities in mapping are the sampled sky distribution ($\mathcal{D}$) and the dirty beam ($\mathcal{B}$), an approximation to the true sky distribution is formed by the collection of delta-functions which when convolved with the dirty beam reproduce the dirty map, or

$$\uparrow_{1\ldots n} \otimes \mathcal{B} = \mathcal{D}. \tag{A.19}$$

At every $n^{\text{th}}$ iteration of the process, the peak in the residual image corresponding to $\mathcal{D} - (\uparrow_{n-1} \otimes \mathcal{B})$ is assigned a delta function. The amplitude of the delta function is a fraction of the largest residual in the image (technically called the *clean loop gain*), and the delta function is added to $\uparrow_{n-1}$ to form $\uparrow_n$. The process stops at either a pre-determined iteration limit $n$, or when the residual

RMS noise reaches a set level.

A more efficient form of the CLEAN algorithm is the Clark-clean algorithm. The Högbom clean requires $m^2$ operations on an $m \times m$ map. The Clark-clean algorithm uses the idea of major and minor cycles where a minor cycle builds up delta functions over a small region around the largest residuals of emission and calculates the full $m \times m$ map over major cycles, thus reducing the computation for wide-field convolutions. The minor cycle assumes emission is zero outside a few dirty beam widths, and effectivly builds up a map of minor-cycle patches.

The first technique for cleaning a dirty map is to recover the dirty beam. This is achieved by inverting the sampling function inherent in recording the visibilities. The sampling function consists of 3 terms:

- a term which consists of a binary representation of the $uv$ plane, a 1 represents a visibility was recorded at a given $uv$ co-ordinate;
- an anti-aliasing term which consists of a tapering function of the data usually a Gaussian centred on the origin;
- and finally a gridding term. This component grids the $uv$ data points so they are sampled on an $n \times n$ grid which allows the operation of a discrete Fourier transform of the $uv$ plane.

These three terms are well determined and can be expressed easily by the clean algorithms, so the dirty beam can be established. Figure A.12 show a typical $uv$ coverage for a source at declination $\delta = +40°$ observed for 12 hours with

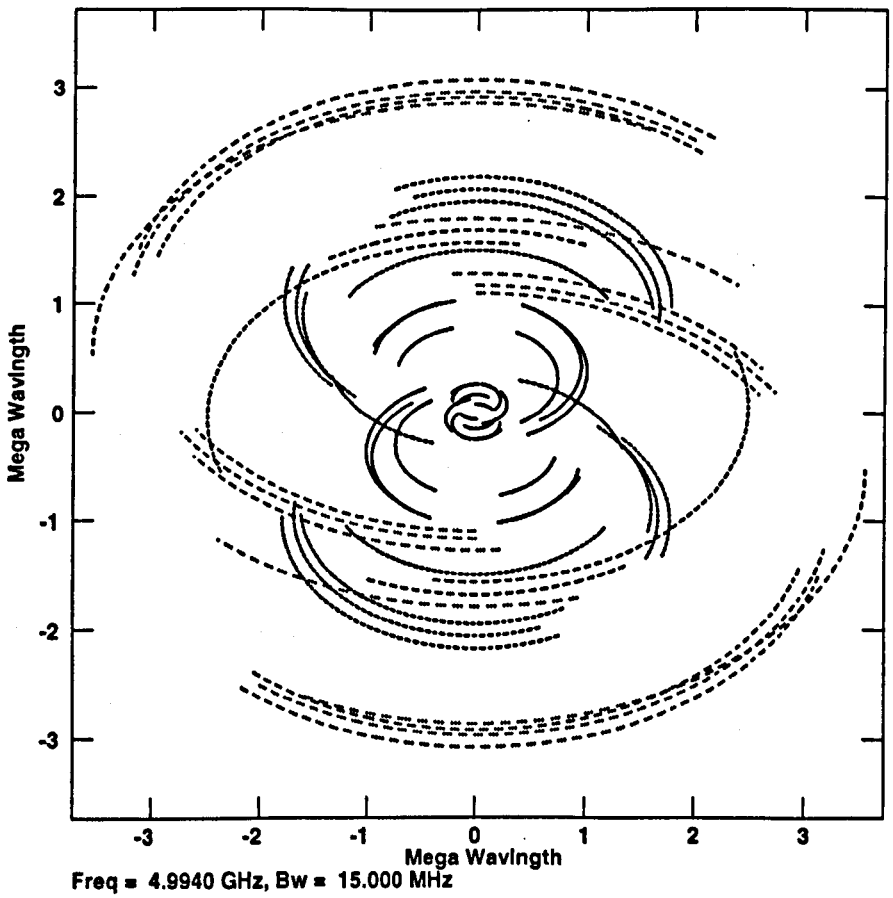


Figure A.12: The *uv* coverage for a source at declination $\delta = 40°$, observed for 12 hours with the MERLIN array. Gaps in the continuous track are due to observations of the phase-calibrator in a multi-calibration observing programme.

MERLIN. The *uv* plane coverage resembles closely the dirty beam shape and the beam is shown in figure A.13.

Figures A.14 and A.15 show a dirty map and subsequent cleaned map. The cleaning process went through 100 iterations which resulted in 42 clean compo-

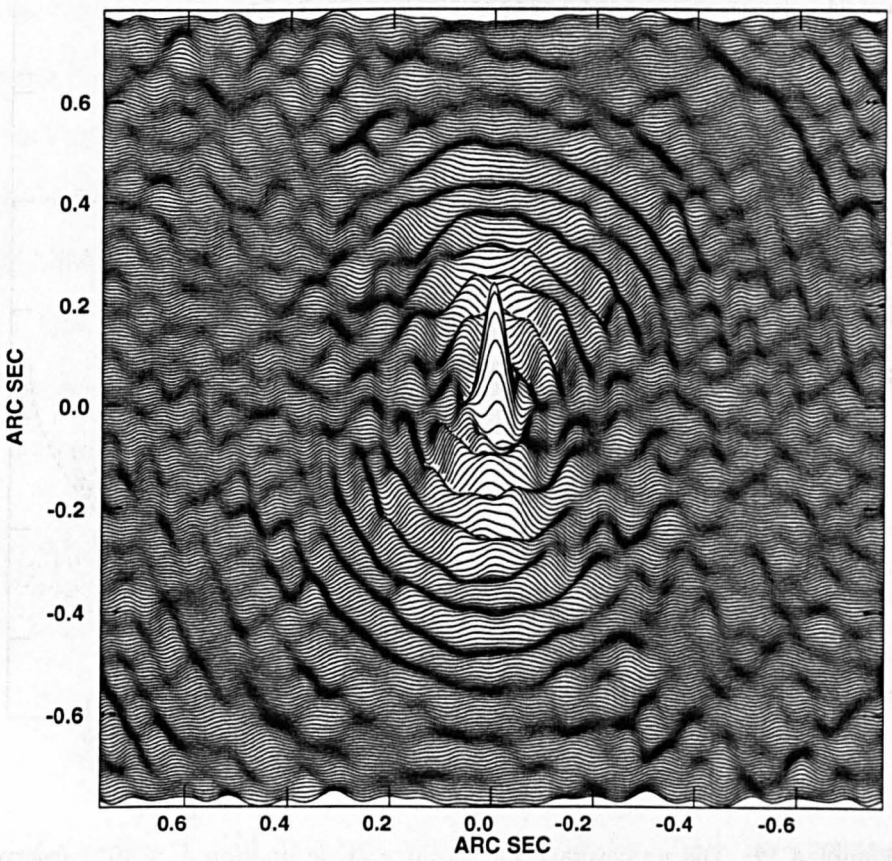


Figure A.13: The dirty beam from the *uv* coverage shown in figure A.12. An automatic scaling to a peak of 1 Jy has been performed, and the beam consists of positive and negative flux components.

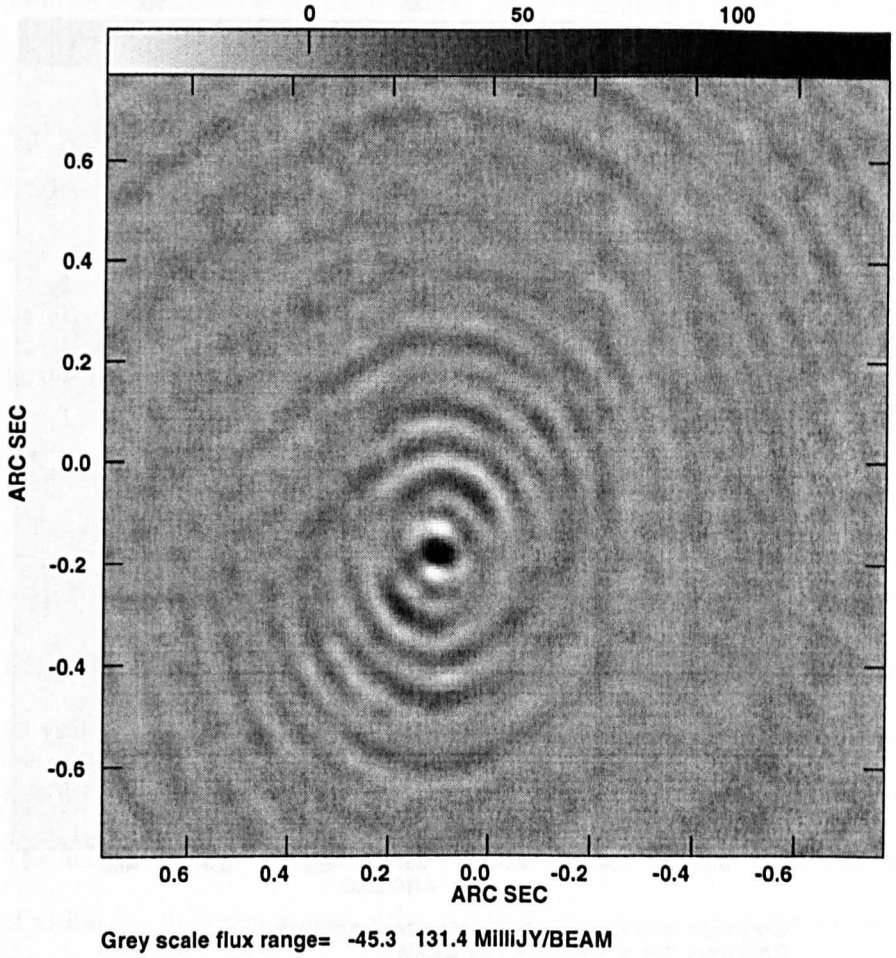


Figure A.14: A dirty map which is the direct Fourier transform of the visibilities multiplied by the sampling function.

nents (delta functions) of varying flux totalling a cleaned flux of 120 mJy. Delta functions are multiplied by the synthesised beam which has a size 51 × 41 mas at a position angle of 60 degrees.

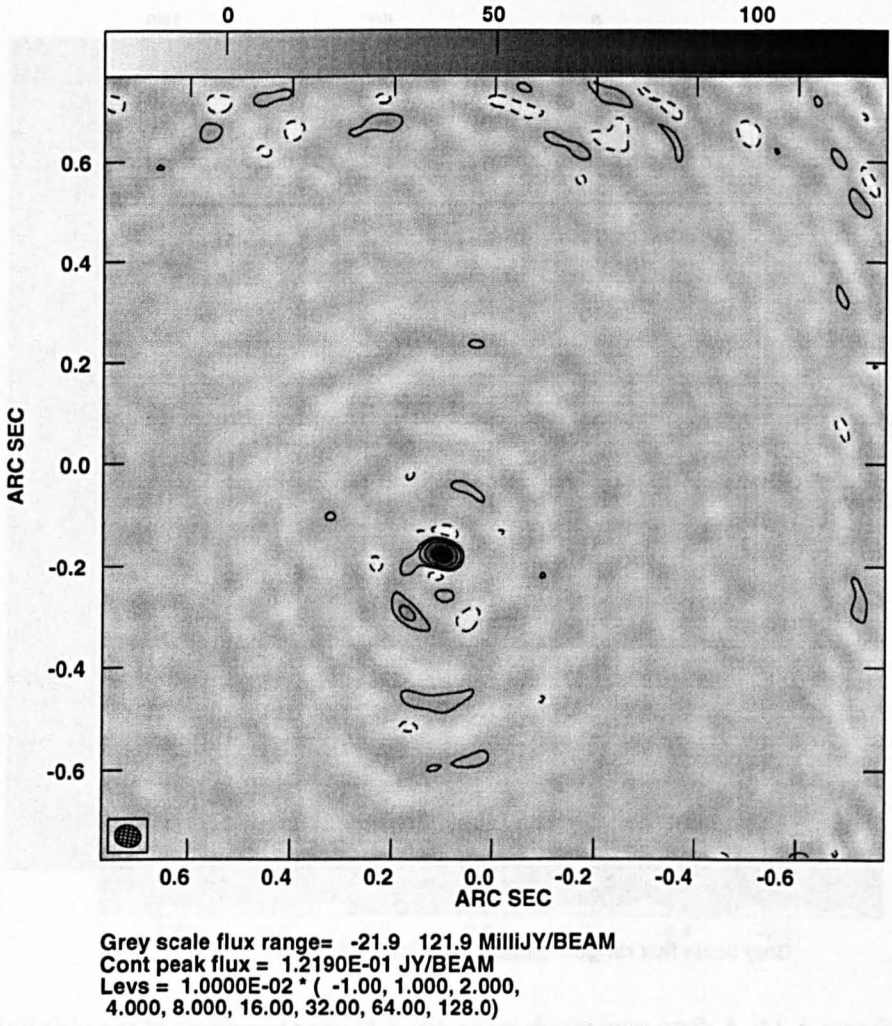


Figure A.15: A CLEANed map following the repeated subtraction of the dirty beam shown in figure A.13, at the brightest points of emission, building up delta components in the map. Each delta function is multiplied by the synthesised beam, which is the resolving power of the interferometer. The synthesised beam is $51 \times 41$ mas and is shown in the bottom right of the map. Contours are included with the grey-scale map to show the low variations in the background of the image.

The cleaning process uses several parameters to recover the sky brightness from an incomplete sample distribution. This is a non-linear technique of image restoration. The sampling function can be modified in order to create different restoring dirty beams and this represents differences in the *uv* plane sampling. This sampling function depends on weighting points differently in the *uv* plane and can vary from full *natural* weighting where all points are given a weight of 1, to full *uniform* weighting where points are weighted depending on their density in the *uv* plane.

An inversion of the naturally and uniformly-weighted visibilities create different dirty beams. The naturally weighted function applies the same weights to all visibility points. This has the consequence of amplifying low surface brightness features, but at the expense of increasing the size of the synthesised beam. The uniform weighting function however, weights each visibility by the density of visibilities in nearby spaces. This results in the inner part of the *uv* plane having a greater sampling and therefore lower weighting. Consequently this increases the spatial resolution of the synthesised beam, but at the expense of low surface brightness regions. There is therefore a trade off of resolution and quality of image. The choice of weighting functions is up to the individual, but for MERLIN data, which has large gaps in mid-range *uv* distance a more uniform weighting produces more realistic results.

### A.3.1 Mapping aberrations and artifacts

There are a number of artifacts that can arise in the mapping process. Some are small and are accounted for automatically by the mapping and cleaning algorithms, but some can produce alarming results.

#### Bandwidth smearing

The most noticeable aberration is that of bandwidth smearing, or chromatic aberration. The equation determining what is recorded on the visibility plane with the observation of a source intensity given by

$$V(u,v) = \iint I(x,y) \exp\left\{2\pi i(ux + vy)\right\} \, \mathrm{d}x \, \mathrm{d}y, \tag{A.20}$$

because the co-ordinate axes, $u$ and $v$ have the units of wavelength, any change of the observing wavelength will alter the projection on the $uv$ plane of the source distribution. A non-zero bandwidth will radially smear the points in the $uv$ plane with increasing severity with distance from the phase-centre. The reduction in intensity due to bandwidth smearing is calculated by

$$\frac{I}{I_0} = \sqrt{\frac{\pi}{2\ln 2\beta^2}} \operatorname{erf}\left(\sqrt{\ln 2}\beta\right) \tag{A.21}$$

where $\beta$ is a smearing function dependent on radial distance from the phase centre and is given by

$$\begin{aligned} \beta &= \frac{\Delta\nu}{\nu}\frac{\theta}{\Theta_B} \\ \beta &= 5 \times 10^{-3}\left(\frac{\Delta\nu}{\mathrm{MHz}}\right)\left(\frac{\theta}{\mathrm{arcsec}}\right) \end{aligned} \tag{A.22}$$

where $\Delta\nu$ and $\nu$ are the bandwidth and central frequency, $\theta$ is the distance from the phase centre and $\Theta_B$ is the synthesised beamwidth size (Thomasson et al. 1994). The second line is specifically applicable to MERLIN. Since $\Theta_B$ is dependent on frequency, the factor $\beta$ is independent of frequency. As an example, for MERLIN observations with a 15 MHz bandwidth at frequencies of a few GHz, a 1% reduction in amplitude occurs at $\theta = 3''$ and a 10% reduction occurs at $\theta = 9''$.

Bandwidth smearing is generally only a problem with continuum observations, as spectral line observations require as small a bandwidth as possible. CLEAN algorithms can account for this aberration by splitting up the continuum bandwidth into smaller sections and cleaning each section separatly. Continuum observations are automatically made up of many channels of a smaller bandwidth, so for example 256 MHz total bandwidth is a result of 32 channels each 4 MHz wide. The CLEAN algorithm takes each channel, maps and cleans it separately, then combines all channel maps to create the full 256 MHz image. This reduces the bandwidth smearing which can be significant for observations with large field of views.

Bandwidth smearing can be used to an advantage if individual channels are mapped and cleaned in this controlled way, which is the technique of *bandwidth synthesis*. As the frequency changes with the band, the $uv$ distance of a baseline, as measured in wavelengths, changes. If the frequency is low, there can be as much as 30% extra coverage of the $uv$ plane from the extra $uv$ points. This is demonstrated in figure A.16 which is of observations at a frequency $\nu = 1.667$ GHz and bandwidth $\Delta\nu = 132$ MHz using the Australia Telescope Compact Array. ATCA is a short baseline-instrument which can utilise very large bandwidths. This has the advantage that $uv$ distances of around 10–20 k$\lambda$ are recorded and bandwidth synthesis can contribute greatly.

**Other aberrations**

Other aberrations in interferometry exist, but for the average observation the effect is much less than with bandwidth smearing. However, in the context of this thesis it is worth mentioning them.

The aberration of the projection of the 3D sky onto a 2D plane gives rise to the '3D sky' aberration. The difference in the sky sphere and the image plane is $1 - \cos\theta$. If a source is offset from the pointing center (which is generally the same as the phase centre) then the intensity drops by a fraction $f$ where

$$f^{1/2} = \ln 2 \, \frac{\theta}{\Theta_{\rm B}^2} \tag{A.23}$$

where angles are measured in radians. If angles are given in arcsec then a 1%

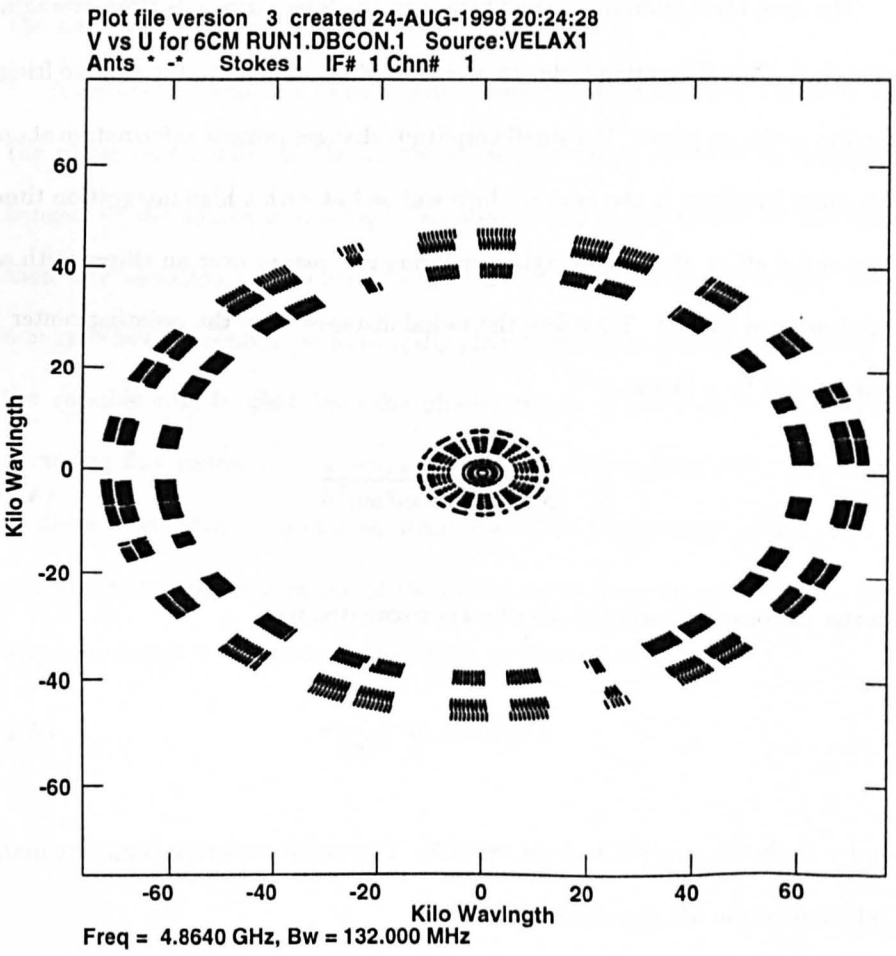


Figure A.16: An example of bandwidth synthesis with the Australia Telescope Compact Array. Observations were taken at 1667 MHz with a bandwidth of 132 MHz. Since $uv$ spacing is small as a consequence to the small baselines, with a large bandwidth there is significant spread in the $uv$ plane (gaps in the circumference are due to gaps in the observing programme).

reduction occurs at $\theta = 150\sqrt{\Theta_B}$ and a 10% reduction occurs at $\theta = 280\sqrt{\Theta_B}$. This is small for most observations.

The final aberration mentioned here, and the least serious, is time-averaging smearing. This aberration is due to averaging changes in amplitude due to fringe cutting in the $uv$ plane. The small amplitude changes provide information about the small structure in the image, which will be lost with a high integration time. The radial effect of time-averaging smearing is constant over an ellipse with an axial ratio of cosec $\delta$. Therefore the radial distance from the pointing center is compressed by a factor

$$\theta' = \sqrt{l^2 + m^2 \sin^2 \delta} \tag{A.24}$$

so the factor of smearing, $f$, can be approximated to

$$f \simeq 3.4 \times 10^{-5} \frac{\theta'}{\Theta_B} \tau \tag{A.25}$$

and $\tau$ is the integration time in seconds. The radial smearing is approximatly half that of the 3D sky aberration.

### Variable source flux

The first assumption of aperture synthesis is that the flux of a source is constant over the synthesis time. With most aperture synthesis observations completed in around 12 hours, this assumption holds true for nearly all sources. However,

with the more energetic binaries like Cyg X-3 and GRS 1915+105 the flux can change by a factor of up to 10 in as little time as a few hours. This would violate the assumption above, and lead to mapping artifacts.

A natural consequence of an interferometric array is that sources offset from the phase centre will vary in amplitude as the source cuts the interferometer fringes. If the source is varying in amplitude due to the nature of the source, then any variation in amplitude will result in artifacts in the image; usually non-zero delta functions symmetrically placed about the phase-centre (or about the variable core if offset from the phase-centre). If the source in question is a varying flux source with a resolved core then this varying flux will result in artifacts resembling a bipolar jet structure. Care is therefore needed, and the options are to take 'snapshots' of the source, or to form images from the times when the flux is constant or only varying by around 10%.

# Bibliography

Alexander, P. (1987). A study of spectral ageing in the radio galaxy 3C 234 and its implications. *MNRAS*, 225:27.

Baan, W. (1985). Powerful extragalactic masers. *Nature*, 315:26–31.

Baan, W. and Haschick, A. (1984). The peculiar galaxy IC 4553 - VLA-A observations of the OH megamaser. *ApJ*, 279:541–549.

Baan, W., Wood, P., and Hascick, A. (1982). Broad hydroxyl emission in IC 4553. *ApJ*, 260:L49–L52.

Barrett, A., Schwartz, P., and Waters, J. (1971). . *ApJ*, 162:L101.

Belloni, T., Mendez, M., King, A., van der Klis, M., and van Paradijs, M. (1997). A unified model for the spectral variability in GRS 1915+105. *ApJ*, 488:L109.

Blandford, R., McKee, C., and Rees, M. (1977). Super-luminal expansion in extragalactic radio sources. *Nature*, 267:211–216.

Bowers, R. and Deeming, T. (1984). *Astrophysics I: Stars.* Jones and Bartlett publishers.

Brinkman, A., Parsignault, D., Giaconni, R., H., G., Kellogg, E., Schreier, E., and Tanabaum, H. (1972). Cygnus X-3. *IAU Circ.*, 2446.

Castro-Tirado, A., Geballe, T., and Lund, N. (1996). Infrared Spectroscopy of the Superluminal Galactic Source GRS 1915+105 During the September 1994 Outburst. *ApJ*, 461:L99.

Chaty, S., Mirabel, I., Duc, P., Wink, J., and Rodríguez, L. (1996). Infrared and millimeter observations of the galactic superluminal source GRS 1915+105. *A&A*, 310:825–830.

Cherepashchuk, A. and Moffat, A. (1994). Cyg X-3 as a benchmark for fundamental properties of Wolf-Rayet stars. *ApJ*, 424:L53.

Cheung, A., Rank, D., Townes, C., Thornton, D., and Welch, W. (1969). Further microwave emission lines and clouds of amonia in our Galaxy. *Nature*, 221:626.

Cohen, R. (1989). Compact maser sources. *Rep. Prog. Phys.*, 52:881–943.

Collison, A. and Nedoluha, G. (1995). A nonlocal calculation of circumstellar OH maser emission. *ApJ*, 442:311.

Cooke, B. and Elitzur, M. (1985). Water masersin late-type stars. *ApJ*, 295:175–182.

Eenens, P. and Williams, P. (1994). Terminal velocities of Wolf-Rayet winds from infrared HeI lines. *MNRAS*, 269:1082.

Eggleton, P. (1983). Approximations to the radii of Roche lobes. *ApJ*, 268:368–369.

Elitzur, M. (1992). *Astronomical masers*, volume 170 of *Astrophysics and Space Science Library*. Kluwer.

Ergma, E. (1995). Sipral-in and coalescence. In Alpar, M., Kiziloğlu, U., and van Paradijs, J., editors, *The lives of the Neutron Stars*, volume 450 of *NATO ASI series*, pages 449–462. Kluwer.

Fender, R.P,(1995). *Multiwavelength behaviour of Cygnus X-3 and related objects*. PhD thesis, The Open University.

Fender, R.P., Bell Burnell, S.J., Garrington, S., Spencer, R.E., and Pooley, G.G. (1995). Simultaneous millimetre and radio observations of Cygnus X-3 in a quiescent radio state. *MNRAS*, 274:663–638.

Fender, R.P., Bell Burnell, S.J., and Waltman, E.B. (1997a). The radio-jet X-ray binaries. *Vistas Astron.*, 41:3–13.

Fender, R.P., Garrington, S., McKay, D., Muxlow, T.W.B., Pooley, G.G., Spencer, R.E., Stirling, A.M., and Waltman, E.B. (1998a). MERLIN observations of GRS 1915+105. In Ogley, R.N. and Bell Burnell, S.J., editors, *2nd Workshop in Galactic Sources with Relative Jets*, New AR.

Fender, R.P., Garrington, S., McKay, D., Muxlow, T.W.B., Pooley, G.G., Spencer, R.E., Stirling, A.M., and Waltman, E.B. (1998b). MERLIN observations of GRS 1915+105. *MNRAS (preprint)*.

Fender, R.P., Hanson, M., and Pooley, G.G. (1999). Infrared spectroscopic variability of Cygnus X-3 in outburst and quiescence. *MNRAS*, in press: .

Fender, R.P. and Pooley, G.G. (1998). Infrared synchrotron oscillations in GRS 1915+105. *MNRAS*, 300:573.

Fender, R.P., Pooley, G.G., Brocksopp, C., and Newell, S.J. (1997b). Rapid infrared flares in GRS 1915+105: evidence for infrared synchrotron emission. *MNRAS*, 290:L65–L69.

Frank, J., King, A., and Raine, D. (1992). *Accretion power in astrophysics*. Cambridge University Press.

Giacconi, R., Gorenstein, P., Gursky, H., and Waters, J. (1967). An X-ray survey of the Cygnus region. *ApJ*, 273:L119–L127.

Greenhill, I. (1997). Masers in Active Galactic Nuclei. In Peterson, B., Cheng, F.-Z., and Wilson, A., editors, *Emission Lines in Active Galaxies: New methods and techniques*, number 159 in IAU Col, page 394. San Francisco.

Greiner, J., Morgan, E., and Remillard, R. (1996). ROSSI X-Ray timing explorer obsevations of GRS 1915+105. *ApJ*, 473:L107.

Harding, A. and Muslimov, A. (1998). Particle acceleration zones above pulsar polar caps: electron and positron pair formation fronts. *ApJ*, 508:328–346.

Hjellming, R. and Johnston, K. (1981). Structure, strength, and polarization changes in radio source SS433. *Nature*, 290:100–107.

Ho, L. (1998). Supermassive Black Holes in Galactic Nuclei: Observational Evidence and Astrophysical Consequences. In Chakrabarti, S., editor, *Observational evidence for Black Holes in the Universe.* ?

Hughes, P. and Miller, L. (1991). Introduction: Synchrotron and inverse-Compton radiation. In Hughes, P., editor, *Beams and Jets in Astrophysics*, number 19 in Cambridge Astrophysics Series, page 1. Cambridge University Press.

Jenness, T. and Lightfoot, J. (1997). *SCUBA users guide.* Starlink, sun/216 edition.

Johnson, H. (1966). Astronomical measurements in the infrared. *Ann. Rev. Astron. Astrophys.*, 4:193.

Kardashev, N. (1962). Nonstationariness of spectra of young sources of non-thermal radio emission. *Soviet Astronomy - AJ*, 6(3):317.

Kellermann, K. (1966). . *Austr. J. Phys.*, 19:195.

Lang, K. (1980). *Astrophysical formulae.* Springer-Verlag, Berlin.

Leahy, J.P. (1991). Interpretation of large scale extragalactic jets. In Hughes, P., editor, *Beams and jets in astrophysics*, number 19 in Cambridge Astrophysics Series, page 100. Cambridge University Press.

Maisack, M., Kendziorra, E., Pan, H., Skinner, G., Englhauser, J., Reppin, C., Efremov, V., and Sunyaev, R. (1994). Compton reflecton in Scorpius X-1 and Cygnus X-3? *ApJS*, 92:473.

Mason, K., Cordova, F., and White, N. (1986). Simultaneous X-ray and infrared observations of Cyg X-3. *ApJ*, 306:700–706.

Massi, M., Paredes, J., Estalella, R., and Felli, M. (1993). High resolution radio map of the X-ray binary LSI+61° 303. *A&A*, 269:249–254.

Mirabel, I., Dhawan, V., Chaty, S., Rodríguez, L., Martí, J., Robinson, C., Swank, J., and Geballe, T. (1997). Accretion instabilities and jet formation in GRS 1915+105. *A&A*, 330:L9–L12.

Mirabel, I. and Rodríguez, L. (1994). A superluminal source in the Galaxy. *Nature*, 371:46.

Mirabel, I., Rodríguez, L., Chaty, S., Sauvage, M., Gerard, E., Duc, P.-A., Castro-Tirado, A., and Callanan, P. (1996). Infrared observations of an energetic outburst in GRS 1915+105. *ApJ*, 472:L111.

Miyoshi, M., Moran, J., Herrnstein, J., Greenhill, L., Nakai, N., Diamond, P.,

and Inoue, M. (1995). Evidence for a black hole from high rotation velocities in a sub-parsec region of NGC4258. *Nature*, 373:127.

Molnar, L., Reid, M., and Grindlay, J. (1988). VLBI observations of expansion in Cygnus X-3. *ApJ*, 331:494–508.

Newell, S.J. (1996). *Multi-wavelength observations of X-ray binaries.* PhD thesis, The University of Manchester.

Newell, S.J., Garrett, M., and Spencer, R.E. (1998). Superluminal Expansion and Contraction in Cyg X-3. *MNRAS*, 293:17.

Ogley, R.N., Bell Burnell, S.J., and Newell, S.J. (1997). Comments on the superluminal motion in Cyg X-3. *MNRAS*, 285:187.

Pacholczyk, A. (1970). *Radio Astrophysics.* Freeman, San Francisco.

Pooley, G.G. and Fender, R.P. (1997). The variable radio emission from GRS 1915+105. *MNRAS*, 292:925–933.

Richards, A.M.S. (1997). *Circumstellar envelopes of red supergiant stars.* PhD thesis, The University of Manchester.

Rieke, G. and Lebofsky, M. (1985). The interstellar extinction law from 1 to 13 microns. *ApJ*, 288:618.

Rybicki, G. and Lightman, A. (1979). *Radiative processes in astrophysics.* Wiley.

Sams, B., Eckart, A., and Sunyaev, R. (1996). Near-infrared jets in the galactic microquasar GRS 1915+105. *Nature*, 382:47–49.

Schmutz, W., Geballe, T., and Schild, H. (1996). Cyg X-3: evidence for a Black Hole. *A&A*, 311:L25.

Snyder, L. and Buhl, D. (1974). Detection of new stellar sources of vibrationally excited silicon monoxide maser emission at 6.95 millimeters. *AJ*, 197:329–340.

Spencer, R.E. (1979). A radio jet in SS433. *Nature*, 282:483–484.

Spencer, R.E., Swinney, R., Johnston, K., and Hjellming, R. (1986). The 1983 September radio outburst of Cygnus X-3: relativistic expansion at 0.35*c*. *ApJ*, 309:694.

Stewart, R., Caswell, J., Haynes, R., and Nelson, G. (1993). Circinus X-1 - A runaway binary with curved radio jets. *MNRAS*, 261:593–598.

Sylvester, R., Barlow, M., Nguyen-Q-Rieu, Liu, X.-W., Skinner, C., Cohen, R., Lim, T., Cox, P., Truong-Bach, Smith, H., and Habing, H. (1997). Detection by ISO of the far-infrared OH pumping lines in IRC+10420. *MNRAS*, 291:L42–L46.

Taylor, J., Fowler, L., and McCollough, P. (1979). Measurements of general relativistic effects in the binary pulsar PSR 1913+16. *Nature*, 277:437–440.

Terasawa, N. and Nakamura, H. (1995). Ionization structure in Cygnus X-3: Iron anomaly in Wolf-Rayet stars? *A&A*, 295:443.

Thomasson, P., Garrington, S., Muxlow, T.W.B., and Leahy, J.P. (1994). *MERLIN user guide*. University of Manchester.

Tingay, S., Jauncey, D., Preston, R., Reynolds, J., Meier, D., Murphy, D., Tzioumis, A., McKay, D., Kesteven, M., Lovell, J., Campbell-Wilson, D., Ellingsen, S., Gough, R., Hunstead, R., Jones, D., McCollough, P., Migenes, V., Quick, J., Sinclair, M., and Smits, D. (1995). Relativistic motion in a nearby bright X-ray source. *Nature*, 374:141.

van Buren, D. and Kong, M. (1996). ISOCAM-LW dark frames are simply related. Technical report, IPAC.

van Kerkwijk, M., Charles, P., Geballe, T., King, D., Miley, G., Molnar, L., van den Heuvel, E., van der Klis, M., and van Paradijs, J. (1992). Infrared helium emission lines from Cygnus X-3 suggesting a Wolf-Rayet star companion. *Nature*, 355:703–705.

van Kerkwijk, M., Geballe, T., King, D., van der Klis, M., and van Paradijs, J. (1996). The Wolf-Rayet counterpart of Cygnus X-3. *A&A*, 314:521.

Waltman, E.B., Foster, R., Pooley, G.G., Fender, R.P., and Ghigo, F. (1996). Quenched radio emission in Cygnus X-3. *AJ*, 112:2690.

Waltman, E.B., Ghigo, F., Johnston, K., Foster, R., Fiedler, R., and Spencer, J. (1995). The evolution of outbursts in Cygnus X-3. *AJ*, 110:290.

Weaver, H., Williams, D., Dieter, N., and Lum, W. (1965). Observations of a strong unidentified microwave line and of emission from the OH molecule. *Nature*, 208:29.

Westphal, Kristian, J., Huchra, J., Shectman, S., and Brucato, R. (1972). Search for the visible counterpart of the September 2, 1972 radio outburst in Cygnus. *Nature*, 239:134.

Wilkinson, P., Narayan, R., and Spencer, R.E. (1994). The scatter broadened image of Cygnus X-3. *MNRAS*, 269:67.

Wiren, S., Valtaoia, E., Teresranta, H., and Kotilainen, J. (1992). A complete sample of Northern Hemisphere active galactic nuclei - Differences in flux and spectra at high radio frequencies. *AJ*, 104:1009–1017.

Wittels, J., Knight, C., Shapiro, I., Hinteregger, H., Rogers, A., Whitney, A., Clark, T., Hutton, L., Marandino, G., Neill, A., Rönnäng, B., Rydbeck, O., Klemperer, W., and Warnock, W. (1975). Fine structure of 25 extragalactic radio sources. *ApJ*, 196:13.

Wright, A. and Barlow, M. (1975). The radio and infrared spectrum of early-type stars undergoing mass loss. *MNRAS*, 170:41 – 51.